Karlsruhe Institute of Technology

Shrinkage and Creep of Alkali-Activated Slag Concrete: new insights through advanced multiscale characterization and micro-mechanical modeling

Zur Erlangung des akademischen Grades eines

Doktors der Ingenieurwissenschaften
(Dr.-Ing.)

von der KIT-Fakultät für
Bauingenieur-, Geo- und Umweltwissenschaften
des Karlsruher Instituts für Technologie (KIT)

genehmigte
Dissertation

von

Richard Caron

Tag der mündlichen Prüfung: 06.07.2023

Referent: Prof. Dr.-Ing. Frank Dehn
Korreferentin: Assoc. Prof. Dr. Marijana Serdar

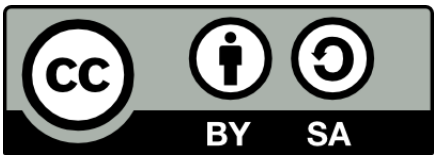

Science sans conscience
n'est que ruine de l'âme

Knowledge without the ability to understand
is but the poverty of the soul

Science without conscience
is but the ruin of the soul

Rabelais, *Pantagruel*, 1532

Acknowledgments

Before being any technical project, my Ph.D. has been the fruit of intense collaborations and human exchanges. I would like to thank all the people who have been on my side for the past three years.

I want to express my deepest gratitude to Prof. Dr.-Ing Frank Dehn for his uninterrupted encouragement throughout my research project. He supported me to think out of the box and accepted the questioning that I eventually put on the table. Without his constant trust, advice and suggestions, this work would not have been possible.

Special thanks to Assoc. Prof. Dr. Marijana Serdar for her involvement and kind support during the whole project.

I would like to say sincere thanks to my committee members, Prof. Dr. Katja Emmerich, Prof. Dr. Frank Schilling and Prof. Dr.-Ing. habil. Thomas Seelig for their support.

I could not have undertaken this research project without Dr. Ravi Patel who helped me to structure my Ph.D. and pushed me to explore the different technical aspects investigated in this work.

Many thanks to Prof. Dr. John Provis for the exciting exchanges about mix design, calorimetry, and pore structure, but also on the role of concrete in society and holistic problems.

Thanks to Prof. Dr. Susan Bernal and Dr. Maria Criado for sharing their data on isothermal calorimetry and for their review and advice on this topic.

Special thanks to Prof. Dr. Barbara Lothenbach and Dr. George-Dan Miron for their kindness and support on thermodynamic modeling and chemical experiments.

Vielen Dank an Dr. rer. nat. Andreas Bogner für seine wertwollen Hinweise hinsichtlich meiner experimentellen Untersuchungen, insbesondere bezüglich der Nanoindentation. Danke an Jonas Kaltenbach, M.Sc. für die Unterstützung beim Polieren der Proben am IFG.

Je tiens également à remercier Dr. Matthieu Vandamme pour ses explications à propos de l'indentation.

Ein besonderer Dank gilt auch Dr.-Ing. Vladislav Kvitsel und Dr.-Ing. Engin Kotan für ihre Unterstützung und ihre detaillierten Hinweise, die mir sehr geholfen haben.

Un grand merci au Prof. Dr. Guillaume Habert pour les échanges fructueux sur la place du béton pour nos sociétés et sur les solutions auxquelles il faudrait réfléchir pour réduire les catastrophes à venir.

Thanks to Dr.-Ing. Anja Buchwald for the exciting discussions on the place of concrete in society and on the levers to mitigate its impacts.

Darüber hinaus danke ich dem ganzen Baustofflabor für die notwendige Hilfe bei jeder Betonage und den zahlreichen Baustoffprüfungen, insbesondere Dipl.-Ing. Astrid Paul, Marcel Weinhold, Patrick Wehres, Wolfgang Graf und Joachim Held. Danke an alle meine Kollegen in der Messtechnik und der Werkstatt für ihre beachtliche Arbeit. Mein Dank gilt ebenso meinen Kolleginnen und Kollegen aus dem Physik- und Chemielabor, insbesondere Andrea Ochs, Ute Kiefer und Stephan Gehlsen für ihre Unterstützung während meiner Promotion.

Vielen Dank an meine Institutskolleginnen und -kollegen Dr.-Ing. Michael Vogel, Dr.-Ing Frank Altmann, Dipl.-Geol. Petra Schlager, Eva Wünschel, M.Sc. und die Promovierende Annika Schultheiß, M.Sc., Dipl.-Geol. Dipl.-Min. Astrid Hirsch, Attila Ibuk, M.Sc., David Alos Shepherd, M.Sc., Julia Sonntag, M.Sc., Matthias Mohs, M.Sc., Moritz Boxheimer M.Eng. und Sebastian Bruckschlögl, M.Sc. Besonderen Dank an Vanessa Mercedes Kind, M.Sc. für die Zusammenarbeit insbesondere beim Doktoranden-Forum und an Carla Neuhaus, M.Sc. für ihre endlose Unterstützung. Un ringraziamento speciale a Laura Rossi, M.Sc. per il tuo incoraggiamento negli ultimi tre anni. Herzlichen Dank auch an Jan Höffgen, M.Sc., Felix Dathe, M.Sc., Sarah Lamparter, M.Sc. und Dr. rer. nat. Nadja Werling für ihre Hilfe in den letzten Jahren.

Thanks to all my colleagues from DuRSAAM Yubo Sun, M.Sc., Zhiyuan Xu, M.Sc., Ivana Krajnovic, M.Sc., Lazar Azdejkovic, M.Sc., Dr. Antonino Runci, Olivera Bukvic, M.Sc., Andres Arce, M.Sc. and Tamara Chidiac, M.Sc. Special thanks to Cassandre Le Galliard, M.Sc., Anastasija Komkova, M.Sc. and Luiz Miranda de Lima, M.Sc. for the numerous discussions and exchanges during the whole project.

Many thanks also to Prof. dr. ir. Stijn Matthys, Prof. dr. ir. Geert de Schutter, Assoc. Prof. Dr. G. Guang Ye, Prof. Dr. Triantafillou Thanasis and Assoc. Prof. Dr. Catherine Papanicolaou.

Ein besonderes Dankeschön gilt allen Studierenden, die ich im Rahmen ihrer Abschlussarbeit betreuen durfte: Thies Buschke, B.Sc., Mithat Akdas, B.Sc., Anna-Katharina Hauser, M.Sc., Ann-Kathrin Kraus, M.Sc., Hangyu Liu, M.Sc.und Lars Kehrle, B.Sc. Mein Dank gilt auch den Studierenden, die mich bei den experimentellen Untersuchungen unterstützt haben.

I would like to extend my sincere thanks to all my friends who supported me during these intense years. Special gratitude goes to Laury, Paloma, Julia, Capucine, Anatole, Antoine, Leïla, Baptiste, Pierre, Johanna, Emma, ... Un grand merci à ma famille, en particulier mon frère Lucien, et mes sœurs Alice et Mathilde, Chris également, ma mamie et mes parents pour leurs encouragements.

Abstract

This thesis aims to accurately model short-term and long-term strains of alkali-activated slag (AAS) concrete. In addition to the elastic strain when a load is applied, cementitious materials experience shrinkage and creep over time. Shrinkage is defined as a volumetric change in the material without any load. Creep corresponds to delayed deformations due to sustained loading.

Slag is a by-product of the steel industry that can be used to make concrete when it is mixed with an alkali solution. In this thesis, two AAS mixes with different sodium-silicate solutions are studied on both paste and concrete.

In the first part of this thesis, the shrinkage and creep of AAS concrete are compared to existing engineering models for ordinary Portland cement (OPC). In sealed conditions, the results show that AAS strains are much higher than that of OPC. The engineering models can be extended using scaling factors. Due to the higher drop in internal relative humidity in AAS concrete compared to OPC, both drying shrinkage and drying creep are relatively low. For these strains, the existing models are not satisfactory to describe the shrinkage of AAS. For this reason, the microstructure of AAS must be investigated in detail.

The second part of this thesis deals with the understanding of the evolution of the microstructure of AAS. Reaction kinetics is monitored by isothermal calorimetry and scanning electron microscopy, and the degree of reaction is predicted using single-particle models. The phase assemblage is determined at several ages with complementary experimental methods. The main reaction product is Calcium-Aluminum-Silicate-Hydrates (C-A-S-H). Depending on the mix, different secondary products are characterized. The experimental data allows for the validation of thermodynamic modeling using the Pitzer ion activity model and CASH+, cemdata18 and zeolite20 databases. From the coupled kinetics-thermodynamics model, the phase assemblage of AAS can be predicted for any given time.

In the third part of this thesis, analytical micromechanics-based multi-scale homogenization methods are used to predict the strains of AAS paste and concrete. Concrete is heterogeneous at several scales and the description of the microstructure must cover the following components: matrix of reaction products, capillary water, unreacted slag, sand and aggregates. The volume fractions of the phases are obtained from the coupled kinetics-thermodynamics model presented in the second part of the thesis. The mechanical properties of each phase are obtained from nano-indentation tests. The multi-scale model is validated against experimental Young's modulus tests on both paste and concrete.

Thereafter, the creep behavior at the nano-scale is downscaled from the results of creep measured on concrete. The results indicate that the observed creep of AAS concrete is due to deviatoric stresses applied to the matrix of reaction products. The contact creep modulus obtained from nanoindentation tests provides a good estimation of the long-term creep rate of the matrix of reaction products. The short-term creep could correspond to water movement modeled by a Kelvin-Voigt unit while the long-term creep could be due to shear stresses of C-A-S-H or to the preferential orientation of C-A-S-H along the compressive stress.

Finally, shrinkage is predicted by the extended capillary theory. This theory hypothesizes that the capillary pressure generates elastic strains and delayed strains in the microstructure. The analysis also reveals that the consumption of ions from the initial alkali solution is an important mechanism of the shrinkage of AAS.

Zusammenfassung

Ziel der vorliegenden Arbeit ist die Modellierung von Kurzzeit- und Langzeitverformungen von Beton aus alkalisch-aktiviertem Hüttensand (AAS). Zusätzlich zu der elastischen Verformung bei Belastung erfährt Beton Schwinden und Kriechen. Als Schwinden werden volumetrische Verringerungen des Materials ohne Belastung bezeichnet. Kriechen beschreibt die zeitabhängigen bleibenden Verformungen unter konstanter Dauerlast.

Hüttensand ist ein Nebenprodukt der Stahlindustrie, welches nach Reaktion mit einer Alkalilösung als Bindemittel für Beton eingesetzt werden kann. In dieser Arbeit werden zwei AAS-Mischungen mit unterschiedlichen Natriumsilikatlösungen sowohl als Leim als auch als Beton untersucht.

Im ersten Teil der Arbeit werden das Schwinden und Kriechen von AAS-Beton mit bestehenden Ingenieurmodellen für Beton unter Verwendung von Portlandzement (OPC) verglichen. Ergebnisse an versiegelten Proben zeigen, dass die Verformungen der AAS-Betone deutlich höher sind als die von OPC-Beton und dass die Ingenieurmodelle mithilfe von Skalierungsfaktoren angepasst werden können. Aufgrund des höheren Abfalls der inneren relativen Feuchtigkeit im AAS-Beton im Vergleich zu OPC sind sowohl das Trocknungsschwinden als auch das Trocknungskriechen bei AAS-Beton geringer. Jedoch sind die Ingenieurmodelle nicht ausreichend genau, um das Schwinden von AAS-Beton zu beschreiben. Daher muss die Mikrostruktur von Beton unter der Verwendung von AAS im Detail untersucht werden.

Der zweite Teil der Arbeit befasst sich mit dem Verständnis der Mikrostrukturentwicklung von AAS. Die Reaktionskinetik wird durch isotherme Kalorimetrie und Rasterelektronenmikroskopie bestimmt und der Reaktionsgrad anhand von Einzelpartikelmodellen vorhergesagt. Die Phasenzusammensetzung wird zu verschiedenen Zeitpunkten mit komplementären experimentellen Methoden erfasst. Die Hauptprodukte sind Calcium-Aluminium-Silikat-Hydrate (C-A-S-H). Je nach Mischung werden unterschiedliche Nebenprodukte charakterisiert. Diese experimentellen Daten ermöglichen die Validierung der thermodynamischen Modellierung unter Verwendung des Pitzer-Ionenaktivitätsmodells und der Datenbanken CASH+, cemdata18 und zeolite20. Mit Hilfe des gekoppelten Kinetik-Thermodynamik-Modells wird die Entwicklung der Phasenzusammensetzung von AAS vorhergesagt.

Im dritten Teil der Arbeit werden analytische Mikromechanik-basierte Multiskalen–Homogenisierungsmethoden verwendet, um die Verformungen von AAS-Leim und -Beton vorherzusagen. Beton ist auf mehreren Skalen heterogen und die Beschreibung der Mikrostruktur muss die folgenden Komponenten umfassen: Reaktionsproduktmatrix, Kapillarwasser, unreagierte Hüttensandpartikel, Sand und grobe Gesteinskörnungen. Die

Volumenanteile der Phasen werden mit Hilfe des im zweiten Teil der Arbeit vorgestellten gekoppelten Kinetik-Thermodynamik-Modells berechnet. Die mechanischen Eigenschaften jeder Phase werden aus Nanoindentationstests erhalten. Das Multiskalenmodell wird anhand von experimentellen Elastizitätsmodulprüfungen sowohl an Leim als auch an Beton validiert. Anschließend wird das Kriechverhalten auf Nanoebene von den an Beton gemessenen Kriechergebnissen herunterskaliert. Die Ergebnisse zeigen, dass das beobachtete Kriechen von AAS-Beton auf deviatorische Spannungen zurückzuführen ist, die auf die Reaktionsproduktmatrix wirken. Der aus Nanoindentationstests erhaltene Kontaktkriechmodul gibt eine gute Abschätzung der Langzeit-Kriechgeschwindigkeit der Reaktionproduktmatrix. Das Kurzzeit-Kriechen könnte einer durch eine Kelvin-Voigt-Einheit modellierten Wasserbewegung entsprechen. Das Langzeit-Kriechen könnte auf Scherspannungen innerhalb der C-A-S-H-Phasen oder auf einer bevorzugten Ausrichtung von C-A-S-H entlang der Druckspannung beruhen.

Abschließend wird das Schwinden durch die erweitere Kapillartheorie vorhergesagt. Diese Theorie beruht auf der Annahme, dass der Kapillardruck sowohl elastische Verformungen als auch verzögerte auftretende Kriechverformungen in der Mikrostruktur erzeugt. Die Analyse zeigt zudem, dass der Verbrauch von Ionen aus der anfänglichen Alkalilösung einen wichtigen Mechanismus des Schwindens von AAS darstellt.

Contents

List of Publications

Some parts of this Ph.D. have already been published:

- Caron, R., Patel, R. A., Dehn, F. Activation kinetic model and mechanisms for alkali-activated slag cements *Construction and Building Materials* **323**, 126577 (2022). DOI: 10.1016/j .conbuildmat.2022.126577
- Caron, R., Patel, R. A., Dehn, F. Extension of the *fib* MC 2010 for basic and drying shrinkage of alkali-activated slag concretes. *Structural Concrete* **23**, 3960–3973 (2022). DOI: 10.1002/suco.202100901
- Caron, R., Patel, R. A., Miron, G. D., Le Galliard, C., Lothenbach, B., Dehn, F. Microstructure development of slag activated with sodium silicate solution: Experimental characterization and thermodynamic modeling. *Journal of Building Engineering* **71**, 106398 (2023). DOI: 10.1016/j .jobe.2023.106398
- Caron, R., Patel, R. A., Bogner, A., Dehn, F. Multi-scale experimental investigation and analytical micro-mechanical modeling to determine Young's modulus of alkali-activated slag concrete. *Construction and Building Materials* **383**, 131272 (2023). DOI: 10.1016/j .conbuildmat.2023.131272
- Caron, R., Patel, R. A., Dehn, F. Experimental study on basic and drying creep for an alkali-activated slag concrete and comparison with existing creep models. *Structural Concrete* **64**, 1-16 (2023). DOI: 10.1002/suco.202300134

In addition, other contributions have been made within the framework of this thesis.

Articles as second author:

- Provis, J. L., Caron, R., Miranda de Lima Junior, L. AACM and Low Carbon Concrete. *ICT YEARBOOK 2022-2023*, 116–124. (2023)

Conference papers:

- Caron, R., Dehn, F., Microstructure and mechanical properties of slag activated with sodium silicate. *Proceedings of International Structural Engineering and Construction* 9 (2022)
- Caron, R., Patel, R. A., Dehn, F., Applicability of the *fib* Model Code 2010 for predicting strength and shrinkage behaviour of alkali-activated slag concrete. *Proceedings of the 14th fib PhD Symposium in Civil Engineering* (2022)

Conferences:

- Caron, R., Dehn, F. Microstructure and mechanical properties of slag activated with sodium silicate. *Proceedings of International Structural Engineering and Construction* 9 (2022)
- Caron, R., Patel, R. A., Dehn, F. Applicability of the *fib* Model Code 2010 for predicting strength and shrinkage behaviour of alkali-activated slag concrete. *Proceedings of the 14th fib PhD Symposium in Civil Engineering* (2022)
- Caron, R., Dehn, F. Mechanical Properties and shrinkage of Alkali-Activated Slag Concrete. *4th International Rilem Conference on Microstructure Related Durability of Cementitious Composites: Microdurability 2020* (2020)
- Caron, R. Kinetic analysis of alkali-activated slag with waterglass. *MAI/ITECH Workshop: Micromechanics of cementitious materials* (2021)

Posters:

- Caron, R., Patel, R. A., Dehn, F. Time-evolution of microstructure and elastic properties of alkali-activated slag paste and concrete with coupled kinetic-thermodynamic-micromechanical modelling. *4th International Conference on the Chemistry of Construction Materials* (2022)

1 Context

For the past 200 years, human societies have been able to prosper thanks to their increased capability of converting energy. Their development was accompanied by increased life expectancy, reduced starvation, faster and cheaper means of transport and globalization with exchanges between all the parts of the world. The past 200 years have also been marked by an intensified amount of innovative and revolutionary discoveries made possible by the exploitation of ever more materials in variety and quantity. It is also in the past 200 years that anthropogenic stresses on the environment have been the most severe. Assessing the question of sustainability, i.e. the ability of people to co-exist in the long-term on Earth, requires that the human environmental footprint stays lower than the biocapacity of Earth to regenerate. Should this not be respected, human presence on Earth will be naturally self-regulated.

In this chapter, it is argued that material research can play a role in developing a sustainable society if, and only if, it is anchored in a broad reconsideration of the functioning of society. To that end, a global contextualization of means of production, extraction, consumption and externalities of anthropogenic activities is necessary. The chapter is split into four sections. The first one provides a broad picture of the impacts of human activities on the environment and human beings. It is also pointed out that the exploitation of natural resources is becoming more complicated. The second section discusses the incompatibility between the system paradigms and sustainability. It is emphasized that personal interests often go against the common good. Questionable mechanisms govern political choices targeting business-as-usual. It is also shown that business-as-usual has terrible consequences for most of the population. The third section deals with potential alternatives to the current organization of society to reduce the different anthropogenic negative externalities. It is emphasized that these alternatives are all dependent on a common denominator, namely the redefinition of human true needs. The fourth section illustrates how the search for sustainable solutions in the cement industry can not be decoupled from the search for sustainable solutions on a larger scale.

1.1 1001 alarming observations

In this section, the impact of anthropogenic activities on the function of modern society is analyzed. The section starts with global observations of environmental changes and their causes. It is then followed by impacts on human beings. Finally, it is emphasized that even without the two first issues, the sustainability of society is compromised by the fact that material extraction is becoming more challenging.

1.1.1 Planetary boundaries and environmental impact of human activities

The equilibrium of the Earth's system in the Holocene era has allowed the development of agriculture and the relative stability of modern societies. However, several upheavals in the different natural cycles and phenomena have been observed in the past decades. The Stockholm resilience center theorized the nine planetary boundaries that should not be exceeded to maintain this equilibrium (see Figure 1.1 [1]). Five of them are exceeded today: climate change, biodiversity, chemical flows, chemical pollution and land use. The CO_2 concentration in the atmosphere is 412 ppm in 2020, higher than the target of 350 ppm [1] because of the more than 1000 Gt of CO_2 released into the atmosphere between 1970 and 2016 [2]. Over the same period, the population sizes of mammals, birds, amphibians, reptiles and fish decreased by 68 % [3]. Additionally, the rate of biodiversity loss is more than one order of magnitude higher than what it should be [1]. The flows of nitrogen and phosphorous are between two and three times higher than the limit for chemical pollution. More than 70 % of the Earth's land is damaged [4] and the amount of damaged forest is too high [1]. The sixth planetary boundary concerns ocean acidification, caused by absorption of atmospheric CO_2. It has been accelerating in the past decades and the pH value of oceans has dropped by 0.1 over the past two centuries [5]. The seventh planetary boundary is ozone depletion. In the eighties, the ozone layer was in a worrying state, but with the suspension of ozone-depleting substances, especially refrigerants, the depletion has ended and the layer is progressively recovering. The quantification of freshwater use, the eighth planetary boundary, is difficult but the size of arid zones on the planet is increasing [6, 7]. Finally, the ninth planetary boundary, namely the atmospheric aerosol loading, has not been quantified yet.

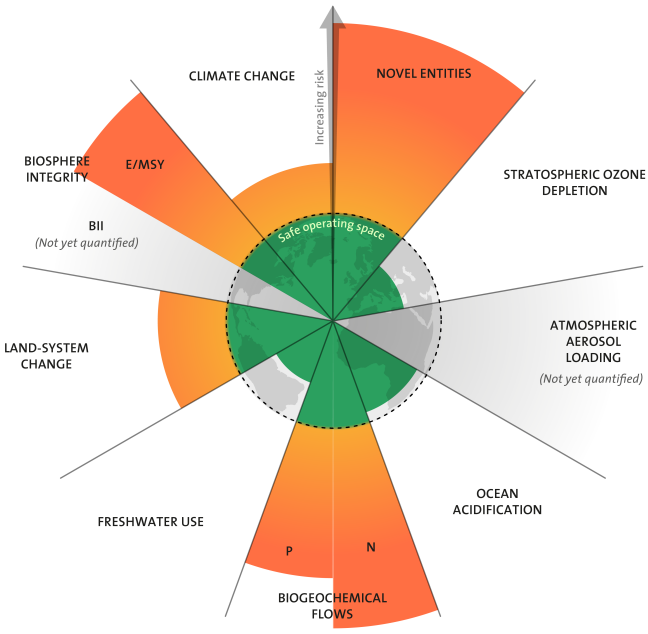

Figure 1.1: Planetary boundaries identified in [1]. Exceeding them greatly increases the risk of destabilizing natural cycles.

Human activities are the primary causes of the breaking of the different planetary boundaries. Firstly, the expansion of human societies requires ever more exploitation of untouched areas and the surface of unspoiled nature has been drastically reduced over the past decades. The current land use on Earth is provided in Figure 1.2 [4]. Land-system changes have impacts on most of the other planetary boundaries. Since soils are polluted by human activities and natural habitats are destroyed (e.g. deforestation in Amazonia [8] or cropland and pasture [4]), there is a reduction in the natural habitats for many species of wildlife, which then become endangered or extinct. In oceans fishing is responsible for destroying biodiversity, depleting fish populations and other populations by bycatch and increasing waste pollution [9]. Secondly, damages are also due to resource extraction. The extraction of fossil fuels destroys landscapes, affects biodiversity and generates local pollution [10, 11]. For instance, fracking gas pollutes water tables and causes small earthquakes [12]. This is also true for the extraction of other materials like metals. Stewart sums up the systemic impacts of mines [13]: "Across the world, mining contributes to erosion, sinkholes, deforestation, loss of biodiversity, significant use of water resources, dammed rivers and ponded waters, wastewater disposal issues, acid mine drainage and contamination of soil, ground and surface water, all of which can lead to health issues in local populations". Water pollution due to runoffs, infiltrations, spillage of chemical products, mining dam failure, releases of CO_2 emissions, sulfur dioxide, nitrogen dioxide, carbon dioxide, fine particles, dioxins, furans, polycyclic aromatic hydrocarbons (PAH) and benzene [14] can be added to the list. The extractions of these raw materials are exploited by other sectors such as transport and the digital world, whose direct CO_2 emissions are also major with 8.4 Gt CO_2eq and 2.1 Gt CO_2eq per year, respectively [15, 16]. Oil extraction also allowed the skyrocketing consumption of plastic which, in combination with the lack of waste management, gave birth to the seventh continent in the Pacific Ocean also named the great Pacific garbage patch, where ocean plastics converge inside an area of 1.6 million km^2 [17].

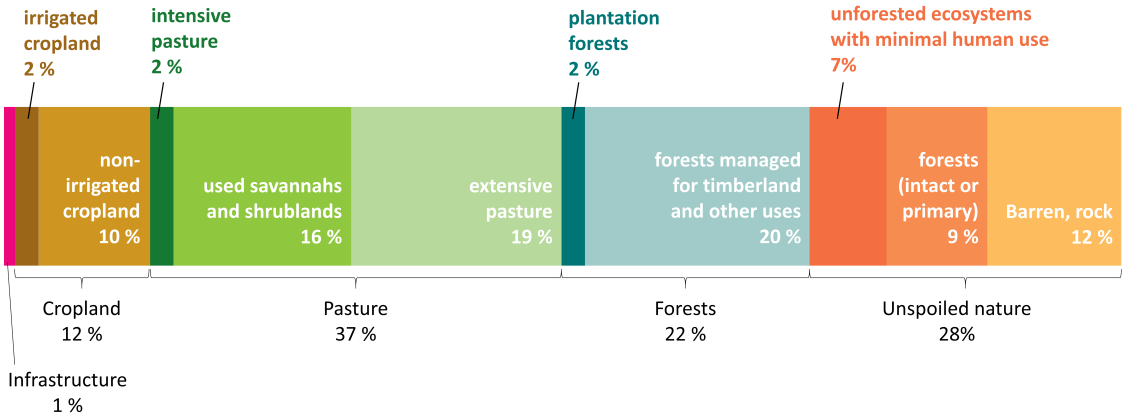

Figure 1.2: Land use on Earth split into infrastructure, pasture, forests and unspoiled nature. Adapted from [4].

The increase in human-caused stress on the environment destabilizes the Earth's system. On the one hand, the overshoot day, defined as the calendar date on which humanity's ecological footprint is higher than the planet's biocapacity, is coming earlier and earlier [18]. In 1970, the overshoot day was on December 29 meaning that human activities were already damaging Earth's regeneration capacities at that time. At that time, 3.5 billion humans were living on Earth and the world's GDP per capita was around $800 per year. Yet, in 2022, more than 8 billion humans live on Earth and in 2018 the GDP per capita was around $11 000. Accordingly, the overshoot day is nowadays much earlier. In 2022, it was on July 28. Thus, the question of demography must also be put on the table. On the other hand, the accumulation of greenhouse gas leads dangerously to exceeding tipping points from which mechanisms of climate change become self-perpetuating [19]. In this case, climate change would become even more irreversible and unmanageable.

1.1.2 Suffering populations because of human activities

Beyond their consequences on nature, anthropogenic activities are also harmful to living conditions, working conditions and human health.

The first ones to be affected by the productivist system are local populations. Many activities generate pollution, which companies do not deal with. For instance, garment factories pollute water with microplastics and chemicals from the different treatments of fibers and these pollutants are released into rivers [20]. Extraction of raw materials also impacts local populations. For example, in the lithium triangle (Chile - Argentina - Bolivia), groundwater is exploited for the extraction of lithium at the expense of the inhabitants [21]. Expropriation is another threat to populations living above deposits of coveted resources. Inhabitants of the German village Lützerath have been expelled by authorities to extend the coal mine Garzweiler II. In Brazil, the rights of indigenous populations in Amazonia have been neglected for years by projects like deforestation or dams [22]. In China, the construction of the Three Gorges Dam implied the expropriation of 1.24 million residents [23]. In the United States, indigenous populations were dispossessed of their territories by settlers willing to extract more materials [24].

In addition to the suffering of local populations, the rights of the workforce are also not respected. Child labor continues to this day and has been reported all over the world, especially in Africa [25]. In China, the company Foxconn, a subcontractor of Apple, parks and detains between 200 000 and 300 000 workers [26]. Slavery has also been divulged within Uyghur camps on behalf of Zara, H&M or Adidas for instance [27]. In the garment industry, and specifically in the fast fashion industry, workers are underpaid and often have no social security [28].

Consumables also have impacts on human health. Food products full of sugar, pesticides or other chemicals present health dangers from diabetes to cancers or disturbance of the hormonal system [29–31]. Moreover, plastics and per- and poly-fluoroalkyl substances (PFAS) pollute every ecosystem and are dangerous for human health [32, 33]. The propagation of these products could also explain the global trend of reduced men's sperm quality

between 1973 and 2018, as shown by a recent study [34]. Addictive behaviors like alcohol consumption, cigarette consumption, sports betting and social media have been and are still being promoted despite their well-known damaging impacts on mental health [35, 36]. In addition, the toxicity of human activities impacts everyone. The fine particle thresholds are higher than the recommendations of the World Health Organization (WHO) [37, 38] mainly due to wood combustion for heating, industrial processes, agriculture and vehicles. As a consequence, 800 000 people died of air pollution in Europe in 2019 [39]. The accumulation of health hazards due to excessive consumption of poisonous goods could explain why life expectancy does not increase anymore in the USA or in Europe since 2010 [2, 15]. Since 2020, life expectancy has even been decreasing due to the covid-pandemic and other pandemics could be expected due to the release of frozen viruses from melting permafrost [40] or from the increasing risks due to contact with wildlife [41].

1.1.3 Accessibility of resources

Another aspect of the sustainability of societies lies in the correct exploitation of resources to avoid resource depletion in too short a period of time. For the past 2000 years, societies have extracted more resources in greater diversity. This has been made possible by improvements in geological mapping, extraction technologies and large investments. This increase has been particularly true for the past fifty years during which, despite effective miniaturization, larger quantities per capita are consumed [42] (see Figure 1.3). However, the concentration of metals in exploited mines is decreasing [14, 43] which means that more water, energy and chemical reactants are needed to extract the same quantity of metal [14, 44, 45]. Therefore, the extraction of metals becomes more difficult. Accessibility to water also becomes problematic. On the one hand, the amount of water stored in glaciers is depleted due to climate change [46] and they can not act as water reservoirs in summer. On the other hand, groundwater shortage is expected due to increased reliance on groundwater pumping [47].

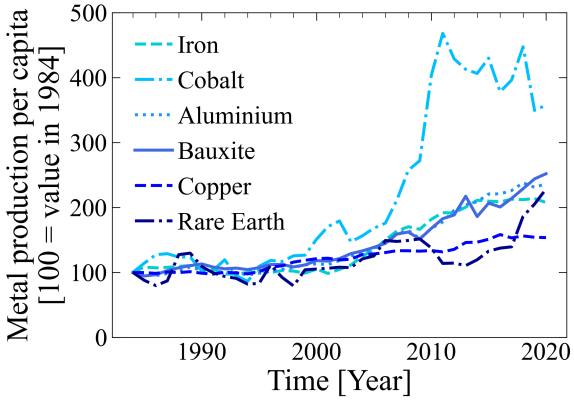

Figure 1.3: Increase in the consumption of selected metals per capita since 1984 [42]

The reduced access to resources is particularly problematic since the functioning of contemporary societies has become crucially dependent on them. Water is not only necessary to provide drinking water or for irrigation but it is also crucial for industry and metal extraction, as stated previously. Likewise, crops are not only used for feeding the population or pasture but are also used to produce biofuels. Other planned transitions such as the use of renewables and electric cars require huge amounts of materials, and especially metals [48]. According to the Net Zero Emission scenario from the International Energy Agency (IEA), three billion electric vehicles should be on the road in 2050 with a total storage capacity of 3 TWh [48]. Yet, 53.2 kg of copper and 39.9 kg of nickel are required for the fabrication of an electric car still according to the IEA [48]. This means that the IEA plans the extraction of at least 150 Mt of copper and 120 Mt of nickel in 2050. Comparatively, 20 Mt of copper and 2.5 Mt of nickel were extracted worldwide in 2020 [42]. Hence, beyond the ecological issues associated with extraction, the investments and the costs in energy and water will be tremendous.

Finally, contemporary societies are prospering thanks to the availability of cheap oil. Fossil fuels are at the core of every sector: extraction [45], heating [49], agriculture [50], plastics [51], transport [51], concrete [52], etc.. In 2021, more than 80 % of the primary energy consumed comes from fossil fuels [53]. Certain sectors are even in synergy thanks to oil consumption, for instance, industry and transport. More transport induces more potential for the industry, and more industrial products induce better vehicles to transport faster, further and cheaper. However, two limits exist to the availability of cheap oil. The first limit is the accessibility of oil and gas reservoirs. The energy return on investment for oil and gas has been decreasing for the past decades, meaning that even more energy is needed to extract fuel, which itself delivers energy [54]. The second limit is the finiteness of fossil fuel reserves. The peak for conventional oil has been reached in 2007 and oil prospecting has been less and less successful [55]. For natural gas, the peak was reached in 2020 [55]. Due to these two limits, less energy will be available each year from now on and peak oil and peak gas eventually lead to peak metal, peak steel, peak concrete, peak plastic, etc..

In summary, human activities have already caused five of nine planetary boundaries to be broken and destabilized natural cycles. In addition, they result in many social issues all over the world regarding living conditions, working conditions and human health. Finally, even if the previous end-of-chain externalities were solved, the systemic organization of modern societies relies on resources, which are becoming more difficult to extract and whose accessible reserves are eventually depleted.

1.2 1001 system drifts

The observations raised in the previous section are the consequences of a systemic organization that has not been designed to last, but rather to meet immediate interests. In this section, different aspects of non-sustainable structures and policies are described. Then, the focus is placed on the present and expected consequences of the current system.

1.2.1 When private interests matter more than the common good

The first problem to be illustrated here is the unequal distribution of wealth and the increasing gap between the wealthiest and the poorest. According to the "World Inequality Report 2022" [56], the richest 10 % of people in the world possess 76 % of wealth worldwide, while the poorest 50 % possess only 2 % [56]. The within-country differences in income between the richest and the poorest rose between 1980 and 2020. The merit of the richest being richer is questionable knowing that annual tax losses are evaluated at US$483 billion worldwide and that the main abuses come from companies and wealthy individuals hiding assets and income streams offshore [57]. Wealth concentration induces power concentration in the hands of a few persons or groups of people. Without denying its indisputable virtues, the democratic system in the Occident is not immune to abuses of power like revolving doors [58], conflicts of interest [59, 60] or corruption at the highest national and international levels [61]. In addition, the functioning of representative democracy is endangered when political decisions are motivated by private interests. For example, the lobby "Eamonn Bates Europe Public Affairs" is funded by companies using a lot of plastic. It opposed propositions for a deposit return scheme in Europe [62] because it would, of course, cost companies currently making or using plastic more. Consequently, this lobby is delaying concrete action to stop filling the seventh continent for example (see Section 1.1.1). The Corporate Europe Observatory recalls the worrying dominance of corporate lobbies within the European Union which influence the decision-making process [59].

Systemic use of power can also be used in research and science by merchants of doubt to defend private interests rather than the common good [63]. Among the textbook cases, the tobacco industry funded lots of research topics related to cancer to put into doubt the fact that smoking increases the risk of cancer [63, 64]. This industry successfully managed to delay thirty years of regulations although scientific consensus on the health impacts was reached in the seventies. Another textbook case regards the use of pesticides and their toxicity for bees. As for cigarettes, many research projects were funded by the pesticide industry to find other culprits for dying bees. What is very characteristic of this case is that in the end, sincere scientists looking at all the generated scientific results were unable to say clearly why bees had disappeared in Europe [65]. Nevertheless, most of the pesticides have eventually been banned in the European Union thanks to a final consensus on their harmfulness. Recent studies also disclosed that the main oil and gas companies were fully aware of the causes and consequences of climate change as early as the seventies [66]. Yet, revealing the results of their internal research would have given them no excuse not to act to reduce their impact. It would have been an act of self-destruction or the very least reduced their profits, and so they pretended to know nothing about it. Among these companies, Exxon can be mentioned to have developed one of the most accurate models for climate change, far better than the initial models of the IPCC for instance [66]. Incidentally, all these examples show that contemporary science and research are far from being neutral or objective.

It is also important to recall that despite the increased awareness and conviction of citizens and politicians to reduce CO_2 emissions, a new record of CO_2 emissions has been reached in 2022 [67]. And CO_2 is only a small part of the problem, as stated in Section 1.1.1. Consumers carry some of the responsibility for the current social and environmental disasters. For example, participating in the consumerist society and looking for the smallest prices leads to social and environmental dumping, i.e. the delocalization of means of production to countries where regulations are more permissive. To fight against these obvious cognitive dissonances, i.e. the contradiction between principles and actions, consumers can choose to ignore the impact of their consumption [68]. They can also be tempted to compensate for their most damaging behaviors by engaging in green tourism on the other side of the world or buying carbon compensation after an airplane journey. But these compensations can be seen as a refusal to think for oneself and to realize that the root problem is flying, the root problem is perpetuating destructive behaviors.

Hence, the responsibility is shared by people from all different walks of life. Politicians, consumers, industries, producers, publicists, scientists, etc. take part voluntarily or involuntarily in the social and environmental destruction and bias the official paradigms and visions for the future of societies. In the next section, some incoherencies of the paradigms of the system are analyzed.

1.2.2 Incoherencies of the paradigms of the system

Contemporary society has been founded on a set of problematic beliefs which are today deeply anchored in everyday life. The first belief is that technology is the answer to any emerging issues like shortages, depletion or pollution. However, the history of the past 200 years shows that technology answered some problems and greatly simplifies the life of some people today, but it also has a huge cost and generates other problems such as for fossil fuels, cars, planes, pesticides or all kinds of chemicals (see Sections 1.1.1 and 1.1.2). Moreover, the rate of innovation, defined as the number of patents per worker, for the economy as a whole is decreasing, as emphasized in a few studies [69, 70]. It means that new innovations are achieved with the participation of more researchers because of the increased complexity of products. In the end, the cost of innovation becomes higher and, from a purely economic point of view, it could become unattractive to innovate to solve problems. In addition, the rebound effect, i.e. the reduction of the beneficial effects of a measure or a technology due to the transfer of environmental impact from one activity to another, must be assessed and limited for any innovation. A few recent examples show disappointing results. For instance, a recent study showed that insulating housing has not brought any significant reduction in energy consumption in the UK [71]. In a newly insulated home, residents prefer to increase the temperature to increase their comfort instead of heating to the same temperature as beforehand. The same kind of rebound effect has been observed in the automotive industry. Despite the development of more efficient engines, only slight emission reductions are observed in comparison to fifty years ago, since cars are heavier, bigger and faster [72]. In 2023, the development of electric cars without envisaging a reduction of the vehicle characteristics (size, maximal power and autonomy)

and fleet size is questionable. Without denying the better performance of electric cars in terms of CO_2 emissions on a life cycle, the central question is not the type of vehicle but the reorganization of mobility and transport [73]. Solving partly the CO_2 emissions of cars generates other issues such as resource management (see Section 1.1.3). Thus, technological development should not carry any promise of sustainability. Technology is just a tool and must be evaluated with its use and associated quantities.

The second belief is that an energy transition to renewables is possible. Although, for the past 200 years, the exploitation of new types of energy has only had a cumulative effect rather than a replacement effect (see Figure 1.4 [74]).

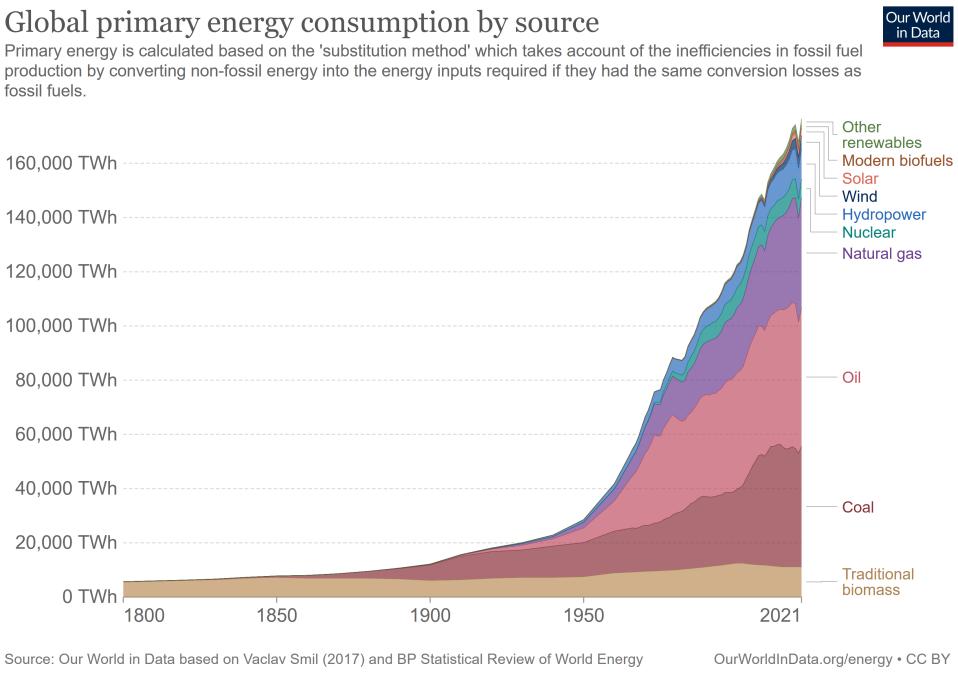

Figure 1.4: World consumption of primary energy [74]. Since 1800, an accumulation of sources of energy rather than a transition from one source to another can be observed.

As Fressoz explains it [75], instead of replacing coal consumption, oil consumption was added to it just as coal had not replaced wood. The same difficulties are faced for the "clean energy transition", supported by the European Green Deal for example [76]. Firstly, renewables are fabricated thanks to the use of non-renewable energies for the extraction, refinement and transport of metals. Secondly, they have a limited service life (e.g. 20-30 years for wind turbines [77, 78]), so the term “renewable” is only true for the usage and not for the whole life cycle assessment. Thirdly, 1 kWh obtained with a solar panel does not equal 1 kWh contained in a hundred mL of oil, as the latter is more easily transportable, transformable and storable [79]. Fourthly, it is also worth mentioning that, just like the extraction of coal and wood facilitated each other through a positive loop during the 19^{th} century, the extraction of fossil fuels is eased by the use of renewables. Among the classical examples that can be quoted, Aramco, the state-owned oil company of Saudi

Arabia, installed 126 695 photovoltaic panels to enable the extraction of fossil fuels [80]. Another example is the Hywind Tampen project of the Norwegian company Equinor. It is the largest offshore wind farm worldwide and is used to power offshore oil and gas platforms [81]. In light of the above, the figures of 2019 of the Statistical Review of World Energy [53] are not surprising: oil consumption increased by 2.0 EJ, natural gas increased by 3.0 EJ, coal decreased by 0.9 EJ and renewables increased by 3.2 EJ (around 40 % of the increase). Thus, the worldwide development of renewables is slower than the development of fossil fuels.

The third belief regards green finance and green investments. The report "Banking on climate chaos 2022" reported that $742 billion were invested in fossil fuels in 2021. Despite the engagement of most of the banks to reach net zero by 2050, investments in fossil fuels have increased between 2016 and 2019. Yet, no new investment in fossil fuel projects is a requirement to reach net zero by 2050, according to the IEA [51]. Without strong regulations, companies will not change their business model, as illustrated by the projects EACOP from Total [82] and Willow project from ConocoPhillips [83]. Furthermore, the European Green Deal claims that Europe has decoupled CO_2 emissions and economic growth, since “between 1990 and 2018, greenhouse gas emissions [were reduced] by 23 %, while the economy grew by 61 %” [76]. However, it should be noted here that looking at the CO_2 emissions only of a few countries does not provide an accurate global picture. These numbers do not take into account the imported CO_2 emissions, that is to say when a product is imported into the European Union. In France, the official figures indicate that half of the CO_2 footprint is imported [84]. The emissions as a result of foreign investments of multinational companies and banks are also not included in the footprint of the country where such companies are registered.

The fourth belief is the feasibility of a closed-loop circular economy in a growing economy. To that end, the treatment and recycling of goods at the end of life must seriously be considered and promoted. However, their efficiency and implementation are often overestimated. For example, Coca-Cola can recycle only 30 % of its products, of which only 9 % correspond to plastic bottles [85]. What is striking is that Coca-Cola lobbied against the deposit system with the lobby "Eamonn Bates Europe Public Affairs", as stated in Section 1.2.1. Moreover, even if recycling can be very efficient for metals [85–87], it is much less efficient for other products like plastic for which downcycling is inevitable. As a matter of fact, several virgin recycled plastic bottles are necessary to produce one bottle with the same properties as an original one [85]. Hence, even if plastic waste was properly collected, the extraction and the transformation of oil would be still needed to keep the number of bottles sold constant, even more so to sell more. Once again, effort should first be made to question a system promoting one-time-use products instead of betting on technology, here recycling. Also, innovation is a crucial hypothesis for a system promoting economic growth. In practice, innovation is implemented by planned obsolescence to allow the constant renewal of items [88, 89]. This precisely goes against the principle of a circular economy as shown by the example of smartphones [90]. In that sense, the European Green Deal promoting both circular economics and economic growth is theoretically inconsistent [76].

The previous paragraphs have shown two things. Firstly, the implementation of potential solutions is for the moment not sufficient to counter the current issues. Secondly, these potential solutions are widely advertised so that the root causes of the problems are not put into question. This leads to a new form of business-as-usual whose consequences are described in the next section.

1.2.3 The social consequences of business-as-usual

The first consequence of business-as-usual is the increasing tensions regarding resource management. Mineral and metal extractions generate lots of negative externalities, as shown in Section 1.1, and have never been so coveted [48]. Populations living around mines will still suffer for the needs of others, for example, to develop electric cars and renewables. This makes Sonter et al. write that "Renewable energy production will exacerbate mining threats to biodiversity" [91]. Despite all the efforts that could be made from now on, some changes are irreversible at human time scales. Even without any new greenhouse gas emissions, global surface temperatures will increase and climate change consequences will be more frequent. At “only” 1.5 °C of global warming, premature deaths will increase with higher propagation of diseases, hot temperature extremes over land will be eight times more frequent, drought will be two times more frequent and heavy precipitations 1.5 times more frequent [4]. Though, every new release of CO_2 increases the number of problems [4]. Some islands, like Tuvalu in Oceania, will eventually disappear due to rising water [92] and regions around the equator are facing a drop in crop yields and are becoming literally uninhabitable, as stated by the IPCC [4]. As a result, waves of migration are expected to become more frequent [47], increasing international tensions.

In addition to the decrease in well-being caused by environmental changes, other tensions can be expected. On the one hand, conflicting usage of resources that would need to be evaluated democratically is often solved by the law of the strongest. Some examples have already been presented in the previous sections, such as lithium extraction in the lithium triangle, or coal extraction in Germany. The EACOP project in Uganda led by Total leads to the expropriation of populations and harassment by the company and the government [93]. It must be underlined that some of these projects in poorer countries are led by rich companies, often for consumers in rich countries. This adds a geopolitical asymmetry to the different issues. On the other hand, fighting against destructive projects is becoming even more dangerous. Activists, scientists, officials and journalists are intimidated or threatened as is the case in Brazil [94] or in France [95]. Furthermore, murders of environmental activists reach new records with more than 227 cases in 2020 according to "Global Witness" [96]. A final system malfunction concerns the increasing repression exerted by governments all over the world. It is unsettling to observe it in democracies. In 2023, many observers report excessive use of force by French police to contain demonstrations [97, 98]. The misuse of power actually went further after the Ministry of Interior threatened to reduce funding of one of these observers, the non-governmental organization "La Ligue des Droits de l’Homme" ("the Human Rights League") [99].

Nonetheless, these increases in tensions and decreases in well-being have already been predicted. In 1972, the Club of Rome already warned on the unsustainability of a global growing economy in their report "The Limits to Growth" [100]. All the results of their models indicated that the human population and well-being in society eventually decrease rapidly if birth rate, consumption and pollution are not controlled and limited. Their results indicate that the scenario following the current trends leads to a collapse, as Diamond defines it [46]: "a drastic decrease in human population size and/or political/economical/social complexity over a considerable area, for an extended time". This author identified twelve threats for contemporary societies that are close to the planetary boundaries defined by Steffen et al. [1] and to other issues described in Section 1.1: deforestation and habitat construction, soil problems, water management problems, overhunting, overfishing, effects of introduced species on native species, human population growth, increased per-capita impact of people, human-caused climate change, buildup of toxic chemicals in the environment, energy shortages and full human utilization of the Earth's photosynthetic capacity. Tainter proposes another definition of collapse [101]. For him, it is the rapid simplification of society, in terms of political, social and economic organization. The cause is the decreasing margin of returns for investment in complexity, i.e. the increasing cost of complexity for the same output. Recently, a few events illustrated the level of complexity of the globalized world. The Covid-19 pandemic highlighted the high complexity emerging from globalization in the health sector [102]. In 2021, the blockage of the Suez Canal threatened the supply of toilet paper [103]. War in Ukraine highlights the complexity of the grain market and threatens worldwide populations to fall with starvation [104]. The complexity of the global market makes the functioning of the system vulnerable and could be the premise of a collapse.

Two conclusions can be drawn from this section. The first one is that problems must be solved with a holistic vision. Solving the problems of one piece of the puzzle often puts even more pressure on other pieces and results in worsening the overall issue. The second one is that the current context is alarming enough to be willing to leave the business-as-usual model. The organization of society must eventually promote the common good before private interests that fuel today's paradigms. The consequences of denial or refusal of this questioning include a decrease in well-being, an increase in inequalities, an increase in repression, and eventually collapse.

1.3 1001 solutions to implement

Section 1.1 presented to what extent the functioning of current societies is not sustainable. Section 1.2 insisted on the failures of the system to correctly assess this question. The current section starts by trying to define the objective and the different types of measures that must be taken. Then, it is emphasized that a correct methodology is needed to make the right decisions in a finite world. Finally, the focus is placed on democracy and its tools.

1.3.1 From defining the correct objective to the practical implementation of sustainability

If the goal is to develop a sustainable society in accordance with planetary boundaries, where everyone on the planet has the same chance of reaching self-fulfillment from one generation to another, the primary needs of human beings must be understood and reassessed. Homo sapiens have been able to survive, reproduce and build prosperous societies by developing certain behaviors, like exploiting more and earning more, that are today outdated or even dangerous for the current and next generations [105]. Given the enhanced means of production, efforts should be made to use resources wisely and sparingly and to avoid the overexploitation of the workforce and damage to the environment. To take concrete action, it's necessary to overcome the prisoner's dilemma, the situation in which the Pareto optimum for the group is not obtained when the payoff of egoistic strategies is higher [106]. To that end, the first thing to do is to reorient human behavior and aim at maximizing the common good. This calls for a redefinition of social status and social success by choosing more virtuous role models and creating more virtuous narratives [107, 108].

Many solutions have already been proposed to reduce environmental and social impacts. Some of them can be easily implemented with a bit of political conviction. As supported by the authors of the World Inequality Report [56], a stronger and more efficient approach should be taken to the redistribution of wealth and revenues. Piketty [109] recalls that in the USA in the 20^{th} century, the richest were taxed by at least 80 % and it did not prevent the social and economic development of the country. Moreover, it was shown that the richest people have the largest environmental footprint [110]. Some political measures must be taken to prohibit the most damaging behaviors such as a ban on private jets, reducing meat consumption and limiting the speed, power and size of cars. More globally, the establishment of a theoretical carbon budget per capita [111] could be tested to aim for a low carbon economy [112]. These solutions do not require a high cost for their implementation. The main hurdle is only political conviction, as the measures can be regulated directly by lawmakers. Yet, even if they are necessary, at least from a symbolic point of view and for an ideal of equity, they are not sufficient.

Solving sustainability problems also requires systemic changes in society. An example lies in the intrinsic relationship between the development of megacities and the industrialization of agriculture. In 2018, there were 33 megacities with more than 10 million inhabitants spread across the entire planet [113]. This can be explained by the fact that cities allow the concentration of jobs and wealth. Though, these megacities raise many issues such as premature death due to air pollution [114], the heat island effect, higher stress and higher frequency of traffic jams [115]. Certain cities like Beijing and Shanghai decided to limit their population to limit the aforementioned issues [116]. Nevertheless, the problem of high population density in big cities goes beyond these issues. It is argued that the increase in the number and size of megacities has been made possible by the industrialization of agriculture, which has permitted a reduction in the number of farmers and has increased their individual productivity. However, this industrialization

has implied mechanization, monoculture and higher utilization of pesticides and artificial fertilizers [50, 117]. The consequences are loss of biodiversity, higher soil degradation, deforestation, disruption of natural cycles of nitrogen, potassium and phosphate, higher dependency on fossil fuels and higher complexity of the agribusiness [117]. The think-tank "The Shift Project" conducted a holistic analysis of the organization of French society to counter these impacts and improve resilience [118]. They recommend the de-urbanization of the most populated cities while increasing the number of jobs in the agricultural sector. Their preliminary results indicate that around 450 000 direct jobs in this sector should be generated by 2050 with the development of more virtuous farming practices such as agroecology [118]. Other systems must also be re-considered in depth like industry [14] or transport and mobility [73]. These changes involve a redesign of social paradigms and require acceptance and collaboration from many actors working side by side and of much higher complexity than simply eating less meat.

Thus, with the objective of maximizing the common good within the planetary limits, individual and collective choices must evolve.

1.3.2 Making decisions in a finite world

Any societal decision has costs and provides benefits. To evaluate them, a consistent methodology must be developed to compare different projects. For CO_2 footprints of products and services, the framework of the three scopes must be generalized and systematically applied. As a reminder, scope 1 corresponds to the CO_2 emissions directly emitted by an activity, e.g. driving vehicles. Scope 2 corresponds to the indirect emissions of an activity, e.g. emissions due to electricity production that a company buys. Scope 3 accounts for the CO_2 emissions coming from the whole supply chain of production, e.g. the emissions to extract and transport raw materials to a factory, and downstream emissions from the use of the company's product [119, 120]. Only such holistic approaches can help fight against misinformation. It also helps to limit greenwashing campaigns such as "CO_2-free electric cars" by providing clear and relevant information to the general public. Yet, CO_2 is not the only planetary boundary or the sole issue and life cycle assessments should be generalized for water consumption, water pollution, toxicity, biodiversity, soil pollution, human rights of workers, etc. This should enable the cost-benefit ratio of products to be evaluated and raise awareness of the consumers. To make the grading system efficient, full transparency on which material was produced for which application should be provided. In summary, the evaluation of costs vs. benefits in a finite world is key to making the best decisions.

Moreover, to increase awareness of the social and environmental costs of human activities, a significant part of industry must be local and thus re-localized in some countries. As a direct consequence, pollution, toxicity, loss of biodiversity and respect for human rights would be re-localized too and the distance between consumers and producers or production means would be much shorter. In fact, since no activity is perfectly clean, the polluting repercussions of any consumption would be more palpable to consumers and citizens. The same reasoning can be made for the human rights of locals and workers. Thanks to relocalization, the population may be willing to pay a higher price for the same goods and

services in order to give decent salaries to their fellow citizens. This can also reduce over-consumption and limit the rebound effect emerging from the discovery of new resources or reservoirs. Eventually, it must lead to a deep re-think of usage.

As stated in Section 1.1.1 past and present activities have largely damaged nature. To counter this, increasing efforts should be made to ensure the regeneration of nature and safe living conditions, such as providing access to drinking water, handling pests, diseases and pandemics and managing the increased flood risks [121]. At the same time, less energy and capacity will eventually be available (see Section 1.1.3). So, more problems will be faced with fewer technical levers to answer them. Therefore, instead of money being spent on catalyzers of catastrophes, it should be invested in the adaptation of societies to low-energy and low-resource solutions for the current and upcoming disasters. This requires a paradigm change. Some concepts of regenerative activities have already been proposed in different sectors. For example, in the sector of construction, the regenerative design aims at going further than limiting the impact of buildings [122]. It aims at emulating living ecosystems to improve the local environment [123]. In agriculture, the regenerative paradigm employs the natural symbiosis between living entities to restore degraded soils, forests, desertified lands and watercourses. The circular economy also belongs to regenerative thinking. All these approaches encourage moving from an anthropocentric vision to a rather biocentric paradigm where humans and the natural environment can co-evolve [124].

1.3.3 Innovating in the framework of democracy

The methods presented in the previous section should lead to informed decisions. Democracy should provide the framework to promote sustainability, equity and justice. It can be reinvented or completed by experiments as it could have been done with the Convention Citoyenne pour le Climat in France [125]. In this experiment, 150 citizens chosen randomly were gathered and trained on environmental issues for six months. In the end, they made 150 legislative proposals that should have been voted on in parliament without filtering. Even if the outcome is a failure due to the French government's failure to uphold the promises made [126], this experiment proved that citizens are willing to engage and can propose coherent laws when they are given the opportunity. It also showed that the citizens' perception of the issues changes when they can discuss them with experts. In addition, it can be noted that despite a variety of backgrounds and opinions at the start of the experiment, most of the proposed laws were voted with an overwhelming majority. Environmental issues go beyond partisan rifts and do not need to be carried by a political party. Finally, the influence of lobbies against randomly chosen citizens is reduced since (i) the lobbies can create a close relationship only as soon as the members of such an assembly are known (ii) the effectiveness of lobbying is decreased if the assembly and the members are renewed each time (iii) during the assembly process, real experts with less personal interests are called to educate citizens on a subject matter, even if this must also be controlled to avoid the drifts presented in Section 1.2.1.

Other measures in the democratic system should be taken to improve law enforcement and control the proper functioning of institutions. This requires more efficient supervisory authorities. In democracy, the first thing to be verified is power influence. Both Alexis de Tocqueville [127] and Adam Smith [128] argue that strong governments are necessary in contrast to the laissez-faire doctrine. In *The Wealth of Nations*, the latter defends regulation that should "limit the natural liberty of a few individuals, which might endanger the security of the whole society" [128]. Actually, they both are critical of corporate impunity. Recent disclosures of social, environmental or fiscal scandals seem to show that this ideal has been somehow forgotten. The risk of getting caught and severely condemned is not high enough and supervisory authorities should be provided more funds and means. For example, finance must be better regulated to avoid global crises [129], fiscal evasion [57] and other abuses, as stated in Section 1.2.1. This can be extended to any sector. In agribusiness, many cases of abuse have been reported since the supervisory bodies have limited capacity [130]. The situation of breeders is also a good example. It shows that without decent wages, entrepreneurs depend on buyers who impose their prices and are prisoners of their debts [46, 131]. Better rules and regulations are necessary to avoid these abuses within and between countries.

The democratic ideal and the will to build a society based on equality and sustainability must also be credible internationally. If the European Union wants to carry this ideal, it should face its contradictions. Forbidding the use of some toxic pesticides on its territory but allowing their export and commercialization in other countries [132, 133] is at best absurd, at worst hypocritical and cynical, even more so when these pesticides are found in products imported into the European Union [134]. Climate and social justice must be thought of in an international framework worldwide. Even if the credibility of Conferences Of the Parties (COP) can be questioned - COP 28 will be chaired by the CEO of the national oil company Abu Dhabi National Oil Company - it puts the question of climate justice on the international agenda. The richest countries have a huge climate debt as they have historically contributed the most to CO_2 emissions [135] and they should be required to compensate poorer countries for the damage caused. International laws are also a powerful tool in the fight against globalized companies which too often escape the disasters they cause far away from their headquarters. For example, in 2021, Shell was condemned for the damage caused in Nigeria due to oil spills [136]. The significance of this case is that not only Shell Nigeria was condemned but that the parent company, Royal Dutch Shell, must also pay part of the compensation. Even though it remains a rare case of international justice for such cases, and even though international justice needs more capacity, it is a first step in climate justice.

In summary, reinventing democracy is both a requirement and part of the solution to achieve more sustainability and justice for human beings. Here again, awareness of the problems and political conviction are a requirement.

1.4 The role of the cement and concrete industry

This section aims to illustrate different points presented previously applied to the current situation of the concrete industry. It is emphasized that concrete has a significant role in the development of modern societies. Then, the CO_2-cost for making cement, the most important constituent of concrete, is discussed, as well as the considered solutions and the limits of the current paradigm. Finally, the total CO_2 cost of concrete as well as the other environmental damages are assessed. It is argued that any debate implying concrete and sustainability can not be envisaged without a more holistic vision involving other sectors and political choices.

1.4.1 Concrete at the center of economic development

Concrete is the most commonly used building material. It is a mixture of cement, water, sand and aggregates. It is a cheap material [137] which can be locally produced by extracting limestone available all over the planet. It generates structures with good mechanical properties designed to last 50-100 years. For these reasons, it is directly linked to economic development. In fact, the economic development of China between 1980 and 2010 is directly correlated with the use of concrete as shown in Figure 1.5 [138]. Concrete has become a necessary part of many crucial sectors such as energy (e.g. drilling, dams, power plants), real estate (e.g. housing, offices, hospitals, schools), industry (e.g. factories) and transport (e.g. roads, railways, airports). In addition, concrete plays an important role in any transition plan. For instance, the IEA forecast a 25 % increase in cement production by 2050, mainly due to economic growth in developing countries [139]. Modern developed countries still require high concrete consumption. In France, 35 % of cement goes into road maintenance [140]. Also for green-oriented investments, concrete is necessary. Many low-carbon energy means of production, such as wind turbines, dams or nuclear power plants, are made of concrete. Furthermore, the extraction of metals necessary for the so-called energy transition (see Section 1.2.2) is enhanced by concrete infrastructure. It is thus irrefutable that concrete is a centerpiece of the organization of contemporary society at the same level as fossil fuels or metals.

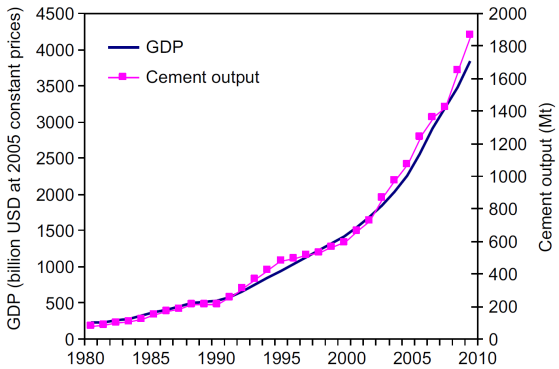

Figure 1.5: Historical China's gross domestic product and cement production [138]

The production and utilization of concrete are in synergy with the aforementioned resources. On the one hand, cement facilitates the exploration and extraction of any resource by stabilizing drilling in the soil. On the other hand, the extraction of limestone is made with bulldozers made of metals and functioning with diesel. The synergy is all the more marked between the concrete industry and the transport industry. Transport of huge quantities of resources in a globalized system is made possible by building harbors, airports, roads, warehouses, etc. made of concrete. In particular, heavy truck traffic would be reduced without concrete and, obviously, concrete would not be used as much if it could not be easily transported. However, this synergy also leads to a vicious cycle. The road's upper layers contain high quantities of concrete that must be designed for trucks of several tens of tonnes and must be regularly maintained due to the progressive deterioration of roads with traffic [141]. Yet, in Région île de France – the region of Paris – around 10-15 % of trucks transport building materials. Therefore, these trucks damage roads, roads that must be then repaired with cement and aggregates... transported by the same trucks. Such a vicious cycle can only be broken by political choices driven by a redefinition of the needs of society. To summarize, concrete has a predominant role in modern society. More than a sole causal link between concrete consumption and economic development, concrete provides infrastructure that enables the development of other activities. However, a part of the activities leads to vicious cycles causing overconsumption of concrete. This is problematic considering the negative externalities of the production of concrete.

1.4.2 The environmental costs of making cement

The main global environmental impact of cement production is global warming [142]. In this section, the other impacts like acidification or eutrophication will not be discussed. Most of the CO_2 emitted by concrete production comes from the production of cement and more precisely the production of its main constituent: clinker [142]. It is produced by heating limestone (made of calcium carbonate $CaCO_3$) to 1450 °C in a kiln. The corresponding chemical reaction, named decarbonation, reads:

$$CaCO_3 \rightarrow CaO + CO_2 \tag{1.1}$$

This reaction emits around 850 kg of CO_2 per tonne of clinker produced. Around 60-70 % of these emissions are emitted due to the stoichiometry of the reaction and around 30-40 % are emitted by burning fuel, usually coal [143]. In 2014, 4100 Mt of cement were produced and 2252 Mt of CO_2 were emitted [139]. To reduce these emissions, a few technological improvements can be considered.

The first one is to reduce the amount of clinker in cement. In fact, cement is a generic term, which is used for many different types with varying oxide composition, particle size, and proportions of clinker and other components like gypsum, limestone, slag, fly ash or clay called supplementary cementitious materials. Gypsum controls the setting time of concrete and can correspond up to 3-5 % (mass) of cement. Limestone can have beneficial effects up to 5 % (mass) in the cement, but its content must be limited as it is

mainly inert [137]. Slag and fly ash can be used in higher proportions but the allocation of CO_2 emissions is more complicated as they are by-products from steel production and coal electricity generation, respectively. As discussed in [144], benefits to reduce global warming are worth it with an allocation by economic value, but with an allocation by mass value, these materials present no benefit regarding CO_2 emissions. The availability of slag and fly ash is also problematic [137]. In particular, coal power plants emit the most CO2 when compared to other sources of electricity [145]. So, the production of fly ash must drop in the next years to reduce global CO_2 emissions. Clays must be calcined at 600-800 °C to be reactive. The preparation of clay as a binder presents the advantage of not emitting CO_2 from decarbonation but it is not a CO_2-free solution since fuel must still be burnt for the calcination to take place.

The second solution is to increase the use of alternative fuels to replace coal and reach high temperatures in the kiln. Alternative fuels are separated into two categories: industry wastes, such as scrap tires or oils, and biomass. These alternative fuels could be used to replace up to 60 % of fossil fuels [143]. However, this solution presents a few limitations. Firstly, burning waste will still emit CO_2 during their combustion [146]. Secondly, biomass is commonly regarded as a CO_2-neutral fuel [139, 147] but a few studies contest this assumption [148–151]. In addition, using land to produce fuel is in competition with agriculture to feed the population.

The third main solution to reach CO_2 neutrality in the cement industry is the implementation of carbon capture in clinker factories. Many technologies are in development and some industrial-scaled prototypes are about to be launched [152]. They could capture between 60 % and 90 % of the CO_2 emissions of cement production. However, the practical implementation remains difficult in the current factories and these technologies would increase the electrical consumption [139, 152]. Also, the captured CO_2 must be mainly stored (Carbon Capture Storage or CCS) as the need for CO_2 by other industrial processes (Carbon Capture Utilization or CCU) is negligible [152]. Worldwide and accounting for all industries, enhanced oil recovery, a combination of carbon capture storage and utilization (CCUS) concentrates 73 % of captured carbon [153]. In this process, CO_2 is injected into oil or gas reservoirs to facilitate the extraction of these fossil fuels. Thus, accounting for Scope 3 (see Section 1.3.2), this process does not lead to a CO_2-neutral activity, as oil and gas are eventually burnt and emit CO_2 [153]. Thus, the technological propositions should go beyond the simple cement industry – if carbon neutrality is a serious objective.

To summarize, complementary technological solutions could be implemented to reduce CO_2 emissions in the production of cement. However, these solutions could shift the problems to other sectors leading to a global rebound effect (see Section 1.2.2). Finally, as stated by Favier et al. [154] in Europe, "it is important to note that the 40 % observed reduction between 1990 and 2015 is mainly (30 %) due to the reduction in cement demand that followed the 2008 economic crisis" and consequently only 10 % are due to technological improvements.

1.4.3 The environmental costs of making concrete

As shown in [52, 146], the production of the other components of concrete emits much less CO_2. Thus, the main strategies to reduce the footprint of concrete aim at using less cement for the same functional unit. The first idea is to reduce the amount of cement per cubic meter of concrete by strictly respecting the exposure class [142]. In this context, each piece of concrete in a building has specific performance requirements depending on where it is used. Therefore, the cement type and quantities in concrete should be optimized on a case-by-case basis to reach the right performance. In this vein, using the correct concrete composition for the correct performance could also help reduce the carbon footprint of concrete [155]. This is specifically true for the development of alternative binders [156]. Finally, around 20 % of the emissions of CO_2 could be avoided by optimizing the geometry of structures to use as little concrete as possible [142]. The implementation of all the previous technological improvements could reduce CO_2 emissions per unit of concrete by 55 % [154].

The above-mentioned technological improvements only regard scopes 1 and 2 and a part of scope 3: the upstream part of concrete production. However, they do not include the other part of scope 3: the downstream part of concrete production, for which types of activities, by which company and for which purpose (see Section 1.3.2). These downstream impacts are largely neglected when it comes to evaluating the sustainability of projects. The German Sustainable Building Council (DGNB – Deutsche Gesellschaft für Nachhaltiges Bauen) delivers certificates to buildings of organizations requesting them based on the following criteria: ecological quality, economic quality, sociocultural and functional quality, technical quality, process quality and site evaluation [157]. Nevertheless, it is questionable to deliver certificates of sustainability to buildings promoting the aviation sector (e.g. Zentrale Düsseldorf Airport), the automotive industry (e.g. Neubau Porsche Zentrum Pragsattel Stuttgart, Bauwo BMW Hodenhagen, Mercedes-Benz Autohaus Berlin Süd), mass consumption (e.g. Wien Mitte the mall, A10 center Wildau bei Berlin, City Arkaden Klagenfurt, City Arkaden Wuppertal, Phoenix-Center Hamburg) and specifically fast fashion (e.g. Zalando Headquarter Berlin Bauteil A) [157]. Evaluating the sustainability of a company necessarily involves including its business model. Considering all the arguments given in the previous sections (see e.g. Section 1.1.2), it leaves no doubt that any building belonging to Zalando can not be associated with the notion of sustainability. In that sense, the certificates delivered by DGNB can be highly confusing as they might give the impression that a company could be sustainable if it owns low-impact buildings. In fact, it is the open door to green-washing. Hence, sustainability can not be regarded as a material-related property and the scope 3 of CO_2 emissions must be assessed more seriously in the concrete industry.

In the previous section, it was stated that the quantities of cement produced (and thus of concrete) could be questioned to assess seriously the questions of CO_2 emissions of the sector. CO_2 is not the only argument to reduce concrete consumption. A closed-loop circular economy can only work if what is recycled corresponds to consumption. However, in 2013 in Germany, the Netherlands and the UK, the quantities of recycled concrete

aggregates used for building concrete were 12 %, 16 % and 29 % respectively [158]. Without even discussing the issue of downcycling [159], the supply of recycled concrete aggregate is too low compared to the demand for concrete. In other words, either more infrastructure should be demolished or fewer construction projects should be undertaken. Thus, the case of the concrete industry is the perfect example of the theoretical inconsistencies of the Green Deal funded by the European Commission (see Section 1.2.2): a circular economy aiming at closing the loop is incompatible with an expanding society, i.e. with economic growth.

The previous paragraphs dealt mainly with the question of CO_2 emissions. Nevertheless, the production of concrete also generates other pollution notably due to the emission of nitrogen, sulfur and fine particles [160]. Some of this pollution is accounted for in life cycle assessments (LCA) [144, 161] and some solutions exist like effective filtration systems [142]. Concrete production can also be the cause of local resource scarcity [142]. In addition, solving the problem related to emissions - even after calculating seriously the scope 3 of CO_2 emissions of concrete - does not solve the other issues related to the other planetary boundaries (see Section 1.1.1), in particular land-system change and biodiversity. Concrete plays an important role in soil artificialization due to infrastructure projects. Yet, soil artificialization is linked to biodiversity extinction as shown in [162, 163]. In both France and Germany, so-called developed countries, more than 20 000 ha have been artificialized in 2020 [164, 165]. This corresponds to the destruction of a habitat of 50 m^2 every 8 seconds. It is even more worrying knowing that the official objective in Germany is to reach an artificialization rate of 30 ha per day by 2050 [165]. Promoting this objective simply means accepting greater environmental destruction. Hence, it becomes urgent to include other planetary boundaries in the sustainability question for the concrete industry and not limit it to CO_2 emissions.

In conclusion, the analysis of the concrete industry perfectly illustrates the current problems in assessing sustainability. Firstly, the issue of sustainability has not yet been seriously assessed in 2023. This is supported by the fact that only the CO_2 problem has been questioned and, even for this issue, the analysis is not carefully assessed, e.g. the downstream activities (scope 3, see Section 1.3.2) are still not integrated into CO_2 calculations. Secondly, the only solutions envisaged are technological, with the risk of a rebound effect (see Section 1.2.2). They can even be regarded as greenwashing where promises of revolutionary technologies simply hide a business-as-usual approach that refuses to question the usage of concrete and the quantities used. Thirdly, these two last points - usage and quantities of concrete - necessarily call for a holistic vision and a deconstruction of the silo vision (Section 1.2). Concrete provides enormous benefits for economic development and exacerbates at the same time pressures on the environment. The cost-benefit ratio must be better evaluated in extended LCA calculations and lead to well-informed choices optimizing the common good within a country and between countries. Considering that most of the planetary boundaries have already been broken and that the most developed countries have not reached any sustainable state, the goal of sustainability imposes a drastic decrease in the production of concrete.

1.5 Summary

Modern societies have an excessive environmental and social impact due to too many highly damaging activities. These activities depend on certain resources which become increasingly difficult to access and the decline in extraction is inevitable.

Certain of these problems have been put on the agenda of international institutions and politics. Nevertheless, the debate is undermined by some personal interests which surpass the interests of the common good. As a consequence, incoherent paradigms are defended and lead to a business-as-usual scenario. This business-as-usual scenario has terrible consequences for the environment and most of the population. Thus, holistic visions and solutions are still needed to answer the whole set of environmental and social issues.

To have a chance at addressing the current issues, a deep reconsideration of human essential needs and desires is mandatory. Political conviction and education are the two first requirements. Solving social and environmental problems also involves a higher awareness of the problems by the population and better decision-making tools, especially in a finite world with eventually less energy and capacity available. It is crucial to understand that sustainability is not a material-related or a product-related attribute but rather a usage-related attribute. Finally, a stronger democracy with more regulations is the ultimate tool to tackle the issues discussed.

The concrete industry is used as an illustration to answer sustainability issues. Firstly, this industry must improve the current life cycle assessments to include downstream impacts and all the planetary boundaries. Secondly, it can not exclusively rely on technological improvements to be more virtuous. It means that the questions of quantities and usage must also be assessed. From there, proper evaluation of the cost-benefit ratio should decide what society can afford.

1.6 Conclusion

This contextualization appeared to be necessary after personal exchanges that the author has had during the past years with experts in his field but also other scientists and non-scientists. The author's limitations of knowledge can not be measured and are without any doubt very large. However, as far as the author knows, such an attempt at contextualization is missing in the concrete research field. It might be a simple oversight or a deep ignorance of how concrete affects – directly or indirectly – human societies – past, present and future - due to positive and negative externalities. Experts willing to solve the issue of sustainability must embrace complexity and by definition accept to partly lose their status of expert. Without any doubt, what precedes is of course the subjective perception of the author, who is largely biased by his own history, education and personal situation.

This contextualization can not aim at convincing or persuading anyone. Scientists have been warning the public about the presented topics for more than 50 years and no real change has occurred, as the record of CO_2 emissions beaten in 2022 shows. It seems that a

real reassessment of the functioning of society is for the moment not possible. There is a paradigm conflict between standard living – either the one of the richest or the one that is aimed for by the poorest – and taking care of the environment which requires a degrowth, even a stop, of most of human activities. To counter this obvious cognitive dissonance that individuals face, new confusing narratives have been developed such as the myths of almighty technology, green finance, carbon compensation and decoupling between impacts and economic growth. Their failures are blatant. Thus, other narratives must be developed to galvanize ideas into real action. Even if we will have to make decisions without certitude that they are sufficient to fully solve problems, we should at least ask relevant questions to avoid solutions that we know will fail.

2 Introduction

Cement is a vital material for contemporary societies. More than 4100 Mt of cement are produced yearly to construct buildings and infrastructures worldwide. However, the major role of concrete is accompanied by intensive carbon dioxide (CO_2) emissions due to cement making process. Overall, the cement industry represents 7 % of anthropogenic CO_2 emissions responsible for climate change [139]. The use of alternative binders, such as alkali-activated materials, is one of the strategies to reduce this impact.

2.1 Cement, the ultimate material for economic and social development

Cement is the second-most used material by human societies after water. Mixed with water, sand and aggregates, it allows the production of concrete. In comparison to most other materials, concrete has the property of changing state, from viscous to solid in a few hours at ambient temperature and pressure. This facilitates the construction of structural geometries in large quantities anywhere on Earth. As they present good durability and mechanical performance, concrete structures are designed to last at least 50 to 100 years. Concrete has good resistance to compressive loading with compressive strength ranging from tens to hundreds of MPa. Though, it is brittle in tension and its flexural strength is around 3-5 MPa. This can lead to the formation of cracks and affect the service life of structures. For this reason, concrete is often reinforced with rebars and fibers (mainly steel) that improve the ductility of the structure and prevent the formation of wide cracks. These steel reinforcements are protected by the high pH value of the pore solution of concrete. However, the pH value may be reduced due to chemical attacks coming from the surrounding environment. Ingresses in the concrete such as chloride, carbon dioxide (CO_2) and acids are the main chemical dangers for reinforcements. When the chemical elements come in contact with the reinforcements, depassivation takes place and corrosion is initiated affecting the service life of the structure. Exposure classes have been defined to normatively control this risk. They give the minimal requirements of concrete performance given the function of concrete in the structure depending on the surrounding environment. Other risks for concrete structures exist such as freeze-thaw cycles or the exposure to fire.

Between 1950 and 2020, the world population has quintupled while the production of cement has multiplied by more than 30 times (see Figure 2.1) [137]. As a matter of fact, concrete is used everywhere (buildings, roads, bridges, railways, energy installations, industries, pipes, pavers ...) to keep up with population growth because its main raw materials are available everywhere and at low cost. The production of cement costs around 50-100 € per tonne, i.e. 15-30 € per cubic meter of concrete [137]. As a result, the use of concrete is predominant over other construction materials and the current functioning of societies would be very different without or just with lower concrete production.

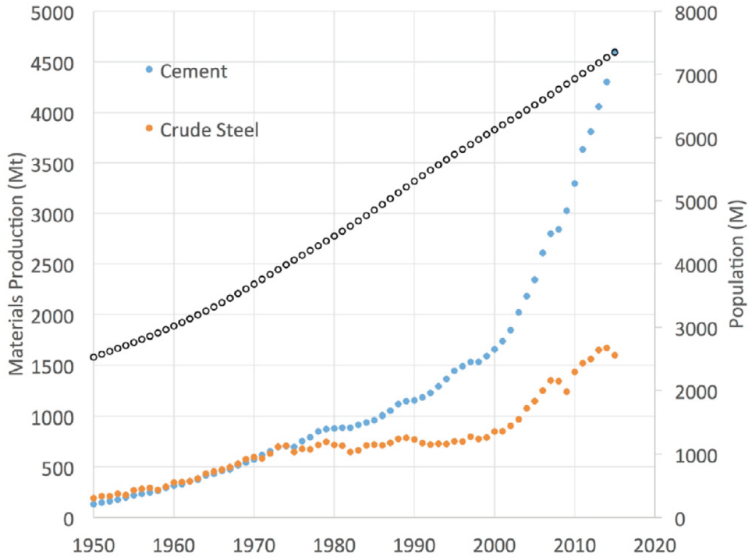

Figure 2.1: Evolution of world population, crude steel and cement production [137]

2.2 Cement production process

Cement is a powder principally made of calcium oxide (CaO) and silicon oxide (SiO_2). The cement production process is illustrated in Figure 2.2 [142]. The most important raw material for cement production is limestone, made of calcium carbonate ($CaCO_3$), which must be quarried, transported and crushed. After a few sub-steps including homogenization and preheating, limestone is calcined in the rotary kiln up to 1450 °C to form CaO through the chemical reaction named decarbonation:

$$CaCO_3 \rightarrow CaO + CO_2 \tag{2.1}$$

It is then cooled and ground to obtain a fine powder named clinker. This clinker can be blended with Supplementary Cementitious Materials (SCMs) such as gypsum, slag, fly ash, etc., before or after the calcination, to obtain what is known as cement.

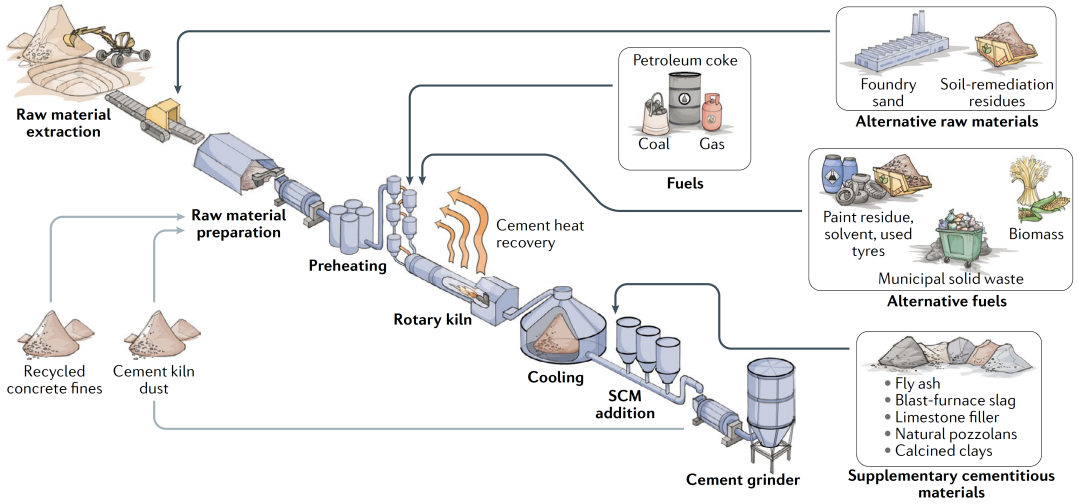

Figure 2.2: Process of making cement, adapted from [142]

In 2014, the cement industry produced 4100 Mt of cement corresponding to the emission of 2252 Mt of CO_2 [139]. The production of one tonne of clinker releases around 850 kg of CO_2 [139, 147]. 500-550 kg (60-70 % of the CO_2 emissions) are due to the decarbonation of $CaCO_3$ (see Eq. (2.1)). The rest of the CO_2 emissions is emitted from the combustion of fuel, mainly coal, to reach the high temperature in the rotary kiln. Depending on the moisture content of the material, the thermal energy needed to reach 1450 °C varies between 3000 and 6000 MJ/t clinker [146]. For example, the International Energy Agency (IEA) takes 3100 MJ/t cement as an average [139]. For the whole sector, it corresponds to the consumption of 12 EJ per year of primary energy (2 % of the energy consumption worldwide [53]). Electricity is also needed in clinker production, cement production and grinding of raw materials [147]. The electricity demand is estimated to be around 91 kWh / t cement in 2014 [139], corresponding to 373 TWh per year for the whole industry (around 1.5 % of the worldwide electricity production [53]).

2.3 The challenges of the concrete industry to reduce CO_2 emissions

Climate change is one of the nine planetary boundaries identified by the Stockholm Resilience Center [1]. The cause of global climate change over the past 200 years is anthropogenic activity [166], materialized by the increase in the yearly CO_2 emissions, as seen in Figure 2.3 [2]. CO_2 is the most emitted greenhouse gas by human activities with 36.8 Gt emitted into the atmosphere in 2022 [67]. Yet, natural CO_2 sinks can absorb only 20.5 Gt CO_2 per year [167]. This imbalance implies that the CO_2 concentration in the atmosphere increases. Hence, more energy is stored in the atmosphere and global temperature increases on Earth. Temperature changes endanger the climate stability of

the Holocene that has enabled the development of agriculture, the emergence of cities and the organization of civilizations. It is thus of huge importance to drastically reduce anthropogenic CO_2 emissions.

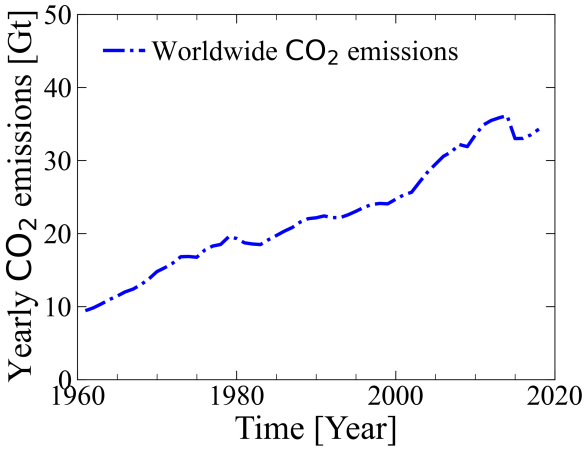

Figure 2.3: Evolution of CO_2 emissions because of human activities since 1960 [2]

As shown in the previous section, around 850 kg of CO_2 are emitted for each tonne of cement on average. At the concrete scale, 300 kg of CO_2 are emitted for each cubic meter when transport is also accounted for [52]. To reduce the emissions of this sector, different strategies can be envisaged. First, alternative fuels, such as scrap tires or waste oil, or biomass can replace fossil fuels up to 60 % in the rotary kiln [143]. However, fossil fuels still represented more than 95 % of the fuel mix in 2014 [139]. The second strategy is to reduce the clinker/cement ratio and increase the quantity of SCMs in cement. In Europe, cement is classified into six groups depending on the type and proportions of SCMs that are present in it according to DIN EN 197-1 [168]. These latter can be used to optimize the properties of cement. For instance, gypsum is a source of sulfur and helps control the setting time of cement. Worldwide in 2014, the clinker/cement ratio [kg/kg] was equal to 0.65 and the IEA foresees that it could be reduced to 0.60 in 2050 [139]. For this, new SCMs have been investigated like limestone calcined clay cement to replace clinker [169]. The third action for reducing the CO_2 footprint of the cement industry is limiting the over-dimensioning of concrete structures. This can be reduced by using a lower amount of cement per cubic meter [142]. In 2020, 300 kg of cement on average are used per cubic meter of concrete, but according to a few researchers, this value could drop to 150 kg by reducing overestimated safety margins, optimizing mix design and optimizing the geometry of structures [142]. Fourthly, carbon capture in cement plants could be implemented to avoid CO_2 emissions in the atmosphere [152]. Nevertheless, this approach requires big investments and more regulations on CO_2 prices [142]. Additionally, proper storage and utilization of the captured CO_2 should be developed. A sum up of the potential reductions of CO_2 emission is given in Figure 2.4. Finally, another solution, complementary to the ones listed previously, should be considered: the use of alternative binders.

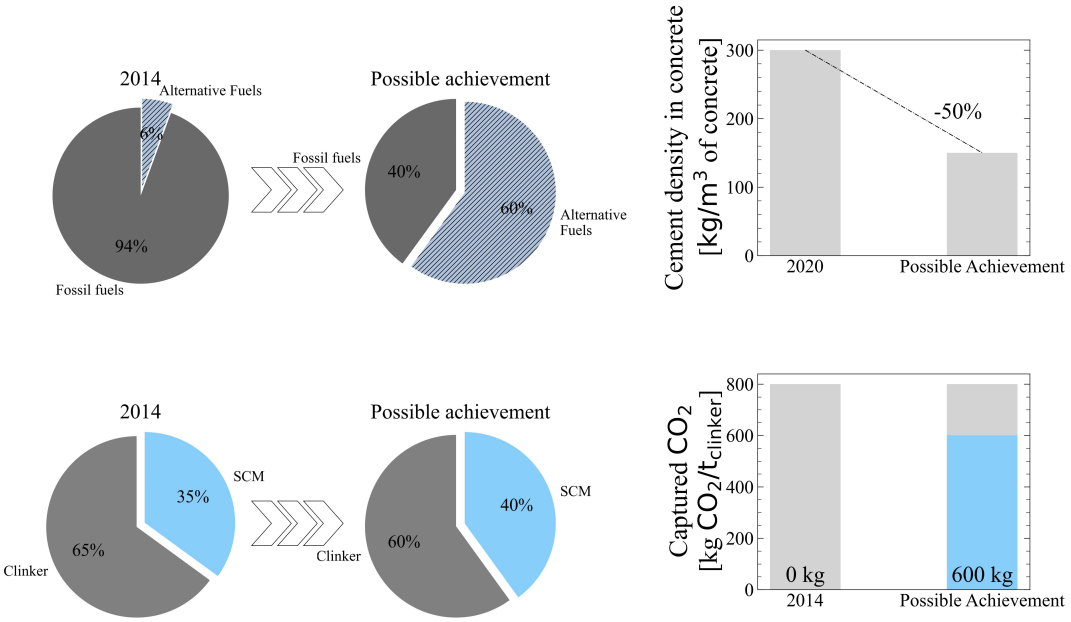

Figure 2.4: Potential technological improvements to reduce CO_2 emissions of the cement industry. Above left: Use of alternative fuels. Above right: Reducing the amount of cement in concrete. Below left: Use of more SCMs in the mix design. Below right: Carbon Capture in cement plants.

2.4 Classical clinker and alternative binders

As said in Section 2.3, the main constituent of cement is clinker. Clinker reacts with water to form a hardening paste that binds aggregates together and gives cohesion to hardened concrete. The main phases of clinker are alite (C_3S), belite (C_2S), aluminate (C_3A) and ferrite (C_4AF). Alite is responsible for early-age strength development, while belite is responsible for long-term strength. Aluminate controls the initial setting time of concrete. Ferrite allows the reduction of the melting point of CaO and SiO_2 in the kiln. The formula of these phases, as well as their usual proportions in clinker, are given in Table 2.1. As illustrated in Figure 2.5, it is necessary to reach high temperatures to initiate the decarbonation of limestone and obtain the wanted phases. Also, the temperature influences the phase distribution significantly and the differences in phase proportions of clinker come from heterogeneities in temperature time spent by limestone in the kiln.

Table 2.1: Description of the main clinker phases in cement

Phase	Formula	Proportions in clinker
Alite - C_3S	$3\ CaO \cdot SiO_2$	45 – 75 %
Belite - C_2S	$2\ CaO \cdot SiO_2$	7 – 32 %
Aluminate - C_3A	$3\ CaO \cdot Al_2O_3$	0 – 13 %
Ferrite - C_4AF	$4\ CaO \cdot Al_2O_3 \cdot Fe_2O_3$	0 – 13 %

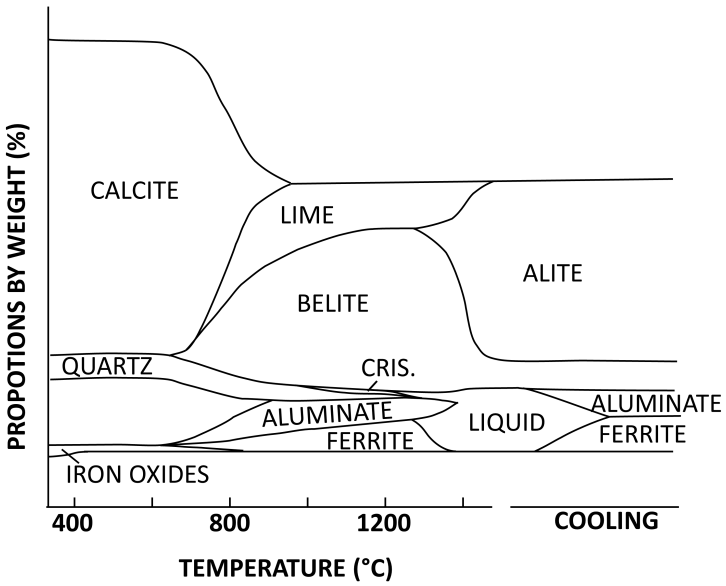

Figure 2.5: Variations in the expected phases composition during the formation of clinker. The raw materials are calcined up to 1450 °C in the kiln and cooled after (adapted from [170])

The most common cement is ordinary Portland cement (OPC) and is mainly composed of the previous phases obtained after limestone decarbonation (Eq. 2.1). The search for alternative binders attempts to reduce the CO_2 emitted either by decarbonation or due to burning fossil fuels to reach high temperatures. Among the most mature alternative binders, calcium sulfoaluminate, belite-rich Portland clinker, belite-ye'elimite-ferrite, carbonatable calcium silicate cement and magnesium oxides derived from magnesium silicates can be mentioned [171–173]. For calcium sulfoaluminate, belite-rich Portland clinker and belite-ye'elimite-ferrite, the proportion of alite in clinker is reduced or removed to lower the required temperature in the kiln [171]. Carbonatable calcium silicate cement contains specific phases that can rapidly carbonate, i.e. react with CO_2 and bind it to the material [171]. It is relevant in practice for the precast industry that can use CO_2 curing chambers. The production of magnesium oxides derived from magnesium silicates presents the advantage of not releasing CO_2 from the intrinsic chemical reaction but only from burning fuels. In addition, the generated concrete that is obtained after mixing with water and aggregates has a higher potential for absorbing CO_2 [173]. Other alternatives exist to replace OPC: alkali-activated materials (AAMs).

2.5 Alkali-activated materials (AAMs)

To obtain AAM concrete, two products must be mixed: the precursor and the activator. Precursors are powders made of different oxides such as calcium, silicon, aluminum or magnesium oxide. These are either by-products of industries, e.g. slag from steel production and fly ash from coal electricity generation, or they come from natural deposits, e.g. clays such as kaolin. In the latter case, they must be heat-treated to be reactive. Recent studies have shown the potential for using other by-products and wastes such as municipal solid waste [174], slags from other industries [175], mining waste [176], wood biomass [177], glass powder [177], cement kiln dust [178] and fluid catalytic cracking catalyst residue [179]. In comparison to cement, AAM precursors have a lower calcium oxide (CaO) content than cement and higher silicon oxide (SiO_2) and aluminum oxide (Al_2O_3) content. For example, slag is made at 30-40 % (mass) of CaO; depending on the CaO content, fly ash is classified as class C (more than 20 % CaO content), or class F (less than 7 %); metakaolin, which is a heat-treated clay, is made mainly of SiO_2 and Al_2O_3. The activator is an alkali that can be either in solid form or diluted in solution. The AAM are non-hydraulic precursors, meaning that they do not harden with water alone. Using alkaline solutions provides a high pH value and makes the precursors react. In the context of AAMs, the most studied activators are sodium hydroxide, sodium silicate and sodium carbonate.

The kinetics and reaction products of AAMs differ from those of cement hydration and also from one AAM to another. Instead of generating Calcium-Silicate-Hydrates (C-S-H), Portlandite and Ettringite, which are classical reaction products for OPC, low-calcium binders form geopolymer gel mainly made of silicon and aluminum [156]. For high-calcium AAM precursors, such as class C fly ash and slag, geopolymer phases can be formed as well as Calcium-Aluminum-Silicate-Hydrates (C-A-S-H) gel that is similar to C-S-H [180, 181]. The reaction processes and the performances of AAM concrete are various and depend a lot on the precursor type, the activator type and the activator content. For example, slag reacts faster than fly ash at ambient temperature and the reaction of slag depends also on the activator solution [182]; sodium silicate-activated slag has a higher compressive strength than sodium hydroxide-activated slag on average, with values varying by twice as much depending on the alkalinity and the amount of silicate in the solution [183, 184]; chloride ingress is lower for alkali-activated slag than for alkali-activated fly ash [185].

Despite these differences between AAMs, some general trends can be identified in comparison to cement concrete. The durability of AAMs is higher since they have (i) better carbonation resistance [186, 187]; (ii) lower damage in case of alkali-silicate reaction [188]; (iii) better resistance against sulfate attacks and acid attacks [189, 190]; (iv) lower chloride penetration [185]; (v) better bond with steel reinforcement [191] and (vi) better tensile strength with fibers [192]. However, AAMs can incur worse concrete workability [193] and have higher shrinkage and creep [194].

According to Provis [155, 156], these advantages and drawbacks of AAMs can be exploited to develop the correct mix design for the required practical application. In that sense, the development of AAMs – or other binders – should not aim at replacing the classical cement-based concrete completely but rather increase material possibilities for resource

optimization and targeted performances. In addition to a deeper understanding of the chemical and physical properties of the materials, the last obstacle to the practical use of AAMs is the lack of standardization. As explained in [195], the first hurdle is the lack of specific testing methods to evaluate the performances. For instance, the accelerated carbonation test used for cement-based concrete was found to be unrepresentative of the carbonation behavior for alkali-activated materials [196, 197]. Construction guidelines are also needed to notably predict mechanical properties but the variety of AAM concretes hinders a simple standardization. Despite these difficulties, AAMs have already been used for different applications. For example, 300 m^3 of concrete were used in 2021 to support the foundation of step-free access at the Chatham railway station in UK [198]. It avoided the emission of 62 tonnes of carbon compared to the same project made with traditional concrete.

In this thesis, the focus lies on the mechanical properties of alkali-activated slag (AAS) concrete. Slag is one of the most commonly used precursors as alkali-activated material. It is a by-product of the steel industry, which is obtained through the use of a flux to remove aluminum and silicon impurities during the melting of iron ore. Glassy slag is obtained from a rapid cooling treatment of this flux made with jet water of air under pressure. This treatment is important, as the crystallization of slag at ambient temperature would reduce its reactivity. Slag is then granulated to obtain a fineness comparable to that of OPC. In the following, the term slag refers directly to the final granulated product of this process.

3 Research scope and objectives

The objective of this thesis is to understand and predict the shrinkage and creep of alkali-activated slag (AAS). Experiments are made with one type of slag provided by Ecocem (Netherlands) whose oxide composition is given in Table 3.1.

Table 3.1: Chemical composition of the anhydrous slag used in the thesis

Oxide	CaO	SiO_2	Al_2O_3	MgO	Fe_2O_3	Na_2O	SO_3	Oth.
Mass(%)	38.8	36.3	12.8	8.0	0.6	0.3	1.9	1.3

This slag was used for two mix designs made of two different sodium silicate solutions. The sodium silicate solutions were obtained by mixing commercial sodium hydroxide, waterglass Betol 39 T from the company Woellner GmbH and tap water. Both mixes had the same water/slag ratio w/s = 0.40 [kg/kg] for paste and w/s = 0.45 [kg/kg] for concrete. This increase in water content was necessary to ensure the good workability of fresh concrete. The alkalinity coefficient n was equal to 5.0 [g Na_2O / 100 g slag] for both mixes. The silica modulus M_S, corresponding to the molar ratio between SiO_2 and Na_2O in the solution, was equal either to 0.5 or 2.2 [mol SiO_2 / mol Na_2O] and the corresponding mixes are referred to as mix lS and mix hS, respectively. For both mixes, the precursor content was equal to 450 kg/m^3 of concrete. Rhine sand and gravel were used for concrete. The distribution of aggregates was such as sand represented 40 % of the volume of aggregates, middle-size gravel (2-8 mm) 30 %, and big-size gravel (8-16 mm) also 30 %. The characteristics of both mix designs are summarized in Table 3.2.

Table 3.2: Studied mix designs for both paste and concrete

Paste		Mix lS	Mix hS
w/s	[kg/kg]	0.40	0.40
n	[g Na_2O / 100 g slag]	5.0	5.0
M_S	[mol SiO_2 / mol Na_2O]	0.5	2.2
Concrete		**Mix lS**	**Mix hS**
w/s	[kg/kg]	0.45	0.45
n	[g Na_2O / 100 g slag]	5.0	5.0
M_S	[mol SiO_2 / mol Na_2O]	0.5	2.2
Precursor content	[kg/m^3 of concrete]	450	
Fine Agg. (0-2 mm)	[Vol-%]	40	
Coarse Agg. (2-8 mm)	[Vol-%]	30	
Coarse Agg. (8-16 mm)	[Vol-%]	30	

These mixes were chosen because they have a setting time of more than one hour, which was long enough to permit the casting of concrete specimens. Furthermore, the compressive strengths of both mixes were sufficient to consider them for structural applications. Experiments were performed at several levels, from the nano-scale to the macro-scale with paste and concrete specimens. Empirical and analytical micromechanics-based models are applied and compared to experimental results. In addition to creep and shrinkage tests, the experimental program included measurements of reaction kinetics, phase assemblage, porosity, nanoindentation, internal relative humidity, Young's modulus and compressive strength for both mixes. These further experimental tests were used to justify the hypotheses made in the analytical micromechanics-based model.

4 Main findings of this thesis

In this chapter, the scientific outputs of this thesis are presented. Firstly, measurements of shrinkage and creep of AAS concrete are presented and compared to existing engineering models in **Paper 1** and **Paper 2**. Since the existing models are not satisfactory to explain the mechanisms of shrinkage and creep, the focus is placed on the development of the microstructure of AAS in **Paper 3** and **Paper 4**. From the description of the microstructure, multi-scale analysis is applied to predict Young's modulus in **Paper 5**, creep in **Paper 6** and finally shrinkage in Chapter 5. The approach followed in this thesis is schematically plotted in Figure 4.1.

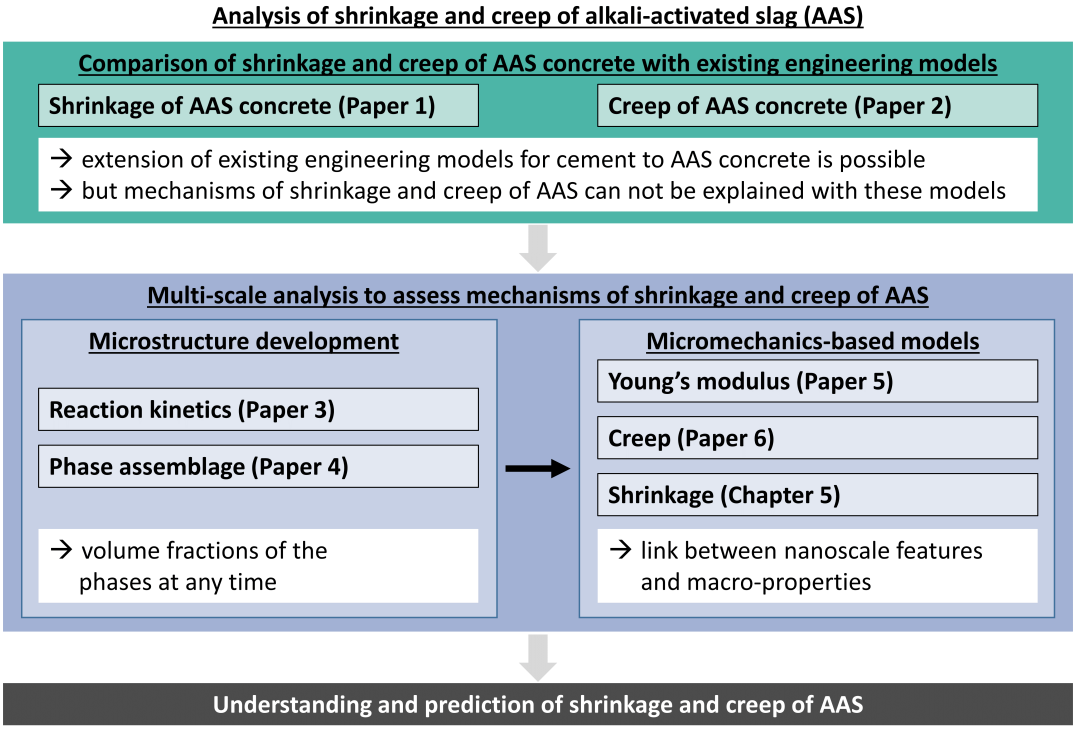

Figure 4.1: Approach followed in this thesis

4.1 Extension of existing empirical models for creep and shrinkage

Empirical models allow the determination of all kinds of properties by means of a few analytical equations. Such models have been widely developed for cement-based concrete so that engineers can have quick estimations of the performances of their concrete. The *fib* Model Code (MC) 2010 [199] is such a model and predicts mechanical properties of OPC concrete based on the sole value of compressive strength at 28 days measured on cylinders. However, these models are not suitable for mix designs with alternative binders and in the best case, scaling parameters must be used to extend them. In **Paper 1** and **Paper 2** shrinkage and creep of AAS were measured and compared to existing engineering models, viz. the *fib* MC 2010 and the B4s model [200]. These two studies conclude that the models for shrinkage and creep in sealed conditions can be extended using scaling parameters. However, the extensions for shrinkage and creep in drying conditions were more difficult. The main explanation for that was attributed to the higher changes in the internal relative humidity compared to OPC. Thus, a deeper understanding of these mechanical properties based on the specific microstructure of this material was necessary to explain the proper mechanisms of shrinkage and creep of AAS.

4.2 Analytical multi-scale micromechanics-based models

Micromechanics aims at describing the local and global strains and stresses of a material. Thus, its goal is to predict the mechanical states of each phase of the material and of the material at the macroscale. Among others, it allows the estimation of the mechanical properties of heterogeneous materials. To that end, the representative volume element (RVE) must be defined to cover the different heterogeneities. It must have a characteristic size big enough to describe the correct homogenized behavior. Since by definition concrete is a highly heterogeneous material made of reaction products, pores, unreacted particles, sand and aggregates, it is particularly relevant to use techniques of homogenization from micromechanics. The multi-scale model applied in this thesis is a succession of homogenization steps to capture the heterogeneities of concrete from the nanometer to the centimeter. This implies the definition of different RVEs. For AAS, the heterogeneity at the nano-scale (1 nm – 10 nm) consists of two matrices of reaction products referred to as the matrix of reaction products. Then, capillary water is contained in pores of characteristic size 50 nm – 100 nm that are included in the matrix of reaction products. Unreacted slag particles are the last component of AAS paste and are considered at the micro-scale (1 µm – 100 µm). At the millimeter scale, sand grains can be regarded as inclusions in the paste to form mortar. Lastly, at the scale above, coarse aggregates can be regarded as inclusions in mortar. A sum up of the considered microstructure is plotted in Figure 4.2.

Each step requires hypotheses on the geometry of the microstructure, the volume fractions and the mechanical properties of each phase and the used homogenization scheme. The corresponding strategy to obtain this information is plotted in Figure 4.3. The temporal

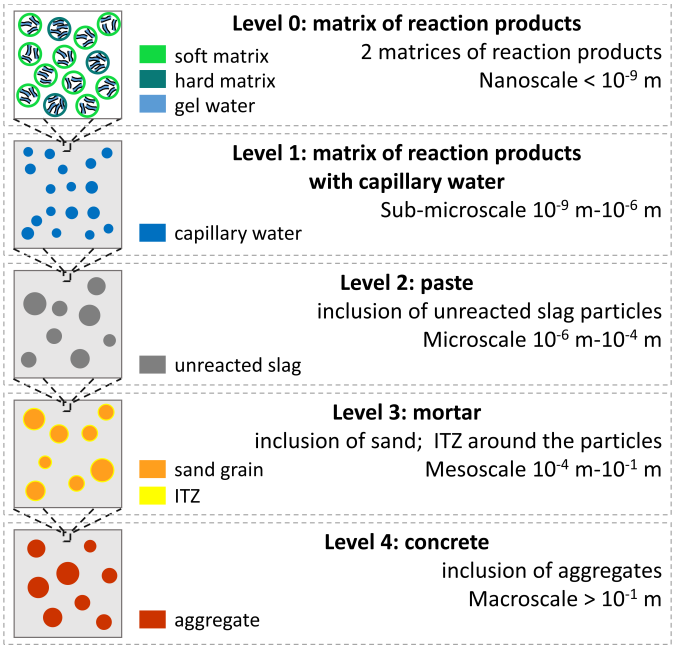

Figure 4.2: Description of the microstructure of AAS concrete at different scales

evolution of the microstructure is obtained from a coupled kinetics-thermodynamics model and the mechanical properties are obtained from nanoindentation tests. From there, the analytical multi-scale micromechanics-based model can be applied to predict Young's modulus and creep. Shrinkage strains are obtained from the description of the microstructure and the mechanical behavior of AAS. The main outputs of this thesis, corresponding to the different steps of Figure 4.3, are presented in the next sections.

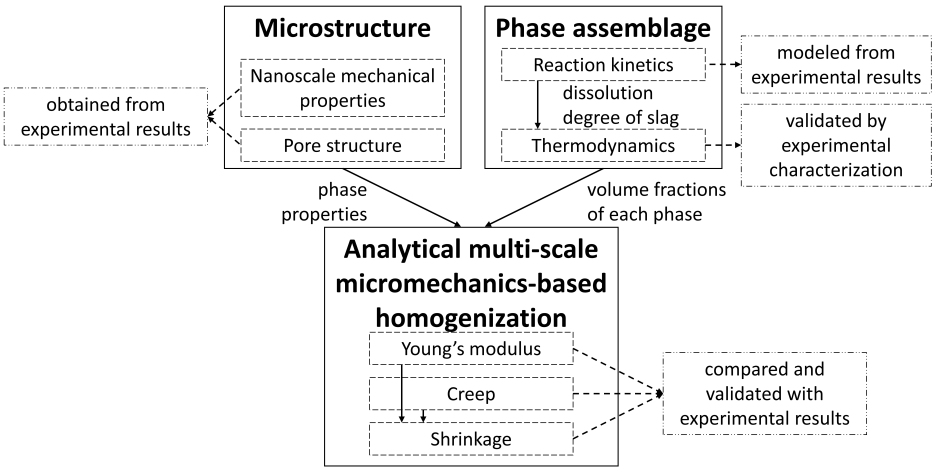

Figure 4.3: Strategy followed in this thesis to determine the evolution of mechanical properties of AAS concrete

4.3 Models for the rate of reaction of sodium silicate-activated slag

The dissolution of binders is necessary to form the paste that binds the aggregates together. This dissolution takes time and modeling its kinetics is important to predict the time evolution of concrete properties.

The hydration of ordinary Portland cement (OPC) can be described as follows. The first steps are the initial dissolution and surface wetting of the unreacted particles followed by an induction period. After a few hours, an acceleration period and a deceleration period take place, characterized by a peak of the heat of reaction. The change in heat of reaction can be monitored by isothermal calorimetry since the hydration of cement is exothermic. The nuclei of hydration products agglomerate and grow around the unreacted particles. This peak is followed by a diffusion-governed mechanism during which the dissolved ions must go through the shell of reaction products. Different models have been developed to describe and predict the progress of cement hydration. One of the most used is the Parrot & Killoh model [201], which is based on solid-state kinetic models for single-particle. The model consists in taking the minimal reaction rate of three parallel mechanisms, namely nucleation, contraction volume and diffusion. This model has been widely applied to predict the phase assemblage evolution and the strength of cement-based materials [202, 203].

However, the model in its original form is irrelevant for sodium silicate-activated slag. In fact, the Parrot & Killoh model can only predict a one-peak reaction while the reaction of slag with sodium silicate is a two-peak reaction [204]. In the literature, a few empirical models have been applied to predict the degree of reaction of sodium silicate-activated slag [205] but they do not explain the mechanisms of activation of slag. Therefore, **Paper 3** assesses this problem. A new kinetics model is proposed based on the succession of kinetic-governing single-particle models. This model can predict a two-peak evolution. It is shown that the activation of slag can be modeled as the succession of six kinetic governing models: (i) nucleation and growth, (ii) contraction volume, (iii) constant rate, (iv) nucleation and growth, (v) contraction volume, (vi) diffusion. It is interesting to note that the three last mechanisms correspond to the order of mechanisms taking place in the Parrot & Killoh model and that the main difference between the activation of slag and hydration of cement concerns the first hours of reaction due to the silicate crystals present initially in the alkaline solution. It is hypothesized that these crystals act as nuclei initiating the first nucleation and growth process. Still in **Paper 3**, the model is also applied against isothermal calorimetry data extracted from the literature and the parameters of the model are calibrated against mix design parameters. It is found that the slag quality coefficient $\frac{CaO+MgO}{SiO_2}$ [kg/kg] can be used to classify the type of slag. Yet, the sole results from isothermal calorimetry do not permit the effective evaluation of the degree of dissolution of slag.

To determine quantitatively the evolution of the degree of dissolution of slag, Scanning Electron Microscopy (SEM) tests have been carried out on paste at several ages. This

is presented in **Paper 4**. This experimental technique allows the quantification of the volume of unreacted slag particles and indirectly the degree of dissolution of slag. The results indicate that the slag dissolves up to 50-60 % during the first 28 days of reaction for the studied mixes. For OPC, it was shown that the results obtained with isothermal calorimetry and thermodynamic modeling [206, 207] compare well with SEM results. In fact, thermodynamic modeling can provide the heat release of reaction, i.e. the difference of enthalpy during the hydration of OPC, when the enthalpies of formation of unreacted materials and reaction products are known. This model was applied to AAS to retrofit the enthalpy of formation of the studied slag. The obtained value of -14.8 kJ/g is in the good range with results from the literature [208, 209] and validates the extension of this methodology for AAS. Thus, the degree of dissolution of slag can be predicted from the coupled results of isothermal calorimetry and thermodynamics without SEM.

4.4 Models for microstructure development of AAS

Cementitious materials are hardening materials. As explained in the previous paragraph, the degree of dissolution of the precursor increases with time. This changes the type and the amount of reaction products, the porosity and the pore size distribution.

The main product of the reaction of OPC is Calcium-Silicate-Hydrates (C-S-H). Crystalline phases such as Portlandite and Ettringite, and other secondary products can also form [181]. These phases can be predicted from thermodynamic modeling given a certain degree of reaction [181]. For AAS, some models have been proposed [181, 210] but they still need refinements. The main reaction product of AAS is Calcium-Aluminum-Silicate-Hydrates (C-A-S-H), which has a similar structure to C-S-H with a higher aluminum uptake in it, as modeled by Myers et al. [180]. This model has been completed recently by Kulik et al. [211] and Miron et al. [212] to also account for alkali uptake in the structure. Yet, the secondary products of AAS are different from OPC. Hydrotalcite and zeolitic precursors, both in non-crystalline forms, have often been chemically characterized [213, 214]. For this reason, additional thermodynamic datasets on these reaction products are necessary to predict the correct phase assemblage. The Cemdata 18 database is used in particular for hydrotalcite and magnesium-silicate-hydrates. For zeolites the zeolite20 database from Ma et al. [215, 216] is used. The latter has the advantage of being consistent with thermodynamic data for cementitious materials and relies on measured solubilities. **Paper 4** presents the results of thermodynamic modeling using the new C-A-S-H model augmented with the zeolite20 dataset. In addition, it was also found that both Pitzer and Debye-Hückel ion activity models provide identical results after two days of reaction. The computed phase assemblages were also compared with experimental results in **Paper 4**. It included X-Ray Diffraction, Fourier Differential Thermogravimetry, Differential Thermal Analysis, Fourier-Transform Infrared Spectroscopy and Al Magic Angle Spinning Nuclear Magnetic Resonance. The comparison indicates that the model predicts qualitatively the correct phase assemblage for the studied mixes. However, more quantitative characterizations and tests on more mixes would be needed in the future to completely validate the model.

The computed phase assemblage shows that the C-A-S-H gel is the main product of AAS. Its structure is close to that of C-S-H gel, the main product of OPC. Many models exist to describe these two gels. C-S-H has historically been modeled as a mixture of tobermorite and jennite [217, 218]. Two types of C-S-H coexist in cementitious materials: low-density (LD) C-S-H and high-density (HD) C-S-H which have different packing densities by definition [219]. With nanoindentation tests, Constantidines & Ulm found that the volume fraction of LD C-S-H represents 67 % of the volume fraction of C-S-H and the volume fraction of HD C-S-H 33 % [220]. Jennings described C-S-H particles and internal water as globules in the CM-II model [221]. In this model, LD C-S-H represents 60 % of the whole C-S-H in a paste with a water/cement ratio of 0.5 [kg/kg]. As in [220], nanoindentation tests were performed on AAS paste in the present thesis. The corresponding results are presented in **Paper 5**. As for OPC, the interpretation of the nanoindentation tests revealed the presence of two clusters. Yet, as explained in the previous paragraph, the main secondary products of AAS are amorphous. Thus, contrary to Portlandite crystals in OPC for example, it was not possible to characterize them directly from nanoindentation results. Since the indented area is too large, it is believed that the two obtained clusters do not correspond directly to a low-density C-A-S-H and a high-density C-A-S-H but to mixtures of reaction products with different densities. To avoid any confusion, these two clusters were named soft matrix and hard matrix. The proportion of soft matrix is 71-82 % and the proportion of hard matrix is 18-29 %. These values are close to the results reported in the literature for OPC [220, 221]. The values of Young's moduli of both matrices were found to be equal to 19.1 GPa and 37.6 GPa, independently of the mix design. They are in the lower range of that characterized for OPC [222].

Two other important features of microstructure are the pore structure and the water contained in it. Porosity can be split into two main categories: gel porosity and capillary porosity. Several definitions can be found in the literature [221, 223, 224]. In this thesis, gel porosity is defined as the water chemically bound to C-A-S-H layers and in pores smaller than 50 nm. Capillary porosity consists of pores bigger than 50 nm either empty or filled with water, which is not chemically bound to the C-A-S-H gel. For OPC, the Powers model [225] predicts the amounts of gel and capillary porosity as a function of the amount of reacted material and generated products. For Jennings [226], the amount of gel porosity in volume is between 26 % and 36 % of that of generated products, depending on the type of C-S-H formed. According to Brouwers [227], this range should be between 27 % and 32 %. In this thesis on AAS, a constant value of 28 % is proposed between the volume of gel water and the volume of C-A-S-H gel. This value was obtained by measuring water losses during a cycle of saturation-drying with different drying temperatures (see **Paper 4**). Subtracting this volume of gel water from the volume of water obtained through the thermodynamic model allows the calculation of capillary porosity.

4.5 Multi-scale homogenization micromechanics-based models for AAS

Paper 5 aims at determining Young's modulus of paste and concrete. For this, Young's moduli and Poisson's coefficient of each phase are taken either from nanoindentation tests as described previously or from the literature. The results of the model compare well with the experiments on paste and concrete. Sensitivity analyses indicate that the most significant parameters of the model are Young's modulus of aggregates and Young's modulus of the soft matrix. It is also shown that the interfacial transition zone (ITZ) does not play a significant role in Young's modulus of AAS concrete. Finally, the prediction of Young's modulus for any desired AAS mix with the same degree of reaction shows that the activator composition has a more important influence than the slag composition.

In **Paper 6**, the creep properties of the matrix of reaction products are downscaled from the creep behavior of AAS concrete, which was measured experimentally. The downscaling is performed with multi-scale homogenization micromechanics-based model. Two main hypotheses are made. First, the description of the microstructure that was validated in **Paper 5** for the study about Young's modulus is the same with the exception that the ITZ is not considered for this analysis. The second hypothesis is that the matrix of reaction products is the only phase that creeps, i.e. unreacted particles, sand grains and aggregates are purely elastic materials. The results indicate that the cause of the creep of AAS concrete is the deviatoric creep of the matrix of reaction products. Creep during the first minutes of loading would be due to reversible water movements and creep. After a few hours, the creep of AAS follows a logarithmic behavior that could be due to the sliding of C-A-S-H layers or to a preferred orientation of C-A-S-H layers. Finally, the contact creep modulus obtained from the interpretation of nanoindentation tests is a correct estimation of the deviatoric creep modulus of the reaction product phase.

5 Autogenous shrinkage of alkali-activated slag paste

This chapter focuses on the autogenous shrinkage of AAS paste. Autogenous shrinkage refers to the shrinkage of AAS in sealed conditions, i.e. without moisture exchange with the surrounding environment. As reviewed in **Paper 1**, three main theories have been developed to explain shrinkage of cementitious materials, viz. the capillary pressure theory [228, 229], the surface tension theory [230–233] and the disjoining pressure theory [234, 235]. The results of **Paper 1** indicate that the autogenous shrinkage of AAS is much higher than that of ordinary Portland cement (OPC). This questions the mechanisms behind the shrinkage of AAS. Recently, the works from Li et al. [205, 228, 236] provided new insights into the mechanisms of shrinkage of AAS paste. They showed that the capillary pressure theory could be extended by considering the effect of dissolved ions in the pore solution and the creep generated by the capillary pressure. For creep, they used the prediction of the creep coefficient from van Breugel [237] for OPC.

In what follows, the autogenous shrinkage of both mixes of this thesis is measured and predicted with the extension of the capillary pressure theory developed by Li et al. [236]. However, instead of the creep model from [237], the current study uses the creep model of **Paper 6**. This model needs the determination of the volume fractions of the phases. This is done using the coupled kinetic-thermodynamic model of **Paper 3** and **Paper 4**. Besides, the latter model also enables the determination of the molar fraction of water in the pore solution, which is a parameter of the model, as it will be explained in Section 5.2. In addition, the evolution of Young's and bulk moduli of paste is obtained from the model of **Paper 5**.

5.1 Methods

Autogenous shrinkage of paste was measured on $4 \times 4 \times 16$ cm^3 prisms. They were covered with aluminum-butyl foil to prevent water loss. Two measuring pins were set in paste during the casting at both extremities to measure the change in length of the specimen. The measurements were carried out using a Digital Indicator ID-C 543-250 B (Mitutoyo, Japan) every day during the first week, and then at least once every three days up to 28 days. The ambient temperature was 20 °C.

The relative humidity in AAS paste is measured with DKRF505-XXS sensors of Humi Probe-Series provided by the company Driesen + Kern GmbH (Germany). The accuracy

of the measurement is ± 2.5 %. The sensors were calibrated in controlled environment test chambers with different relative humidity: 99 %, 85 %, 65 % and 50 %. The relative humidity was measured on paste cylindrical specimens of 10 cm height and 7 cm diameter. During the casting of these specimens, four metal rods of 7 cm height and 0.3 cm diameter were put in the cement paste. These metal rods were removed after four hours of reaction to create artificial holes in which the relative humidity sensors were directly placed.

The saturation degree of water in the pore solution is determined from the results of **Paper 4**:

$$S = \frac{m - m_{0\%}}{m_{100\%} - m_{0\%}} \tag{5.1}$$

where m [kg] is the mass of the sample at a certain degree of reaction, $m_{100\%}$ [kg] is the mass after the saturation of the sample at a relative humidity equal to 100 % and $m_{0\%}$ [kg] is the mass of the sample after drying at 105 °C.

5.2 Modeling of the autogenous shrinkage of AAS paste

In this section, the modeling approach for autogenous shrinkage of AAS paste is presented. It is based on the extension of the capillary pressure theory presented by Li et al. [236].

In poromechanics, the Kelvin equation describes the equilibrium between a phase in liquid state and vapour state [229, 238]:

$$ln(RH) = \frac{2\gamma V_{l,mol}}{r_K RT} \tag{5.2}$$

where RH [-] is the relative humidity, γ [N.m^{-1}] is the liquid/vapor surface tension. γ = 73 mN.m^{-1} for water and is supposed to remain constant in the case of aqueous solutions, as in [228]. $V_{l,mol}$ [L.mol^{-1}] is the molar volume of the liquid, equal to 18 L.mol^{-1} for water. Lura [229] suggested that the effect of ions on the molar volume is minimal and $V_{l,mol}$ can be kept constant for aqueous solutions. R is the universal gas constant (R = 8.314 J.K^{-1}.mol^{-1}), T [K] the temperature and r_K [m] the Kelvin radius.

When a solvent is in equilibrium with its vapor phase, Eq. (5.2) is extended to [229, 236]:

$$ln(RH) = \frac{2\gamma V_{l,mol}}{r_K RT} + ln(x^l_{solv}) \tag{5.3}$$

where x^l_{solv} [mol/mol] is the molar fraction of the solvent in the liquid. In the current study, the solvent is water and $x(H_2O)$ replaces x^l_{solv} in Eq. (5.3).

$x(H_2O)$ is obtained from the kinetic-thermodynamic model using the Pitzer model with the CASH+ model. The details about the thermodynamic model are provided in **Paper 4**. $x(H_2O)$ is equal to:

$$x(H_2O) = \frac{n(H_2O)}{n(H_2O) + \sum_i n_i} \tag{5.4}$$

where $n(H_2O)$ is the number of moles of water in the pore solution and n_i is the number of moles of the species i (except water) present in the pore solution.

Laplace's law gives a relationship between r_K and the capillary pressure σ_{cap} that develops in a porous material due to the meniscus formation [229]:

$$\sigma_{cap} = -\frac{2\gamma}{r_k} \tag{5.5}$$

Inserting Eq. (5.5) in Eq. (5.3), σ_{cap} is expressed in function of $RH_K = \frac{RH}{x(H_2O)}$:

$$\sigma_{cap} = -\frac{ln(RH_K)RT}{V_{l,mol}} = -\frac{ln(RH/x(H_2O))RT}{V_{l,mol}} \tag{5.6}$$

The capillary pressure induces a linear strain ϵ_{lin} [239]:

$$\epsilon_{lin} = \frac{S\sigma_{cap}}{3}(\frac{1}{K} - \frac{1}{K_S}) \tag{5.7}$$

with K [GPa] the bulk modulus of the paste, which is obtained from the analysis in **Paper 5** and K_S [GPa] the bulk modulus of the skeleton, which can be assumed equal to 44 GPa [229, 240]. S [-] is the saturation degree of the paste.

In addition to the linear strain, it is assumed that the capillary pressure causes a creep strain [236]. In this case, the total shrinkage $\epsilon(t)$ is split into:

$$\epsilon(t) = \epsilon_{lin}(t) + \epsilon_{creep}(t) \tag{5.8}$$

with $\epsilon_{creep}(t)$ the creep component of shrinkage. The results of **Paper 6** show that the cause of creep of AAS is the deviatoric strain of the matrix of reaction products, while spherical strains at the microscale generate very low creep strains. It is thus hypothesized that the capillary pressure σ_{cap} generates complex stress states σ_{dev} in the matrix of reaction products due to heterogeneities of the microstructure. For the numerical implementation, $\sigma_{dev}(t) = \sigma_{cap}(t)$.

$\epsilon_{creep}(t)$ corresponds to the accumulation of the creep strains generated by each increment of capillary pressure-induced stresses. The numerical implementation is made by discretizing time into t_1, t_2, ..., t_n:

$$\epsilon_{creep}(t) = \sum_{i=2}^{n} J^p_{1111}(t, t_i)\Delta\sigma_{dev,i} \tag{5.9}$$

where $\Delta\sigma_{dev,i} = \sigma_{dev}(t_i) - \sigma_{dev}(t_{i-1})$ represents the stress increment between t_{i-1} and t_i. $J^p_{1111}(t, t_i)$ corresponds to the 1111-component of the tensor compliance creep of paste (Level 2) at time t when loaded at t_i. It is obtained from the multi-scale model of **Paper 6**.

At the scale of the matrix of reaction products (Level 0), creep is modeled as purely deviatoric with the following deviatoric compliance $J^{rpm}(t, t_i)$:

$$J^{rpm}(t, t_i) = \frac{1}{E_h}(1 - exp(-\frac{t - t'}{\tau})) + \frac{1}{C_h} ln(t - t' + 1) \tag{5.10}$$

with E_h = 200 GPa, τ = 0.002 d, C_h = 100 GPa, which are in a similar range to the results of **Paper 6**.

5.3 Results and discussion

The measured saturation degree S, the relative humidity RH, the computed molar fraction of water in the pore solution $x(H_2O)$ and $RH_K = \frac{RH}{x(H_2O)}$ are plotted in Figure 5.1 for both mix lS and mix hS. The saturation degree of both mixes remains high for both mixes (see Figure 5.1 A). The measured relative humidity is much higher for the mix hS than for the mix lS (Figure 5.1 B). In [228], the measured relative humidity was equal to 75 % after 7 days with a silica modulus M_S equal to 1.5 [mol SiO_2 / mol Na_2O]. Thus, it seems that the silica modulus of the activator solution has a predominant role in the measured internal relative humidity. Nevertheless, for both mixes, the measured values are low compared to relative humidity measured for OPC [229, 241]. During the first days of the reaction, $x(H_2O)$ strongly increases for the mix hS (see Figure 5.1 C), meaning that much of the ions initially present in the alkali solution react to form reaction products. In contrast, $x(H_2O)$ of the mix lS increases more progressively. For OPC, it was reported that $x(H_2O)$ remains constant with time [242]. It is quite interesting to see that the evolution of RH_K (Figure 5.1 D) is quite similar for both mix lS and mix hS. However, this change in RH_K is mainly the result of the reduction of the measured RH for mix lS, or of the steep increase of $x(H_2O)$ for the mix hS. The fact that the absolute value of RH_K is lower for the mix lS is coherent with the Mercury Intrusion Porosimetry (MIP) measurements of **Paper 4**. The structure of the mix lS has finer pores compared to the mix hS and smaller pores are associated with lower RH (see Eq. (5.2)). Besides, the fact that the computed RH_K is greater than 1 at early ages for the mix hS could be an artifact of the computation of the thermodynamic calculation. It could also come from the fact that Eq. (5.3) is valid if the pore solution is regarded as an ideal solution [243]. This hypothesis is questionable for the pore solution of the mix hS at early ages since $x(H_2O)$ is relatively low. Yet, high RH_K can cause swelling of the matrix and this would explain why more cracks were observed for the mix hS (see **Paper 4**). Also, due to high RH_K, water could be squeezed out of the matrix, explaining the tendency of bleeding for AAS [244].

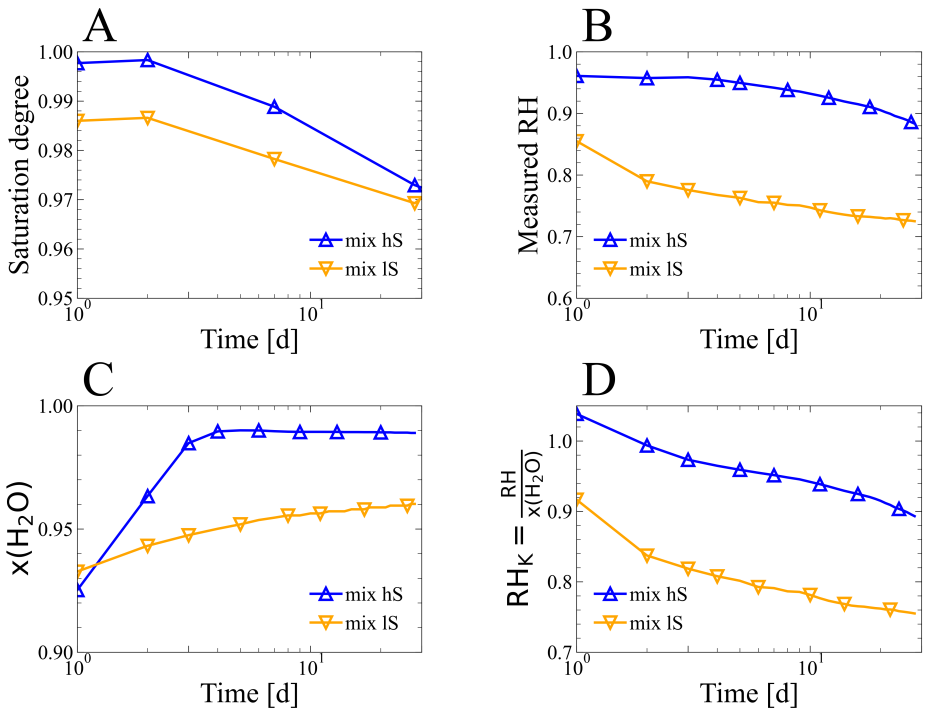

Figure 5.1: Temporal evolution of microstructure features of mix lS and mix hS: (A) Saturation degree; (B) relative humidity; (C) molar fraction of water in the pore solution $x(H_2O)$; (D) $RH_K = \frac{RH}{x(H_2O)}$

The capillary pressure σ_{cap} as expressed in Eq. (5.6) is plotted in Figure 5.2. It can be seen that the mix lS undergoes a higher capillary pressure and that the evolution of capillary pressure is slightly higher for the mix lS between 1 and 28 days (-26.2 MPa for mix lS and -20.4 MPa for mix hS).

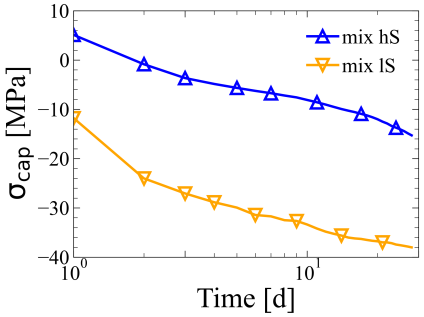

Figure 5.2: Development of capillary pressure in the paste for both mix lS and mix hS

The autogenous shrinkage experiment results as well as the corresponding modeling results on paste for both mixes are given in Figure 5.3. The computed linear shrinkage due to the capillary pressure is insufficient to explain the measured shrinkage. It can be seen that the linear shrinkage for mix lS is lower than the one of the mix hS, despite a higher capillary pressure (see Figure 5.2). This could be due to the faster development of Young's modulus for the mix lS (see **Paper 5**). It can also be seen that the creep part is higher for the mix lS. This could be due to the higher increase in capillary pressure especially during the first days of the reaction.

The model provides good results for the mix lS. For the mix hS, the model predicts a shrinkage of -5600 µm/m instead of the -7500 µm/m that was measured, corresponding to an error of 25 %. This could be explained by the presence of more cracks in this mix (see **Paper 4**) leading to more heterogeneities and deviatoric strains of the matrix.

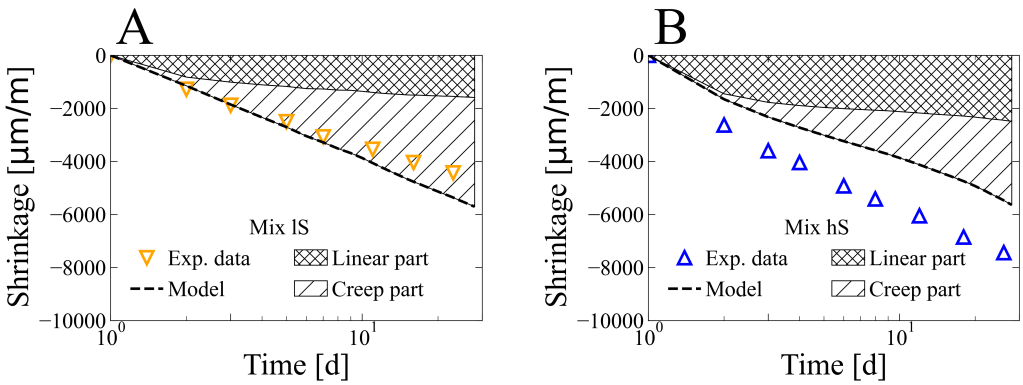

Figure 5.3: Experimental and modeling results of autogenous shrinkage for (A) mix lS and (B) mix hS

5.4 Concluding remarks and perspectives

The mechanisms discussed in Section 5.3 are coherent with observations done for autogenous shrinkage of AAS. Autogenous shrinkage was reported higher when M_S increases for AAS [245] and also alkali-activated fly ash [246]. This can be explained by a lower $x(H_2O)$ at early ages and a higher ion consumption. The same effect is observed for an increase in the alkalinity coefficient n [245, 247]. Increasing n increases the speed of reaction and thus accelerates the ion consumption and the increase in $x(H_2O)$. This effect is predominant over the faster increase in the degree of reaction [247] (i.e. higher Young's modulus and resistance to creep) and the autogenous shrinkage is higher.

The mechanisms and models of the present chapter are specific to the autogenous shrinkage of AAS. For OPC, it was shown that shrinkage can be predicted with linear poroelasticity without any creep effect (see Eq. (5.7)) when the relative humidity of concrete remains higher than 75 % [224]. This condition is valid for OPC [229, 241] and does not need further extensions. Moreover, the effect of dissolved salts for OPC is limited and $x(H_2O)$

is believed to remain constant with time [229, 242]. In addition, OPC presents very few cracks from autogenous shrinkage.

However, the creep mechanism presented before could explain the drying shrinkage of OPC. In this case, the relative humidity drops and causes gradients of moisture and capillary pressure in the material.

6 Conclusions and outlook

6.1 Conclusions

In this thesis, microstructure and nano-scale mechanical properties of alkali-activated slag were investigated to model and predict shrinkage and creep through multi-scale micromechanics-based modeling. The reaction kinetics of alkali-activated slag can be modeled by a succession of single-particle models. Its evolution mainly depends on the composition of the alkali solution. The high pH value of the alkaline solution accelerates slag dissolution. The silicate crystals present in the sodium silicate act as seeds for the nucleation of the reaction products. The influence of the slag composition on kinetics can be described by the slag quality coefficient $\frac{CaO+MgO}{SiO_2}$. The degree of dissolution of slag is around 50 % after 28 days. C-A-S-H is the main reaction product and the main secondary products are hydrotalcite and zeolitic precursors. The phase assemblage can correctly be predicted by thermodynamic modeling. The use of the Pitzer ion activity model is useful at early-age when the ionic strength is high. After two days of reaction, the Debye-Hückel ion activity model predicts the same result as the Pitzer model. It is recommended to use the CASH+ database to model C-A-S-H. In addition, the datasets from the zeolite20 and cemdata18 databases can be used to predict the phase assemblage of alkali-activated slag. The volume fraction of water contained in the C-A-S-H gel is found equal to 28 % of the volume fraction of C-A-S-H, in the same range as what was found for C-S-H. The amount of capillary water is low for alkali-activated slag.

From the description of the microstructure, analytical micromechanics-based multi-scale homogenization models can be applied to link the mechanical properties at the nano-scale and the macro-scale. At the nano-scale, two matrices of reaction products are present. Their corresponding modulus of elasticity can be regarded as independent of the mix design. For paste and concrete Young's modulus, the developed homogenization model provides accurate results compared to experimental tests performed in this thesis. For creep, the results on concrete were downscaled to model the creep of the matrix of reaction products. The results indicate that the contact creep modulus obtained by nanoindentation was a good estimate of the deviatoric contact creep modulus of the matrix of reaction products. The analysis also shows that the deviatoric strains of the matrix of reaction products are the main cause of the creep of concrete, while the spherical strains have a negligible influence. The deviatoric creep at the nano-scale can be split into two components. The first one could represent reversible water movements just after the loading, while the second one could be due to the progressive sliding or the preferred orientation of C-A-S-H gel particles.

Autogenous shrinkage can be predicted after determining the evolution of the microstructure and the creep behavior of the material. Poromechanics is used to describe the linear strains generated by capillary pressure. Due to the consumption of ions present in the initial alkali solution during the hardening, the increase in the water fraction volume in the pore solution is much higher than for the hydration of cement and cannot be neglected in the calculation of shrinkage. The capillary pressure causes also creep strains at the nano-scale in turn explaining the autogenous shrinkage of AAS paste.

6.2 Outlook and perspectives

From the results of this thesis, recommendations for future work can be proposed.

Further experimental investigations with different mix designs of sodium silicate-activated slag should be performed. In particular, systematic determination of the degree of dissolution of the slag with time is recommended. Also, quantification of the formed reaction products would strengthen the validation of the kinetics-thermodynamics model. At early-age, the composition of the pore solution could be determined experimentally to quantify the consumption of ions from the alkali solution.

For creep, short-time sustained loading could be applied on old concrete specimens, whose reaction rate is low. By measuring creep strains and recovered strains, the hypothesis of the reversibility of early-stage creep due to water movements could be confirmed or invalidated.

In addition, the irreversible creep strains due to the solidification of the paste at early-age could be quantified. To that end, loadings could be applied to the concrete after a few hours of reaction.

Regarding the impacts of microcracks on shrinkage, further numerical analyses could be performed to prove the development of deviatoric stresses through spherical stresses applied to the heterogeneous matrix. Furthermore, the influence of microcracks on shrinkage could be modeled with a damage coefficient.

Bibliography

1. Steffen, W. *et al.* Planetary boundaries: Guiding human development on a changing planet. *Science* **347,** 137. ISSN: 0036-8075 (2015).
2. The World Bank. World Bank Open Data. (accessed: 05.04.2023). https://data.worldbank.org/ (2023).
3. World Wide Fund for Nature (WWF). *Bending the curve of biodiversity loss* ISBN: 9782940529995 (WWF, Gland, 2020).
4. Masson-Delmotte, V. *et al.* in *Climate Change 2021: The Physical Science Basis. Contribution of Working Group I to the Sixth Assessment Report of the Intergovernmental Panel on Climate Change* chap. IPCC, 2021: Summary for Policymakers. (2021).
5. Jacobson, M. Z. Studying ocean acidification with conservative, stable numerical schemes for nonequilibrium air-ocean exchange and ocean equilibrium chemistry. *Journal of Geophysical Research* **110,** 260. ISSN: 0148-0227 (2005).
6. Goodmann, A. & Laura, P. Drought-stricken Spain braces for exceptionally high temperatures expected to break April records. *CNN.* (accessed: 05.05.2023). https://edition.cnn.com/2023/04/27/europe/spain-high-temperature-heat-climate-intl/index.html (2023).
7. Gustin, G. An Agricultural Drought In East Africa Was Caused by Climate Change, Scientists Find. *Inside Climate News.* (accessed:01.05.2023). https://insideclimatenews.org/news/27042023/east-africa-drought-climate-change-attribution/ (2023).
8. Morton, D. *et al.* Cropland Expansion Changes Deforestation Dynamics in the Southern Brazilian Amazon. *Proceedings of the National Academy of Sciences of the United States of America* **103,** 14637–41 (Oct. 2006).
9. Tabrizi, A. Seaspiracy. (accessed: 22.04.2023). https://www.seaspiracy.org/ (2021).
10. Sütő, L. in *Anthropogenic Geomorphology* (eds Szabó, J., Dávid, L. & Lóczy, D.) 131–154 (Springer Netherlands, Dordrecht, 2010). ISBN: 978-90-481-3057-3.
11. Wylie, S., Wilder, E., Vera, L., Thomas, D. & McLaughlin, M. Materializing Exposure: Developing an Indexical Method to Visualize Health Hazards Related to Fossil Fuel Extraction. *Engaging science, technology, and society* **3,** 426–463 (2017).
12. Ellsworth, W. L. Injection-Induced Earthquakes. *Science* **341,** 1225942. ISSN: 0036-8075 (2013).
13. Stewart, A. G. Mining is bad for health: a voyage of discovery. *Environmental Geochemistry and Health* **42,** 1153–1165. ISSN: 0269-4042 (2020).

14. Systext. Rapport d'étude - Controverses minières - Volet 1: Pour en finir avec certaines contrevérités sur la mine et les filières minérales (2021).
15. Our World in Data. Our World in Data. (accessed: 05.04.2023). https://ourworldindata.org/ (2023).
16. The Shift Project. Plan de transformation de l'économie française: focus sur les usages numériques. (accessed: 05.05.2023). https://theshiftproject.org/les-usages-numeriques/ (2020).
17. Lebreton, L. *et al.* Evidence that the Great Pacific Garbage Patch is rapidly accumulating plastic. *Scientific Reports* **8,** 4666. ISSN: 2045-2322. https://doi.org/10.1038/s41598-018-22939-w (2018).
18. Earth Overshoot Day. Last year, Earth Overshoot Day fell on July 28. (accessed: 17.04.2023). https://www.overshootday.org/.
19. Armstrong McKay, D. I. *et al.* Exceeding 1.5°C global warming could trigger multiple climate tipping points. *Science (New York, N.Y.)* **377,** eabn7950 (2022).
20. European Parliament. The impact of textile production and waste on the environment (infographic). (accessed: 05.05.2023). https://www.europarl.europa.eu/news/en/headlines/society/20201208STO93327/the-impact-of-textile-production-and-waste-on-the-environment-infographic (2022).
21. Silva, M. South America's 'lithium triangle' communities are being 'sacrificed' to save the planet. *Euronews.* (accessed: 05.05.2023). https://www.euronews.com/green/2022/10/28/south-americas-lithium-triangle-communities-are-being-sacrificed-to-save-the-planet (2023).
22. Stone, D. Amazon Tribes Stand Up for Their Survival. *National Geographic.* (accessed: 20.04.2023). https://www.nationalgeographic.com/photography/article/amazon-river-dams-displacement-indigenous-elkaim (2017).
23. The Editors of Encyclopaedia Britannica. History and controversy of the Three Gorges Dam. *Britannica.* (accessed: 22.04.2023). https://www.britannica.com/topic/Three-Gorges-Dam/History-and-controversy-of-the-Three-Gorges-Dam.
24. Clark, B. The Indigenous Environmental Movement in the United States: Transcending Borders in Struggles against Mining, Manufacturing, and the Capitalist State. *Organization & Environment* **15,** 410–442 (2002).
25. International Labour Organization and United Nations Children's Fund 2021. Child Labour - Global estimates 2020, trends and the road forward. https://data.unicef.org/resources/child-labour-2020-global-estimates-trends-and-the-road-forward/ (2021).
26. Merchant, B. Life and death in Apple's forbidden city. *The Guardian.* (accessed: 20.04.2023). https://www.theguardian.com/technology/2017/jun/18/foxconn-life-death-forbidden-city-longhua-suicide-apple-iphone-brian-merchant-one-device-extract (2017).

27. United Nations News. China responsible for 'serious human rights violations' in Xinjiang province: UN human rights report. (accessed: 05.05.2023). https://news.un.org/en/story/2022/08/1125932 (2022).

28. Perrin, E. & Bovon, G. Fast Fashion - Les dessous de la mode à bas prix. *Production: ARTE France, Premières Lignes.* https://boutique.arte.tv/detail/fast-fashion-les-dessous-de-la-mode-a-bas-prix (2021).

29. Bretveld, R. W., Thomas, C. M., Scheepers, P. T., Zielhuis, G. A. & Nel, R. Pesticide exposure: the hormonal function of the female reproductive system disrupted? *Reproductive biology and endocrinology : RB&E* **4,** 30 (2006).

30. Mnif, W. *et al.* Effect of endocrine disruptor pesticides: a review. *International journal of environmental research and public health* **8,** 2265–2303 (2011).

31. Leemans, M., Couderq, S., Demeneix, B. & Fini, J.-B. Pesticides With Potential Thyroid Hormone-Disrupting Effects: A Review of Recent Data. *Frontiers in endocrinology* **10,** 743. ISSN: 1664-2392 (2019).

32. Rai, P. K., Lee, J., Brown, R. J. C. & Kim, K.-H. Environmental fate, ecotoxicity biomarkers, and potential health effects of micro- and nano-scale plastic contamination. *Journal of hazardous materials* **403,** 123910 (2021).

33. Clark, M. The (PFAS)T and the Furious: Applying Hazardous Waste Management Frameworks to the Global Presence of PFAS. *Journal of Air Law and Commerce* **87,** 533. ISSN: 0021-8642 (2022).

34. Levine, H. *et al.* Temporal trends in sperm count: a systematic review and meta-regression analysis of samples collected globally in the 20th and 21st centuries. *Human reproduction upyear* **29,** 157–176 (2023).

35. Keles, B., McCrae, N. & Grealish, A. A systematic review: the influence of social media on depression, anxiety and psychological distress in adolescents. *International Journal of Adolescence and Youth* **25,** 79–93. ISSN: 0267-3843 (2020).

36. Qureshi-Hurst, E. Anxiety, alienation, and estrangement in the context of social media. *Religious Studies* **58,** 522–533. ISSN: 0034-4125 (2022).

37. World Health Organization. WHO global air quality guidelines. Particulate matter (PM2.5 and PM10), ozone, nitrogen dioxide, sulfur dioxide and carbon monoxide. *Geneva: World Health Organization. Licence: CCBY-NC-SA 3.0 IGO.* https://www.who.int/publications/i/item/9789240034228 (2021).

38. World Health Organization. Ambient (outdoor) air pollution. (accessed: 05.04.2023). https://www.who.int/news-room/fact-sheets/detail/ambient-(outdoor)-air-quality-and-health (2022).

39. Lelieveld, J. *et al.* Cardiovascular disease burden from ambient air pollution in Europe reassessed using novel hazard ratio functions. *European heart journal* **40,** 1590–1596 (2019).

40. Emerson, J. B. *et al.* Host-linked soil viral ecology along a permafrost thaw gradient. *Nature microbiology* **3,** 870–880 (2018).

41. Petrovan, S. O. *et al.* Post COVID-19: a solution scan of options for preventing future zoonotic epidemics. *Biological reviews of the Cambridge Philosophical Society* **96,** 2694–2715 (2021).

42. World Mining Data. World Mining Data. (accessed: 05.04.2023). https://www.world-mining-data.info/ (2022).

43. Mudd, G. M. The Environmental sustainability of mining in Australia: key mega-trends and looming constraints. *Resources Policy* **35,** 98–115. ISSN: 0301-4207. https://www.sciencedirect.com/science/article/pii/S0301420709000531 (2010).

44. Northey, S., Mohr, S., Mudd, G. M., Weng, Z. & Giurco, D. Modelling future copper ore grade decline based on a detailed assessment of copper resources and mining. *Resources, Conservation and Recycling* **83,** 190–201. ISSN: 09213449 (2014).

45. Norgate, T. & Haque, N. Energy and greenhouse gas impacts of mining and mineral processing operations. *Journal of Cleaner Production* **18,** 266–274. ISSN: 09596526 (2010).

46. Diamond, J. M. *Collapse: How societies choose to fail or succeed* ISBN: 0670033375 (Penguin Books, London, New York, NY, and Toronto, 2006).

47. Intergovernmental Panel on Climate Change. Summary for Policymakers. *Global Warming of 1.5°C: IPCC Special Report on Impacts of Global Warming of 1.5°C above Pre-industrial Levels in Context of Strengthening Response to Climate Change, Sustainable Development, and Efforts to Eradicate Poverty,* 1–24 (2022).

48. International Energy Agency (IEA). The Role of Critical Minerals in Clean Energy Transitions, IEA, Paris, License: CC BY 4.0. https://www.iea.org/reports/the-role-of-critical-minerals-in-clean-energy-transitions (2016).

49. International Energy Agency (IEA). Heating. Paris, License: CC BY 4.0, (accessed: 22.04.2023). https://www.iea.org/reports/heating (2022).

50. Markussen, M. & Østergård, H. Energy Analysis of the Danish Food Production System: Food-EROI and Fossil Fuel Dependency. *Energies* **6,** 4170–4186 (2013).

51. International Energy Agency (IEA). World Energy Outlook 2022. Paris, License: CC BY 4.0, (accessed: 22.04.2023). https://www.iea.org/reports/world-energy-outlook-2022 (2022).

52. Flower, D. J. M. & Sanjayan, J. G. Green house gas emissions due to concrete manufacture. *The International Journal of Life Cycle Assessment* **12,** 282–288. ISSN: 0948-3349 (2007).

53. British Petroleum (BP). Statistical Review of World Energy. https://www.bp.com/en/global/corporate/energy-economics/statistical-review-of-world-energy.html (2022).

54. Hall, C. A., Lambert, J. G. & Balogh, S. B. EROI of different fuels and the implications for society. *Energy Policy* **64,** 141–152. ISSN: 03014215 (2014).

55. Auzanneau, M. & Chauvin, H. *Pétrole, le déclin est proche* ISBN: 978202-1480757 (Éditions du Seuil, Paris, 2021).

56. Chancel, L., Piketty, T., Saez, E., Zucman, G. & al. World Inequality Report 2022, World Inequality Lab. (accessed: 22.04.2023). https://wir2022.wid.world/ (2022).

57. Tax Justice Network. The State of Tax Justice 2021. https://taxjustice.net/reports/the-state-of-tax-justice-2021/ (2021).

58. France Corruption. L'observatoire des pantouflages. (accessed: 20.04. 2023). https://francecorruption.fr/pantouflages/ (2023).

59. Corporate Europe Observatory. Captured states - When EU governments are a channel for corporate interests. (accessed: 20.04.2023). https://corporateeurope.org/en/2019/02/captured-states (2019).

60. Disclose. Pétrole et paradis fiscaux : les intérêts cachés de la ministre de la transition énergétique. (accessed: 20.04.2023). https://disclose.ngo/fr/article/petrole-et-paradis-fiscaux-les-interets-caches-de-la-ministre-de-la-transition-energetique (2022).

61. BBC. EU corruption scandal: MEP denies Qatar bribery after €1.5m seized. (accessed: 20.04.2023). https://www.bbc.com/news/world-europe-63952993 (2022).

62. Corporate Europe Observatory. Packaging lobby's support for anti-litter groups deflects tougher solutions. *National Geographic.* (accessed: 04.04.2023). https://corporateeurope.org/en/power-lobbies/2018/03/packaging-lobby-support-anti-litter-groups-deflects-tougher-solutions.

63. Oreskes, N. & Conway, E. M. *Merchants of doubt: How a handful of scientists obscured the truth on issues from tobacco smoke to global warming* Paperback. ed. ISBN: 1408824833 (Bloomsbury, London, 2012).

64. McGoey, L. *The unknowers: How strategic ignorance rules the world* ISBN: 97817803263-75. https://ebookcentral.proquest.com/lib/kxp/detail.action?docID=5900256 (Zed Books, London, UK, 2019).

65. Girel, M., Foucart, S., Vasselin, P. & Cuveillier, F. La fabrique de - l'ignorance. *Production: ARTE France, Zed.* https://boutique.arte.tv/detail/la-fabrique-de-lignorance (2020).

66. Supran, G., Rahmstorf, S. & Oreskes, N. Assessing ExxonMobil's global warming projections. *Science (New York, N.Y.)* **379,** eabk0063 (2023).

67. IEA, Paris. CO2 Emissions in 2022, IEA. Paris, License: CC BY 4.0, (accessed: 05.05. 2023). https://www.iea.org/reports/co2-emissions-in-2022 (2023).

68. d'Adda, G., Gao, Y., Golman, R. & Tavoni, M. It's so Hot in Here: Information Avoidance, Moral Wiggle Room, and High Air Conditioning Usage. *SSRN Electronic Journal* (2018).

69. Huebner, J. A possible declining trend for worldwide innovation. *Technological Forecasting and Social Change* **72,** 980–986. ISSN: 00401625 (2005).

70. Arnold, M., Tainter, J. A. & Strumsky, D. Productivity of innovation in biofuel technologies. *Energy Policy* **124,** 54–62. ISSN: 03014215 (2019).

71. Peñasco, C. & Anadón, L. D. Assessing the effectiveness of energy efficiency measures in the residential sector gas consumption through dynamic treatment effects: Evidence from England and Wales. *Energy Economics* **117,** 106435. ISSN: 01409883 (2023).

72. Meilhan, N. Comment faire enfin baisser les émissions de CO2 des voitures. (accessed: 20.04.2023). https://www.strategie.gouv.fr/publications/faire-enfin-baisser-emissions-de-co2-voitures (2019).

73. Bigo, A. La voiture électrique, solution idéale pour le climat ? *Bon pote.* (accessed: 20.04.2023). https://bonpote.com/la-voiture-electrique-solution-ideale-pour-le-climat/#Conclusion_que_retenir_de_tout_cela (2023).

74. Our World in Data. Our World in Data. (accessed: 03.05.2023). https://ourworldindata.org/energy-production-consumption (2023).

75. Fressoz, J.-B. & Locher, F. *Les révoltes du ciel: Une histoire du changement climatique : (XVe-XXe siècle)* ISBN: 9782021058147 (Éditions du Seuil, Paris, 2020).

76. European Commission. Communication from the Commission to the european parliament, the European Council, the Council, the European Economic and Social Committee and the Committee of the Regions: The European Green Deal. https://eur-lex.europa.eu/legal-content/EN/TXT/PDF/?uri=CELEX:52019DC0640 (2019).

77. Jensen, J. Evaluating the environmental impacts of recycling wind turbines. *Wind Energy* **22** (Oct. 2018).

78. Ortegon, K., Nies, L. F. & Sutherland, J. W. Preparing for end of service life of wind turbines. *Journal of Cleaner Production* **39,** 191–199. ISSN: 09596526. https://www.sciencedirect.com/science/article/pii/S0959652612004441 (2013).

79. Mignerot, V. *L'énergie du déni: Comment la transition énergétique va augmenter les émissions de CO_2* ISBN: 9782374252797 (Rue de l'échiquier, Paris, 2021).

80. Aramco. Renewables not that new. (accessed: 17.03.2023). https://www.aramco.com/en/magazine/elements/2020/renewables-not-that-new (2020).

81. Hywind Tampen. Hywind Tampen: the world's first renewable power for offshore oil and gas. (accessed: 17.03.2023). https://www.equinor.com/energy/hywind-tampen.

82. Map for Environment. The East African Crude Oil Pipeline – EACOP a spatial risk perspectivea. (accessed: 05.04.2023). https://mapforenvironment.org/story/The-East-African-Crude-Oil-Pipeline-EACOP-a-spatial-risk-perspective/111 (2021).

83. Cabral, S. Willow Project: US government approves Alaska oil and gas development. *BBC.* (accessed: 17.04.2023). https://www.bbc.com/news/world-us-canada-64943603 (2023).

84. Ministère de la transition écologique et de la cohésion des territoires. Estimation de l'empreinte carbone de 1995 à 2020. (accessed: 17.03.2023). https://www.statistiques.developpement-durable.gouv.fr/estimation-de-lempreinte-carbone-de-1995-2020 (2021).

85. Berlingen, F. *Recyclage: Le grand enfumage : comment l'économie circulaire est devenue l'alibi du jetable* nouv. ed. de poche. ISBN: 97823-74253176 (éditions Rue de l'échiquier, Paris, 2021).

86. Bihouix, P. *L'âge des low tech: Vers une civilisation techniquement soutenable* Édition revue et augmentée d'une postface inédite. ISBN: 9782757889510 (Éditions du Seuil, Paris, 2021).

87. van der Voet, E. *Environmental risks and challenges of anthropogenic metals flows and cycles* (United Nations Environment Programme and International Resource Panel, Nairobi, Kenya and Paris, France, 2013).

88. Fishman, A., Gandal, N. & Shy, O. Planned Obsolescence as an Engine of Technological Progress. **275512.** Tel-Aviv University > Foerder Institute for Economic Research. https://ideas.repec.org/p/ags/isfiwp/275512.html (1991).

89. Satyro, W. C., Sacomano, J. B., Contador, J. C. & Telles, R. Planned obsolescence or planned resource depletion? A sustainable approach. *Journal of Cleaner Production* **195,** 744–752. ISSN: 09596526 (2018).

90. Barros, M. & Dimla, E. From planned obsolescence to the circular economy in the smartphone industry: an evolution of strategies embodied in product features. *Proceedings of the Design Society* **1,** 1607–1616 (2021).

91. Sonter, L. J., Dade, M. C., Watson, J. E. M. & Valenta, R. K. Renewable energy production will exacerbate mining threats to biodiversity. *Nature communications* **11,** 4174 (2020).

92. The World Bank Group. Climate Risk Country Profile: Tuvalu. (accessed: 16.03.2023). https://climateknowledgeportal.worldbank.org/country-profiles (2021).

93. Caramel, L. Uganda's EACOP pipeline: Insurer Marsh targeted by complaint filed with OECD. *Le Monde.* (accessed: 20.04.2023). https://www.lemonde.fr/en/le-monde-africa/article/2023/02/08/uganda-s-eacop-pipeline-insurer-marsh-targeted-by-complaint-filed-with-oecd_6014929_124.html (2023).

94. Torres, M. & Sue, B. Intimidation of Brazil's enviro scientists, academics, officials on upswing. *Mongabay.* (accessed: 22.04.2023). https://news.mongabay.com/2021/04/intimidation-of-brazils-enviro-scientists-academics-officials-on-upswing/ (2021).

95. Baldos, R. Une journaliste spécialisée dans l'agriculture menacée en Bretagne. *La Croix.* (accessed: 20.04.2023). https://www.la-croix.com/Economie/journaliste-specialisee-lagriculture-menacee-Bretagne-2021-04-07-1201149772 (2021).

96. Global Witness. Last line of defence. https://www.globalwitness.org/en/campaigns/environmental-activists/last-line-defence/ (2021).

97. Amnesty International. Manifestations en France: un recours excessif à la force et aux arrestations abusives. (accessed: 22.04.2023). https://www.amnesty.fr/actualites/france-manifestations-un-recours-excessif-a-la-la-force-et-aux-arrestations-abusives (2023).

98. Commissioner for Human Rights. Demonstrations in France: freedoms of expression and assembly must be protected against all forms of violence. (accessed: 22.04.2023). https://www.coe.int/en/web/commis sioner/-/manifestations-en-france-les-libertés-d-expression-et-de-réun ion-doivent-être-protégées-contre-toute-forme-de-violence (2023).

99. Darame, M. & Lamothe, J. Gérald Darmanin menace de remettre en question les subventions publiques accordées à la Ligue des droits de l'homme. *Le Monde.* (accessed: 22.04.2023). https://www.lemonde.fr/politique/article/2023/04/05/gerald-darmanin-menace-de-remettre-en-question-les-subventions-publiques-accordees-a-la-ldh_6168412_823448.html (2023).

100. Meadows, D., Meadows, D., Randers, J. & Behrens, W. W. *The limits to growth: A report for the Club of Rome's Project on the Predicament of Mankind* 2. ed. ISBN: 0876631650 (Universe Books, New York, 1972).

101. Tainter, J. A. *The collapse of complex societies* ISBN: 9780521386739 (Cambridge Univ. Press, Cambridge, 2011).

102. Natarajan, K. V. & Prasad, S. A supply chain perspective on India's COVID-19 crisis: Lessons from the second wave and preparing for a potential third wave. *Journal of global health* **11,** 03116 (2021).

103. Kay, G. From toilet paper to coffee, here are some of the products that could soon be in short supply because of the Suez Canal blockage. *Business Insider.* (accessed: 20.04.2023). https://www.businessinsider.com/toilet-paper-coffee-products-delayed-suez-canal-blockage-impact-2021-3 (2021).

104. Newey, S. 'We can no longer afford to eat': Ukraine war pushes millions into starvation. *The Telegraph.* (accessed: 20.04.2023). https://www.telegraph.co.uk/global-health/climate-and-people/can-no-longer-afford-eat-ukraine-war-pushes-hundreds-thousands/ (2022).

105. Bohler, S. *Le bug humain: Pourquoi notre cerveau nous pousse à détruire la planète et comment l'en empêcher* ISBN: 9782221240106 (R. Laffont, Paris, 2019).

106. Jaeger, C. C. Klaus Hasselmann and Economics. *Journal of Physics: Complexity* **3,** 041001 (2022).

107. Dion, C. *Petit manuel de résistance contemporaine: Récits et stratégies pour transformer le monde* Nouvelle édition revue et augmentée. ISBN: 9782330155575 (Actes sud and Impr. Normandie Roto Impression, Arles and 61-Lonrai, 2021).

108. Hopkins, R. *From what is to what if: Unleashing the power of imagination to create the future we want* ISBN: 9781603589062. https://ebookcentral.proquest.com/lib/kxp/detail.action?docID=5900404 (Chelsea Green Publishing, White River Junction, Vermont and London, UK, 2019).

109. Piketty, T. *Capital and Ideology* ISBN: 9780674245075. https://ebookcentral.proquest.com/lib/kxp/detail.action?docID=6028824 (The Belknap Press of Harvard University Press, Cambridge. Massachusetts and London, England, 2020).

110. Ivanova, D. & Wood, R. The unequal distribution of household carbon footprints in Europe and its link to sustainability. *Global Sustainability* **3,** 25 (2020).

111. Acar, S., Söderholm, P. & Brännlund, R. Convergence of per capita carbon dioxide emissions: implications and meta-analysis. *Climate Policy* **18,** 512–525. ISSN: 1469-3062 (2018).

112. Messner, D., Schellnhuber, J., Rahmstorf, S. & Klingenfeld, D. The budget approach: A framework for a global transformation toward a low-carbon economy. *Journal of Renewable and Sustainable Energy* **2,** 031003 (2010).

113. United Nations - Population Division. *The World's Cities in 2018: Data Booklet* ISBN: 9789210476102 (United Nations, New York, 2018).

114. Khomenko, S. *et al.* Premature mortality due to air pollution in European cities: a health impact assessment. *The Lancet. Planetary health* **5,** e121–e134 (2021).

115. Organisation for Economic Co-operation and Development (OECD). Demystifying compact urban growth: Evidence from 300 studies from across the world. *OECD Regional Development Working Papers.* 10.1787/20737009 (2018).

116. Haas, B. China's Shanghai sets population at 25 million to avoid 'big city disease'. *The Guardian.* (accessed: 17.04.2023). https://www.theguardian.com/world/2017/dec/26/chinas-shanghai-sets-population-25-million--big-city-disease (2017).

117. Billen, G. *et al.* Reshaping the European agro-food system and closing its nitrogen cycle: The potential of combining dietary change, agroecology, and circularity. *One Earth* **4,** 839–850. ISSN: 25903322 (2021).

118. The Shift Project. Plan de transformation de l'économie française: Agriculture et alimentation. (accessed: 17.04.2023). https://theshiftproject.org/plan-de-transformation-de-leconomie-francaise-agriculture-et-alimentation/ (2020).

119. Greenhouse Gas Protocol. Corporate Value Chain (Scope 3) Standard. https://ghgprotocol.org/corporate-value-chain-scope-3-standard (2011).

120. Read, S. What is the difference between Scope 1, 2 and 3 emissions, and what are companies doing to cut all three? *World Economic Forum.* (accessed: 24.04.2023). https://www.weforum.org/agenda/2022/09/scope-emissions-climate-greenhouse-business/ (2022).

121. World Economic Forum. Nature Risk Rising: Why the Crisis Engulfing Nature Matters for Business and the Economy. (accessed: 24.04.2023). http://www3.weforum.org/docs/WEF_New_Nature_Economy_Report_2020.pdf (2020).

122. Reed, B. Shifting from 'sustainability' to regeneration. *Building Research & Information* **35,** 674–680. ISSN: 0961-3218 (2007).

123. Rhodes, C. J. The imperative for regenerative agriculture. *Science-progress* **100,** 80–129. ISSN: 0036-8504 (2017).

124. Cole, R. J. Transitioning from green to regenerative design. *Building Research & Information* **40,** 39–53. ISSN: 0961-3218 (2012).

125. Convention citoyenne pour le climat. Les propositions de la Convention Citoyenne pour le Climat. (accessed: 20.04.2023). https://www.conventioncitoyennepourleclimat.fr/les-travaux-de-la-convention-3/ (2021).

126. Le Monde avec AFP. La convention citoyenne pour le climat juge sévèrement la prise en compte de ses propositions par le gouvernement. *Le Monde.* (accessed: 20.04.2023). https://www.lemonde.fr/politique/article/2021/02/28/la-convention-citoyenne-pour-le-climat-juge-severement-la-prise-en-compte-de-ses-propositions-par-le-gouvernement_6071474_823448.html (2021).

127. De Tocqueville, A. *De la démocratie en Amerique* ISBN: 9782081220874 (Flammarion, [Paris], 2010).

128. Smith, A. *The wealth of nations* ISBN: 9781505577129 ([CreateSpace Independent Publishing Platform], Middletown, DE, 2014).

129. Danielsson, J. Financial and Monetary Systems: Here's how to avoid systemic economic crises in future. *World Economic Forum.* (accessed: 22.04.2023). https://www.weforum.org/agenda/2022/11/regulatory-systemic-financial-crisis-illusion-control/ (2022).

130. Brusset, C. *Vous êtes fous d'avaler ça ! Un industriel de l'agro-alimentaire dénonce : [un guide de survie en magasin]* ISBN: 9782290133330 (J'ai lu, Paris, 2017).

131. Dion, C. & Pons, N. *Animal: Chaque génération a son combat, voici le nôtre* ISBN: 9782330146870 (Actes sud, Arles, 2021).

132. Sarkar, S., Dias Bernardes Gil, J., Keeley, J., Möhring, N. & Jansen, K. *The use of pesticides in developing countries and their impact on health and the right to food: Study requested by the DEVE committee* ISBN: 9789284676736 (Publications Office of the European Union, Luxembourg, Luxembourg, 2021).

133. Greenpeace France. Mordue de viande, l'Europe alimente la crise climatique par son addiction au soja. (accessed: 05.04.2023). https://www.greenpeace.fr/mordue-de-viande-leurope-alimente-la-crise-climatique-par-son-addiction-au-soja/ (2019).

134. UFC Que choisir. Pesticide cancérogène. Contamination massive de produits au sésame. (accessed: 20.04.2023). https://www.quechoisir.org/actualite-pesticide-cancerogene-contamination-massive-de-produits-au-sesame-n84707/ (2020).

135. Matthews, H. D. Quantifying historical carbon and climate debts among nations. *Nature Climate Change* **6,** 60–64. ISSN: 1758-678X (2016).

136. Kaamil, A. 'Finally some justice': court rules Shell Nigeria must pay for oil damage. *The Guardian.* (accessed: 05.05.2023). https://www.theguardian.com/global-development/2021/jan/29/finally-some-justice-court-rules-shell-nigeria-must-pay-for-oil-damage (2021).

137. Scrivener, K. L., John, V. M. & Gartner, E. M. Eco-efficient cements: Potential economically viable solutions for a low-CO2 cement-based materials industry. *Cement and Concrete Research* **114,** 2–26. ISSN: 00088846 (2018).

138. Ke, J., McNeil, M., Price, L., Khanna, N. Z. & Zhou, N. Estimation of CO2 emissions from China's cement production: Methodologies and uncertainties. *Energy Policy* **57,** 172–181. ISSN: 03014215 (2013).

139. International Energy Agency (IEA). Technology Roadmap - Low- Carbon Transition in the Cement Industry. Paris, License: CC BY 4.0. https://www.iea.org/reports/technology-roadmap-low-carbon-transition-in-the-cement-industry (2018).

140. Fressoz, J.-B. Café des Sciences: Jean-Baptiste Fressoz, De l'utopie atomique au déni climatique. (accessed: 05.05.2023). https://www.youtube.com/watch?v=p5VEy2IjDMs (2022).

141. Magalhães, N. Sable : un extractivisme ordinaire ? (accessed: 17.04.2023). https://www.youtube.com/watch?v=dNF96GTBF_E (2022).

142. Habert, G. *et al.* Environmental impacts and decarbonization strategies in the cement and concrete industries. *Nature Reviews Earth & Environment* **1,** 559–573 (2020).

143. European Cement Research Academy; Cement Sustainability Initiative. Development of State of the Art-Techniques in Cement Manufacturing: Trying to Look Ahead; CSI/ECRATechnology Papers 2017. *Duesseldorf, Geneva.* https://ecra-online.org/research/technology-papers (2017).

144. Chen, C., Habert, G., Bouzidi, Y., Jullien, A. & Ventura, A. LCA allocation procedure used as an incitative method for waste recycling: An application to mineral additions in concrete. *Resources, Conservation and Recycling* **54,** 1231–1240. ISSN: 09213449 (2010).

145. Bruckner, T. *et al.* Energy Systems. *In: Climate Change 2014: Mitigation of Climate Change. Contribution of Working Group III to the Fifth Assessment Report of the Intergovernmental Panel on Climate Change [Edenhofer, O., R. Pichs-Madruga, Y. Sokona, E. Farahani, S. Kadner, K. Seyboth, A. Adler, I. Baum, S. Brunner, P. Eickemeier, B. Kriemann, J. Savolainen, S. Schlömer, C. von Stechow, T. Zwickel and J.C. Minx (eds.)]. Cambridge University Press, Cambridge, United Kingdom and New York, NY, USA.* (2014).

146. Habert, G., Billard, C., Rossi, P., Chen, C. & Roussel, N. Cement production technology improvement compared to factor 4 objectives. *Cement and Concrete Research* **40,** 820–826. ISSN: 00088846 (2010).

147. The European Cement Association (CEMBUREAU). 2050 Carbon Neutrality Roadmap. https://cembureau.eu/library/reports/2050-carbon-neutrality-roadmap/ (2020).

148. Kendall, A., Chang, B. & Sharpe, B. Accounting for time-dependent effects in biofuel life cycle greenhouse gas emissions calculations. *Environmental science & technology* **43,** 7142–7147. ISSN: 0013-936X (2009).

149. Cherubini, F., Peters, G. P., Berntsen, T., Strømmann, A. H. & Hertwich, E. CO2 emissions from biomass combustion for bioenergy: atmospheric decay and contribution to global warming. *GCB Bioenergy* **3,** 413–426. ISSN: 17571693 (2011).

150. Holtsmark, B. Quantifying the global warming potential of CO_2 emissions from wood fuels. *GCB Bioenergy* **7,** 195–206. ISSN: 17571693 (2015).

151. Baral, A. & Malins, C. Comprehensive carbon accounting for identification of sustainable biomass feedstocks. *The International Council on Clean Transportation* (2014).

152. Kehrle, L. D. Carbon Capture Storage und Carbon Capture Utilization in der Betonindustrie. Bachelor Thesis (2023).

153. Robertson, B. & Mousavian, M. The carbon capture crux: Lessons learned. *Institute for Energy Economics and Financial Analysis.* https://ieefa.org/resources/carbon-capture-crux-lessons-learned (2022).

154. Favier, A., de Wolf, C., Scrivener, K. & Habert, G. A sustainable future for the European Cement and Concrete Industry: Technology assessment for full decarbonisation of the industry by 2050 (2018).

155. Provis, J. L. A concrete future. *Communications Engineering* **1** (2022).

156. Provis, J. L. Geopolymers and other alkali activated materials: why, how, and what? *Materials and Structures* **47,** 11–25. ISSN: 1359-5997 (2014).

157. Deutsche Gesellschaft für Nachhaltiges Bauen (DGNB). DGNB pre-certified and certified projects. (accessed: 05.04.2023). https://www.dgnb-system.de/en/projects/.

158. European Cement Research Academy. Closing the loop: What type of concrete reuse is the most sustainable option? *Technical Report A-2015/1860.* %7Bhttps://www.theconcreteinitiative.eu/newsroom/publications/165-closing-the-loop-what-type-of-concrete-re-use-is-the-most-sustainable-option%7D (2015).

159. Di Maria, A., Eyckmans, J. & van Acker, K. Downcycling versus recycling of construction and demolition waste: Combining LCA and LCC to support sustainable policy making. *Waste management (New York, N.Y.)* **75,** 3–21 (2018).

160. Miller, S. A. & Moore, F. C. Climate and health damages from global concrete production. *Nature Climate Change* **10,** 439–443. ISSN: 1758-678X (2020).

161. Komkova, A. & Habert, G. Environmental impact assessment of alkali-activated materials: Examining impacts of variability in constituent production processes and transportation. *Construction and Building Materials* **363,** 129032. ISSN: 09500618 (2023).

162. Quintero, J. D. & Mathur, A. Biodiversity offsets and infrastructure. *Conservation biology : the journal of the Society for Conservation Biology* **25,** 1121–1123 (2011).

163. Kissling, W. D. *et al.* Towards global interoperability for supporting biodiversity research on essential biodiversity variables (EBVs). *Biodiversity* **16,** 99–107. ISSN: 1488-8386 (2015).

164. Centre d'études et d'expertise sur les risques, l'environnement, la mobilité et l'aménagement (Cerema). Les déterminants de la consommation d'espaces. Période 2009-2019 – Chiffres au 1er janvier 2019 (2020).

165. Umweltbundesamt. Siedlungs- und Verkehrsfläche. https://www.umweltbundesamt.de/daten/flaeche-boden-land-oekosysteme/flaeche/siedlungs-verkehrsflaeche (2023).

166. The Intergovernmental Panel on Climate Change. *Climate Change 2021: The Physical Science Basis. Contribution of Working Group I to the Sixth Assessment Report of the Intergovernmental Panel on Climate Change* (eds Masson-Delmotte, V. *et al.*) (Cambridge University Press, Cambridge, United Kingdom and New York, NY, USA, 2021).

167. Le Quéré, C. *et al.* Global Carbon Budget 2018. *Earth System Science Data* **10,** 2141–2194 (2018).

168. EN 197-1. Cement - Part 1: Composition, specifications and conformity criteria for common cements (2011).

169. Ston, J. & Scrivener, K. Basic creep of limestone–calcined clay cements: An experimental and numerical approach. *Theoretical and Applied Fracture Mechanics* **103,** 102270. ISSN: 01678442 (2019).

170. Taylor, H. F. W. *Cement chemistry* 2. ed., repr. ISBN: 0727725920 (Telford Publ, London, 2003).

171. Gartner, E. & Sui, T. Alternative cement clinkers. *Cement and Concrete Research* **114,** 27–39. ISSN: 00088846 (2018).

172. Winnefeld, F. & Lothenbach, B. Hydration of calcium sulfoaluminate cements — Experimental findings and thermodynamic modelling. *Cement and Concrete Research* **40,** 1239–1247. ISSN: 00088846 (2010).

173. Winnefeld, F., Leemann, A., German, A. & Lothenbach, B. CO2 storage in cement and concrete by mineral carbonation. *Current Opinion in Green and Sustainable Chemistry* **38,** 100672. ISSN: 24522236 (2022).

174. Chen, H. *et al.* Preparation of Alkali Activated Cementitious Material by Upgraded Fly Ash from MSW Incineration. *International journal of environmental research and public health* **19** (2022).

175. Pontikes, Y. *et al.* Slags with a high Al and Fe content as precursors for inorganic polymers. *Applied Clay Science* **73,** 93–102. ISSN: 01691317 (2013).

176. Pacheco-Torgal, F., Castro-Gomes, J. P. & Jalali, S. Investigations on mix design of tungsten mine waste geopolymeric binder. *Construction and Building Materials* **22,** 1939–1949. ISSN: 09500618 (2008).

177. Silva, G. J. B., Santana, V. P. & Wójcik, M. Investigation on mechanical and microstructural properties of alkali-activated materials made of wood biomass ash and glass powder. *Powder Technology* **377,** 900–912. ISSN: 00325910 (2021).

178. Kalina, L., Bílek, V., Kiripolský, T., Novotný, R. & Másilko, J. Cement Kiln By-Pass Dust: An Effective Alkaline Activator for Pozzolanic Materials. *Materials (Basel, Switzerland)* **11.** ISSN: 1996-1944 (2018).

179. Tashima, M. M. *et al.* Alkali activated materials based on fluid catalytic cracking catalyst residue (FCC): Influence of SiO2/Na2O and H2O/FCC ratio on mechanical strength and microstructure. *Fuel* **108,** 833–839. ISSN: 00162361 (2013).

180. Myers, R. J., Bernal, S. A. & Provis, J. L. A thermodynamic model for C-(N-)A-S-H gel: CNASH_ss. Derivation and validation. *Cement and Concrete Research* **66,** 27–47. ISSN: 00088846 (2014).

181. Lothenbach, B. *et al.* Cemdata18: A chemical thermodynamic database for hydrated Portland cements and alkali-activated materials. *Cement and Concrete Research* **115,** 472–506. ISSN: 00088846 (2019).

182. Chithiraputhiran, S. & Neithalath, N. Isothermal reaction kinetics and temperature dependence of alkali activation of slag, fly ash and their blends. *Construction and Building Materials* **45,** 233–242. ISSN: 09500618 (2013).

183. Fernández-Jiménez, A. & Puertas, F. Structure of Calcium Silicate Hydrates Formed in Alkaline-Activated Slag: Influence of the Type of Alkaline Activator. *J. Am. Ceram. Soc.* **86,** 1389–1394 (2003).

184. Taghvayi, H., Behfarnia, K. & Khalili, M. The Effect of Alkali Concentration and Sodium Silicate Modulus on the Properties of Alkali-Activated Slag Concrete. *Journal of Advanced Concrete Technology* **16,** 293–305. ISSN: 1346-8014 (2018).

185. Lee, N. K. & Lee, H. K. Influence of the slag content on the chloride and sulfuric acid resistances of alkali-activated fly ash/slag paste. *Cement and Concrete Composites* **72,** 168–179. ISSN: 09589465 (2016).

186. Nedeljković, M., Zuo, Y., Arbi, K. & Ye, G. in *High Tech Concrete: Where Technology and Engineering Meet* (eds Hordijk, D. & Luković, M.) 2213–2223 (Springer International Publishing, Cham, 2018). ISBN: 978-3-319-59470-5.

187. Robayo-Salazar, R. A., Aguirre-Guerrero, A. M. & Mejía de Gutiérrez, R. Carbonation-induced corrosion of alkali-activated binary concrete based on natural volcanic pozzolan. *Construction and Building Materials* **232,** 117189. ISSN: 09500618 (2020).

188. Wang, W. & Noguchi, T. Alkali-silica reaction (ASR) in the alkali activated cement (AAC) system: A state-of-the-art review. *Construction and Building Materials* **252,** 119105. ISSN: 09500618 (2020).

189. Komljenović, M., Baščarević, Z., Marjanović, N. & Nikolić, V. External sulfate attack on alkali-activated slag. *Construction and Building Materials* **49,** 31–39. ISSN: 09500618 (2013).

190. Komljenović, M. M., Baščarević, Z., Marjanović, N. & Nikolić, V. Decalcification resistance of alkali-activated slag. *Journal of hazardous materials* **233-234,** 112–121 (2012).

191. Ding, Y., Dai, J.-G. & Shi, C.-J. Mechanical properties of alkali-activated concrete: A state-of-the-art review. *Construction and Building Materials* **127,** 68–79. ISSN: 09500618 (2016).

192. Amran, M. *et al.* Fiber-reinforced alkali-activated concrete: A review. *Journal of Building Engineering* **45,** 103638. ISSN: 23527102 (2022).

193. Provis, J. L. & Winnefeld, F. Outcomes of the round robin tests of RILEM TC 247-DTA on the durability of alkali-activated concrete. *MATEC Web of Conferences* **199,** 02024 (2018).

194. Ma, J. & Dehn, F. Shrinkage and creep behavior of an alkali-activated slag concrete. *Structural Concrete* **18,** 801–810. ISSN: 14644177 (2017).

195. Rossi, L. *et al.* Future perspectives for alkali-activated materials: from existing standards to structural applications. *RILEM Technical Letters* **7,** 159–177 (2022).

196. Bernal, S. A. *et al.* Accelerated carbonation testing of alkali-activated binders significantly underestimates service life: The role of pore solution chemistry. *Cement and Concrete Research* **42,** 1317–1326. ISSN: 00088846 (2012).

197. Bernal, S. A., Provis, J. L., Mejía de Gutiérrez, R. & van Deventer, J. S. J. Accelerated carbonation testing of alkali-activated slag/metakaolin blended concretes: effect of exposure conditions. *Materials and Structures* **48,** 653–669. ISSN: 1359-5997 (2015).

198. DB Group. Largest Cemfree Pour for Network Rail in the UK. (accessed: 05.04.2023). `https://dbgholdings.com/largest-cemfree-pour-for-network-rail-in-the-uk/` (2020).

199. FIB. *fib* Model Code for Concrete Structures 2010. *International Federation for Structural Concrete (fib), Lausanne* (2013).

200. RILEM draft recommendation: TC-242-MDC multi-decade creep and shrinkage of concrete: material model and structural analysis. *Materials and Structures* **48,** 753–770. ISSN: 1359-5997 (2015).

201. Parrot, L. J. & Killoh, D. C. Prediction of Cement Hydration. *British Ceramic Proceedings,* 41–53 (1984).

202. Fernández, Á., Lothenbach, B., Alonso, M. C. & García Calvo, J. L. Thermodynamic modelling of short and long term hydration of ternary binders. Influence of Portland cement composition and blast furnace slag content. *Construction and Building Materials* **166,** 510–521. ISSN: 09500618 (2018).

203. Lavergne, F., Ben Fraj, A., Bayane, I. & Barthélémy, J. F. Estimating the mechanical properties of hydrating blended cementitious materials: An investigation based on micromechanics. *Cement and Concrete Research* **104,** 37–60. ISSN: 00088846 (2018).

204. Shi, C. & Day, R. L. A calorimetric study of early hydration of alkali-slag cements. *Cement and Concrete Research* **25,** 1333–1346. ISSN: 00088846 (1995).

205. Li, Z., Zhang, S., Liang, X. & Ye, G. Cracking potential of alkali-activated slag and fly ash concrete subjected to restrained autogenous shrinkage. *Cement and Concrete Composites* **114,** 103767. ISSN: 09589465 (2020).

206. Haha, M. B., de Weerdt, K. & Lothenbach, B. Quantification of the degree of reaction of fly ash. *Cement and Concrete Research* **40,** 1620–1629. ISSN: 00088846 (2010).

207. Scrivener, K. L. Backscattered electron imaging of cementitious microstructures: understanding and quantification. *Cement and Concrete Composites* **26,** 935–945. ISSN: 09589465 (2004).

208. Matousek, J. W. The thermodynamic properties of slags. *JOM* **60,** 62–64 (2008).

209. Zajac, M., Skocek, J., Lothenbach, B. & Mohsen, B. H. Late hydration kinetics: Indications from thermodynamic analysis of pore solution data. *Cement and Concrete Research* **129,** 105975. ISSN: 00088846 (2020).

210. Myers, R. J., Bernal, S. A., Gehman, J. D., van Deventer, J. S. & Provis, J. L. The Role of Al in Cross-Linking of Alkali-Activated Slag Cements. *Journal of the American Ceramic Society* **98,** 996–1004. ISSN: 00027820 (2015).

211. Kulik, D. A., Miron, G. D. & Lothenbach, B. A structurally-consistent CASH+ sublattice solid solution model for fully hydrated C-S-H phases: Thermodynamic basis, methods, and Ca-Si-H2O core sub-model. *Cement and Concrete Research* **151,** 106585. ISSN: 00088846 (2022).

212. Miron, G. D., Kulik, D. A., Yan, Y., Tits, J. & Lothenbach, B. Extensions of CASH+ thermodynamic solid solution model for the uptake of alkali metals and alkaline earth metals in C-S-H. *Cement and Concrete Research* **152,** 106667. ISSN: 00088846 (2022).

213. Haha, M. B., Lothenbach, B., Le Saout, G. & Winnefeld, F. Influence of slag chemistry on the hydration of alkali-activated blast-furnace slag — Part I: Effect of MgO. *Cement and Concrete Research* **41,** 955–963. ISSN: 00088846 (2011).

214. Bernal, S. A., Provis, J. L., Rose, V. & Mejía de Gutierrez, R. Evolution of binder structure in sodium silicate-activated slag-metakaolin blends. *Cement and Concrete Composites* **33,** 46–54. ISSN: 09589465 (2011).

215. Ma, B. & Lothenbach, B. Thermodynamic study of cement/rock interactions using experimentally generated solubility data of zeolites. *Cement and Concrete Research* **135,** 106149. ISSN: 00088846 (2020).

216. Ma, B. & Lothenbach, B. Synthesis, characterization, and thermodynamic study of selected Na-based zeolites. *Cement and Concrete Research* **135,** 106111. ISSN: 00088846 (2020).

217. Taylor, H. F. W. Tobermorite, jennite, and cement gel. *Zeitschrift für Kristallographie - Crystalline Materials* **202,** 41–50. https://doi.org/10.1524/zkri.1992.202.14.41 (1992).

218. Scrivener, K. L., Juilland, P. & Monteiro, P. J. Advances in understanding hydration of Portland cement. *Cement and Concrete Research* **78,** 38–56. ISSN: 00088846 (2015).

219. Vandamme, M. & Ulm, F.-J. Nanoindentation investigation of creep properties of calcium silicate hydrates. *Cement and Concrete Research* **52,** 38–52. ISSN: 00088846 (2013).

220. Constantinides, G. & Ulm, F.-J. The effect of two types of C-S-H on the elasticity of cement-based materials: Results from nanoindentation and micromechanical modeling. *Cement and Concrete Research* **34,** 67–80. ISSN: 00088846 (2004).

221. Jennings, H. M. Refinements to colloid model of C-S-H in cement: CM-II. *Cement and Concrete Research* **38,** 275–289. ISSN: 00088846 (2008).

222. Wilson, W., Sorelli, L. & Tagnit-Hamou, A. Automated coupling of NanoIndentation and Quantitative Energy-Dispersive Spectroscopy (NI-QEDS): A comprehensive method to disclose the micro-chemo-mechanical properties of cement pastes. *Cement and Concrete Research* **103,** 49–65. ISSN: 00088846 (2018).

223. Muller, A. C. A. Characterization of porosity & C-S-H in cement pastes by 1H NMR (2014).

224. Wyrzykowski, M., McDonald, P. J., Scrivener, K. L. & Lura, P. Water Redistribution within the Microstructure of Cementitious Materials due to Temperature Changes Studied with 1 H NMR. *The Journal of Physical Chemistry C* **121,** 27950–27962. ISSN: 1932-7447 (2017).

225. Powers, T. C. & Brownyard, T. L. *Studies of the Physical Properties of Hardened Portland Cement Paste* in (1946).

226. Jennings, H. M., Thomas, J. J., Gevrenov, J. S., Constantinides, G. & Ulm, F.-J. A multi-technique investigation of the nanoporosity of cement paste. *Cement and Concrete Research* **37,** 329–336. ISSN: 00088846 (2007).

227. Brouwers, H. The work of Powers and Brownyard revisited: Part 1. *Cement and Concrete Research* **34,** 1697–1716. ISSN: 00088846 (2004).

228. Li, Z., Lu, T., Liang, X., Dong, H. & Ye, G. Mechanisms of autogenous shrinkage of alkali-activated slag and fly ash pastes. *Cement and Concrete Research* **135,** 106107. ISSN: 00088846 (2020).

229. Lura, P., Jensen, O. M. & van Breugel, K. Autogenous shrinkage in high-performance cement paste: An evaluation of basic mechanisms. *Cement and Concrete Research* **33,** 223–232. ISSN: 00088846. https://www.sciencedirect.com/science/article/pii/S0008884602008906 (2003).

230. Bangham, D. H., Fakhoury, N. & Mohamed, A. F. The Swelling of Charcoal. Part II. Some Factors Controlling the Expansion Caused by Water, Benzene and Pyridine Vapours. *Proceedings of Royal Society of London,* 81–89 (1932).

231. Feldman, R. F. & Serada, P. J. A New model for hydrated Portland cement and its practical implications. *National Research Council of Canada* **53,** 53–59 (1970).

232. Hiller, K. H. Strength Reduction and Length Changes in Porous Glass Caused by Water Vapor Adsorption. *Journal of Applied Physics* **35,** 1622–1628. ISSN: 0002-3264 (1964).

233. Wittmann, F. H. Creep and shrinkage mechanisms. Part II in "Creep and Shrinkage in Concrete Structures". *(ed) by Bazant ZP, Wittmann FH, John Wiley & Sons,* 129–163 (1982).

234. Churaev, N. V. & Derjaguin, B. V. Inclusion of Structural Forces in the Theory of Stability of Colloids and Films. *Journal of Colloid and Interface Science* **103,** 542–553 (1985).

235. Wittmann, F. H. & Beltzung, F. Fundamental aspects of the interaction between hardened cement paste and water applied to improve prediction of shrinkage and creep of concrete: A Critical Review. *Journal of Sustainable Cement-Based Materials* **5,** 106–116. ISSN: 2165-0373 (2016).

236. Li, Z., Lu, T., Chen, Y., Wu, B. & Ye, G. Prediction of the autogenous shrinkage and microcracking of alkali-activated slag and fly ash concrete. *Cement and Concrete Composites* **117,** 103913. ISSN: 09589465 (2021).

237. van Breugel, K. *Relaxation of young concrete* `https://repository.tudelft.nl/islandora/object/uuid:da1c2e2e-1cef-4583-9deb-9e1c1f548df9?collection=research` (1980).

238. Coussy, O. *Poromechanics* 2nd ed. ISBN: 047009270X. `https://onlinelibrary.wiley.com/doi/book/10.1002/0470092718` (Wiley, Chichester, 2004).

239. Bentz, D. P., Garboczi, E. J. & Quenard, D. A. Modelling drying shrinkage in reconstructed porous materials: application to porous Vycor glass. *Modelling and Simulation in Materials Science and Engineering* **6,** 211–236. ISSN: 0021-9797 (1998).

240. Di Bella, C., Wyrzykowski, M. & Lura, P. Evaluation of the ultimate drying shrinkage of cement-based mortars with poroelastic models. *Materials and Structures* **50,** 453. ISSN: 1359-5997 (2017).

241. Jensen, O. M. & Hansen, P. F. Autogenous relative humidity change in silica fume-modified cement paste. *Advances in Cement Research* **7,** 33–38 (1995).

242. Lura, P. & Lothenbach, B. Influence of pore solution chemistry on shrinkage of cement paste. *RILEM Proceedings Pro071: Advances in Civil Engineering Materials,* 191–200 (2010).

243. Luo, L., Wang, Y., Zhan, X.-c., Li, L.-l. & Li, C.-r. Calculating critical relative humidity from solubility according to nonelectrolyte Wilson nonrandom factor model. *Drug Development and Industrial Pharmacy* **38,** 484–489 (2012).

244. Chindaprasirt, P. & Cao, T. in *Handbook of Alkali-Activated Cements, Mortars and Concretes* (eds F. Pacheco-Torgal, J.A. Labrincha, C. Leonelli, A. Palomo & P. Chindaprasirt) 113–131 (Woodhead Publishing, Oxford, 2015). ISBN: 978-1-78242-276-1. `https://www.sciencedirect.com/science/article/pii/B9781782422761500058`.

245. Kumarappa, D. B., Peethamparan, S. & Ngami, M. Autogenous shrinkage of alkali activated slag mortars: Basic mechanisms and mitigation methods. *Cement and Concrete Research* **109,** 1–9. ISSN: 00088846. `10.1016/j.cemconres.2018.04.004` (2018).

246. Ma, Y. & Ye, G. The shrinkage of alkali activated fly ash. *Cement and Concrete Research* **68,** 75–82. ISSN: 00088846 (2015).

247. Melo Neto, A. A., Cincotto, M. A. & Repette, W. Drying and autogenous shrinkage of pastes and mortars with activated slag cement. *Cement and Concrete Research* **38,** 565–574. ISSN: 00088846 (2008).

Paper 1

Extension of the *fib* MC 2010 for basic and drying shrinkage of alkali-activated slag concretes

Publisher's version

Published in *Structural Concrete*

Volume 23 (6), 2022, pp. 3960-3973

DOI: 10.1002/suco.202100901

Authors: **Richard Caron**, Ravi A. Patel, Frank Dehn

Received: 20 December 2021 | Revised: 10 March 2022 | Accepted: 14 April 2022

DOI: 10.1002/suco.202100901

ARTICLE

fib CEB-FIP WILEY

Extension of the *fib* MC 2010 for basic and drying shrinkage of alkali-activated slag concretes

Richard Caron[1,2] | **Ravi A. Patel**[1,2] | **Frank Dehn**[1,2]

[1]Institute of Building Materials and Concrete Structures (IMB), Karlsruhe Institute of Technology (KIT), Germany

[2]Materials Testing and Research Institute (MPA), Karlsruhe Institute of Technology (KIT), Germany

Correspondence
Richard Caron, Institute of Building Materials and Concrete Structures, Karlsruhe Institute of Technology (KIT); Materials Testing and Research Institute (MPA), Karlsruhe Institute of Technology (KIT), Germany.
Email: richard.caron@kit.edu

Funding information
Horizon 2020 Framework Programme, Grant/Award Number: 813596

Abstract

Alkali-activated slag is an alternative to ordinary Portland cement that has been studied for the past 20 years. One of the main challenges for its practical use is understanding and controlling its shrinkage behavior. In this study, new experimental results for two alkali-activated slag concrete mixes are presented under both sealed and unsealed conditions. The results show that basic shrinkage increases with increased sodium silicate ratio. Under unsealed conditions, the age to exposure to drying has a most significant impact on the final drying shrinkage. Finally, the mechanisms explaining shrinkage of such materials are discussed and the*fib* Model Code 2010 is extended for alkali-activated slag concrete using the new experimental results. The extended model consists of four parameters influencing the final values and the speed of both basic shrinkage and drying shrinkage. It is extensively compared with experimental datasets from the literature and improves significantly predictions compared with the original models for both basic and drying shrinkage. This demonstrates clearly the feasibility to extend it for predicting shrinkage of alkali-activated slag concrete.

KEYWORDS

alkali-activated slag concrete, *fib* model code 2010, shrinkage

1 | INTRODUCTION

Alkali-activated materials (AAMs) are alternatives to ordinary Portland cement (OPC) as binders for concrete. Slag is a by-product from the steel industry and is considered as one of the most promising precursors for AAMs. It hardens and gains reasonable compressive strength when it is mixed with alkali solutions, in particular sodium silicate (waterglass).[1] Alkali-activated slag (AAS) concrete presents a low permeability and a good resistance to chloride ingress.[2,3] The key challenges hindering the use of AAS include a quicker setting,[4,5] a faster carbonation,[6,7] and a higher shrinkage in comparison to OPC systems.[8] Nevertheless, both AAS and OPC systems can be regarded as poro-visco-elastic materials, with similar mechanical properties[9] and a comparable pore structure, the matrix of AAS though being denser.[10] The main reaction product of AAS is Calcium-Alumino-Silicate-Hydrate (C-A-S-H), which has similar properties as

Discussion on this paper must be submitted within two months of the print publication. The discussion will then be published in print, along with the authors' closure, if any, approximately nine months after the print publication.

Institute of Building Materials and Concrete Structures, Karlsruhe Institute of Technology (KIT), 76131 Germany

Calcium-Silicate-Hydrate (C-S-H) with more aluminum incorporation in the nano-structure. C-A-S-H is considered to be the key reaction product while considering shrinkage of AAS concrete.[11]

In the context of dimensional stability of concrete, creep and drying shrinkage are two important factors to be considered. Creep refers to deformations under sustained load, while drying shrinkage occurs due to the removal of moisture from concrete. The removal of moisture can occur under sealed conditions due to consumption of moisture during the reaction. Induced strain from this phenomenon is referred to as basic shrinkage. Both creep and drying shrinkage can build up complex stress states that can lead to cracking under restrained conditions.[8,12,13] This causes a reduction of mechanical performances and durability of the concrete. In practice, for OPC-cement-based concrete, creep- and shrinkage-induced strains are often predicted using engineering models such as ACI 209R-92,[14] the model of Bazant-Baweja B3,[15,16] the model from Gardner and Lockman GL2000,[17] CEB FIP models,[18–21] and the *Fédération internationale du béton (fib)* Model Code 2010.[22] The Bazant-Baweja B3 model has been further updated and extended for blended cements with fly ash and slag in the B4 model.[23,24] Both *fib* MC 2010 and B4 model propose creep and shrinkage predictions from the compressive strength. The advantage of the *fib* Model Code 2010 is that all input parameters are related to the compressive strength f_{cm}, the type of cement, and the curing conditions, which are readily available to engineers. It has been recently extended for recycled aggregate concrete.[25] Chen et al. adapted also the Eurocode 2, a modified model from CEB/FIP model, for Supplementary Cementitious Materials (SCM).[26]

Three main theories have been developed for OPC systems to explain shrinkage resulting from the removal of moisture in terms of physical mechanisms. The first one is the capillary pressure theory wherein concrete is regarded as a poro-elastic material. Shrinkage is due to the capillary pressure developing in its pores after the consumption of water from the chemical reaction of hydration.[27–31] The second one is the surface tension theory which focuses on the mechanical equilibrium of water molecules in a porous material.[32–35] The third one is the disjoining pressure theory. It is based on the idea of adsorbed water removal from the surfaces of the pore walls of the porous material.[36,37] More recently, a creep theory has emerged in which shrinkage is considered as the deformation due to the viscoelastic behavior of concrete caused by the load induced by the capillary pressure.[11,38]

The shrinkage mechanisms for AAS concrete remain still unclear. According to some authors,[10,39] higher shrinkage observed for AAS in comparison to OPC would be explained through the capillary pressure theory. The denser pore structure of AAS leads to a higher capillary pressure and correspondingly a higher shrinkage.[10] It was also stated that drying shrinkage and water loss were not directly correlated.[10,29] For Song et al.,[40] keeping a high internal relative humidity in the AAS matrix reduces the basic shrinkage, in accordance with the capillary pressure theory. Ye et al.[29] showed that when samples are dried at different relative humidity steps, the correlation between the imposed external relative humidity and the final shrinkage at each relative humidity is different for AAS than for OPC. For them, further mechanisms should occur like creep effects at high relative humidity or pore-collapse in the case of step-wise drying. As reported by Li et al.,[31] the capillary theory should not be the only mechanism explaining shrinkage: the reduction of the steric-hydration force and creep effects should be considered to predict basic shrinkage of AAS paste.

In the context of AAS concrete, only few studies measuring both basic and drying shrinkage are available.[41] Second, very few engineering model extensions exist and can be applied to AAS concrete. This contribution addresses both issues and presents new experimental results for two new AAS concrete mixes for both basic shrinkage and drying shrinkage. Using these experimental data, the applicability of the existing *fib* MC 2010 for AAS is evaluated and an approach to extend the *fib* MC 2010 for AAS concrete for both basic and drying shrinkage is presented. The model extension is rigorously tested against 23 different datasets available in the literature, many of which only provide information on total shrinkage.

TABLE 1 Chemical composition of the anhydrous slag

Oxide	CaO	SiO_2	Al_2O_3	MgO	Others
Mass (%)	38.8	36.3	12.8	8.0	4.1

2 | MATERIALS AND METHODS

In this section, details on the material and the mixes used for new experiments reported in this study are presented. This is followed by the experimental methods and used protocols.

2.1 | Materials

Two AAS concrete mixes were tested using the slag provided by Ecocem (Netherlands). The chemical composition of the slag was measured using energy dispersive x-ray fluorescence (XRF) M4 Tornado spectrometer

TABLE 2 Fresh concrete characteristics, compressive strength, and Young's modulus of the concretes

Mix		Mix lS	Mix hS
w/s	[kg/kg]	0.45	0.45
n	[Na_2O g/100 g slag]	5.0	5.0
M_S	[SiO_2/Na_2O mol/mol]	0.5	2.2
Precursor content	[kg/m^3 of concrete]	450	
Sand (0–2 mm)	[vol-%]	40	
Agg. (2–8 mm)	[vol-%]	30	
Agg. (8–16 mm)	[vol-%]	30	
Flow diameter	[cm]	50	65
Density	[kg/m^3]	2.25	2.32
Air content	[%]	1.60	1.60
f_{cm}	[MPa]	56	76
E_{ci}	[GPa]	32	30

(Bruker GmbH Karlsruhe, Germany) and is given in Table 1. This composition is in the range of CaO, SiO_2, Al_2O_3, and MgO content in comparison to what can be found in the literature.[42–46] The slag coefficient $\frac{CaO+MgO}{SiO_2}$, considered as the main parameter for slag oxide composition[47,48] is in the lower range in comparison to other mixes. Two sodium silicate solutions were used for activation of slag to obtain two different mixes. Both mixes had the same water-to-slag ratio w/s equal to 0.45 and the same alkalinity coefficient $n = 5.0$ [Na_2O g/100 g slag] but different sodium silicate ratios M_S [SiO_2/Na_2O mol/mol]. The mix with M_S equal to 0.5 was designated mix lS, while the mix with molar ratio 2.2 was designated mix hS. The concrete was cast with the same precursor content of 450 kg/m^3 of concrete.

The flow spread, the density, and the air content of the fresh concrete were tested following the norms DIN EN 12350-5,[49] DIN EN 12350-6,[50] and DIN EN 12350-7,[51] respectively. Characteristic compressive strength after 28 days was measured following the norms DIN EN 12390-3[52] with three cubes of nominal size 100 mm while the Young's modulus after 28 days was determined following the norm DIN EN 12390-13[53] (method B) on six cylinders of diameter 100 mm and height 285 mm. Both mix designs and their characteristics are summarized in Table 2. For these tests, the samples were covered with plastic foil until testing in a chamber at 20 °C.

2.2 | Methods

2.2.1 | Casting of samples

The alkali solutions were prepared 24 h before their first contact with the slag and the aggregates, so that the temperature of the solution was stabilized at the ambient temperature (20 °C). The casting procedure was the following: the slag, the sand, and the aggregates were first mixed together during half a minute. Then, the solution was added and the whole was mixed for a minute. After 30 s of resting, the concrete was mixed for 2 min. Cylinders of diameter 100 mm and height 285 mm were then filled. The specimens were demolded after 1 day and covered with plastic foils when the storage conditions required it. All the samples were stored at a temperature of 20 °C.

2.2.2 | Evolution of mechanical properties with time

The development of compressive strength and Young's modulus with time were determined with cylinders of diameter 100 mm and height 285 mm after 2, 7, 14, 28, and 56 days. The cylinders were covered with plastic foil and stored at 20°C until the test day. The norm DIN EN 12390-13[53] (method B) was followed for the determination of the Young's modulus. For each test day, three cylinders were used to first determine the compressive strength. Then, the Young's modulus was determined by loading three other cylinders at a loading equal to one-third of the compressive strength. These cylinders were then loaded until failure. Overall, the presented compressive strength was thus an average of six values for each test day. The shrinkage of the concrete was measured following the norm DIN EN 12390-16 [DIN EN 12390-16][54] with the same sample geometry. Measurements were carried out at least for 100 d. For both mixes, different storage conditions were investigated. Basic shrinkage was measured with covered specimens. Drying shrinkage was studied at a relative humidity of 65% with different

TABLE 3 Experimental plan for shrinkage tests

Name	Mix	t_S [d]	RH [%]
lS-BS	lS	n.a.	n.a.
lS-DS-1d	lS	1	65
lS-DS-7d	lS	7	65
lS-DS-28d	lS	28	65
lS-DS-RH-43%	lS	7	43
lS-DS-RH-85%	lS	7	85
hS-BS	hS	n.a.	n.a.
hS-DS-1d	hS	1	65
hS-DS-7d	hS	7	65
hS-DS-28d	hS	28	65

Note: n.a. stands for not applicable.

exposure ages to drying (1, 7 and 28 days). The following nomenclature was assigned to each test: XX-YY(−Zd) with XX the name of the mix (XX = lS or XX = hS), YY the curing condition (YY = BS for sealed conditions, YY = DS for drying conditions), and Z the exposure age, if applicable (Z = 1, 7, or 28). For the mix lS, two other sets of specimens were sealed during 7 d and then unsealed and stored in curing chambers, respectively, at RH of 43% and 85%. For these experiments, the assigned nomenclature was lS-DS-RH-43% and lS-DS-RH-85%, respectively. All the shrinkage tests are summarized in Table 3. Three specimens were used for replication of test results for each condition. The standard deviation of shrinkage measurements for each condition varied between 0.5% and 1.5%, except for the specimens exposed to drying after 1 day, for which the standard deviation was equal to 4% for the mix lS and 6% for the mix hS.

3 | EXISTING MODELS FOR STRENGTH DEVELOPMENT AND SHRINKAGE IN THE *FIB* MC 2010 AND ITS ADAPTATION TO AAS

In this section, the original models as proposed in the *fib* MC 2010 for both strength development and shrinkage are recalled. Then, the proposed extensions for these models are presented.

3.1 | Strength development with the *fib* MC 2010

The strength development of concrete as a function of time (t [days]) in the *fib* MC 2010 is modeled using the 28 days compressive strength f_{cm}:

TABLE 4 Coefficient s for different types of precursor to determine the strength development

f_{cm} [MPa]	Strength class of cement	s
≤ 60 MPa	32.5 N	0.38
≤60 MPa	32.5 R, 42.5 N	0.25
≤60 MPa	42.5 R, 52.5 N, 52.5 R	0.20
60	All classes	0.20

$$f_{cm}(t) = \beta_{cc}(t) \cdot f_{cm}(t=28) \tag{1}$$

with,

$$\beta_{cc} = exp\left[s\left(1-\left(\frac{28}{t}\right)^{0.5}\right)\right] \tag{2}$$

where s is the coefficient characteristic to the strength class of the binder (given in Table 4). Similarly, the development of the Young's modulus ($E_{ci}(t)$) with time is predicted from the value of the Young's modulus at 28 days $E_{ci}(t=28)$:

$$E_{ci}(t) = \beta_E(t) \cdot E_{ci}(t=28) \tag{3}$$

where,

$$\beta_E = [\beta_{cc}(t)]^{0.5} \tag{4}$$

3.2 | Shrinkage modeling with the *fib* MC 2010

The total shrinkage $\varepsilon_{cs}(t)$ is the sum of both basic shrinkage $\varepsilon_{cbs}(t)$ and drying shrinkage $\varepsilon_{cds}(t,t_s)$:

$$\varepsilon_{cs}(t) = \varepsilon_{cbs}(t) + \varepsilon_{cds}(t,t_s) \tag{5}$$

where t is the concrete age in days and t_s is the concrete age in days at the beginning of drying. The basic shrinkage is calculated with:

$$\varepsilon_{cbs}(t) = \varepsilon_{cbs0}(f_{cm}) \cdot \beta_{bs}(t) \tag{6}$$

where,

$$\varepsilon_{cbs0}(f_{cm}) = -\alpha_{bs}\left(\frac{0.1 \cdot f_{cm}}{6+0.1 \cdot f_{cm}}\right)^{2.5} \cdot 10^{-6} \tag{7}$$

and

TABLE 5 Coefficient α_{bs}, α_{ds1} and α_{ds2} for different types of cement

Strength class of cement	α_{bs}	α_{ds1}	α_{ds2}
32.5 N	800	3	0.013
32.5 R, 42.5 N	700	4	0.012
42.5 R, 52.5 N, 52.5 R	600	6	0.012

$$\beta_{bs}(t) = 1 - exp\left(-0.2 \cdot \sqrt{t}\right) \tag{8}$$

where f_{cm} is the mean compressive strength at the age of 28 days, α_{bs} is a coefficient dependent on the type of cement (see Table 5).

The drying shrinkage can be predicted with:

$$\varepsilon_{cds}(t) = \varepsilon_{cds0}(f_{cm}) \cdot \beta_{RH}(RH) \cdot \beta_{ds}(t - t_s) \tag{9}$$

where

$$\varepsilon_{cds0}(f_{cm}) = [(220 + 110 \cdot \alpha_{ds1}) \cdot exp(-\alpha_{ds2} \cdot f_{cm})] \cdot 10^{-6} \tag{10}$$

$$\beta_{RH}(RH) = \begin{cases} -1.55 \cdot \left[1 - \left(\frac{RH}{100}\right)^3\right] & \text{for } 40 \le RH \le 99\% \cdot \beta_{s1} \\ 0.25 & \text{for } RH \ge 99\% \cdot \beta_{s1} \end{cases} \tag{11}$$

$$\beta_{ds}(t - t_s) = \left(\frac{(t - t_s)}{0.035 \cdot h^2 + (t - t_s)}\right)^{0.5} \tag{12}$$

$$\beta_{s1} = \left(\frac{35}{fcm}\right)^{0.1} \le 1.0 \tag{13}$$

RH is the relative humidity of the ambient atmosphere, h is the notional size of the specimen, and α_{ds1}, α_{ds2} are dependent on the type of cement (see Table 5).

3.3 | Adaptation of the *fib* MC 2010 to alkali-activated slag concrete

The *fib* MC 2010 models described above are applicable for OPC-cement-based concrete. In order to extend it to AAS concrete, the same approach as that proposed by Tosic et al.[25] for the shrinkage of recycled aggregate concrete is applied. The Equations (5), (8), and (12) are adapted with four new coefficients, ξ_{cbs1}, ξ_{cbs2}, ξ_{cds1}, and ξ_{cds2}:

$$\varepsilon_{cs}(t, t_s) = \xi_{cbs1} \cdot \varepsilon_{cbs}(t) + \xi_{cds1} \cdot \varepsilon_{cds}(t, t_s) \tag{14}$$

$$\beta_{bs}(t) = 1 - exp\left(-0.2 \cdot \xi_{cbs2} \cdot \sqrt{t}\right) \tag{15}$$

$$\beta_{ds}(t - t_s) = \left(\frac{(t - t_s)}{0.035 \cdot \xi_{cds2} \cdot h^2 + (t - t_s)}\right)^{0.5} \tag{16}$$

If the four introduced coefficients are equal to 1, Equations (14), (15), and (16) correspond to Equation (5), (8), and (12) from the original *fib* MC 2010. The term $\xi_{cbs1}\varepsilon_{cbs0}(f_{cm})$ can be seen as the final basic shrinkage of the material. This implies that a higher ξ_{cbs1} results in a larger final basic shrinkage. Likewise, $\xi_{cds1}\varepsilon_{cds0}(f_{cm}) \cdot \beta_{RH}(RH)$ can be regarded as the final drying shrinkage of the material and thus an increase in ξ_{cds1} leads to an increase in the final drying shrinkage.

ξ_{cbs2} and ξ_{cds2} are related to the speed of basic and drying shrinkage, respectively. If ξ_{cbs2} is greater than 1, the basic shrinkage is faster than the one predicted by the *fib* MC 2010 for OPC concrete. If ξ_{cds2} is lower than 1, the drying shrinkage is faster than the one predicted by the *fib* MC 2010 for OPC concrete.

In literature, higher shrinkage has been reported for AAS with waterglass when compared with OPC for paste, mortar, and concrete samples. For paste with n = 4.7 g Na_2O/100 g slag and M_S = 1.5 mol/mol, Li et al.[55] found that the basic shrinkage of the activated slag was around 14 times higher after 7 days than the one for cement. For mortar, the basic shrinkage was found to be four to six times higher after 6 months than cement.[30,40,56,57] The results from Ballekere Kumarappa et al.[30] suggested that a higher n or a higher M_S result in a higher basic shrinkage. Still for mortars, the total shrinkage after 6 months of AAS was measured between 1.5 and 7 times higher than for cement for different ambient relative humidity conditions.[56–60] The results from Atis et al.[58] also indicated that a higher n resulted in more shrinkage, and that an increase of M_S also drastically increased the shrinkage. Ye et al.[61] showed that the total shrinkage of AAS was between 1.5 and 2 times higher after 25 days for mortars with a drying exposure age equal to 7 days. For concrete samples, drying and total shrinkage were found to be between 1.5 and 3 times higher after 2 months for AAS with waterglass than for OPC.[10,62,63] Shrinkage as a function of n and M_S was studied by Taghvayi et al.[63] on the concrete level. Their conclusions were in line with that of Ballekere Kumarappa et al.[30] and Atis et al.[58] that M_S had a much larger effect on shrinkage than n. Note that Taghvayi et al.[63] did not distinguish basic shrinkage and drying shrinkage with the convention from the *fib* MC 2010. For this reason, the relative importance of both types of shrinkage could not be assessed from their results.

The Equations (14), (15), and (16) were calibrated on experimental results obtained in this study. The

parameters ξ_{cbs1} and ξ_{cbs2} were calibrated with the results of basic shrinkage, while ξ_{cds1} and ξ_{cds2} were calibrated with the results of drying shrinkage. The calibration was done with the least squares method on the average values of the measured shrinkage. The optimization for the basic (resp. drying) shrinkage was done with the following objective function:

$$\mathcal{F}_{obj}(\xi_1,\xi_2,t_0) = \omega_1 \cdot \left(\mathcal{F}^{model}(\xi_1,\xi_2,t \le t_0) - \mathcal{F}^{exp}(t \le t_0)\right)^2 + \omega_2 \cdot \left(\mathcal{F}^{model}(\xi_1,\xi_2,t > t_0) - \mathcal{F}^{exp}(t > t_0)\right)^2 \quad (17)$$

for which $\mathcal{F}^{model}$ is the model function for basic (resp. drying) shrinkage, $\mathcal{F}^{exp}$ is the corresponding experimental data, $\xi_1 = \xi_{cbs1}$ (resp. ξ_{cds1}) and $\xi_2 = \xi_{cbs2}$ (resp. ξ_{cds2}). ω_1 is the weight affected to the early-age part of the curve, ω_2 the weight affected to the late-age part of the curve, and t_0 the shifting time chosen arbitrarily between early-age and late-age. By definition, $\omega_1 + \omega_2 = 1$. Studying the optimization with different objective functions, that is, different weights and shifting times allows the evaluation of the sensitivity of the obtained results with potential biases due to the difference of amount of data for early and late age. The optimization done with the same dataset but with different values of weights and shifting times showed that the obtained model parameters varied at most by 15% for ω_1 in range of [0.15, 0.6], ω_2 in range of [0.4,0.85], and t_0 in range of [10 d, 50 d]. Based on this sensitivity analysis, the model parameters reported in this study are that obtained when the function $\xi_{cbs1} \cdot \varepsilon_{cbs}(t \le t_0, \xi_{cbs2})$ (resp. $\xi_{cds1} \cdot \varepsilon_{cds}(t \le t_0, \xi_{cds2})$) is directly optimized on the experimental results using the simplified objective function with ω_1 equal to 1, ω_2 equal to 0, and $t_0 \to \infty$ in Equation (17). In order to ensure that the optimized parameters correspond to the global minimum and not to a local minimum, the optimization was carried out with different initial guesses that always resulted in the same model parameters.

It should be noted that the comparison between shrinkage values and the adapted *fib* MC 2010 model for AAS concrete should be made with caution. Indeed, for this model the role of final shrinkage value (both basic and drying) is primordial. Nevertheless, shrinkage rates of the experiments led in this study seem to be stabilized, and the extrapolated final values should be in the good range of the final true values. For AAS concrete, only few results are available for long term. The results from Collins et al.[10] indicated that the speed of shrinkage was not very affected by the used precursor and thus the results can be compared directly in terms of amplitude.

4 | RESULTS

In this section, the experimental results are presented and discussed. This is followed by comparing them to existing models from the *fib* MC 2010. The evaluation of the parameters for the model extensions are also presented in Sections 4.2.2 and 4.2.3.

4.1 | Experimental results

4.1.1 | Strength development

The evolution of measured compressive strength and Young's modulus on sealed cylinders are given in Figure 1. After 7 days, the mixes lS and hS attained 76% and 75%, respectively, of the compressive strength after 28 days. The Young's modulus development is faster than the compressive strength development with values at 7 days equal to 91% and 93% of that at 28 days for the mixes lS and hS, respectively.

4.1.2 | Basic shrinkage

The experimental results for the basic shrinkage of the two mixes are shown in Figure 2. The basic shrinkage of the mix hS is around two times higher than the one of the mix lS. Thus, the increased amount of silicon in the alkali solution induces a higher shrinkage. Such a result is in accordance with study done by Ballekere Kumarappa et al.[30] for mortars. After 50 days, the further shrinkage evolution of the mix hS is very low (99% of final shrinkage achieved within 50 days) when compared with the mix lS.

In comparison to OPC, AAS has a finer pore structure.[10] This leads to a larger capillary pressure and thus to a larger shrinkage due to the self-desiccation, as postulated previously by different researchers.[10,27,28] Chemical shrinkage also contributes significantly to explain basic shrinkage. It refers to the fact that, as reaction products are smaller than the reactants, internal voids are generated in the matrix. These voids are the primary cause of the formation of the meniscus in the pore structure that lead to the development of the capillary pressure. Cartwright et al.[64] showed that the chemical shrinkage of AAS is lower than for cement. For Li et al.,[31] the measured chemical shrinkage of AAS is equal to the one of OPC. Models from Ye et al.[65] and Thomas et al.[66] predict that the chemical shrinkage is above 12 mL/100 g slag, two times higher than the chemical shrinkage of Portland cement.[67] In all, there is no consensus on the relative influence of chemical shrinkage on the higher basic shrinkage observed for AAS.

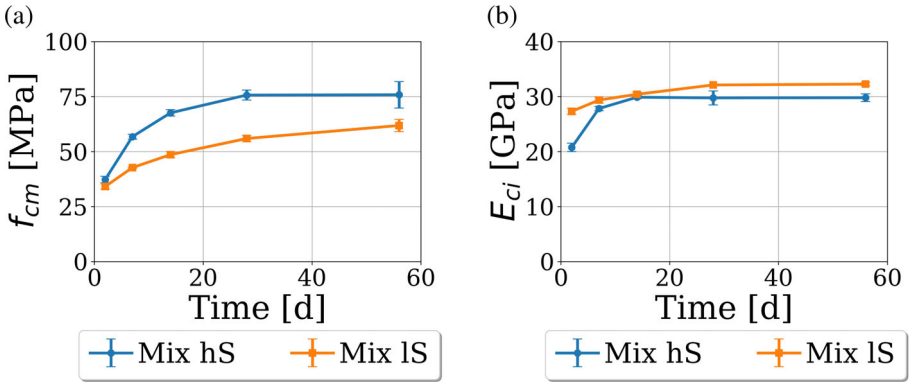

FIGURE 1 Strength development of both mixes. Compressive strength (a); Young's modulus (b). The error bars correspond to the standard deviation done on six samples

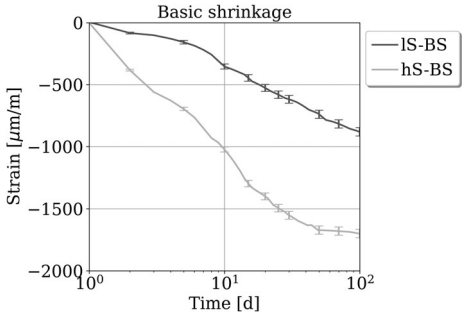

FIGURE 2 Basic shrinkage of both mixes lS and hS

The influence of the bulk modulus and the degree of saturation were discussed on one hand by Di Bella et al.[68] for cementitious systems and on the other hand by Ye et al. for AAS systems.[61] They all agree on the secondary influence of the bulk modulus. However, Di Bella et al.[68] consider that the degree of saturation plays a crucial role on the shrinkage performance, while Ye et al.[61] consider that its influence is quite low.

Basic shrinkage also depends on the drop in internal relative humidity RH_i due to consumption of water during the reaction. For AAS, RH_i is measured at 82%–83%[40,69] or even at 80%[8] and 75%.[31] In comparison, Jensen & Hensen[70] obtained RH_i higher than 80% after 1 year for different water-to-cement ratio for OPC systems with silica fume addition from 0% to 30%. Lura et al.[27] measured a RH_i of 92% after 7 days for OPC. Higher drop in RH_i for AAS can be attributed to more consumption of water during the activation and to the increased presence of alkali ions in pore solution resulting in lower RH in accordance to Raoult's law. The higher drop of relative humidity for AAS systems increases the capillary pressure and can explain the higher shrinkage observed.[31,40,69]

4.1.3 | Drying shrinkage

The Figure 3 shows the experimental results from the present study for drying shrinkage at RH = 65%. The results indicate the predominance of the exposure age. For the mix lS, the total shrinkage is 1289, 975, and 940 μm/m for the samples lS-DS-1d, ls-DS-7d, and ls-DS-28d, respectively, at age 100 days, that is, at drying age of 99, 93, and 72 days, respectively. Correspondingly, the drying shrinkage is 410, 96, and 61 μm/m for the samples lS-DS-1d, ls-DS-7d, and ls-DS-28d, respectively. For the mix hS, after 100 days, the total shrinkage is 3019, 1873, and 1756 μm/m for the samples hS-DS-1d, hS-DS-7d, and hS-DS-28d. This corresponds to a drying shrinkage of 1319, 173, and 56 μm/m for the samples hS-DS-1d, hs-DS-7d, and hs-DS-28d, respectively. Thus, covering the specimens during the first day is necessary for practical applications to reduce drying shrinkage.

The contribution of drying shrinkage to that of overall shrinkage is found to be relatively low for experiments on AAS concretes. For the mix lS, the drying shrinkage is responsible for 31.8%, 9.8%, and 6.4% of the total shrinkage at 100 days for exposure ages of 1, 7, and 28 days, respectively. For the mix hS, the drying shrinkage is responsible for 43.7%, 9.2%, and 3.2% of the total shrinkage at 100 days for exposure ages of 1, 7, and 28 days, respectively.

The results of shrinkage measurements and mass change depending on the ambient relative humidity (43% RH, 65% RH, and 85% RH) for the mix lS with an exposure age of 7 days are given in Figure 4. The mass change is defined as:

$$\Delta M(t) = \frac{M(t)}{M(t = t_s)} * 100 \tag{18}$$

The specimen lS-DS-RH-43% induces a shrinkage as high as for the specimen ls-DS-7d, despite a higher mass loss. As for waterglass-activated slag mortars,[29] lower ambient relative humidity implies higher drying shrinkage. There is the same threshold at relative humidity (between RH = 43% and RH = 65%) as reported by Ye et al.[29]

The specimen lS-DS-RH-85% shrinks less than the specimen under sealed conditions and its mass grows

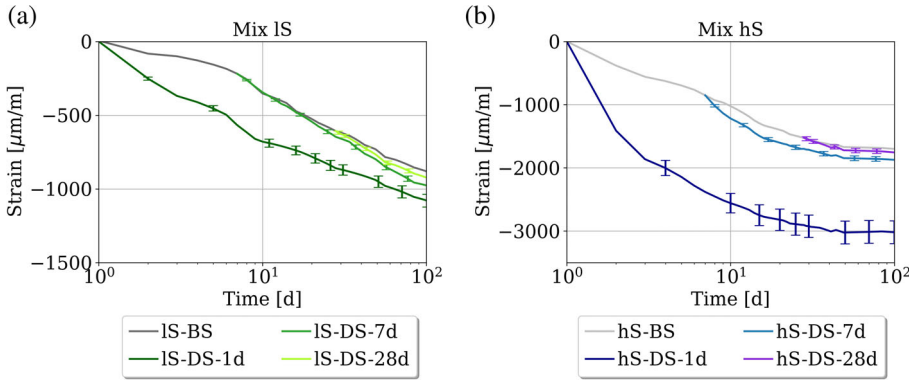

FIGURE 3 Total shrinkage of (a) mix lS and (b) mix hS with different age of exposure to drying. Total shrinkage is defined as the sum of basic shrinkage (under sealed condition) and drying shrinkage

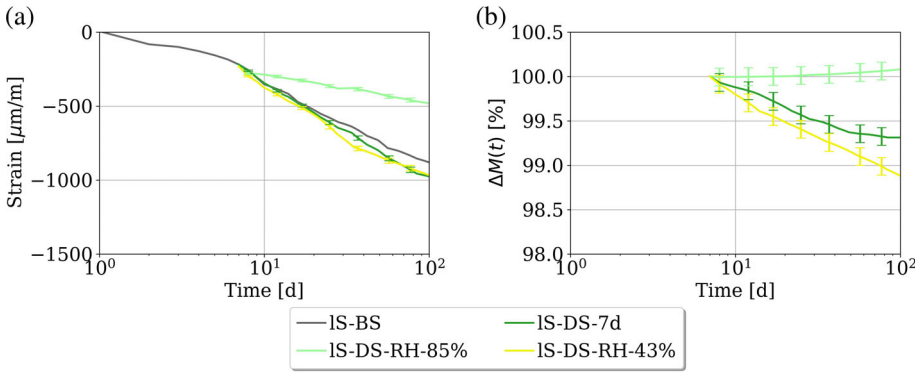

FIGURE 4 Drying shrinkage: Influence of the relative humidity on the mix lS. (a): Shrinkage, (b) mass

with time. As discussed above for the basic shrinkage, the drop of relative humidity in AAS concrete is higher than for cement-based concrete. Thus, when the specimens are exposed to drying, after 7 or 28 days, the imposed RH gradient is low in comparison to OPC-based concrete. The increase in mass after exposure for the specimens lS-DS-RH-85% indicates that the internal relative humidity of the mix lS after 7 days is below 85%, in accordance with Li et al.[8] or Li et al.[31]

4.2 | Calibration of the *fib* MC 2010 for strength and shrinkage on experimental results of AAS

4.2.1 | Type of concrete

As explained in Section 3, shrinkage models in the *fib* MC 2010 distinguish three types of concrete depending on the strength class of cement. Hence it is essential to first define the equivalent strength classes for the two AAS concrete mixes studied experimentally. This equivalent class is obtained by calibrating the model for strength development with experimental data on the coefficient s in Equations (2) and (4). The optimized values of s for both mixes tested are given in Table 6. Based on this calibration and on the compressive strength given in Table 2, the equivalent strength class for both mixes is the class of cements 42.5 R, 52.5 N, 52.5 R, or superior. Thus, the AAS concrete is considered to be equivalent to these types of concrete as defined in the *fib* MC 2010.

TABLE 6 Optimization of the coefficient s for alkali activated slag with waterglass

Mix	*s* following (2)	*s* following (4)
Mix lS	0.21	0.13
Mix hS	0.26	0.23

4.2.2 | Calibration of basic shrinkage experiments

The Figure 5 shows the comparison between the results from this study, the experimental results for three different studies obtained from the literature[55,62,71] and the predictions with the models from the *fib* MC 2010, which are applicable for OPC concrete. The shrinkage results are expressed in terms of the normalized shrinkage $\frac{\varepsilon_{cbs}}{\varepsilon_{cbs0}}$ to have a consistent comparison between different mixes, independently from the compressive strength f_{cm}. Indeed, for the *fib* MC 2010, the ratio $\frac{\varepsilon_{cbs}}{\varepsilon_{cbs0}} = \beta_{bs}(t)$ ranges from 0 to 1. However, as mentioned above and shown in

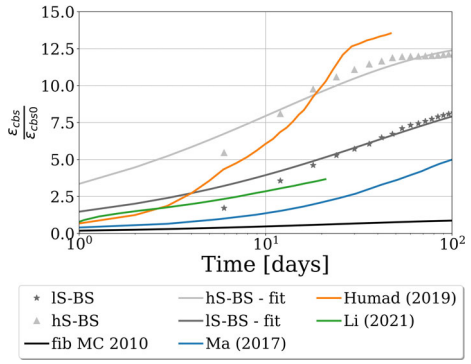

FIGURE 5 Comparison of basic shrinkage results with literature results and the fib MC 2010 prediction. Comparison performed on the ratio ξ_{cbs}/ξ_{cbs0}. Calibration of the curve following the equations (14) and (15)

TABLE 7 Obtained parameters for basic shrinkage extension of the *fib* MC 2010

Specimens	$\xi_{cbs,1}$	$\xi_{cbs,2}$
lS-BS	9.90	0.80
hS-BS	13.0	1.51

Figure 5 the final shrinkage for AAS is much more than that for OPC concrete. The obtained results for both lS and hS mixes with the extension of the *fib* MC 2010 given by Equation (14) are also shown in Figure 5 and correspondingly, the calibrated parameters are given in Table 7. The obtained values for $\xi_{cbs,2}$ indicate that the speed of shrinkage of AAS systems is comparable to the one from the *fib* MC 2010. In accordance to what can be found in the literature,[55,62,71] the final basic shrinkage of AAS concrete, characterized by the value $\xi_{cbs,1}$, is much higher than the final basic shrinkage of OPC-based concrete. In terms of mechanisms, this could be due to the lower relative humidity measured in AAS systems.[8,31,40,69]

4.2.3 | Calibration of drying shrinkage experiments

For drying shrinkage, the predictions using the model from the *fib* MC 2010 and the extension proposed in this study as given by Equation (16) are shown in Figure 6. The calibrated coefficients corresponding to the model extension are provided in Table 8.

As explained in Section 4.1.3, the age of exposure to drying plays an important role on final drying shrinkage for AAS concrete. However, it is not captured by the original *fib* MC 2010. For the strength class f_{cm} (chosen between 56 and 76 MPa) and for exposure ages between

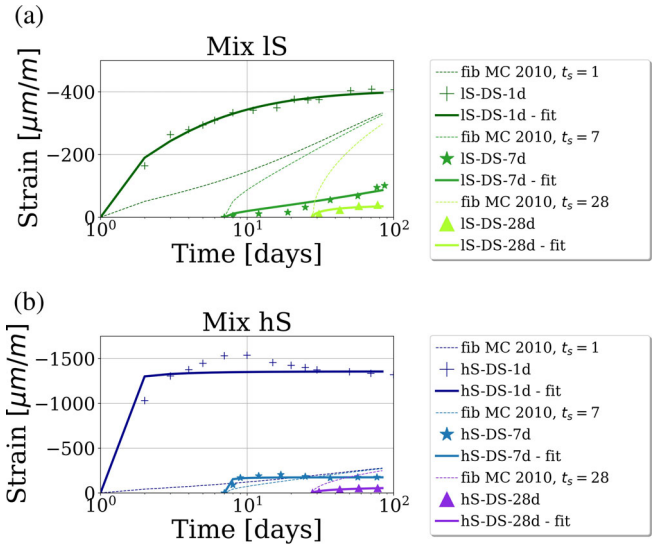

FIGURE 6 Experimental results of drying shrinkage for (a) mix lS (b) mix hS. Dashed lines correspond to the prediction from the fib MC 2010. Plain lines correspond to the adapted model

TABLE 8 Obtained parameters for drying shrinkage extension of the *fib* MC 2010

Specimens	$\xi_{cds,1}$	$\xi_{cds,2}$
lS-DS-1d	8.5×10^{-1}	4.1×10^{-2}
lS-DS-7d	3.6×10^{-1}	2.6
lS-DS-28d	8.3×10^{-2}	1.7×10^{-1}
hS-DS-1d	3.5	2.0×10^{-3}
hS-DS-7d	4.4×10^{-1}	3.3×10^{-3}
hS-DS-28d	1.6×10^{-1}	3.2×10^{-1}

1 and 28 days, the drying shrinkage after 100 days ε_{cds} as predicted by the model from the *fib* MC 2010 is in the range of 248 and 352 µm/m. The specimen lS-DS-1d is the only one with this order of magnitude, whereas hS-DS-1d is largely underestimated. On the other hand, the specimens with later exposure (7 or 28 days) are largely overestimated. This explains why the obtained coefficients $\xi_{cds,1}$ for the proposed model extension decrease with exposure age for each mix. It can also be noted that $\xi_{cds,1}$ is higher than 1, only for the specimen hS-DS-1d, which implies that the absolute value of drying shrinkage of AAS concrete is quite overestimated in the *fib* MC 2010.

Moreover, the relative importance of drying shrinkage when compared with basic shrinkage is overestimated by models from the *fib* MC 2010. These models predict that the drying shrinkage is responsible for more than 70% of the total shrinkage, which is much higher than that reported in this study for AAS concrete (see Section 4.1.3). In addition, the optimized values of $\xi_{cds,2}$ are lower than

1, indicating that the drying shrinkage occurs faster for AAS concrete than OPC concrete. This is especially true for specimens exposed at early age, namely, lS-DS-1d, and hS-DS-1d. This result is in agreement with what can be found in literature.[62,71]

For the specimen lS-DS-RH-85%, the shrinkage is lower than the one of lS-BS (under sealed conditions). This is due to the fact that the RH_i of the samples is less than ambient RH under exposure at 85%. In this last environment condition, there is even an increase in RH_i of the sample and it results consequently expansive strains. This indicates that the bounds of applicability in Equation (11) must be adjusted for AAS concrete from 40%–99% β_{s1} to at least 40%–85% β_{s1}.

5 | APPLICATION OF THE EXTENSION AND VALIDATION

To evaluate the potential relevance of the model extension given by Equations (14), (15), and (16), the four coefficients $\xi_{cbs,1}$, $\xi_{cbs,2}$, $\xi_{cds,1}$, and $\xi_{cds,2}$ are obtained using the results from the present study. Finally, using these defined parameters, the model for total shrinkage is compared with experimental results from the literature to validate it.

5.1 | Calibrated parameters for model extension

Basic shrinkage results of the calibration, given in Table 7, show the importance of the parameter M_S, which is in accordance with Ballekere Kumarappa et al. and Atis et al.[30,58] To account for this, a linear correlation is proposed between $\xi_{cbs,1}$ and M_S. Results on mortars[30] indicate that the alkalinity coefficient n has an equivalent influence on the basic shrinkage. However, due to lack of data on concrete level, for the present study this parameter is not taken into account. The speed of shrinkage, characterized by the coefficient $\xi_{cbs,2}$, is also modeled with a linear curve, from both results lS-BS and hS-BS. Since both calibrations are derived from only two data points, future results of basic shrinkage of AAS with different M_S should help to refine these correlations. Thus the parameters for the extended *fib* model for basic shrinkage can be taken as follows:

$$\begin{cases} \xi_{cbs,1}(M_S) &= 1.83 \cdot M_S + 8.98 \\ \xi_{cbs,2}(M_S) &= 0.41 \cdot M_S + 0.59 \end{cases} \quad (19)$$

For drying shrinkage, the exposure age to drying (t_s) influences greatly the final drying shrinkage. The influence at early-age (1 to 7 days) seems to be greater than that at later ages. Indeed, the activation of slag with sodium-silicate is slower than the hydration of cement and the second acceleration period can occur up to 48 h.[46] Thus, the material behavior is more sensitive to any water loss at early age. For this reason, the calibration of the coefficients in the extended model split into two domains [1, 7] days and [7, 28] days. Between 1 and 7 days, a decreasing exponential model is used, while a linear curve is used between 7 and 28 days. For $\xi_{cds,2}$, the experimental results indicate that lower the t_s, the faster is the drying shrinkage. However, there was a large range of variation of the obtained $\xi_{cds,2}$ up to third order of magnitude (10^{-3}–10^{0}). In comparison with the range of data available from the literature, it was found that fixing $\xi_{cds,2}$ to 0.25 is a good approximation. The value 0.25 also corresponds to the average value of $\xi_{cds,2}$ for the drying shrinkage with exposure after 28 days for mixes lS and hS. Thus, the key parameters for extended *fib* model for drying shrinkage are as below:

$$\begin{cases} \xi_{cds,1}(1 \le t_s \le 7) &= 7.9 \cdot \exp\left(-\left(\frac{t_S}{1.6}\right)^{2.5}\right) + 0.40 \\ \xi_{cds,1}(t_s > 7) &= -1.3 \cdot 10^{-2} \cdot t_S + 4.91 \cdot 10^{-1} \\ \xi_{cds,2}(t_s) &= 0.25 \end{cases} \quad (20)$$

Finally, it is emphasized that the parameters and correlations provided above are based on the limited dataset of the present study. Thus, a future recalibration will be needed on a larger dataset before using the model for practical engineering purposes. In particular, the influence of slag composition on shrinkage should be investigated with the use of either the ratio $\frac{CaO}{SiO_2+Al_2O_3}$ proposed by Chen et al.[26] for SCM or the ratio $\frac{CaO+MgO}{SiO_2}$ that has been used for correlations on degree of reaction of AAS.[47,48]

5.2 | Validation on results from the literature

The proposed extension is validated against the shrinkage results from Ma et al.,[62] Taghvayi et al.,[63] and Humad et al.[71] For the results from Ma et al. and Humad et al., as both total shrinkage and basic shrinkage are distinguished, the model results are also plotted in a distinguished manner. For each mix, all the necessary parameters for the extended model were taken from the papers. The input parameters for models comprises of compressive strength, drying age, notional thickness, relative humidity, and silicate ratio (M_S). The equivalent binder type was determined using the compressive

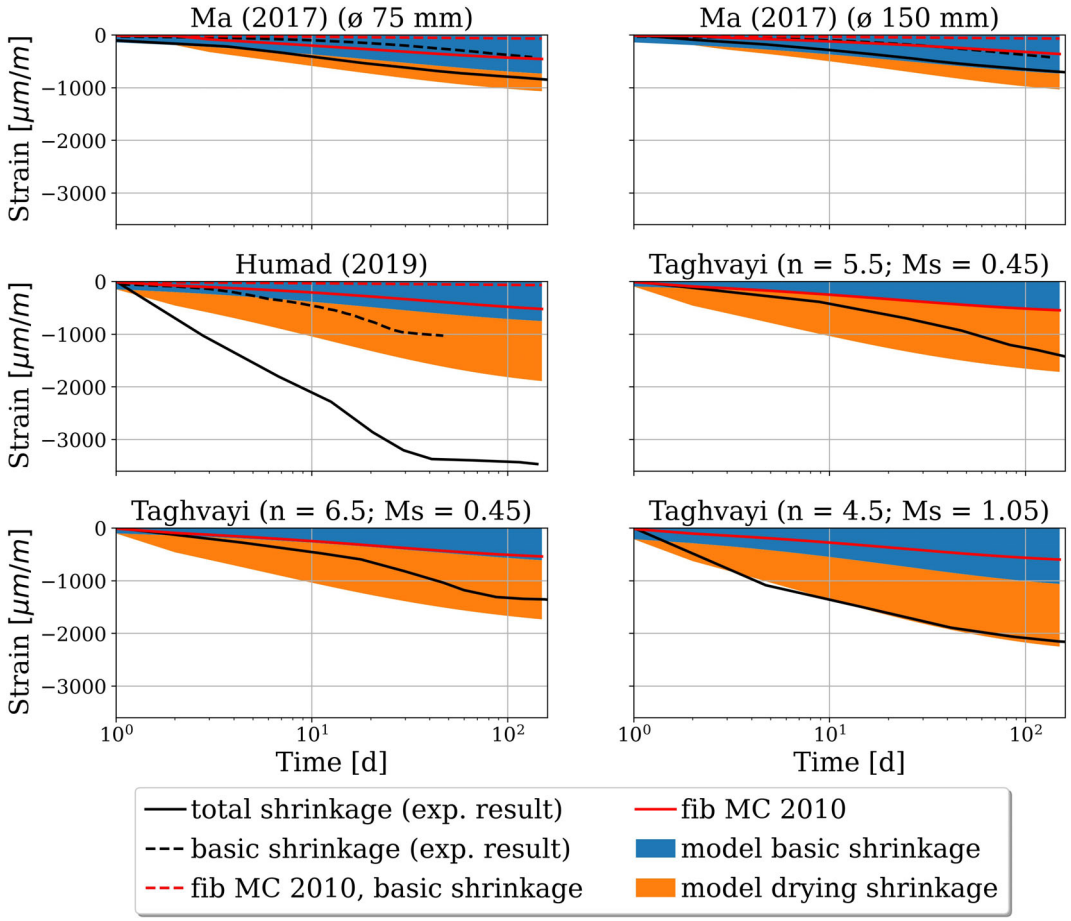

FIGURE 7 Prediction of total shrinkage for dataset extracted from literature (a) Ma et al. (2018) (ø 150 mm), (b) Ma et al. (2018) (ø 150 mm), (c) Humad et al. (2019), (d) Taghvayi et al. (2018) (with $n = 5.5$ and Ms = 0.45), (e) Taghvayi et al. (2018) (with $n = 6.5$ and Ms = 0.45), and (f) Taghvayi et al. (2018) (with $n = 4.5$ and Ms = 1.05)

strength development as shown in Section 4.2.1. The obtained s was approximated to the closest coefficient from Table 4. These inputs are provided in Supporting Information.

The results for shrinkage predictions are given in Figure 7. Since the results from Taghvayi et al.[63] comprise of 20 experiments, only three results are presented here as examples. Additional results can be found in Supporting Information. The basic shrinkage from Ma et al.[62] is overestimated, but the drying shrinkage for both radius 75 and 150 mm are well predicted. In the study done by Humad et al.,[71] the prediction underestimates both basic shrinkage and drying shrinkage but provides significantly better results than models from the *fib* MC 2010. This dataset comes from the blending of a slag with 30.4% CaO, 35% SiO_2, 14.3% Al_2O_3, and 16.1% MgO, with an alkali solution of water/binder ratio equal to 0.36, a sodium silicate content of 5% of mass, and MS equal to 1. One can note that the MgO content is quite high in comparison with the slags from Li et al.[31] and Taghvayi et al.[63] or from the present study. Taghvayi et al.[63] do not distinguish basic shrinkage and drying shrinkage. Thus, only the total shrinkage is analyzed. In all the tested mixes, the prediction using the extended models significantly improves the predictions when compared with the models from *fib* MC 2010.

6 | CONCLUSION

In this study, new experimental results of both basic and drying shrinkage have been presented for AAS concrete. Basic shrinkage is much higher for AAS concrete than for OPC concrete. Furthermore, the basic shrinkage increases with higher M_S. The drying shrinkage is very dependent on the exposure age to drying t_s.

The extended models of the *fib* MC 2010 proposed in this study have been calibrated based on the performed experiments. The four parameters ξ_{cbs1}, ξ_{cds1}, ξ_{cbs2}, and ξ_{cds2} in the model extension influence the final values of basic shrinkage and drying shrinkage and the speed of basic shrinkage and drying shrinkage, respectively. ξ_{cbs1} increases with M_S and is found to be higher than 1, indicating a higher final basic shrinkage when compared with OPC concrete. Higher M_S leads to faster basic

shrinkage. The drying shrinkage is very high for an exposure to drying in early ages and ξ_{cds1} is modeled as a decreasing exponential function during first 7 days. ξ_{cds2} is found to be lower than 1 indicating that the speed of drying shrinkage is faster than the one predicted in the original models from *fib* MC 2010. The calibrated extended model on experimental data presented in this study significantly improves the prediction when compared with the original *fib* MC 2010 for both basic and drying shrinkage on validation datasets taken from the literature. Further calibration is needed on larger datasets to improve the model predictions varying different parameters affecting AAS concrete mixes such as *n* or the MgO content of the slag.

ACKNOWLEDGMENT

The project leading to this application has received funding from the European Union's Horizon 2020 research and innovation programme under the Marie Skłodowska–Curie grant agreement No. 813596.

CONFLICT OF INTEREST

The authors declare that they have no conflict of interest.

DATA AVAILABILITY STATEMENT

The data that support the findings of this study are available from the corresponding author upon reasonable request.

ORCID

Richard Caron https://orcid.org/0000-0002-5741-6440

REFERENCES

1. Fernández-Jiménez A, Puertas F. Structure of calcium silicate hydrates formed in alkaline-activated slag: influence of the type of alkaline activator. J Am Ceram Soc. 2003;86:1389–94.
2. Komljenović MM, Baščarević Z, Marjanović N, Nikolić V. Decalcification resistance of alkali-activated slag. J Hazard Mater. 2012;233–234:112–21.
3. Komljenović M, Baščarević Z, Marjanović N, Nikolić V. External sulfate attack on alkali-activated slag. Construct Build Mater. 2013;49(7):31–9.
4. Chang JJ. A study on the setting characteristics of sodium silicate-activated slag pastes. Cem Concr Res. 2003;33(7):1005–11.
5. Jansson H, Tang L. Parameters influencing the initial setting time of alkali-activated ground granulated blastfurnace slag materials. the nordic concrete federation, 2005.
6. Bakharev T, Sanjayan JG, Cheng YB. Resistance of alkali-activated slag concrete to carbonation. Cem Concr Res. 2001; 31:1277–83.
7. Cadore DE, Angulski da Luz C, Farias de Medeiros MH. An investigation of the carbonation of alkaline activated cement made from blast furnace slag generated by charcoal. Construct Build Mater. 2019;226:117–25.
8. Li Z, Liu J, Ye G. Drying shrinkage of alkali-activated slag and fly ash concrete; a comparative study with ordinary Portland cement concrete. Heron. 2019;64:106107.
9. Thomas RJ, Peethamparan S. Alkali-activated concrete: engineering properties and stress–strain behavior. Construct Build Mater. 2015;93(4):49–56.
10. Collins F, Sanjayan JG. Effect of pore size distribution on drying shrinkage of alkali-activated slag concrete. Cem Concr Res. 2000;30:1401–6.
11. Aili A, Vandamme M, Torrenti JM, Masson B. Is long-term autogenous shrinkage a creep phenomenon induced by capillary effects due to self-desiccation? Cem Concr Res. 2018;108(2):186–200.
12. Hossain AB, Weiss J. The role of specimen geometry and boundary conditions on stress development and cracking in the restrained ring test. Cem Concr Res. 2006;36(1):189–99.
13. Shah HR, Weiss J. Quantifying shrinkage cracking in fiber reinforced concrete using the ring test. Mater Struct. 2006; 39(9):887–99.
14. ACI Committee 209. 209R-92: Prediction of Creep, Shrinkage, and Temperature Effects in Concrete Structures (Reapproved 2008). Technical Documents.
15. Bazant ZP, Baweja S. Creep and shrinkage prediction model for analysis and design of concrete structures- model B_3. Mater Struct. 1995;28:357–65. 415–430, 488–495.
16. Bazant ZP, Baweja S. Creep and Shrinkage Prediction Model for Analysis and Design of Concrete Structures: Model B3. As submitted for: Adam Neville Symposium: Creep and Shrinkage—Structural Design Effects 2000; ACI SP-194, A.Al-Manaseer, ed., Am. Concrete Institute, Farmington Hills, MI: 1–83.
17. Gardner NJ. Design provisions for drying shrinkage and creep of Normal strength concrete. In: Al-Manaseer A, editor. The Adam Neville symposium: creep and shrinkage-structural design effects;SP-194. Farmington Hills, MI: American Concrete Institute; 2000. p. 101–34.
18. Muller HS, Hillsdorf HK. General task group 9. Paris, France: CEB Bomité Euro-Internaional du Béton; 1990. p. 201.
19. CEB. Evaluation of the Time Dependent Properties of Concrete. Bulletin d'Information 1991; No. 199 (Comité European du Beton/Federation Internationale de la Precontrainte, Lausanne, Switzerland, 1991, 201).
20. CEB. CEB-FIP Model Code 1990. CEB Bulletin d'Information 1993; No. 213/214 (Comité Euro-International du Béton, Lausanne, Switzerland), 1993, 33–41.
21. CEB. Structural Concrete—Textbook on Behaviour, Design and Performance. Updated Knowledge of the CEB/FIP Model Code 1990. fib Bulletin 1999;2 V.2(Federation Internationale du Beton, Lausanne, Switzerland), 1990, 37–52.
22. FIB. fib model code for concrete structures 2010. Lausanne: International Federation for Structural Concrete (fib); 2013.
23. Bažant ZP, Hubler MH, Wan-Wendner R. Model B4 for concrete creep and shrinkage including multi-decade applicability. RILEM Mater Struct. 2015;01(48):753–70.
24. Hubler MH, Wendner R, Baant ZP. Comprehensive database for concrete creep and shrinkage: analysis and recommendations for testing and recording. ACI Mater J. 2015;112: 547–58.
25. Tošić N, de La Fuente A, Marinković S. Shrinkage of recycled aggregate concrete: experimental database and application of fib model code 2010. Mater Struct. 2018;51(5):125.
26. Chen J, Kuder KG, Lehman DE, Roeder CW, Lowes LN. Creep modeling of concretes with high volumes of supplementary cementitious materials and its application to concrete-filled tubes. Mater Struct. 2017;50(1):139.

27. Lura P, Jensen OM, van Breugel K. Autogenous shrinkage in high-performance cement paste: an evaluation of basic mechanisms. Cem Concr Res. 2003;33:223–32.
28. Jensen OM. Autogenous deformation and RH-change in perspective. Cem Concr Res. 2001;31:1859–65.
29. Ye H, Cartwright C, Rajabipour F, Radlińska A. Understanding the drying shrinkage performance of alkali-activated slag mortars. Cem Concr Compos. 2017;76(1):13–24.
30. Ballekere Kumarappa D, Peethamparan S, Ngami M. Autogenous shrinkage of alkali activated slag mortars: basic mechanisms and mitigation methods. Cem Concr Res. 2018;109(3):1–9.
31. Li Z, Lu T, Liang X, Dong H, Ye G. Mechanisms of autogenous shrinkage of alkali-activated slag and fly ash pastes. Cem Concr Res. 2020;135:106107.
32. Bangham DH, Fakhoury N, Mohamed AF. The swelling of charcoal. Part II. Some factors controlling the expansion caused by water, benzene and pyridine Vapours. Proc R Soc Lond. 1932;138(834):162–183.
33. Hiller KH. Strength reduction and length changes in porous glass caused by water vapor adsorption. J Appl Phys. 1964; 35(5):1622–8.
34. Feldman RF, Serada PJ. A new model for hydrated Portland cement and its practical implications. NRC of Canada. 1970;53:53–9.
35. Wittmann FH. Creep and shrinkage mechanisms. In: Bazant ZP, Wittmann FH, editors. Part II in "Creep and shrinkage in concrete structures". Chichester: John Wiley & Sons; 1982. p. 129–63.
36. Churaev NV, Derjaguin BV. Inclusion of structural forces in the theory of stability of colloids and films. J Colloid Interface Sci. 1985;103(2):542–53.
37. Wittmann FH, Beltzung F. Fundamental aspects of the interaction between hardened cement paste and water applied to improve prediction of shrinkage and creep of concrete: a critical review. J Sustain Cem-Based Mater. 2016;5(1–2):106–16.
38. Lu T, Li Z, van Breugel K. Modelling of autogenous shrinkage of hardening cement paste. Construct Build Mater. 2020; 264(15):120708.
39. Melo Neto AA, Cincotto MA, Repette W. Drying and autogenous shrinkage of pastes and mortars with activated slag cement. Cem Concr Res. 2008;38(4):565–74.
40. Song C, Choi YC, Choi S. Effect of internal curing by superabsorbent polymers—internal relative humidity and autogenous shrinkage of alkali-activated slag mortars. Construct Build Mater. 2016;123(10):198–206.
41. Mastali M, Kinnunen P, Dalvand A, Mohammadi Firouz R, Illikainen M. Drying shrinkage in alkali-activated binders—a critical review. Construct Build Mater. 2018;190(8):533–50.
42. Bernal SA, San Nicolas R, van Deventer JSV, Provis JL. Water content modifies the structural development of sodium metasilicate-activated slag binders. Revista ALCONPAT. 2015; 5(1):28–39.
43. Criado M, Walkley B, Ke X, Provis J, Bernal S. Slag and activator chemistry control the reaction kinetics of sodium Metasilicate-activated slag cements. Sustainability. 2018;10(12):4709.
44. Zuo Y, Ye G. Preliminary interpretation of the induction period in hydration of sodium hydroxide/silicate activated slag. Materials. 2020;13(21):4796.
45. Chithiraputhiran S, Neithalath N. Isothermal reaction kinetics and temperature dependence of alkali activation of slag, fly ash and their blends. Construct Build Mater. 2013;45:233–42.
46. Gebregziabiher BS, Thomas RJ, Peethamparan S. Temperature and activator effect on early-age reaction kinetics of alkali-activated slag binders. Construct Build Mater. 2016;113(1): 783–93.
47. Winnefeld F, Ben Haha M, Le Saout G, Costoya M, Ko SC, Lothenbach B. Influence of slag composition on the hydration of alkali-activated slags. J Sustain Cem-Based Mater. 2015;4(2): 85–100.
48. Caron R, Patel RA, Dehn F. Activation kinetic model and mechanisms for alkali-activated slag cements. Construct Build Mater. 2022;323:126577.
49. DIN EN 12350-5. Prüfung von Frischbeton—Teil 5: Ausbreitmaß; Deutsche Fassung EN 12350-5:2019. Beuth Verlag 2019;.
50. DIN EN 12350-6. Prüfung von Frischbeton—Teil 6: Frischbetonrohdichte; Deutsche Fassung EN 12350-6:2019. Beuth Verlag 2019.
51. DIN EN 12350-7. Prüfung von Frischbeton—Teil 7: Luftgehalt – Druckverfahren; Deutsche Fassung EN 12350-7:2019. Beuth Verlag 2019.
52. DIN EN 12390-3. Prüfung von Festbeton—Teil 3: Druckfestigkeit von Probekörpern; Deutsche Fassung EN 12390-3:2019. Beuth Verlag 2019.
53. DIN EN 12390-13. Prüfung von Festbeton—Teil 13: Bestimmung des Elastizitätsmoduls unter Druckbelastung(Sekantenmodul); Deutsche und Englische Fassung prEN 12390-13:2019. Beuth Verlag 2019.
54. DIN EN 12390-16. Prüfung von Festbeton - Teil 16: Bestimmung des Schwindens von Beton; Deutsche Fassung EN 12390-16:2019. Beuth Verlag 2019;.
55. Li Z, Lu T, Chen Y, Wu B, Ye G. Prediction of the autogenous shrinkage and microcracking of alkali-activated slag and fly ash concrete. Cem Concr Compos. 2021;117:103913.
56. Palacios M, Puertas F. Effect of shrinkage-reducing admixtures on the properties of alkali-activated slag mortars and pastes. Cem Concr Res. 2007;37(5):691–702.
57. Cartwright C, Rajabipour F, Radlińska A. Shrinkage characteristics of alkali-activated slag cements. J Mater Civ Eng. 2015; 27(7):509.
58. Duran Atiş C, Bilim C, Çelik Ö, Karahan O. Influence of activator on the strength and drying shrinkage of alkali-activated slag mortar. Construct Build Mater. 2009;23(1):548–55.
59. Aydn S, Baradan B. Mechanical and microstructural properties of heat cured alkali-activated slag mortars. Mater Design. 2012; 35:374–83.
60. Matalkah F, Salem T, Shaafaey M, Soroushian P. Drying shrinkage of alkali activated binders cured at room temperature. Construct Build Mater. 2019;201(1):563–70.
61. Ye H, Cartwright C, Rajabipour F, Radlinska A. Effect of Drying Rate on Shrinkage of Alkali-Activated Slag Cements 2014.
62. Ma J, Dehn F. Shrinkage and creep behavior of an alkali-activated slag concrete. Struct Concr. 2017;18(5):801–10.
63. Taghvayi H, Behfarnia K, Khalili M. The effect of alkali concentration and sodium silicate modulus on the properties of alkali-activated slag concrete. J Adv Concrete Technol. 2018; 16(7):293–305.
64. Cartwright C, Rajabipour F, Radlinska A. Measuring the chemical shrinkage of alkali-activated slag cements using the Buoyancy Method. Ninth International Conference on Creep, Shrinkage, and Durability Mechanics (CONCREEP-9), 2013;308–15.
65. Ye H, Radlińska A. Quantitative analysis of phase assemblage and chemical shrinkage of alkali-activated slag. J Adv Concrete Technol. 2016;14(5):245–60.

66. Thomas JJ, Allen AJ, Jennings HM. Density and water content of nanoscale solid C–S–H formed in alkali-activated slag (AAS) paste and implications for chemical shrinkage. Cem Concr Res. 2012;42(2):377–83.
67. Zhang T, Gao P, Luo R, Guo Y, Wei J, Yu Q. Measurement of chemical shrinkage of cement paste: comparison study of ASTM C 1608 and an improved method. Construct Build Mater. 2013;48(2):662–9.
68. Di Bella C, Wyrzykowski M, Lura P. Evaluation of the ultimate drying shrinkage of cement-based mortars with poroelastic models. Mater Struct. 2017;50(1):453.
69. Jia Z, Yang Y, Yang L, Zhang Y, Sun Z. Hydration products, internal relative humidity and drying shrinkage of alkali activated slag mortar with expansion agents. Construct Build Mater. 2018;158(2):198–207.
70. Jensen OM, Hansen PF. Autogenous relative humidity change in silica fume-modified cement paste. Adv Cem Res. 1995; 7(25):33–8.
71. Humad AM, Kothari A, Provis JL, Cwirzen A. The effect of blast furnace slag/Fly ash ratio on setting, strength, and shrinkage of alkali-activated pastes and concretes. Front Mater. 2019;6:113.

AUTHOR BIOGRAPHIES

Richard Caron, Institute of Building Materials and Concrete Structures (IMB), Karlsruhe Institute of Technology (KIT), Germany.
Email: richard.caron@kit.edu

Ravi A. Patel, Materials Testing and Research Institute (MPA), Karlsruhe Institute of Technology (KIT), Germany
Email: ravi.patel@kit.edu

Frank Dehn, Institute of Building Materials and Concrete Structures (IMB), Karlsruhe Institute of Technology (KIT), Germany
Email: frank.dehn@kit.edu

SUPPORTING INFORMATION

Additional supporting information may be found in the online version of the article at the publisher's website.

How to cite this article: Caron R, Patel RA, Dehn F. Extension of the *fib* MC 2010 for basic and drying shrinkage of alkali-activated slag concretes. Structural Concrete. 2022. https://doi.org/10.1002/suco.202100901

Supplementary Material: mix characteristics used for the prediction of results from the literature and further predictions of total shrinkage

This document provides validation of the extension of the *fib* MC 2010 to AAS against additional literature dataset.

Each data is modeled with a type of concrete, based on the evolution of compressive strength with time. Then, *fib* MC 2010 and its extension are applied based on the compressive strength, the mix design, the exposure age to drying and the geometry.

Dataset	f_{cm} [MPa]	binder model
Ma (2017)	42	32.5 R, 42.5 N
Humad (2019)	42	32.5 R, 42.5 N
Taghvayi (n = 3.5; Ms = 0.45)	29	32.5 N
Taghvayi (n = 3.5; Ms = 0.65)	40	32.5 N
Taghvayi (n = 3.5; Ms = 0.85)	52	32.5 N
Taghvayi (n = 3.5; Ms = 1.05)	54	32.5 R, 42.5 N
Taghvayi (n = 4.5; Ms = 0.45)	35	32.5 N
Taghvayi (n = 4.5; Ms = 0.65)	47	32.5 R, 42.5 N
Taghvayi (n = 4.5; Ms = 0.85)	55	32.5 N
Taghvayi (n = 4.5; Ms = 1.05)	60	42.5 R, 52.5 N, 52.5 R
Taghvayi (n = 5.5; Ms = 0.45)	39	32.5 R, 42.5 N
Taghvayi (n = 5.5; Ms = 0.65)	56	32.5 R, 42.5 N
Taghvayi (n = 5.5; Ms = 0.85)	62	32.5 R, 42.5 N
Taghvayi (n = 5.5; Ms = 1.05)	65	32.5 R, 42.5 N
Taghvayi (n = 6.5; Ms = 0.45)	41	32.5 R, 42.5 N
Taghvayi (n = 6.5; Ms = 0.65)	57	32.5 R, 42.5 N
Taghvayi (n = 6.5; Ms = 0.85)	61	32.5 R, 42.5 N
Taghvayi (n = 6.5; Ms = 1.05)	65	42.5 R, 52.5 N, 52.5 R
Taghvayi (n = 7.5; Ms = 0.45)	40	32.5 R, 42.5 N
Taghvayi (n = 7.5; Ms = 0.65)	56	42.5 R, 52.5 N, 52.5 R
Taghvayi (n = 7.5; Ms = 0.85)	61	42.5 R, 52.5 N, 52.5 R
Taghvayi (n = 7.5; Ms = 1.05)	67	42.5 R, 52.5 N, 52.5 R

TABLE 1 Mix characteristics used for the prediction of results from the literature

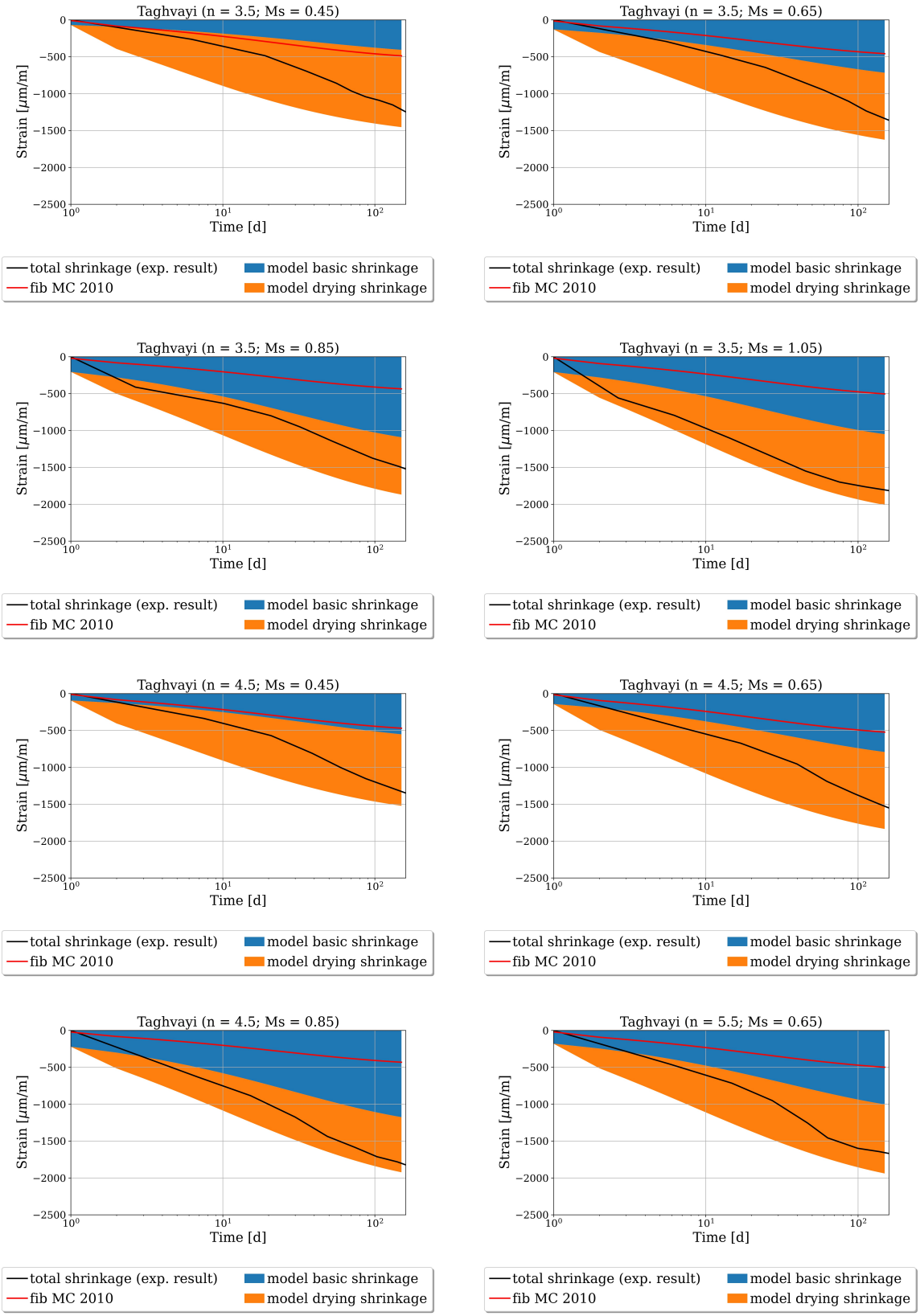

FIGURE 1 Prediction of total shrinkage for dataset extracted from the literature

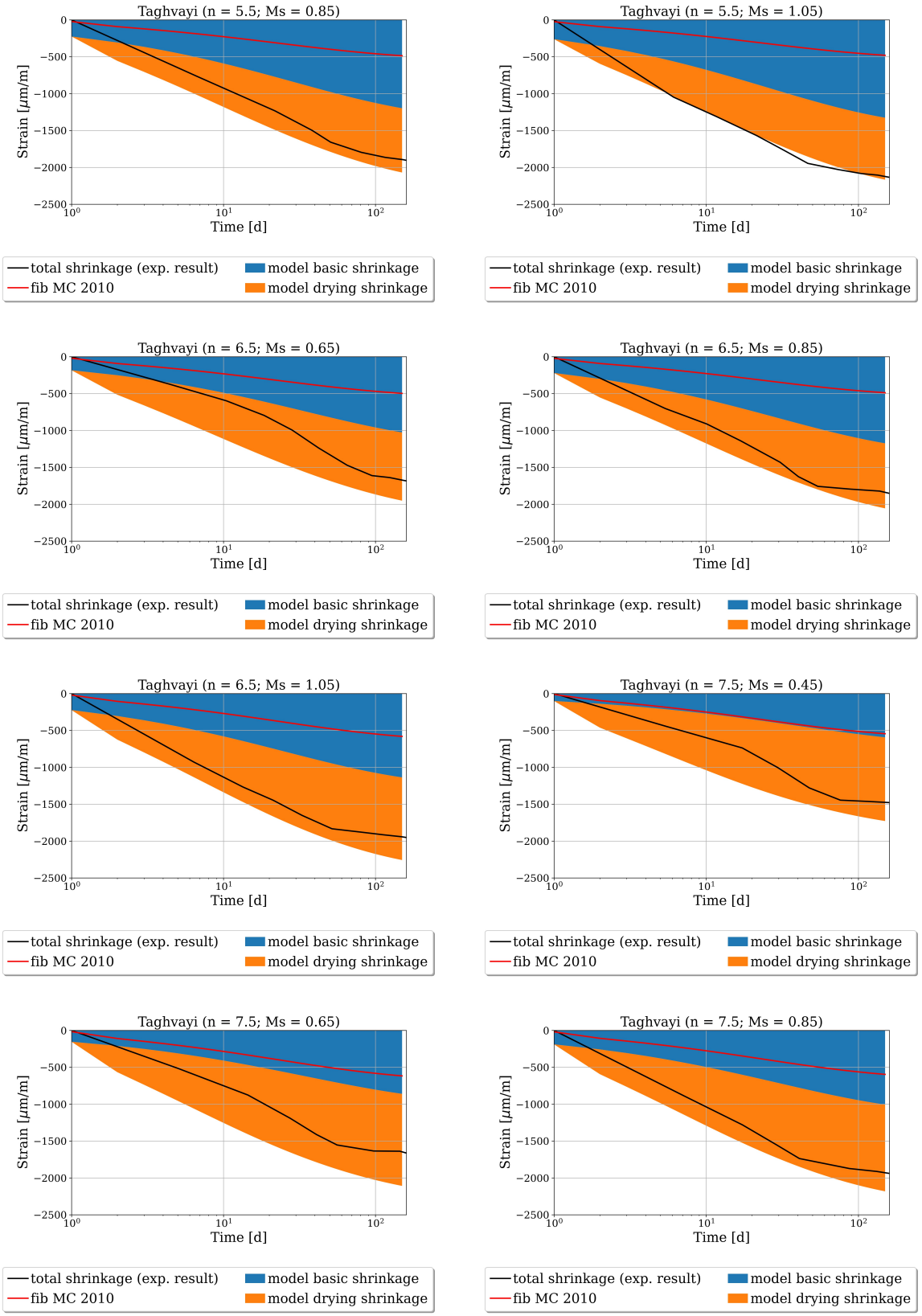

FIGURE 2 Prediction of total shrinkage for dataset extracted from the literature (continued)

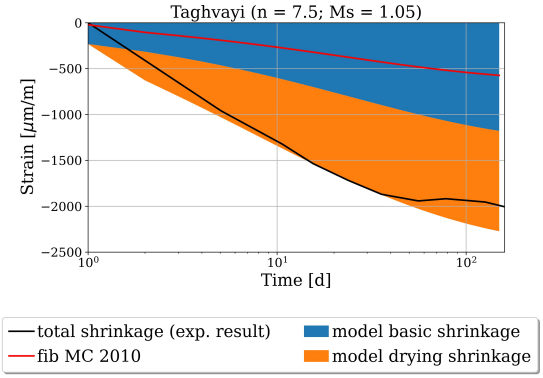

FIGURE 3 Prediction of total shrinkage for dataset extracted from the literature (end)

Paper 2

Experimental study on basic and drying creep for an alkali-activated slag concrete and comparison with existing creep models

Publisher's version

Published in *Structural Concrete*

Volume 64 (48), 2023, pp. 1-16

DOI: 10.1002/suco.202300134

Authors: **Richard Caron**, Ravi A. Patel, Frank Dehn

Received: 20 February 2023 | Revised: 10 April 2023 | Accepted: 19 April 2023

DOI: 10.1002/suco.202300134

ARTICLE

fib CEB-FIP WILEY

Experimental study on basic and drying creep for an alkali-activated slag concrete and comparison with existing creep models

Richard Caron[1,2] | **Ravi A. Patel**[1,2] | **Frank Dehn**[1,2]

[1]Institute of Building Materials and Concrete Structures (IMB), Karlsruhe Institute of Technology (KIT), Karlsruhe, Germany

[2]Materials Testing and Research Institute (MPA), Karlsruhe Institute of Technology (KIT), Karlsruhe, Germany

Correspondence
Richard Caron, Institute of Building Materials and Concrete Structures, Karlsruhe Institute of Technology (KIT), 76131 Germany.
Email: richard.caron@kit.edu

Funding information
Horizon 2020 Framework Programme, Grant/Award Number: 813596

Abstract

Slag is a by-product of the steel industry that can be activated using alkali solutions to form concrete. This study presents new experimental results of basic and drying creep behavior of alkali-activated slag (AAS) concrete. Different parameters affecting creep such as loading age, sample size and creep stress-strength ratio were varied for experimental studies. The results show that the basic creep of AAS concrete is higher than that of ordinary Portland cement (OPC) concrete. The drying creep of AAS is lower than for OPC and this could be explained by a higher internal drying during the activation of slag. The experimental results were used to check the applicability of two existing engineering models, the *fib* MC 2010 and the B4s model, for AAS concrete. It was found that both models could be extended to predict the basic creep of AAS concrete. For drying creep, the B4s could better capture the creep behavior. For the *fib* MC 2010, a new formulation for drying creep would be required.

KEYWORDS

alkali-activated slag, B4s model, creep, *fib* MC 2010

1 | INTRODUCTION

In the past decades, new types of binders have been extensively studied in order to propose alternatives to ordinary Portland cement (OPC). Among them, the activation of slag, fly ash and metakaolin using alkali solutions to form a hardening matrix seems to be a promising approach. Such binder systems are termed as alkali-activated materials (AAMs).[1] In comparison to OPC, alkali-activated slag (AAS) contains higher amounts of silicon and aluminum oxides and less calcium oxide.[2] This difference in oxide content induces different reaction products. However, several studies showed that the compressive strength of this material is comparable to cement-based systems.[3–5] In addition, AAS was proven to have a better resistance to chloride ingress and a lower permeability than cement-based systems.[6,7] Thus, the use of AAS for producing concrete could be a key to increasing the durability and lifespan of structures for certain exposure conditions.

Both OPC and AAS concrete structures experience deformations. If they are excessive, these deformations endanger the safety of the structures and thus reduce their service life. They can occur in loading-free conditions or under sustained load applied on the concrete. In the latter case, the associated deformations are referred to as creep. For bridge structures, surfaces can become non-planar and affect their use[8] or show excessive

deflections.[9] Reactor containments are other examples of structures that undergo high strains under loading. These deformations must be predicted and controlled to reduce the formation of cracks.[10,11] It was also shown that creep can lead to an increase in carbonation[12] and chloride ingress.[13]

Basic creep is defined as the creep that takes place in sealed conditions, i.e. without moisture exchange with the surrounding environment. Drying creep is defined as the additional creep occurring with moisture exchange. Under constant load $\sigma(t) = \widehat{\sigma}$ (MPa) applied on the material at the age t_0 (d), the compliance function $J(t,t_0)$ (1/MPa) is defined as:

$$\varepsilon(t) = \widehat{\sigma} J(t,t_0), \tag{1}$$

where $\varepsilon(t)$ (−) is the strain at time t (d). To predict the strain evolution of cement-based concrete, the compliance function of Equation (1) has been modeled in the B3 model by Bazant and coworkers.[14,15] The B4 model extends and improves the B3 model.[16] It is a semi-empirical creep model based on the solidification theory for aging viscoelasticity and solidifying material.[16] It was first developed to predict the creep strain as a function of the mix design. However, a simplified model, the B4s model, has been developed in which the creep strain is expressed as a function of the characteristic compressive strength.

Another way to define creep strains is to use the experimental creep coefficient $\phi(t,t_0)$ defined as the normalized creep strain by the strain at loading:

$$\phi(t,t_0) = \frac{\varepsilon_{cc}(t,t_0)}{\varepsilon_{ci}(t_0)} = E_c(t_0) \cdot J(t,t_0) - 1, \tag{2}$$

where $E_c(t_0)$ is the modulus of elasticity of concrete at loading age. The *fib* MC 2010 is an empirical model that also predicts the creep strain from the characteristic compressive strength of concrete. This model is based on a modified definition of the creep coefficient:

$$\phi_{MC}(t,t_0) = \phi(t,t_0) \cdot \frac{E_{ci}}{E_c(t_0)}, \tag{3}$$

where ϕ_{MC} is the creep coefficient of the *fib* MC 2010 and E_{ci} is the modulus of elasticity of concrete at 28 days. This model was calibrated experimentally and is valid for creep loading lower than or equal to 40% of the compressive strength at loading age. For both *fib* MC 2010, B4 and B4s models, the basic creep and the drying creep are regarded as additive and independent.

Creep was also studied and compared with the previous engineering models for other binder types as recycled aggregate concretes[17] or alkali-activated fly ash.[18–20] Few studies have been made on the creep of AAS.[21–24] Humad et al.[24] proposed that the relative high creep could come from the increased presence of micro-cracks in the AAS matrix. Zhou et al. proposed an extension of the GL2000 model for AAS with sodium silicate.[21] However, no comparison with both *fib* MC 2010 and B4s models have been formulated so far.

In this study, new results of the creep behavior of AAS concrete are presented. Experiments on both sealed and unsealed conditions were performed. The influences of loading age, specimen diameter and creep stress-strength ratio on the creep behavior of this material were investigated. Two engineering models, namely the *fib* MC 2010 and the B4s model, were calibrated from the experimental results. These two models were originally developed for OPC concretes but they have been extended for other types of concrete. This study aims at examining whether they can be adapted to predict creep behavior of the AAS concrete.

2 | MATERIALS AND METHODS

2.1 | Materials

The slag used in this study was provided by the company Ecocem (Netherlands). Its oxide composition was determined with energy dispersive X-ray fluorescence (XRF) spectrometry with an M4 Tornado (Brucker GmbH Karlsruhe, Germany) (see Table 1). The activator used to make the slag react was a blend of commercial waterglass solution, commercial NaOH solution and tap water. The water glass was Betol 39 T, provided by Wöllner GmbH (Germany). It consists of 64%—mass of water, 8.2%—mass of Na_2O and 27.8%—mass of SiO_2. The NaOH solution had a 50% mass concentration of solid NaOH. The used alkali solution had an alkali dosage (n) equal to 5 (g Na_2O/100 g slag), a silicate ratio (M_S) equal to 0.5 (mol SiO_2/mol Na_2O) and a water/slag ratio w/s equal to 0.45 (kg/kg). This mix design is close to the mix design of the mix S3a of the RILEM round-robin test for alkali-activated concretes.[5,25] The generated concrete had a density of 2.25 kg/m^3. The mix design is summed up in Table 2.

2.2 | Methods

2.2.1 | Mixing procedure, casting and storage

The alkali solution was prepared 24 h in advance so that it reaches the temperature of the surrounding

TABLE 1 Chemical composition of the anhydrous slag.

Oxide	CaO	SiO_2	Al_2O_3	MgO	Fe_2O_3	Na_2O	K_2O	H_2S	Oth.
Mass (%)	38.8	36.3	12.8	8.0	0.6	0.3	0.6	1.0	1.6

TABLE 2 Mix design of the concrete.

Parameter	Unit	Value
w/s	(kg/kg)	0.45
n	(Na_2O g/100 g slag)	5.0
M_S	(SiO_2/Na_2O mol/mol)	0.5
Precursor content	(kg/m^3 of concrete)	450
Sand (0–2 mm)	(Vol-%)	40
Agg. (2–8 mm)	(Vol-%)	30
Agg. (8–16 mm)	(Vol-%)	30
Density	(kg/m^3)	2.25
Compressive strength	(MPa)	56

environment before being mixed with the slag. The dry ingredients were mixed for 30 s. The alkali solution was then added and the mixture was mixed for 1 min. After a resting time of 30 s, the mixture was mixed for 2 min. Cylindrical samples of 100 or 150 mm diameter and 300 mm height were cast. Additionally, cubes of characteristic size equal to 150 mm were cast. All the samples were de-molded after 24 h and covered with aluminum-butyl foil to prevent water loss. When needed, the sealing was removed at the corresponding age for exposure to drying t_s. The surfaces subjected to loading for concrete samples used for Young's modulus and creep tests were ground at an age of at least 6 days to have uniform contact with the loading plates.

2.2.2 | Mechanical tests on concrete samples

The compressive strength of concrete specimens was measured after 28 days with three cubes of characteristic size 150 mm, following the standard DIN EN 12390-3[26] where the samples were covered with plastic foil for the first 7 days and uncovered until the test day. The compressive strength measured with these cubes is given in Table 2 and is regarded as an intrinsic value of the mix design for this study. The ambient conditions were 20°C and 65% relative humidity. The Young's modulus and the compressive strength of cylinders were determined according to EN 12390-13[27] (method B) on six samples with the same geometry and the same curing conditions as the one used for creep tests before each creep measurement.

The deformations of concrete were measured with linear variable differential transformers (LVDTs) provided by the company Hottinger Brüel & Kjaer GmbH (Germany). Three LVDTs were placed at the center of each specimen and spaced at an angle of 120° on the sample. The gauge length for the measurement was 150 mm.

The creep setup is described in Figure 1. It consists of a hollow steel spring filled with hydraulic oil, a loading frame and a pressure pipe with the loading device. The hollow steel was connected to a pressure tank through a pipe filled with oil and nitrogen. After that the specimens equipped with the LVDTs were mounted on the loading frame, the above transverse was put on the spherical cap and fixed with a screw-nut system. Oil was then released from the pressure tank to reach the wanted value of pressure. Throughout the test, the pressure changes were recorded by an absolute pressure transducer P8AP (Hottlinger Baldwin Messtechnik GmbH).

Basic creep was studied for cylinders of 100 mm and 150 mm diameters for the same height of 300 mm with a loading age equal to either 7 or 28 days. Drying creep was always investigated with samples subjected to drying after 7 days. Three loading ages were investigated with specimens of 100 mm diameter: 7, 28 and 100 days. For the loading ages 7 and 28 days, the drying creep of specimens of 150 mm diameter was also measured. The sustained loads during creep experiments were always taken as a percentage of the compressive strength at loading age. For most of the experiments, the creep stress-strength ratio $R_{cr} = \frac{f_{cr}}{f_{cm(t_0)}}$ (%) was kept equal to 33%. Here, $f_{cm}(t_0)$ is the compressive strength at the loading age and f_{cr} is the sustained load during the creep test. With 100 mm diameter specimens, additional studies for R_{cr} equal to 20% and 60% were conducted for unsealed samples at a loading age of 28 days to understand the influence of R_{cr}. The experimental plan for creep tests is summarized in Table 3.

Parallel specimens were used to determine both basic shrinkage and drying shrinkage of the material with the same measuring tool as for creep, i.e., three LVDTs per specimen, without loading. Two replicates were used for each geometry (100 or 150 mm diameter) and each curing condition (always sealed, or sealed for 7 days and then unsealed). Shrinkage contribution was subtracted from the measurements on loaded specimens to obtain creep strains.

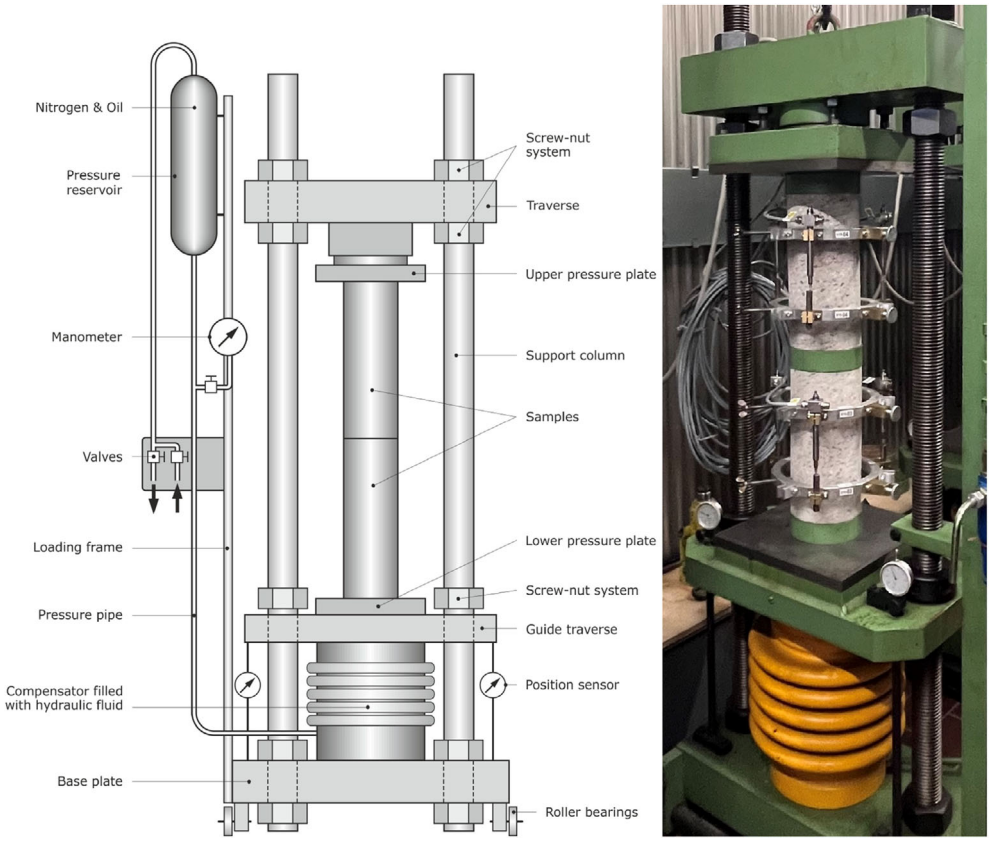

FIGURE 1 Experimental creep setup used in this study.

TABLE 3 Experimental plan for creep experiments.

Name	t_s	t_0	R_{cr}	d
Unit	days	days	%	mm
BC-7d-Ø100	n.a.	7	33	100
BC-28d-Ø100	n.a.	28	33	100
BC-7d-Ø150	n.a.	7	33	150
BC-28d-Ø150	n.a.	28	33	150
DC-7d-Ø100	7	7	33	100
DC-28d-Ø100	7	28	33	100
DC-7d-Ø150	7	7	33	150
DC-28d-Ø150	7	28	33	150
DC-100d-Ø100	7	100	33	100
DC-28d-Ø100-20%	7	28	20	100
DC-28d-Ø100-60%	7	28	60	100

Note: n.a stands for not applicable.

3 | MODELING OF THE CREEP BEHAVIOR OF CONCRETE

3.1 | Creep model based on the *fib* MC 2010

In the *fib* MC 2010, the total strain ε_c (μm/m) at a given time t (d) can be predicted by using:

$$\varepsilon_c(t) = \varepsilon_{ci}(t_0) + \varepsilon_{cc}(t) + \varepsilon_{cs}(t) + \varepsilon_{cT}(t), \quad (4)$$

where $\varepsilon_{ci}(t_0)$ (μm/m) is the initial strain at loading at t_0 (d), $\varepsilon_{cc}(t)$ (μm/m) is the creep strain for $t > t_0$, $\varepsilon_{cs}(t)$ (μm/m) is the shrinkage strain and $\varepsilon_{cT}(t)$ (μm/m) is the thermal strain.

Under the assumption that the applied stress σ_c (MPa) at time t_0 is below 40% of the compressive strength at $t = t_0$, the creep strain is expressed using the creep coefficient $\phi_{cc}(t, t_0)$ (−):

$$\varepsilon_{cc}(t, t_0) = \frac{\sigma_c(t_0)}{E_{ci}} \phi_{cc}(t, t_0) \quad (5)$$

E_{ci} (MPa) is the modulus of elasticity at the age of 28 days.

The creep coefficient is additively decomposed into the basic creep coefficient ϕ_{bc} (−) and the drying creep coefficient ϕ_{dc} (−):

$$\phi_{cc}(t, t_0) = \phi_{bc}(t, t_0) + \phi_{dc}(t, t_0), \quad (6)$$

ϕ_{bc} is predicted using the following function:

$$\phi_{bc}(t, t_0) = \beta_{bc}(f_{cm}) \cdot \beta_{bc}(t, t_0), \quad (7)$$

where

$$\begin{cases} \beta_{bc}(f_{cm}) &= \dfrac{1.8}{(f_{cm})^{0.7}} \\ \beta_{bc}(t,t_0) &= \ln\left(\left(\dfrac{30}{t_{0,adj}}+0.035\right)^2\cdot(t-t_0)+1\right) \\ t_{0,adj} &= t_{0,T}\cdot\left[\dfrac{9}{2+t_{0,T}^{1.2}}+1\right]^{\alpha}\geq 0.5 \text{ days} \end{cases} \quad (8)$$

f_{cm} (MPa) is the mean compressive strength at 28 days. $t_{0,T}$ (d) is the age of concrete at loading (constant in isothermal conditions). $t_{0,adj}$ (d) is the adjusted age at loading accounting for the type and maturity of concrete. α is a coefficient that depends on the strength class of cement: $\alpha=-1$ for strength class 32.5 N; $\alpha=0$ for strength classes 32.5 R and 42.5 N; $\alpha=1$ for strength classes 42.5 R, 52.5 N and 52.5 R.

$\phi_{dc}(t,t_0)$ is estimated using the following function:

$$\phi_{dc}(t,t_0)=\beta_{dc}(f_{cm})\cdot\beta(RH)\cdot\beta_{dc}(t_0)\cdot\beta_{dc}(t,t_0), \quad (9)$$

with

$$\begin{cases} \beta_{dc}(f_{cm}) &= \dfrac{412}{(f_{cm})^{1.4}} \\ \beta(RH) &= \dfrac{1-\dfrac{RH}{100}}{\sqrt[3]{0.1\cdot\dfrac{h}{100}}} \\ \beta_{dc}(t_0) &= \dfrac{1}{0.1+t_{0,adj}^{0.2}} \\ \beta_{dc}(t,t_0) &= \left[\dfrac{(t-t_0)}{\beta_h+(t-t_0)}\right]^{\gamma(t_0)} \end{cases}, \quad (10)$$

where

$$\begin{cases} \gamma(t_0) &= \dfrac{1}{2.3+\dfrac{3.5}{\sqrt{t_{0,adj}}}} \\ \beta_h &= 1.5\cdot h+250\cdot\alpha_{f_{cm}}\leq 1500\cdot\alpha_{f_{cm}} \\ \alpha_{f_{cm}} &= \left(\dfrac{35}{f_{cm}}\right)^{0.5} \end{cases}, \quad (11)$$

RH (%) is the relative humidity of the ambient environment. h (mm) is the notional size of the sample and corresponds to twice the ratio between the cross-section and the perimeter of the sample in contact with the atmosphere.

These functions were derived from experiments with OPC-based concrete. To extend this model to other types of concrete, four parameters were introduced in the revision of Eurocode 2[28]: ξ_{bc1} and ξ_{bc2} corresponding to basic creep, and ξ_{dc1} and ξ_{dc2} corresponding to drying creep. This approach was already used by Tosic et al.[17] to model the creep behavior of recycled aggregate concretes. The extended model is described as:

$$\phi(t,t_0)=\xi_{bc1}\cdot\phi_{bc}(t,t_0)+\xi_{dc1}\cdot\phi_{dc}(t,t_0), \quad (12)$$

and the additional parameters are introduced in:

$$\begin{cases} \widetilde{\beta}_{bc}(t,t_0) &= \ln\left(\left(\dfrac{30}{t_{0,adj}}+0.035\right)^2\cdot\dfrac{(t-t_0)}{\xi_{bc2}}+1\right) \\ \widetilde{\beta}_{dc}(t,t_0) &= \left[\dfrac{(t-t_0)}{\beta_h\cdot\xi_{dc2}+(t-t_0)}\right]^{\gamma(t_0)} \end{cases}, \quad (13)$$

If the values of the four parameters are taken equal to one, the original form is recovered. Comparing the above extension with that proposed in Tosic et al.[29] for basic shrinkage, the role of parameters ξ_{cbs1} and ξ_{cbs2} should correspond to the adaptation of the vertical scaling and the horizontal scaling, respectively. Vertical scaling refers to adapting the asymptotic behavior whereas horizontal scaling refers to controlling the rate of the creep. However, when using Equations (12) and (13), both parameters ξ_{bc1} and ξ_{bc2} have an influence on the asymptotic behavior of basic creep in Equation (13). Indeed, when $\left(\frac{30}{t_{0,adj}+0.035}\right)^2\cdot\frac{(t-t_0)}{\xi_{bc2}}>>1$:

$$\phi(t,t_0)\xrightarrow[\left(\frac{30}{t_{0,adj}}+0.035\right)^2\cdot\frac{(t-t_0)}{\xi_{bc2}}>>1]{}\xi_{bc1}\cdot\beta_{bc}(f_{cm})\cdot\ln\left(\left(\frac{30}{t_{0,adj}}+0.035\right)^2\cdot(t-t_0)\right)-\xi_{bc1}\cdot\beta_{bc}(f_{cm})\cdot\ln(\xi_{bc2}). \quad (14)$$

This causes difficulty in distinguishing the contributions arising from vertical and horizontal scaling for different types of concretes and different testing conditions. To avoid the above-mentioned inconsistency, the following extension is proposed for basic creep in this study:

$$\widetilde{\widetilde{\beta}}_{bc}(t,t_0)=\ln\left(\left(\frac{30}{t_{0,adj}}+0.035\right)^2\cdot(t-t_0)+1\cdot\xi_{bc2}\right). \quad (15)$$

In that case, the vertical scaling is only parameterized by ξ_{bc1} and the horizontal scaling is only parameterized by ξ_{bc2}. The inconvenient of the use of Equation (15) comes from the fact that the value at loading age ($t=t_0$) is not zero since $\widetilde{\widetilde{\beta}}_{bc}(t_0,t_0)=\ln(1\cdot\xi_{bc2})$.

3.2 | Creep model based on the B4s model

The B4s model predicts also the creep behavior of concrete taking the characteristic compressive strength of

Parameter	R	RS	SL
p_1	0.70	0.60	0.80
p_{5H}	8.00	1.00	8.00
s_2	14.2×10^{-3}	29.9×10^{-3}	11.2×10^{-3}
s_5	1.54×10^{-6}	41.8×10^{-6}	150×10^{-6}
$\varepsilon_{s,cem}$	590×10^{-6}	830×10^{-6}	640×10^{-6}
$s_{\varepsilon f}$	−0.51	−0.84	−0.69
$\tau_{s,cem}$	0.027	0.027	0.032
$s_{\tau f}$	0.21	1.55	−1.84

TABLE 4 Parameters of the B4s model for the different cement types: R = normal, RS = rapid hardening, SL = slow hardening.

concrete as an input. It is described by use of the compliance function J (μm/m/MPa), which can be estimated using the following equation:

$$J(t,t_0) = q_1 + J_b(t,t_0) + J_d(t,t_0), \tag{16}$$

in which q_1 (μm/m/MPa) is the asymptotic compliance at loading, J_b (μm/m/MPa) is the basic creep compliance and J_d (μm/m/MPa) is the additional creep compliance due to drying. q_1 is given by:

$$q_1 = \frac{p_1}{E_{cm}}, \tag{17}$$

where p_1 is given in Table 4 and E_{cm} is Young's modulus at 28 days, which can be estimated with:

$$E_{cm} = 4734 \cdot \sqrt{f_{cm}} \tag{18}$$

J_b is decomposed in three terms accounting respectively the aging viscoelastic compliance, the non-aging viscoelastic compliance and the flow compliance:

$$J_b(t,t_0) = q_2 \cdot Q(t,t_0) + q_3 \cdot \ln[1 + (t-t_0)^n] + q_4 \cdot \ln\left(\frac{t}{t_0}\right), \tag{19}$$

with:

$$\begin{cases} q_2 &= s_2 \cdot \left(\frac{f_{cm}}{f_0}\right)^{-1.58} \\ q_3 &= 0.976 \cdot s_2 \cdot \left(\frac{f_{cm}}{f_0}\right)^{-3.19} \\ q_4 &= 4 \times 10^{-3} \cdot \left(\frac{f_{cm}}{f_0}\right)^{-1.16} \end{cases}, \tag{20}$$

where $f_0 = 40$ MPa.

TABLE 5 Values of the aggregate-dependent factor $k_{\tau a}$ for the B4s model.

Aggregate type	$k_{\tau a}$
Diabase	0.06
Quartzite	0.59
Limestone	1.80
Sandstone	2.30
Granite	4.00
Quartz Diorite	15.0

The additional creep compliance due to drying J_d is predicted by using:

$$J_d(t,t_0) = q_5 \cdot \sqrt{|\, e^{-g(t,t_s)} - e^{-g(t_0-t_s)}\,|}, \tag{21}$$

where

$$q_5 = s_5 \cdot \left(\frac{f_{cm}}{f_0}\right)^{-0.45} \cdot \left|k_h \varepsilon_{sh}^{\infty}\right|^{-0.85}, \tag{22}$$

and

$$\begin{cases} k_h &= 1 - h^3 \\ \varepsilon_{sh}^{\infty} &= \varepsilon_s^{\infty} \times 0.57514 \sqrt{\frac{14}{t_0 + \tau_{sh}} + 3} \\ \tau_{sh} &= \tau_0 \cdot k_{\tau a} \cdot (k_s D)^2 \\ \varepsilon_s^{\infty} &= \varepsilon_{s,cem} \cdot \left(\frac{f_{cm}}{f_0}\right)^{s_{ef}} \\ \tau_0 &= \tau_{s,cem} \cdot \left(\frac{f_{cm}}{f_0}\right)^{s_{\tau f}} \end{cases}. \tag{23}$$

D (mm) is the equivalent thickness of the concrete member. The different parameters s_5, $\varepsilon_{s,cem}$, $s_{\varepsilon f}$, $\tau_{s,cem}$ and $s_{\tau f}$ are given in Table 4. k_{ta} is the aggregate factor, given

TABLE 6 Values of the shape factor k_s for the B4s model.

Specimen shape	k_s
Infinite slab	1.00
Infinite cylinder	1.15
Infinite square prism	1.25
Sphere	1.30
Cube	1.55

in Table 5 and k_s is the shape factor given in Table 6. h (−) is the relative humidity.

$g(t-t_s)$ determines the speed of drying creep and is given by

$$g(t-t_s)=p_{5H}\cdot\left[1-(1-h)\cdot\tanh\left(\sqrt{\frac{t-t_s}{\tau_{sh}}}\right)\right], \quad (24)$$

where p_{5H} is a parameter given in Table 4.

In this study, the adaptation of the B4s model is done using the same approach in the past to extend the B4 model to account for various types of admixtures and aggregates.[30] This approach takes parameters corresponding to normal hardening cement as reference (R) and introduces new scaling factors to account for the material differences. When they are set equal to one, the original B4s model is recovered.

For basic creep, three scaling factors ζ_1, ζ_2 and ζ_4 are introduced in the definitions of q_1, q_2, q_3 and q_4:

$$\begin{cases} q_1 &= \dfrac{p_1\cdot\zeta_1}{E_{cm}} \\ q_2 &= s_2\cdot\zeta_2\cdot\left(\frac{f_{cm}}{f_0}\right)^{-1.58} \\ q_3 &= 0.976\cdot s_2\cdot\zeta_2\cdot\left(\frac{f_{cm}}{f_0}\right)^{-3.19} \\ q_4 &= 4\times10^{-3}\cdot\zeta_4\cdot\left(\frac{f_{cm}}{f_0}\right)^{-1.16} \end{cases}, \quad (25)$$

ζ_1 adjusts Equation (17) for estimating the initial strain due to the loading. ζ_2 and ζ_4 are scaling parameters for the basic creep model corresponding to early age and late age creep, respectively.

For the drying creep, the optimization was done on J_d against the experimental drying creep compliance J_d^{exp}, defined as the difference between the compliance in unsealed conditions J^{exp} and the compliance in sealed conditions J_b^{exp}, for samples loaded at the same age. Due to the change in Young's modulus between sealed and unsealed samples, the experimental drying creep compliances do not start at zero but show an offset in the range of 2–5 μm/m/MPa. This offset had a non-negligible impact on the calibration of the parameters of the model. For this reason, it was removed for each experiment for the optimization process and the model for drying creep compliance was compared to:

$$J_d^{exp}=J^{exp}(t,t_0,t_s)-J_b^{exp}(t,t_0)-\left[J^{exp}(t_0,t_0,t_s)-J_b^{exp}(t_0,t_0,t_s)\right]. \quad (26)$$

For drying creep the scaling factor ζ_5 is introduced in Equation (22):

$$q_5=s_5\cdot\zeta_5\cdot\left(\frac{f_{cm}}{f_0}\right)^{-0.45}\cdot\left|k_h\varepsilon_{sh}^{\infty}\right|^{-0.85}. \quad (27)$$

3.3 | Calibration method

The calibration is done using the experimental results obtained in this study. It was performed by applying the least squares method on the average of the obtained curves.

To avoid experimental biases at early stage, weights were applied to early stage and late stage results. The experimental results were split into two-time intervals delimited by the transition time t_w. This transition time varied with 11 values logarithmically-spaced between (10^{-3} and 50) days. For each transition time, the weight for the early-stage result ω_1 and the weight for the late-stage result $\omega_2=1-\omega_1$ varied between 20% and 80%. For each calculation, different initial guesses were tested to obtain the parameters that correspond to the global minimum of the objective function written as

$$\mathcal{F}_{obj}(params,t_w)=\begin{array}{l}\omega_1\cdot\left(\mathcal{F}^{model}(params,t\le t_w)\right. \\ \left.-\mathcal{F}^{exp}(t\le t_w)\right)^2+\omega_2 \\ \cdot\left(\mathcal{F}^{model}(params,t>t_w)\right. \\ \left.-\mathcal{F}^{exp}(t>t_w)\right)^2,\end{array} \quad (28)$$

where $\mathcal{F}^{model}$ is the tested model, $\mathcal{F}^{exp}$ is the experimental result. *params* are the different parameters of the considered model to be calibrated as described in the previous section. The values of the fitted parameters varied at most by 1.5% for different values of weights and transition times in the objective function for all the experiments. The experimental curves were also calibrated without any weights. The results were always in the range of the weighted results. Hence, the results in the following sections correspond to the parameters obtained by performing the calibration without any weights.

4 | RESULTS

In this part, the experimental results of the different mechanical tests are presented. The creep results are expressed in terms of creep compliance J (μm/m/MPa).

4.1 | Experimental Young's modulus and compressive strength results

Table 7 provides Young's modulus and compressive strength according to EN 12390-13.[27] The specimens subjected to drying showed less change in Young's modulus with time and had a lower Young's modulus compared to the sealed samples. As expected, specimens with larger diameters have higher Young's modulus, when exposed to drying. This is coherent with the fact that the drying of samples with larger diameter takes more time.

4.2 | Experimental shrinkage results of AAS concrete

The experimental shrinkage results in both sealed and unsealed conditions are plotted in Figure 2. It can be seen that autogenous shrinkage is high, as already observed in References 23,24. As discussed in a previous study,[3] this could be because of a higher drop in relative humidity during the first days of reaction. As measured in References 31–33, the internal relative humidity of AAS in sealed conditions can drop by 80% after 7 days, while it remains higher than 90% for cement.[34,35] Thus, the capillary pressure in AAS concrete is higher and causes a higher basic shrinkage. Nevertheless, a few authors indicated that the contribution of capillary pressure cannot explain totally basic shrinkage and that other mechanisms should be considered as the reduction of steric-hydration force[33] and creep effects.[36] Moreover, the contribution of drying shrinkage, defined as the difference between experimental results in unsealed conditions and sealed conditions is relatively low in comparison to OPC concrete. For example, in the B3 model,[14,15] only drying shrinkage is taken into account and basic shrinkage is neglected. Thus, the relative humidity gradient between the inside and outside at age of exposure to drying (7 days) is lower for AAS concrete and this leads to lower drying shrinkage.

TABLE 7 Young's modulus and compressive strength results.

Testing age (d)	Exposure age to drying (d)	Diameter (mm)	Young's modulus (GPa)	Compressive strength (MPa)
7	n.a.	100	27.7	40.9
7	n.a.	150	26.7	43.8
28	n.a.	100	30.3	50.4
28	n.a.	150	30.4	57.8
28	7	100	27.7	51.5
28	7	150	29.7	55.8
100	7	100	26.3	56.5

Note: n.a stands for not applicable.

4.3 | Experimental creep results of AAS concrete

The results of basic creep for different specimen diameters and ages are shown in Figure 3. It can be seen that for samples tested in this study, the effect of diameter is not significant on the basic creep behavior of AAS concrete. This is in accordance with the model hypotheses made in both *fib* MC 2010 and B4s models that do not take the notional thickness, and thus the diameter, as a parameter. The initial creep compliance is lower for older samples. This can be explained by the evolution of Young's modulus between both ages (see Table 7). The creep behavior can be discomposed between early-age and late-age deformations. During the first days after applying the load, the specimens loaded at an age of

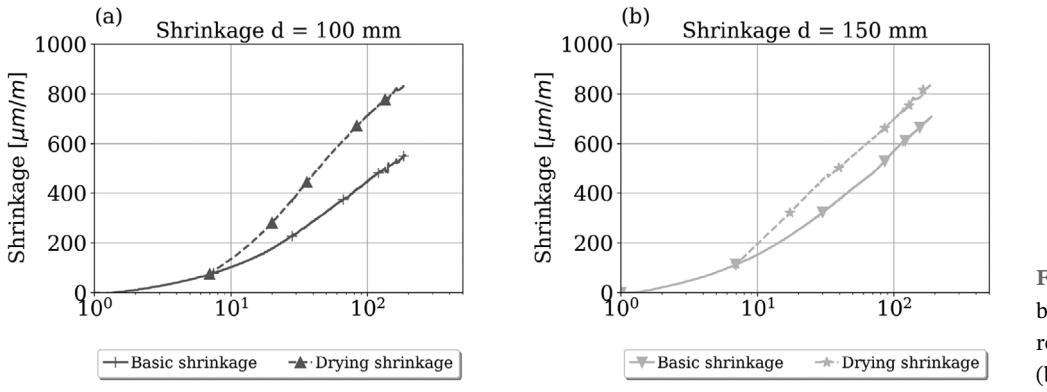

FIGURE 2 Experimental basic and drying shrinkage results (a) for 100 mm diameter (b) for 150 mm diameter.

7 days creep more than the ones loaded at an age of 28 days. This could come from the changes in the microstructure that take place between these ages. Indeed, between 7 and 28 days, as the slag reaction continues, the pore structure becomes denser with smaller pores.[37,38] In particular, at lower degree of reaction, a higher quantity of water in the pore structure is present than after 28 days.[39] This can be put into perspective with the water redistribution in cementitious materials that was observed in Reference 40. The higher water content in the pore structure would induce a higher early-age creep. For the later-age behavior, the rates of creep compliance $L = \frac{dJ}{dt}$ for both 100 and 150 mm diameters and for both loading ages 7 and 28 days are very similar (see Figure 3b). This would support theories that the asymptotic behavior for basic creep depends only on the material as suggested by Vandamme et al.[41] This asymptotic behavior could come from the slipping of C-S-H layers,[42,43] or due to rearrangement of C-S-H, which would result in a reduction of the gel porosity[44] and an increase of the packing density.[41,45] The rate of creep compliance after 100 days for OPC concrete provided in Reference 41 is around 0.05, while it is found to equal 0.13 for AAS in this study. At least two mechanisms could explain the higher creep of AAS. The first one is that the secondary reaction products of AAS are mainly amorphous[46] while portlandite and ettringite, present in OPC concrete as crystalline phases, have a negligible contribution to creep.[47] Hence, with higher amounts of amorphous phases, AAS would creep more. The second explanation could be due to the microstructure of the C-A-S-H gel. Higher uptake of aluminum in the structure, as is the case for AAS in comparison to OPC, increases the amount of bounded water in the C-A-S-H gel.[48] Suwanmaneechot et al.[49] proved that creep increases as the water adsorption thickness increases. For these authors, the mechanism explaining creep is the sliding of C-A-S-H layers. Thus, the higher creep of AAS may be because of more amorphous secondary products and a higher amount of bounded water due to higher aluminum uptake.

The results of drying creep for both 100 and 150 mm diameter specimens are shown in Figure 4. In comparison to basic creep, the creep compliance just after loading for samples loaded at age 7 days is a bit higher (around 2 μm/m/MPa). This comes from the differences in Young's modulus between dried and sealed specimens (see Table 7). As for sealed samples (see Figure 3a), the specimens loaded earlier (i.e., after 7 days) show a much higher increase in compliance from 0 to 10 days (see Figure 4). At later age though, the creep compliance increases much more than the one from sealed samples. The drying creep results for specimens dried after 7 days and loaded after 7, 28 and 100 days, that is, just after drying, 21 days after the start of drying and 93 days after the start of drying, respectively, are shown in Figure 5. It can be seen that the different samples loaded after 7, 28 or 100 days show the same increase in compliance between 10 days and 84 days of loading. In Reference 3 it was already pointed out that the internal drying of AAS is much higher than the one of OPC and that the internal relative humidity drops lower than 85% after 7 days.[33] This means that the moisture gradient with the ambient environment is lower for AAS concrete and that the drying of AAS concrete specimens should be lower than for OPC systems. This would also explain why the difference in drying creep between 100 mm diameter specimens and 150 mm diameter specimens is very low (less than 5 μm/m/MPa after 100 days for loadings at either 7 or 28 days).

The influence of the ratio R_{cr} on creep compliance is plotted in Figure 6 (a). The creep behavior of the sample loaded at 20% of the compressive strength at 28 days $f_{cm,28}$ is very similar to the one loaded at 33% of $f_{cm,28}$. The sample loaded at 60% of $f_{cm,28}$ tends to show higher creep compliance. Such higher creep strains for higher loading have already been reported in the literature for OPC and are explained by the increased formation of microcracks.[50,51] Zhou et al.[21] in past have pointed out that R_{cr} is found to have little influence on the creep coefficient for AAS concrete, which is also evident from

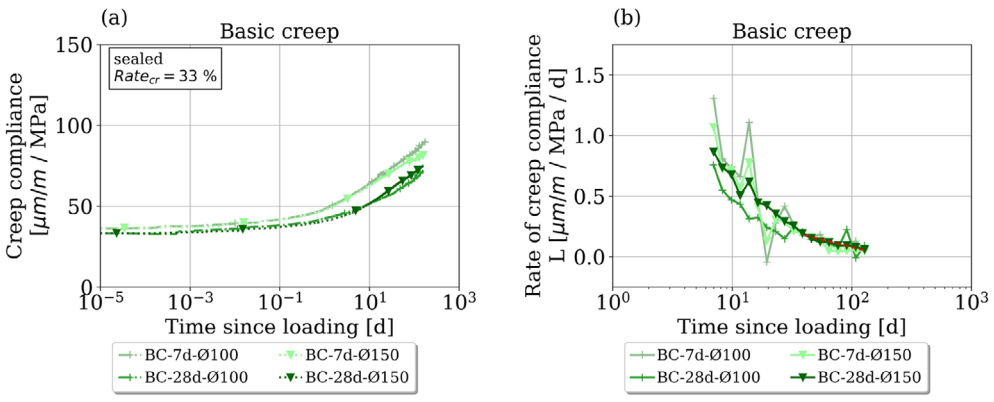

FIGURE 3 Experimental basic creep results for sustained loading from 7 or 28 days with 100 or 150 mm diameters. (a) Creep compliance (b) Rate of creep compliance. On (b) the red line is plotted only to guide the eye.

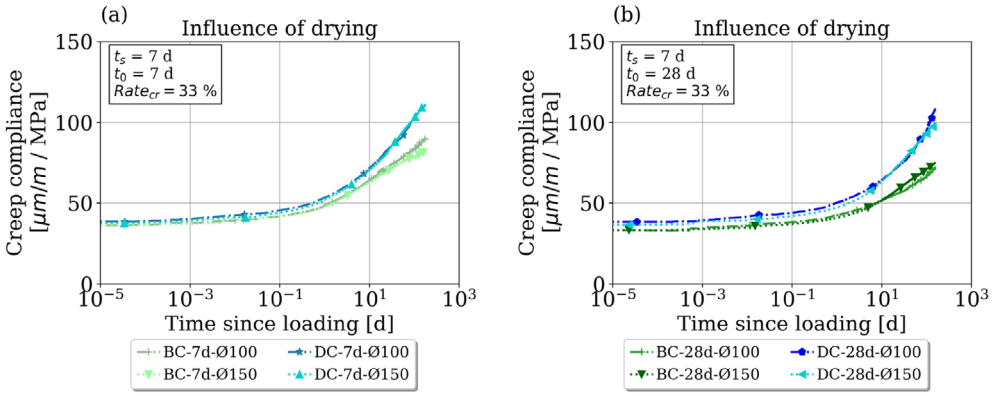

FIGURE 4 Experimental drying creep measured for age of exposure to drying t_s equal to 7 days and loading at ages (a) 7 or (b) 28 days.

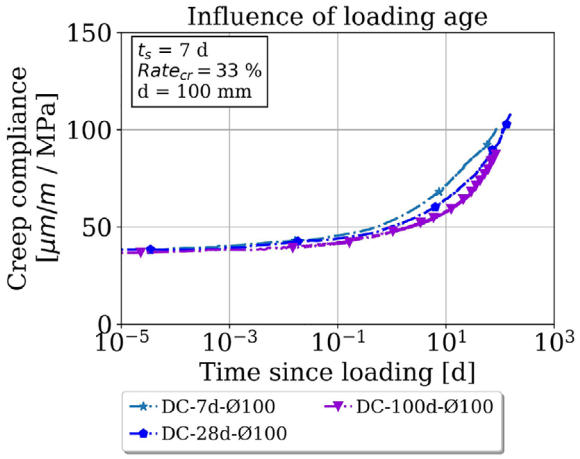

FIGURE 5 Experimental drying creep measured for samples dried from 7 days and loaded at different ages (7, 28 and 100 days).

experimental results from this study as shown in Figure 6 (b). This would mean that despite a higher number of microcracks with higher loads, the creep strain remains linear with R_{cr} up to 60% of the compressive strength. This is contradictory to assumptions made for OPC-based concrete in *fib* MC 2010[52] and B4s model,[30] where the linearity between creep strain and applied load is assumed to be 40% and 45% of the compressive strength, respectively.

5 | CALIBRATION OF CREEP RESULTS FOR AAS WITH EXISTING ENGINEERING MODELS

5.1 | Calibration of creep results for AAS concrete with the *fib* MC 2010

As presented in Section 3, the creep behavior is expressed with the creep coefficient ϕ_{cc} for the *fib* MC 2010. The basic creep coefficient ϕ_{bc} is used for basic creep (Equation 7), while the drying creep coefficient ϕ_{dc} is used for drying creep (Equation 9).

5.1.1 | Calibration of the basic creep results with the *fib* MC 2010

The basic creep model from the *fib* MC 2010 is calibrated for AAS concrete from the results of the specimens BC-7d-Ø100, BC-7d-Ø150, BC-28d-Ø100 and BC-28d-Ø150. The results of the calibration of the *fib* MC 2010 with the Equation (13) are shown in Figure 7 and the calibrated parameters are summarized in Table 8. The original *fib* MC 2010 underestimates the value of the basic creep coefficient by at least factor two. The calibrated extended *fib* MC 2010 as described in Section 3 (Equation 13) underestimates the creep coefficient at early ages. However, at later age, the proposed model is able to capture the basic creep behavior of concrete. The results with the use of the Equation (15) for the calibration for β_{bc} are also given in Figure 7 and Table 8. As expected, the modeled creep coefficient does not start at 0 in comparison to Equation (13). However, the proposed model fits correctly the experimental curves after 10 days of loading. In this case, $\xi_{bc,1}$ characterizes the asymptotic behavior and is in the range (1.7–2.3). The coefficient $\xi_{bc,2}$ is in the range (1.1–1.7) and indicates that the kinetics of creep for AAS concrete is slower than the one of cement.

5.1.2 | Calibration of the drying creep results with the *fib* MC 2010

For drying creep, the calibration was done using the creep results of the samples DC-7d-Ø100, DC-7d-Ø150, DC-28d-Ø100 and DC-28d-Ø150. The use of the equation (Equation 13) with the calibration method presented in Section 3.3 did not allow the convergence of the

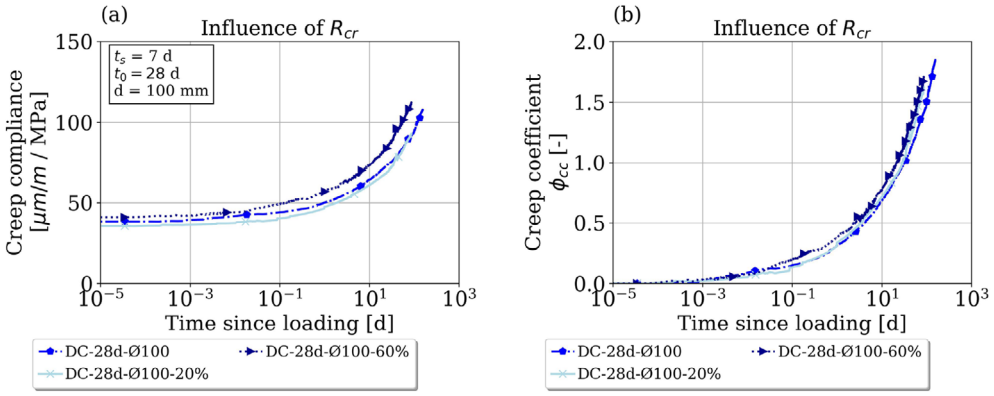

FIGURE 6 Experimental drying creep for samples dried after 7 days and loaded at 28 days at different sustained loads. (a) Creep compliance (b) Creep coefficient.

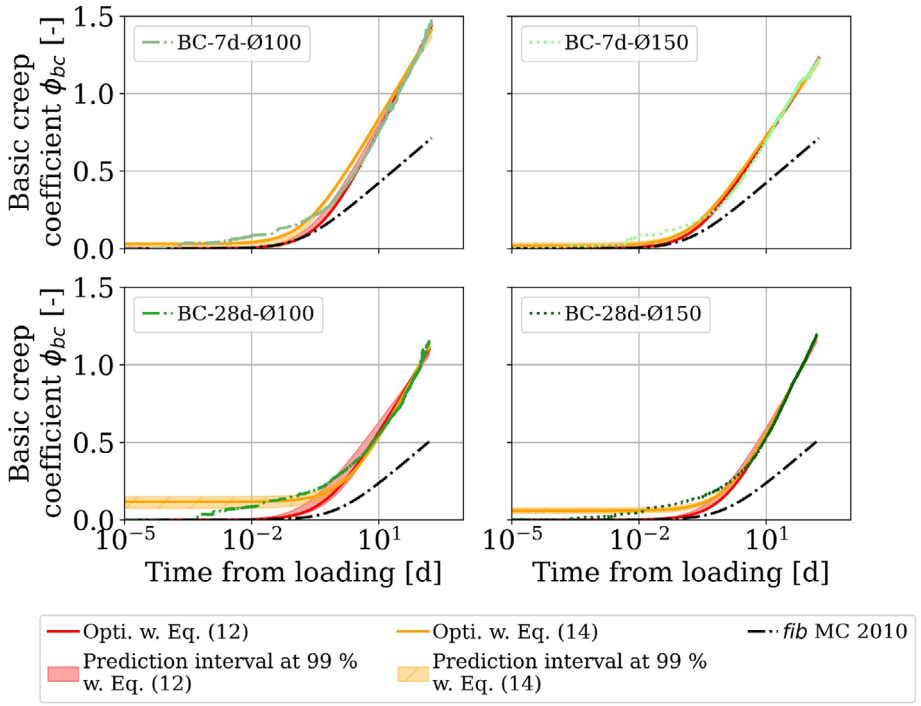

FIGURE 7 Calibration of the basic creep model of the *fib* MC 2010 from experimental results obtained in this study. Calibration is made with both Equations (13) and (15) independently. The prediction intervals correspond to changes in the calibrated parameters from changes in the optimization weights at early stage and late stage.

TABLE 8 Results of the calibration for basic creep with the *fib* MC 2010.

Model Name	Equation (13)		Equation (15)	
	$\xi_{bc,1}$	$\xi_{bc,2}$	$\xi_{bc,1}$	$\xi_{bc,2}$
BC-7d-Ø100	2.37	2.80	1.98	1.15
BC-7d-Ø150	1.81	1.40	1.71	1.11
BC-28d-Ø100	1.96	0.57	2.20	1.68
BC-28d-Ø150	2.39	1.12	2.33	1.28

optimization process, despite trials with several weights and transition times between early-age and late-age. The comparison between the drying creep coefficients ϕ_{dc} from the experiments and the one predicted by the original *fib* MC 2010 are plotted in Figure 8.

At early-age, as explained in Section 4.3, the difference in the creep evolution between sealed and unsealed samples is quite low, resulting in a low drying creep. Up to around 10 days, the drying creep coefficient ϕ_{dc} is overestimated by the *fib* MC 2010. However, after 10 days, the evolution of ϕ_{dc} reaches an asymptotic behavior with a slope higher than predicted by the *fib* MC 2010. These results raise a possible issue on the adaptability of the *fib* MC 2010 to describe the drying creep of AAS with the Equation (8).

In conclusion, the basic creep model of the *fib* MC 2010 can be extended for AAS concrete. After 100 days, the basic creep coefficient is around two times higher for such concrete. For drying creep though, the *fib* MC 2010 could not be adapted with the method proposed in Reference 17.

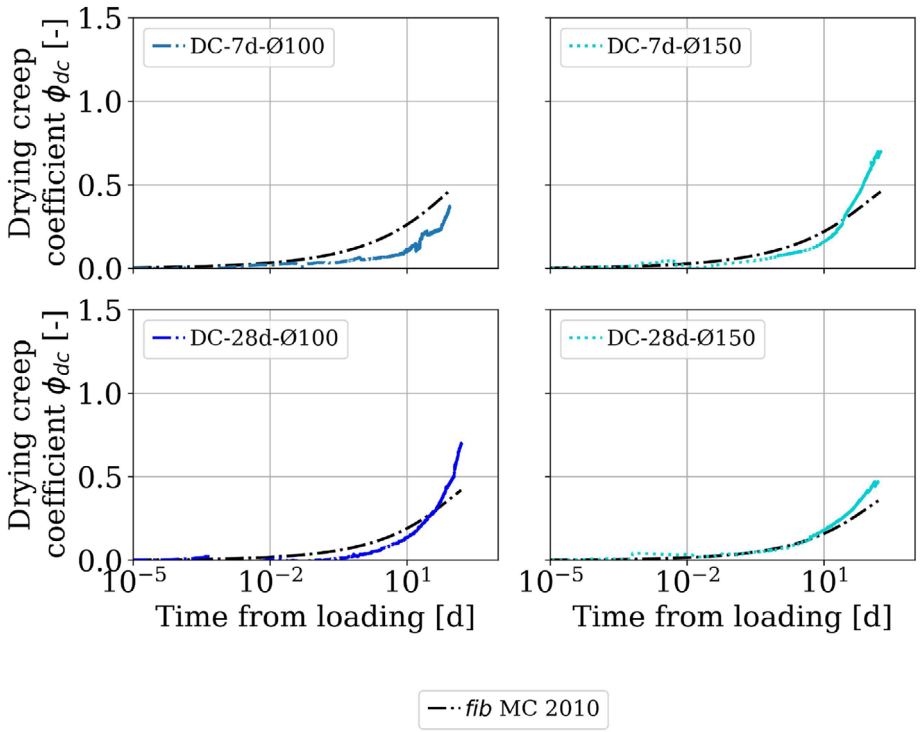

FIGURE 8 Comparison of the drying creep coefficient ϕ_{dc} modeled with the *fib* MC 2010 with the experimental results obtained in this study.

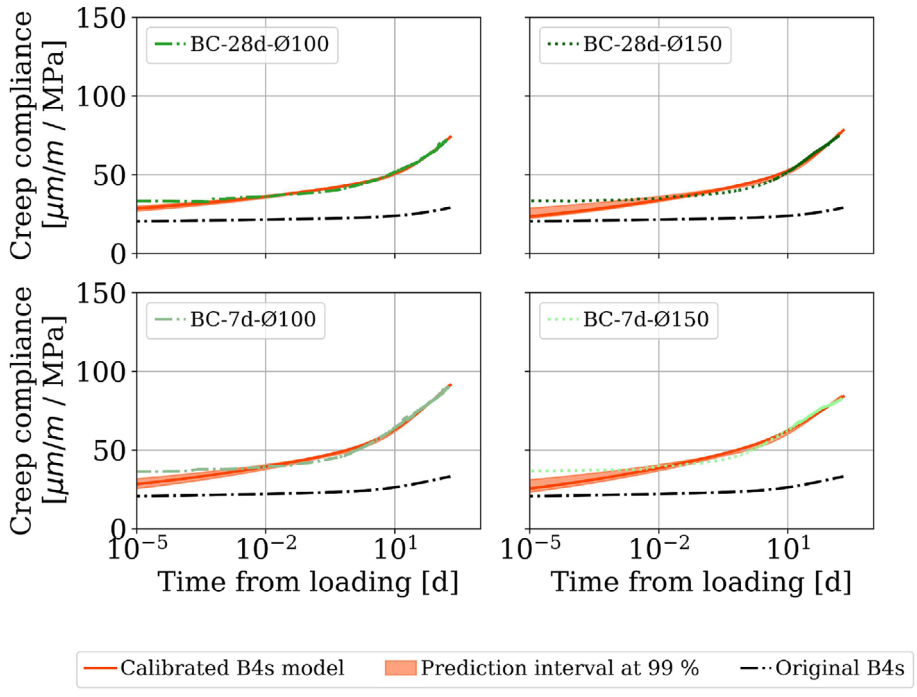

FIGURE 9 Calibration of the basic creep model of the B4s model from experimental results obtained in this study. The prediction interval corresponds to changes in the calibrated parameters from changes in the optimization weights at early stage and late stage.

5.2 | Calibration of creep results for AAS concrete with the B4s model

In the B4s model, the creep behavior is described mathematically by the compliance function, as presented in Section 3 (Equation 16).

5.2.1 | Calibration of the basic creep results with the B4s model

The calibration of the basic creep behavior with the B4s model is plotted in Figure 9 and the corresponding obtained parameters are given in Table 9. The values of

ζ_1 are lower than 1 meaning that the elastic strain due to the initial loading is lower than predicted by the original B4s model. Conversely, the values of ζ_2 are in the range 7–9 indicating that the strain evolution after the loading is relatively higher than for OPC concrete. This indicates that AAS concrete creeps much more in the first hours of loading, in comparison with cement-based systems. The same conclusion could be drawn with an alternative optimization approach where ζ_1 was fixed to 1. In this case, ζ_2 varied between 4.8 and 5.5. For the creep behavior at later-age, ζ_4 values go from 2.24 to 4.01. It means that the creep evolution at late-age is higher than predicted by the B4s model, as was the case for *fib* MC 2010 model. Similar to the *fib* MC 2010, the B4s model can be adapted to describe qualitatively the basic creep behavior of AAS concrete despite much higher values of basic creep.

5.2.2 | Calibration of the drying creep results with the B4s model

As seen in Figure 10, the original B4s model overestimates the drying creep behavior for AAS concrete at the initial stage. However, the appropriate calibration of ζ_5 from Equation (27) provides satisfactory results with the B4s model. The low values of the calibrated parameter ζ_5 (see Table 10) reflect that drying creep is lower in the case of AAS concrete compared to OPC concrete. The lower drying creep for AAS concrete can be attributed to the relatively low external drying due to the relatively low internal humidity of AAS concrete, as explained in Section 4.3.

It should be noted that in comparison to Reference 24, the experimental results of this study did not reach the second part of the characteristic S-curve for creep behavior. This could influence the optimization of ζ_5. For this reason, the results of Table 10 should be referred to with caution.

In conclusion, the B4s model can be extended for AAS concrete for both basic creep and drying creep. The basic creep compliance should be multiplied by a factor between two and three after 100 days. In drying conditions, the extended B4s model describes correctly the creep evolution. Given that the functional forms of the B4s model are based on the solidification theory,[30]

TABLE 9 Results of the calibration for basic creep with the B4s model.

Name	ζ_1	ζ_2	ζ_4
BC-7d-Ø100	0.75	8.1	3.5
BC-7d-Ø150	0.47	9.5	2.2
BC-28d-Ø100	0.98	7.2	4.0
BC-28d-Ø150	0.53	9.7	4.1

TABLE 10 Results of the calibration for drying creep with the B4s model.

Name	ζ_5
DC-7d-Ø100	0.26
DC-7d-Ø150	0.54
DC-28d-Ø100	0.48
DC-28d-Ø150	0.50

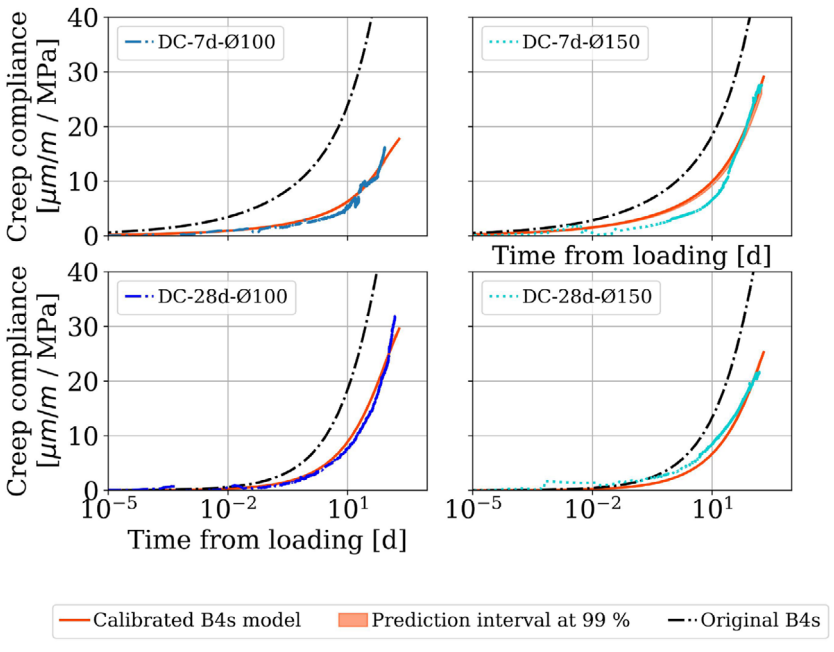

FIGURE 10 Calibration of the additional part of the creep compliance due to drying of the B4s model from the experimental results obtained in this study. The prediction interval corresponds to changes in the calibrated parameters from changes in the optimization weights at early stage and late stage.

this theory could be used in the future to understand the creep behavior of AAS concrete.

6 | CONCLUSION

In this study, new experimental results are presented on the creep of AAS for both sealed and unsealed conditions. The following conclusions can be drawn from this study:

- In comparison to OPC concrete, basic creep is around two times higher after 100 days of loading. The rate of basic creep compliance at late age is also higher for AAS concrete.
- The drying creep of AAS concrete is less significant for AAS concrete for both diameters 100 and 150 mm. It is notably lower than OPC concrete at early-age and this could be explained by a higher internal drying during the chemical reaction between the slag and the alkali solution.
- The linearity of the creep strain with the applied load is valid up to at least 60% of the compressive strength for AAS, while the linearity range is limited to 45% for OPC.
- Both *fib* MC 2010 and B4s models were calibrated from the experimental results presented in this study. Both models could be extended for basic creep. The scaled parameters indicate that AAS concrete creeps around two times more than OPC concrete and that the basic creep rate at late-age is higher.
- For drying creep, the *fib* MC 2010 fails to capture the experimental trend by a simple adaptation of the existing model. A new form function for drying creep would be required to extend the model to AAS concrete. On the contrary, the B4s model was able to correctly capture the drying creep evolution. The scaling factor shows that the drying creep compliance is around two times lower than for OPC concrete.

The above conclusions are subjective to the mix tested in this study. Further studies would be required in the future for varied mix designs and different activator solutions to come up with the appropriate extension of engineering models for AAS concrete.

ACKNOWLEDGMENTS

The project leading to this application has received funding from the European Union's Horizon 2020 research and innovation program under the Marie Skłodowska-Curie grant agreement No 813596. Open Access funding enabled and organized by Projekt DEAL.

CONFLICT OF INTEREST STATEMENT

The authors declare that they have no conflict of interest.

DATA AVAILABILITY STATEMENT

The data that support the findings of this study are available from the corresponding author upon reasonable request.

ORCID

Richard Caron https://orcid.org/0000-0002-5741-6440

REFERENCES

1. Provis JL. Geopolymers and other alkali activated materials: why, how, and what? Mater Struct. 2014;47(1–2):11–25.
2. Garcia-Lodeiro I, Palomo A, Fernández-Jiménez A. 2 - an overview of the chemistry of alkali-activated cement-based binders. In: Pacheco-Torgal F, Labrincha JA, Leonelli C, Palomo A, Chindaprasirt P, editors. Handbook of alkali-activated cements, mortars and concretes. Oxford: Woodhead Publishing; 2015. p. 19–47. https://www.sciencedirect.com/science/article/pii/B9781782422761500022
3. Caron R, Patel RA, Dehn F. Extension of the fib MC 2010 for basic and dryings hrinkage of alkali–activated slag concretes. Struct Concr. 2022;64(48):106107.
4. Fernández-Jiménez A, Puertas F. Structure of calcium silicate hydrates formed in alkaline-activated slag: influence of the type of alkaline activator. J Am Ceram Soc. 2003;86(8):1389–94.
5. Provis JL, Arbi K, Bernal SA, Bondar D, Buchwald A, Castel A, et al. RILEM TC 247-DTA round robin test: mix design and reproducibility of compressive strength of alkali-activated concretes. Mater Struct. 2019;52(5):3683.
6. Komljenović MM, Baščarević Z, Marjanović N, Nikolić V. Decalcification resistance of alkali-activated slag. J Hazard Mater. 2012;233-234:112–21.
7. Komljenović M, Baščarević Z, Marjanović N, Nikolić V. External sulfate attack on alkali-activated slag. Constr Build Mater. 2013;49(7):31–9.
8. Sellin JP, Barthélémy JF, Bondonet G, Cauvin B, Torrenti JM. Delayed deformations of concrete structures: The Savines bridge and the Cheviré bridge. 2015.
9. Bažant ZP, Hon M, Yu Q, Li G-H. Excessive long-time deflections of prestressed box girders. I: record-span bridge in Palau and other paradigms. J Struct Eng. 2012;138:6.
10. Song HW, Kim SH, Byun KJ, Song YC. Creep prediction of concrete for reactor containment structures. Nucl Eng Des. 2002;09(217):225–36.
11. Lundqvist P, Nilsson LO. Evaluation of prestress losses in nuclear reactor containments. Nucl Eng Des. 2011;241(1):168–76.
12. Liu Z, van den Heede P, de Belie N. Effect of the mechanical load on the carbonation of concrete: a review of the underlying mechanisms, test methods, and results. Materials. 2021;14(16):4407.
13. Fu C, Ye H, Jin N, Huang Y. Chloride penetration in reinforced concrete beams under combined sustained loading and drying–wetting cycles. J Mater Civ Eng. 2020;32(4):602.
14. Bazant ZP, Baweja S. Creep and shrinkage prediction model for analysis and design of concrete structures— Model B^3. Mater Struct. 1995;28:357–65.
15. Bazant ZP, Baweja S. Creep and shrinkage prediction model for analysis and design of concrete structures: Model B3. In:

Al-Manaseer A, editor. Adam neville symposium: creep and shrinkage—structural design effects; ACI SP–194. Michigan: American Concrete Institute, Farmington Hills; 2000. p. 1–83.
16. Wendner R, Hubler MH, Bažant ZP. Optimization method, choice of form and uncertainty quantification of model B4 using laboratory and multi-decade bridge databases. Mater Struct. 2015;48(4):771–96.
17. Tošić N, de La Fuente A, Marinković S. Creep of recycled aggregate concrete: experimental database and creep prediction model according to the fib model code 2010. Constr Build Mater. 2019;195:590–9.
18. Wallah S, Rangan B. Low-calcium fly ash-based geopolymer concrete: long term properties. Perth, Australia: Curtin Research Publications. Curtin University of Technology; 2006.
19. Sagoe-Crentsil K, Brown T, Taylor A. Drying shrinkage and creep performance of geopolymer concrete. J Sustainable Cem-Based Mater. 2013;2(1):35–42.
20. Castel A, Foster SJ, Ng T, Sanjayan JG, Gilbert RI. Creep and drying shrinkage of a blended slag and low calcium fly ash geopolymer concrete. Mater Struct. 2016;49(5):1619–28.
21. Zhou X, Wang Y, Zheng W, Chen P, Zeng Y. Effect of stress–strength Ratioon creep property of sodium silicate–based alkali-activated slag concrete. Appl Sci. 2019;9(18):3643.
22. Un CH, Sanjayan JG, San Nicolas R, van Deventer JSJ. Predictions of long-term deflection of geopolymer concrete beams. Constr Build Mater. 2015;94(7):10–9.
23. Ma J, Dehn F. Shrinkage and creep behavior of an alkali-activated slag concrete. Struct Concr. 2017;18(5):801–10.
24. Humad AM, Provis JL, Habermehl-Cwirzen K, Rajczakowska M, Cwirzen A. Creep and long-term properties of alkali-activated Swedish-slag concrete. J Mater Civ Eng. 2021;33(2):635.
25. Provis JL, Winnefeld F. Outcomes of the round robin tests of RILEM TC 247-DTA on the durability of alkali-activated concrete. MATECWeb Conf. 2018;199:02024.
26. DIN EN 12390-3. Prüfung von Festbeton – Teil 3: Druckfestigkeit von Probekörpern; Deutsche Fassung EN 12390-3:2019. Beuth Verlag 2019.
27. DIN EN 12390-13. Prüfung von Festbeton – Teil 13: Bestimmung des Elastizitätsmoduls unter Druckbelastung(Sekantenmodul); Deutsche und Englische Fassung prEN 12390-13:2019. Beuth Verlag 2019.
28. PT1prEN1992-1-1. Eurocode 2: design of concrete structures: part 1–1: general rules and rules for buildings, bridges and civil engineering structures. Brussels: CEN; 2017.
29. Tošić N, de La Fuente A, Marinković S. Shrinkage of recycle daggregate concrete: experimental database and application of fib model code 2010. Mater Struct. 2018;51(5):125.
30. RILEM draft recommendation: TC-242-MDC multi-decade creep and shrinkage of concrete: material model and structural analysis*. Mater Struct. 2015;48(4):753–70.
31. Song C, Choi YC, Choi S. Effect of internal curing by superabsorbent polymers – internal relative humidity and autogenous shrinkage of alkali-activated slag mortars. Constr Build Mater. 2016;123(10):198–206.
32. Jia Z, Yang Y, Yang L, Zhang Y, Sun Z. Hydration products, internal relative humidity and drying shrinkage of alkali activated slag mortar with expansion agents. Constr Build Mater. 2018;158(2):198–207.
33. LiZ LT, Liang X, Dong H, Ye G. Mechanisms of autogenous shrinkage of alkali-activated slag and fly ash pastes. Cem Concr Res. 2020;135:106107.
34. Jensen OM, Hansen PF. Autogenous relative humidity change in silica fume-modified cement paste. Adv Cem Res. 1995;7(25):33–8.
35. Lura P, Jensen OM, van Breugel K. Autogenous shrinkage in high-performance cement paste: an evaluation of basic mechanisms. Cem Concr Res. 2003;33:223–32.
36. Abate SY, Park S, Kim H-K. Parametric modeling of autogenous shrinkage of sodium silicate-activated slag. Constr Build Mater. 2020;262:120747. https://www.sciencedirect.com/science/article/pii/S0950061820327525
37. Collins F, Sanjayan JG. Effect of pore size distribution on drying shrinkage of alkali-activated slag concrete. Cem Concr Res. 2000;30:1401–6.
38. Gruskovnjak A, Lothenbach B, Holzer L, Figi R, Winnefeld F. Hydration of alkali-activated slag: comparison with ordinary Portland cement. Adv Cem Res. 2006;18(3):119–28.
39. Ye H, Radlińska A. Quantitative analysis of phase assemblage and chemical shrinkage of alkali-activated slag. J Adv Concr Technol. 2016;14(5):245–60.
40. Wyrzykowski M, Mcdonald P, Scrivener K, Lura P. Water redistribution within the microstructure of cementitious materials due to temperature changes studied with 1 H NMR. J Phys Chem C. 2017;11(121):27950–62.
41. Vandamme M, Ulm FJ. Nanoindentation investigation of creep properties of calcium silicate hydrates. Cem Concr Res. 2013;52:38–52.
42. Feldman RF. Mechanism of creep of hydrated Portland cement paste. Cem Concr Res. 1972;2:521–40.
43. Vichit-Vadakan W, Scherer G. Beam-bending method for permeability and creep characterization of cement paste and mortar. Proceedings of the 6th international conference on creep, shrinkage and durability mechanics of concrete and other quasi-brittle materials. Cambridge, MA: Elsevier; 2001. p. 27–32.
44. Thomas JJ, Jennings HM. A colloidal interpretation of chemical aging of the C-S-H gel and its effects on the properties of cement paste. Cem Concr Res. 2006;36:30–8.
45. Haist M, Divoux T, Krakowiak KJ, Skibsted J, Pellenq RJM, Müller HS, et al. Creep in reactive colloidal gels: a nanomechanical study of cement hydrates. Phys Rev Res. 2021;3(4):68.
46. Jae Eun O, Monteiro PJM, Jun SS, Choi S, Clark SM. The evolution of strength and crystalline phases for alkali-activated ground blast furnace slag and fly ash-based geopolymers. Cem Concr Res. 2010;40(2):189–96.
47. Li J, ZhangW MPJM. Preferred orientation of calcium aluminosilicate hydrate compacts: implications for creep and indentation. Cem Concr Res. 2021;143(33):106371.
48. Kapeluszna E, Kotwica Ł, Różycka A, Gołek Ł. Incorporation of Al in C-A-S-H gels with various Ca/Si and Al/Si ratio: microstructural and structural characteristics with DTA/TG, XRD, FTIR and TEM analysis. Constr Build Mater. 2017;155:643–53.

49. Suwanmaneechot P, Aili A, Maruyama I. Creep behavior of C-S-H under different drying relative humidities: interpretation of microindentation tests and sorption measurements by multi-scale analysis. Cem Concr Res. 2020;132(1):106036.
50. Rossi P, Tailhan JL, Le Maou F, Gaillet L, Martin E. Basic creep behavior of concretes investigation of the physical mechanisms by using acoustic emission. Cem Concr Res. 2012;42(1):61–73.
51. Tasevski D, Ruiz MF, Muttoni A. Analogy between sustained loading and strain rate effects on the nonlinear creep response of concrete. In: Hellmich C, Pichler B, Kollegger J, editors. Concreep 10. Reston, VA: American Society of Civil Engineers; 2015. p. 1187–93.
52. FIB. *fib* model code for concrete structures 2010. Lausanne: International Federation for Structural Concrete (fib); 2013.

AUTHOR BIOGRAPHIES

Richard Caron, Institute of Building Materials and Concrete Structures, Karlsruhe Institute of Technology (KIT), 76131 Germany. Email: richard.caron@kit.edu.

Ravi A. Patel, Institute of Building Materials and Concrete Structures, Karlsruhe Institute of Technology (KIT), 76131 Germany. Email: ravi.patel@kit.edu.

Frank Dehn, Institute of Building Materials and Concrete Structures, Karlsruhe Institute of Technology (KIT), 76131 Germany. Email: frank.dehn@kit.edu.

How to cite this article: Caron R, Patel RA, Dehn F. Experimental study on basic and drying creep for an alkali-activated slag concrete and comparison with existing creep models. Structural Concrete. 2023. https://doi.org/10.1002/suco.202300134

Paper 3

Activation kinetic model and mechanisms for alkali-activated slag cements

Publisher's version

Published in *Construction and Building Materials*

Volume 323, 2022, 126577

DOI: 10.1016/j.conbuildmat.2022.126577

Authors: **Richard Caron**, Ravi A. Patel, Frank Dehn

Construction and Building Materials 323 (2022) 126577

Contents lists available at ScienceDirect

Construction and Building Materials

journal homepage: www.elsevier.com/locate/conbuildmat

Activation kinetic model and mechanisms for alkali-activated slag cements

Richard Caron [a,b,*], Ravi A. Patel [a,b], Frank Dehn [a,b]

[a] Institute of Building Materials and Concrete Structures (IMB), Karlsruhe Institute of Technology (KIT), DE-76131 Karlsruhe, Germany
[b] Materials Testing and Research Institute Karlsruhe (MPA), Karlsruhe Institute of Technology (KIT), DE-76131 Karlsruhe, Germany

ARTICLE INFO

Keywords:
Kinetic model
Alkali-activated slag
Waterglass
Calorimetry
Single-particle model

ABSTRACT

A new model for reaction kinetics of waterglass-activated slag cements based on calorimetry results has been proposed. The model is based on solid-state kinetic models for single-particle kinetics. It accounts for the different mechanisms during alkali-activation of slag with waterglass considering successive application of single-particle models. The process of alkali-activation of slag with waterglass typically consists of two accelerated periods, separated by an induction period. The first accelerated period is described by the succession of a nucleation and growth process and a contraction volume process and the second accelerated period is described by the succession of a nucleation and growth process, a contraction volume process and a diffusion process. The induction period is described by zero-order kinetics signifying that the dissolution of slag does not stop during this period. The model has been tested against both newly measured experimental data and a comprehensive dataset extracted from the literature to cover wide ranges of slag composition and waterglass solutions. The model is found to successfully describe a wide range of experimental data with R^2 values greater than 0.95 for all datasets. In addition, detailed justification is provided on the choice of the mechanisms proposed in the model together with different hypotheses laid in literature and observations made on microstructure development. Finally, correlations between mix characteristics and parameters of the model are proposed. Interpretations of these correlations seem to be pertinent with experimental observations such as the importance of the pH of the solution on the kinetics, the role of silicon ions as nucleation sites and low apparent activation energies for the diffusion governing step.

1. Introduction

Blast furnace slag is a by-product of steel production and is widely used in the concrete industry. Its main components are CaO, SiO_2, Al_2O_3 and MgO. In comparison to cement, it contains less CaO, and more SiO_2 and Al_2O_3, with various ranges of MgO. Blast furnace slag belongs to the group of precursors that can react with an alkali solution to give a hardening material, such as cement [1]. Examples of such alkali solutions are sodium hydroxide (NaOH), waterglass (Na_2SiO_3) or sodium carbonate (Na_2CO_3). Alkali-activated slag concretes can present appreciable properties such as good mechanical strength, low permeability and good resistance to chemical attacks [1–4].

The reaction products forming in these materials are different from that of Portland cement hydration. An aluminum substituted calcium silicate hydrate (C-A-S-H) with relatively low Ca/Si ratios and uptake of aluminum ions in the polymer network is typically formed as the main binding phase [5]. Mg-rich phases such as layered double hydroxides were identified as secondary reaction products, depending on the amount of MgO in the slag [6]. Zeolite phases like gismondine were also reported [7]. Slag activated with waterglass was shown to present higher compressive strengths than when using other alkali-activators [8,9]. This is associated with the nature of the reaction products formed, and its influence on the pore structure of the material [10].

Studying the kinetics of the chemical reaction gives insights into the potential reactivity of slag at given activation conditions, and thereafter the strength development process [11]. Nevertheless, due to the variety of slag compositions and parameters that can be modified to produce different activating solutions, there is no consensus about how best to predict the evolution of the degree of reaction, formed phases, microstructure, and consequently, the mechanical and durability performances that these materials can develop as a function of mix design and reaction kinetics.

This paper focuses on modeling the degree of reaction of alkali-activated slag via experimental results from isothermal calorimetry. Isothermal calorimetry curves are highly dependent on the activator type used for the activation. Shi & Day [12] described the calorimetry

* Corresponding author at: Institute of Building Materials and Concrete Structures (IMB), Karlsruhe Institute of Technology (KIT), DE-76131 Karlsruhe, Germany.
E-mail addresses: richard.caron@kit.edu (R. Caron), ravi.patel@kit.edu (R.A. Patel), frank.dehn@kit.edu (F. Dehn).

https://doi.org/10.1016/j.conbuildmat.2022.126577
Received 26 July 2021; Received in revised form 16 January 2022; Accepted 21 January 2022
Available online 1 February 2022
0950-0618/

Table 1
Chemical composition of the anhydrous slag.

Oxide	CaO	SiO_2	Al_2O_3	MgO	Na_2O	P_2O_5	K_2O	TiO_2	MnO	Fe_2O_3	Others
Mass (%)	38.8	36.3	12.8	7.95	0.34	0.02	0.6	0.96	0.29	0.62	2.5

curves of activation of slag with waterglass with an initial peak for the dissolution and wetting of slag particles followed by two accelerated reaction peaks. Fernandez-Jimenez et al. [13] studied the activation of slag with different alkali solutions, in particular waterglass. Based on their experimental data, they model the kinetic mechanisms of slag activation with waterglass from the second acceleration peak following the model from Parrot & Killoh [14]. This model is widely used for cement hydration and considers the three mechanisms viz. nucleation and growth, phase boundary interaction and diffusion processes, which occur in parallel. In this model, at a given time, the governing-kinetic mechanism is the one with the lowest rate. Zuo & Ye [15] proposed a model for NaOH activated slag in which the calorimeter curves are separated into the three reaction stages similar to Fernandez-Jimenez et al. [13]. Park et al [16] proposed two models to explain the reaction of slag with alkali solution: first, the mass conservation considering phase transformation; second, hygro-chemical reactions considering chemical affinity. However, these models are applicable only after one day and do not capture early-stage kinetics. Finally, due to the presence of two accelerated periods for the activation of slag by waterglass, some authors [17,18] split the obtained calorimetric curve in two, to separate both peaks and fit each of the curves on the empirical exponential model proposed in [19].

In the present contribution, a new model is proposed for inferring reaction kinetics and mechanisms using calorimeter data. It is considered that the calorimetric curve represents the kinetic of waterglass-activated slag with successive sets of single-particle solid-state kinetic models. This approach with a succession of kinetic governing mechanisms has been previously proposed for cement hydration [20]. In such a model, the conversion factor for each successive governing-kinetic mechanism is rescaled and a reaction mechanism only starts at the end of the previous mechanism. The model proposed in the present study is calibrated and validated against a wide range of experiments described in the literature. These experiments cover several possibilities of mix designs and are completed with two new waterglass-activated slag mix designs investigated experimentally in this study. These two mix designs are of practical importance as they provide stable concrete mixes with comparable strengths and suitable workability. Finally, a detailed justification on the choices of mechanisms used in the model and correlations of model parameters with the composition of slag and activators are presented. The clear advantage of the proposed model is that it is mathematically consistent, it provides insights into mechanisms and it captures both accelerated periods. The content of this paper is organized as follows. Section 2 details calorimeter data from both new measurements and measurements extracted from the literature. The newly developed hydration kinetics model along with the calibration process is described in Section 3. Finally, results and general discussions are presented in Section 4 and 5 and the conclusions are given in Section 6.

2. Isothermal calorimetry data

In this work, isothermal calorimetry data are obtained from two source types; the first one consists of new experiments performed in course of this study and the second consists of data extracted from existing literature sources.

2.1. Material and sample preparation

For the experimental study, a ground blast furnace slag obtained from the Dutch company Ecocem was used. Its elementary composition was determined by a M4 Tornado (Bruker GmbH Karlsruhe, Germany) using an energy dispersive X-ray fluorescence (XRF) spectrometer. The result is given in Table 1.

Table 2
Mix parameters of the experiments led in this study.

Parameter	Mix hS	Mix lS
water/slag [kg/kg]	0.4	0.4
n [g/100 g slag]	5.0	5.0
M_S [mol/mol]	2.2	0.5

For the activation, two alkaline solutions were used in the experiments. Both mixes have the same water/slag ratio w/s of 0.4, the same sodium oxide content: $n = 5.0$ [g/100 g slag] but different silica modulus $M_S = SiO_2/Na_2O$ [mol/mol], 0.5 (mix lS) and 2.2 (mix hS). Indeed, pretests led at the lab showed that the setting time was very short for mixes with M_S between 0.8 and 1.8 with this slag. A summary of the mix parameters can be found in Table 2. Both solutions were obtained by mixing a solution of NaOH, waterglass and distilled water. The NaOH solution had a solute mass concentration of 50 %. Waterglass was provided by Woellner (Betol39T, of solute concentration of 34.5 %, with a molar ratio $M_{S,raw} = 3.4$ [mol/mol]). The solutions were prepared and cooled down at room temperature for 24 h before being mixed with the slag to reach the temperature equilibrium with the surrounding environment (20 °C).

2.2. Measurement technique

The isothermal calorimetry measurements were obtained using an eight-channel TAM Air isothermal calorimeter (TA Instruments, USA) at a temperature of 20 °C.

Around 100 g of paste was prepared outside of the calorimeter for each mix. The mixing time was 2 min, and the paste was homogenized with a vibration table at 50 Hz for 30 s. Two samples per mix of around 5 g each were put inside the calorimeter. Less than 5 min were spent between the first contact of slag with the solution and the final closure of the channel of the calorimeter. Due to the initial instability of the calorimeter, the first data reported is only after 20 min. The measurements were carried out for seven days to get the cumulative heat release $Q(t)$. From it, the degree of reaction α can be interpreted by normalizing it with the maximum heat release Q_{max}:

$$\alpha = \frac{Q(t)}{Q_{max}} \tag{1}$$

2.3. Exploitation of data from the literature

A comprehensive data set of 34 results from isothermal calorimetry was created to evaluate the model against the mix parameters. Data were extracted from the literature [11,17,18,21–25]. They cover large domains of slag compositions with slag quality coefficients $\frac{CaO+MgO}{SiO_2}$ varying from 1.28 to 1.57, different alkali solutions (water/binder w/b, n and M_S) and also temperature variations. The ranges for the first four parameters are summed up in Fig. 1.

3. Model for reaction kinetics

This section provides details of the newly developed reaction kinetic model, including assumptions made and appropriate justifications. The

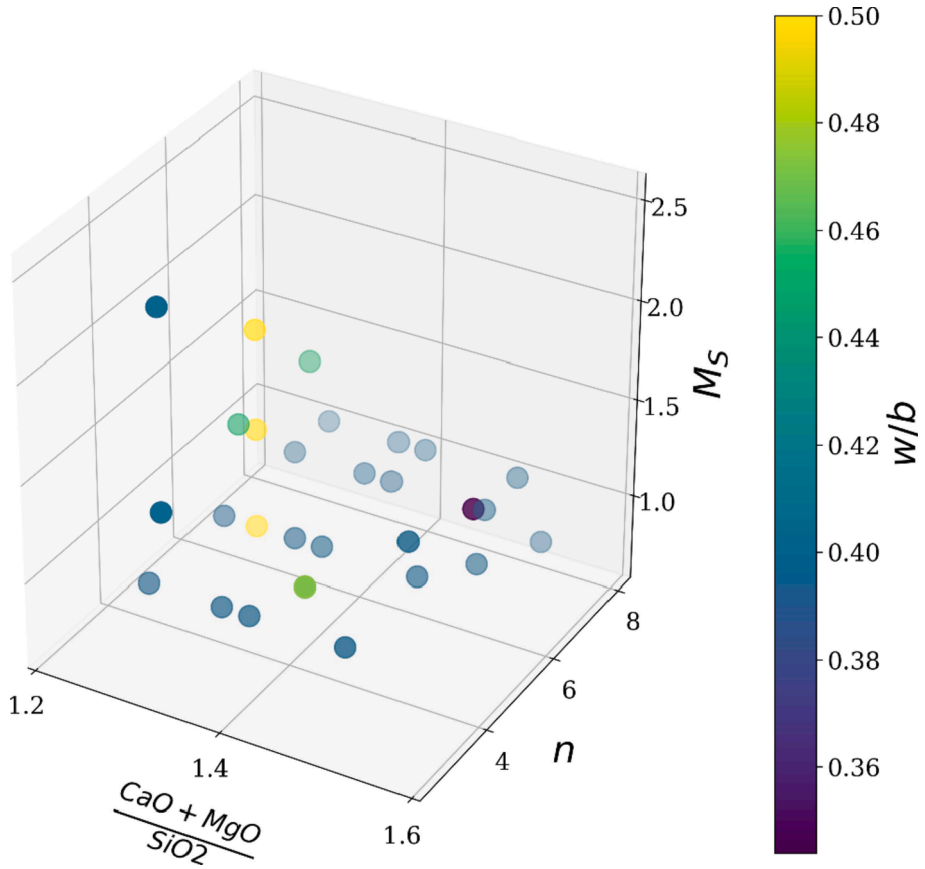

Fig. 1. Parameter ranges of the mixes extracted from the literature.

section ends with details on the implementation of the developed model and adapted calibration procedure.

3.1. Proposed model

The key idea in the developed model is to split the evolution of the degree of reaction into a certain number of steps with each step describing one governing kinetic mechanism. Each mechanism is described by a corresponding function $f(\alpha)$ [-] linking the degree of reaction (α [-]) and its derivative ($\frac{d\alpha}{dt}[h^{-1}]$) through the reaction rate (k $[h^{-1}]$):

$$f(\alpha) = \frac{1}{k}\frac{d\alpha}{dt} \tag{2}$$

Details on the derivation of single-particle models and their physical implications in terms of mechanisms can be found in [26]. The transitions between these steps are taken into account through an overlapping area called transition zone. According to Gebregziabiher et al. [11], nucleation of C-A-S-H occurs during the first hours of the reaction. After the very first hours, Song & Jennings [27] show that the concentration of silicon species decreases drastically. The formation of further binding gel seems then to be controlled by the dissolution of the slag, dependent on the boundary zone between the slag particle and the solution. Zuo & Ye [23] explain the induction period after the first peak by the slow dissolution of silicon. Given the fact that this period presents a constant heat flow, it is modeled here by a reaction with a constant rate. The second peak is often associated with the nucleation and the precipitation of another C-A-S-H gel around the particles. This is followed by a contraction volume process due to the reduction of the surface contact between the slag particles and the surrounding solution and finally by the diffusion through a product layer formed around the slag [13,28]. This succession of governing mechanisms for the second peak is analogous to the hydration of ordinary Portland cement systems [14,29].

Table 3
Equations of solid-state kinetic models used to explain activation of slag with waterglass.

Model	Differential form $f(\alpha) = \frac{1}{k}\frac{d\alpha}{dt}$
Avrami-Erofeyev	$4(1-\alpha)[-\ln(1-\alpha)^{3/4}]$
Contracting volume	$3(1-\alpha)^{2/3}$
Zero-order	1
Ginstling-Brounshtein	$\frac{3}{2((1-\alpha)^{-1/3}-1)}$

In summary, after the early dissolution of slag, the reaction mechanisms of slag activated by waterglass can be conceptualized as a sequence of the following steps 1) nucleation and growth 2) phase boundary interaction 3) induction period 4) nucleation and growth 5) phase boundary interaction 6) diffusion. The equations used to model the mechanisms in this paper can be found in Table 3: the nucleation and growth mechanisms are modeled by the Avrami equation, the phase boundary interactions by the contraction volume equation, the induction period kinetics by a constant rate reaction and the diffusion process by the Ginstling-Brounshtein equation [26]. A discussion about the use of the Ginstling-Brounshtein equation instead of the Jander equation can be found in [30]. An example of the decomposition of the calorimetry curve is presented in Fig. 2. The transition from one reaction mechanism to another is described using sigmoidal functions.

The governing equation for the proposed rate model is written as:

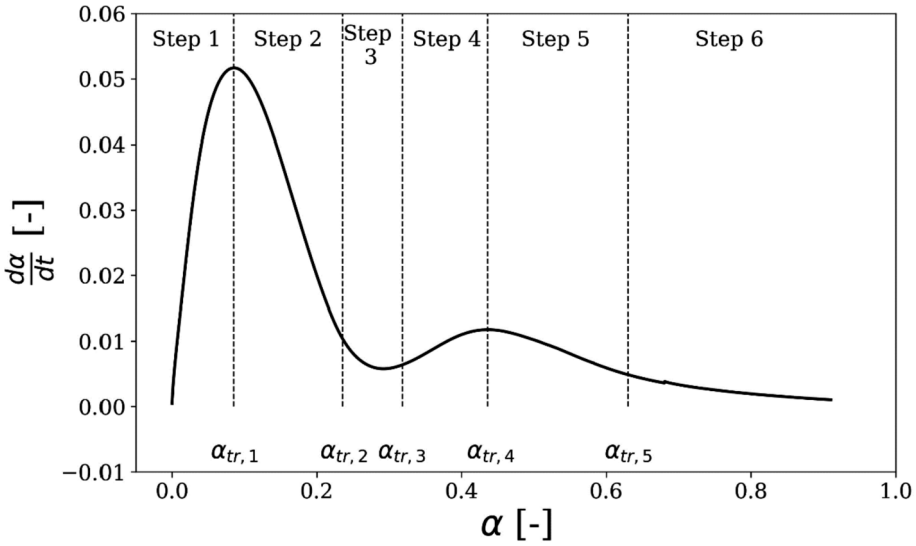

Fig. 2. Scheme of the reaction steps identifiable in an isothermal calorimetry curve of alkali-activated slag cement: example of the mix hS. Each step is delimited by the transition degrees of reaction $\alpha_{tr,i} (1 \leq i \leq 5)$

$$\frac{d\alpha}{dt} = \sum_{i=1}^{M} \left[(\alpha_{i,1} - \alpha_{i,0}) k_i f_i \left(\frac{\alpha - \alpha_{i,0}}{\alpha_{i,1} - \alpha_{i,0}} \right) \cdot Sigm(\alpha, \alpha_{tr,i-1}, \lambda_{i-1}) \cdot (1 - Sigm(\alpha, \alpha_{tr,i}, \lambda_i)) \right]$$

$$Sigm(\alpha, \alpha_{tr,i}, \lambda_i) = \frac{1}{1 + \exp(-\lambda_i(\alpha - \alpha_{tr,i}))} \quad (3)$$

where α is the overall degree of reaction. For each step i, f_i is the functional form of the governing mechanism as described in Table 3, k_i is the kinetic rate for each mechanism, $\alpha_{i,0}$ and $\alpha_{i,1}$ define the degrees of reaction at which the governing kinetic mechanism of the i^{th} step goes from 0 to 100 %. $Sigm(\alpha, \alpha_{tr,i}, \lambda_i)$ is the sigmoidal function used to describe the transition from step i to step (i + 1). $\alpha_{tr,i}$ and λ_i are the parameters controlling the shape of the sigmoidal curve and in turn the region of the overlap.

The overall degree of reaction α is obtained from the calorimetric curve. To convert the calorimeter curve to the degree of reaction, the maximum heat release Q_{max} is obtained by fitting the exponential model to the calorimetry curve [19]. The exponential model is defined as:

$$Q(t) = Q_{max} \exp\left(- \left[\frac{\tau}{t} \right]^{\beta} \right) \quad (4)$$

where τ is a reaction time parameter and β is the reaction slope parameter. Due to the presence of two peaks for activation with waterglass, the above equation is used only from the start of the second peak $t_{st,2}$:

Table 4
Hypotheses made on the local conversion factors.

Reaction step number	Physical mechanism	$\alpha_{i,0}$	$\alpha_{i,1}$
1	Nucleation and growth	0	$\alpha_{tr,1}/0.523$
2	Volume contraction	$\alpha_{1,90\%}$	Calculated with Eq. (9)
3	Induction period	$\alpha_{2,90\%}$	$\alpha_{4,10\%}$
4	Nucleation and growth	$\alpha_{3,90\%}$	$\frac{\alpha_{tr,4}}{0.523} - 0.912\alpha_{4,0}$
5	Volume contraction	$\alpha_{4,90\%}$	Calculated with Eq. (9)
6	Diffusion	$\alpha_{tr,4}$	1

$$Q(t - t_{st,2}, t \geq t_{st,2}) - Q(t = t_{st,2}) = Q_{\infty} \exp\left(- \left[\frac{\tau}{t - t_{st,2}} \right]^{\beta} \right) \quad (5)$$

The heat release accumulated before the beginning of this second peak $Q(t = t_{st,2})$ is then added to Q_{∞} to obtain the maximum heat release Q_{max}. And the degree of reaction is then defined as in (1). The evolution of the degree of reaction is split into steps during which one kinetic-controlling mechanism is predominant. A mechanism is called kinetically predominant for a certain range of degree of reaction when it models more than 99 % of the curve. By hypothesis, each step i $(1 \leq i \leq 6)$, starting from the overall degree of reaction $\alpha_{tr,i-1}$ and ending at the overall degree of reaction $\alpha_{tr,i}$, presents only one predominant mechanism between $\alpha_{i,10\%} = \alpha_{tr,i-1} + 0.1 \cdot (\alpha_{tr,i} - \alpha_{tr,i-1})$ and $\alpha_{i,90\%} = \alpha_{tr,i-1} + 0.9 \cdot (\alpha_{tr,i} - \alpha_{tr,i-1})$. Between $\alpha_{tr,i-1}$ and $\alpha_{i,10\%}$, both mechanisms i^{th} and $(i\text{-}1)^{th}$ occur simultaneously, except for i = 0 where only the first mechanism is present. Similarly, between $\alpha_{i,90\%}$ and $\alpha_{tr,i}$, both mechanisms i^{th} and $(i + 1)^{th}$ occur simultaneously, except for i = 6 where only the last mechanism is present.

The proposed model considers that each kinetic-controlling mechanism has its own local conversion factor α_i $(1 \leq i \leq 6)$, rescaled from the overall degree of reaction:

$$\alpha_i = \frac{\alpha - \alpha_{i,0}}{\alpha_{i,1} - \alpha_{i,0}} \quad (6)$$

The hypotheses on the local conversion factors are the following:

1. Both nucleation and growth processes (1st and 4th steps) are modeled with the Avrami function until the corresponding equation reaches its maximum (corresponding to a conversion factor $\alpha_{max-A4} \approx 0.523$). Solving (6) with $\alpha_i = 0.523$ for $\alpha = \alpha_{tr,i}$, it can be derived (with $\alpha_{1,0} = 0$):

$$\alpha_{1,1} = \alpha_{tr,1}/0.523 \quad (7)$$

$$\alpha_{4,1} = \frac{\alpha_{tr,4}}{0.523} - 0.912\alpha_{4,0} \quad (8)$$

2. Ends of volume contraction models (i = 2 or i = 5) are constrained by the mathematical form of the model (see Table 3). With $\alpha_{i,10\%}$ and $\alpha_{i,90\%}$, and their derivative $\dot{\alpha}_{i,10\%}$ and $\dot{\alpha}_{i,90\%}$ given by the form of the curve:

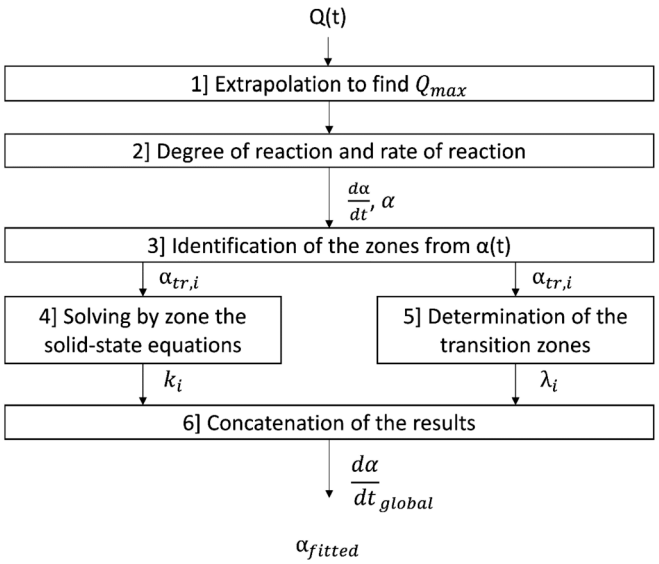

Fig. 3. Implemented numerical scheme from the extraction of the calorimetry curve. The overall degree of reaction is computed and then split into local conversion factors for each step. Single-particle models are fitted on these local conversion factors. The transition zones are optimized with sigmoidal functions. Finally, the fitted degree of reaction is obtained.

$$\alpha_{i,1} = \frac{\alpha_{i,10\%} * \dot{\alpha}_{i,90\%}^{\frac{2}{3}} - \alpha_{i,90\%} * \dot{\alpha}_{i,10\%}^{\frac{2}{3}}}{\dot{\alpha}_{i,90\%}^{\frac{2}{3}} - \dot{\alpha}_{i,10\%}^{\frac{2}{3}}} \tag{9}$$

3. The start of the diffusion process coincides with the transition zone between the reaction steps 4 and 5 (maximum of the second peak).

$$\alpha_{6,0} = \alpha_{tr,4} \tag{10}$$

This is motivated by the fact that the rate of reaction for $\alpha_{6,0}$ diverges to the infinite (see Table 3).

The different scaling hypotheses are summed up in Table 4.

The optimization of each rate coefficient $\frac{d\alpha}{dt_i}$ $(1 \leq i \leq 6)$ is performed on the domain $[\alpha_{i,10\%}, \alpha_{i,90\%}]$, where the kinetic is governed by one predominant mechanism by hypothesis:

$$\frac{d\alpha}{dt}_i = (\alpha_{i,1} - \alpha_{i,0}) * k_i * f_i(\alpha_i) \tag{11}$$

with $f_i(\alpha_i)$ the functions describing the mechanism occurring in step i.

The transition from step i to step i + 1 $(1 \leq i \leq 6)$ can lead to a discontinuous rate of reaction. To reduce the mathematical discontinuity and to pass consistently from a reaction step to another, the sigmoidal function is used:

$$Sigm(\alpha, \alpha_{tr,i}, \lambda_i) = \frac{1}{1 + \exp(-\lambda_i(\alpha - \alpha_{tr,i}))} \tag{12}$$

with λ_i the parameter describing the velocity of the transition and $\alpha_{tr,i}$ the transition degree of reaction between two successive steps. Note that $Sigm(\alpha, \alpha_{tr,i}, \lambda_i)$ increases from 0 to 1 and corresponds to the start of step (i + 1), while $1 - Sigm(\alpha, \alpha_{tr,i}, \lambda_i)$ decreases from 1 to 0 and corresponds to the end of step i. Thus, around a transition degree of reaction $\alpha_{tr,i}$ the kinetic-governing mechanism during step i progressively vanishes and the kinetic-governing mechanism during step (i + 1) appears, both phenomena occurring with the same speed.

3.2. Calibration of the proposed model

The proposed model follows a six-step algorithm (see Fig. 3). After extrapolating the final heat release from the start of the second peak (Eq. 5), the degree of reaction α and its derivative $\frac{d\alpha}{dt}$ are computed. By convention, $\alpha_{tr,0} = 0$ and $\alpha_{tr,6} = 1$. $\alpha_{tr,1}$ corresponds to the local maximum of the first peak and $\alpha_{tr,4}$ corresponds to the local maximum of the second peak. $\alpha_{tr,2}$ and $\alpha_{tr,3}$ are obtained from the local minimum α_{min} between the two peaks (the notation $\dot{\alpha}$ indicates the measured derivative in function of time of the degree of reaction):

$$\dot{\alpha}_{tr,2} = \dot{\alpha}_{min} + C_1(\dot{\alpha}_{tr,1} - \dot{\alpha}_{min}) \tag{13}$$

$$\dot{\alpha}_{tr,3} = \dot{\alpha}_{min} + C_2(\dot{\alpha}_{tr,4} - \dot{\alpha}_{min}) \tag{14}$$

with $C_1 = 0.10$ and $C_2 = 0.10$. $\alpha_{tr,5}$ is given by the user and marks the beginning of the diffusion kinetic-controlled mechanism. It corresponds to the change of slope in the curve $\frac{d\alpha}{dt}$ in function on α from the deceleration period of the second peak. Through initial fitting, it was found that variability of 5 % around the optimized value for $\alpha_{tr,5}$ did not lead to big discrepancies in the result.

To ensure the condition that only one mechanism is dominant at

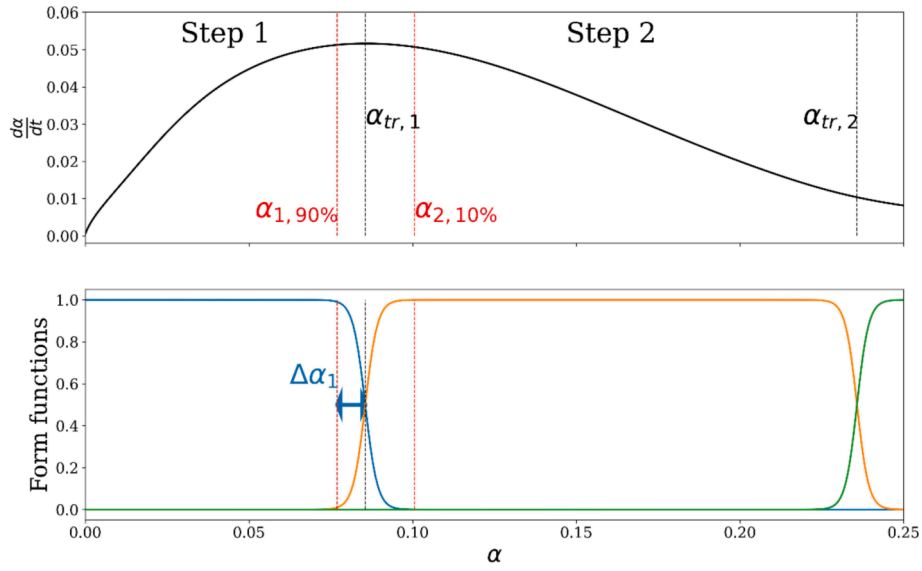

Fig. 4. Above: reaction rate in function of degree of reaction for the mix hS, zoom on both steps 1 and 2. Below: Form functions are built using sigmoidal functions. It allows to take into account the transition zone of width $2{\cdot}\Delta\alpha_1$: here, since step 1 is narrower than step 2 in terms of overall degree of reaction, $\Delta\alpha_1 = \alpha_{tr,1} - \alpha_{1,90\%}$.

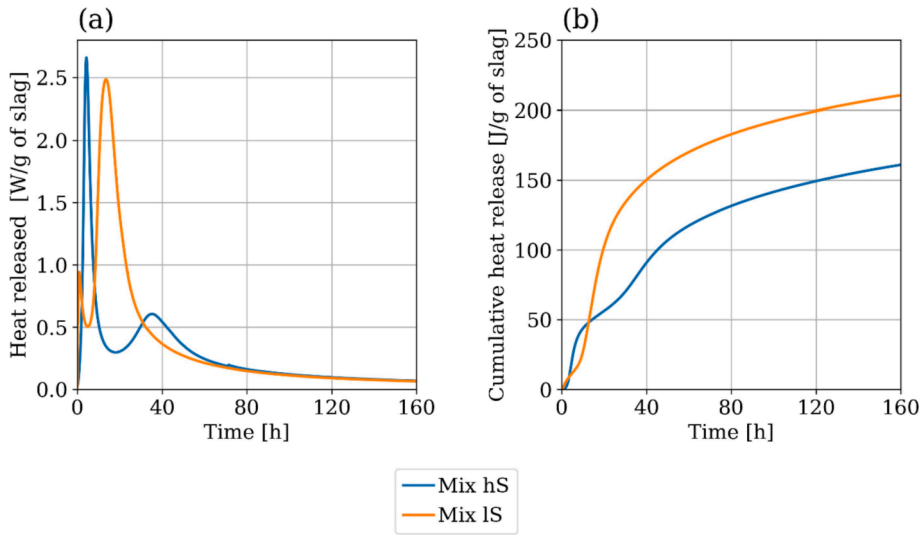

Fig. 5. Experimental results for both mixes hS and lS: (a): heat flow, (b): cumulative heat release.

Table 5
Calibration results for both experimental results.

Mix	*Mix hS*	*Mix lS*
t_{min} [h]	18.1	4.9
Q_∞ [J/g]	131.1	221.2
τ [h]	49.1	19.6
β [-]	1.3	1.0
Q_{tot} [J/g]	185.2	232.9
$\alpha_{tr,1}$ [-]	0.085	0.01
$\alpha_{tr,2}$ [-]	0.236	0.038
$\alpha_{tr,3}$ [-]	0.328	0.073
$\alpha_{tr,4}$ [-]	0.436	0.237
$\alpha_{tr,5}$ [-]	0.65	0.54
k_1 [h^{-1}]	$2.05{\cdot}10^{-1}$	$5.73{\cdot}10^{-1}$
k_2 [h^{-1}]	$1.13{\cdot}10^{-1}$	$9.94{\cdot}10^{-2}$
k_3 [h^{-1}]	$5.85{\cdot}10^{-2}$	$1.54{\cdot}10^{-1}$
k_4 [h^{-1}]	$3.37{\cdot}10^{-2}$	$8.68{\cdot}10^{-2}$
k_5 [h^{-1}]	$1.60{\cdot}10^{-2}$	$3.87{\cdot}10^{-2}$
k_6 [h^{-1}]	$9.39{\cdot}10^{-4}$	$1.20{\cdot}10^{-3}$

more than 99 % in a step between $\alpha_{j,10\%}$ and $\alpha_{j,90\%}$ ($1 \leq j \leq 6$), one must impose that $\forall 1 \leq i \leq 5$:

$$\begin{cases} 1 - Sigm\left(\alpha_{i,90\%}, \alpha_{tr,i}, \lambda_i\right) \geq 99\ \% \\ Sigm\left(\alpha_{i+1,10\%}, \alpha_{tr,i}, \lambda_i\right) \geq 99\ \% \end{cases}$$

Defining $\forall 1 \leq i \leq 5$, $\Delta\alpha_i = \min(\alpha_{tr,i} - \alpha_{i,90\%},\ \alpha_{i+1,10\%} - \alpha_{tr,i})$, λ_i is found as:

$$\lambda_i = \left| \ln\left(\frac{0.01}{0.99}\right) \frac{1}{\Delta\alpha_i} \right| \tag{15}$$

In Fig. 4, such a transition is illustrated.

By convention, for the initial and final transition zones, $\lambda_0 = \lambda_6 = +\infty$, which is equivalent to the Heaviside function at the chosen degree of reaction.

4. Results

4.1. Analysis of experimental results from the present study

The calorimetry curves for both slag mixes assessed in this study are shown in Fig. 5. As expected, these curves present the typical two accelerated peaks. Note that the heat release corresponding to the initial

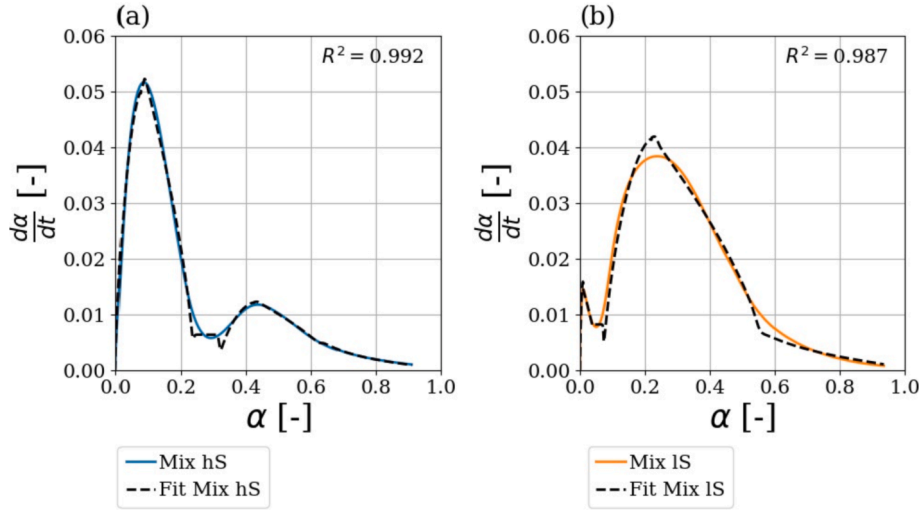

Fig. 6. Fitting of the overall degree of reaction for both mixes.

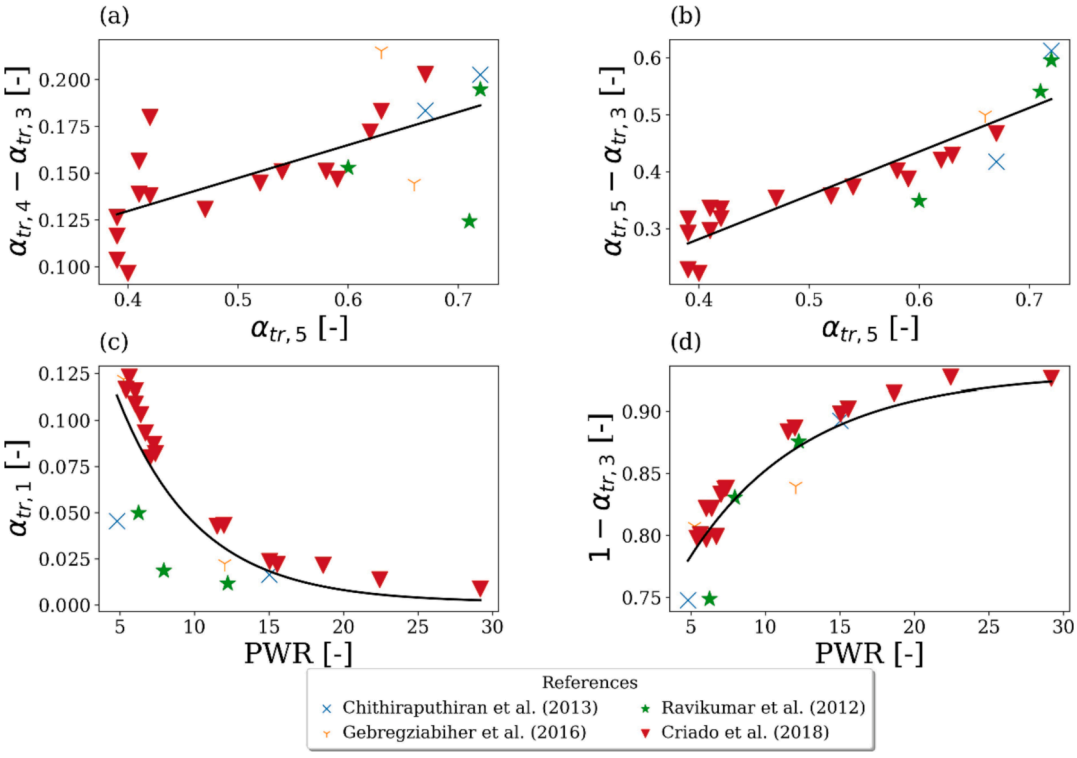

Fig. 7. Correlations between transition degrees of reaction for experiments at temperature 25 °C [11,17,21,24]. Solid lines correspond to the equations (16) to (19).

dissolution and wetting which occurred before the first twenty minutes after mixing is not shown.

The mix hS presents a lower cumulative heat release and both acceleration reaction peaks occur later, compared to the mix lS. This could come from the fact that solutions with lower M_S have a higher pH [31] and higher pH increases the dissolution rate of the slag. The induction period is also larger for the mix hS. This could also be due to a lower pH for the mix hS just like it was observed by Zuo et al. [32] with the increased presence of Si in the activator solution. The higher first peak for the mix hS could come from the fact that the primary C-S-H gel formation is higher for AAS mixes with higher M_S [33]. From Fig. 5 (a), it can also be noted that 75 h onwards, heat flows are comparable for both mixes.

The calibrated parameters for these curves (exponential fit, transition degrees of reaction and fitted reaction rates for each step) are given in Table 5 and global fitted model results are given in Fig. 6.

4.2. Correlations of the model parameters with mix characteristics

The correlations between model inputs and mix characteristics are presented in this section. As a first step, correlations between model input parameters are determined at a fixed temperature (25 °C), to reduce the number of independent model parameters. As a second step, the independent model parameters are correlated with the slag quality coefficient $\frac{CaO+MgO}{SiO_2}$, the most pertinent parameter for the slag composition as proposed by Winnefeld et al. [34] and the alkalinity factor n, from the data present in [24]. The influence of w/b and M_S are also determined with the results from [25] and [11,17,21], respectively. The complete calibrated parameter sets for the literature data [11,17,18,21–25] are provided in supplementary material. For all fits, the R-squared values obtained are higher than 95 %, confirming that the proposed model can capture the kinetic behavior of the activation of slag with waterglass and that the choice of the sequence of mechanisms seems adequate.

Several correlations were observed between model parameters. All

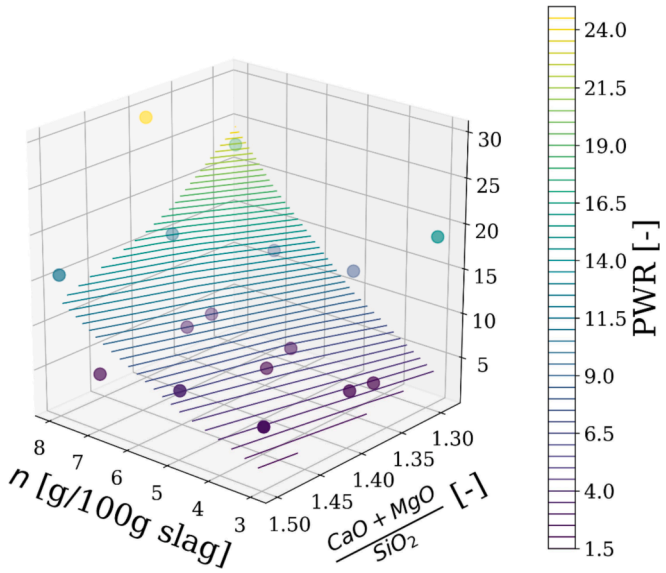

Fig. 8. Correlations on *PWR* from calibrated data of [24] (points). The colored lines correspond to Eq. (20).

transition degrees can be expressed in function of the peak widths ratio ($PWR = \frac{1-\alpha_{tr,3}}{\alpha_{tr,2}-0}$) as it can be seen in Fig. 7. This ratio represents the relative importance of both peaks. Higher *PWR* indicates an activation happening mainly during the second acceleration period. The obtained correlations are the following:

$$\alpha_{tr,4} - \alpha_{tr,3} = 0.18\alpha_{tr,5} + 0.06 \quad (16)$$

$$\alpha_{tr,5} - \alpha_{tr,3} = 0.77\alpha_{tr,5} - 0.03 \quad (17)$$

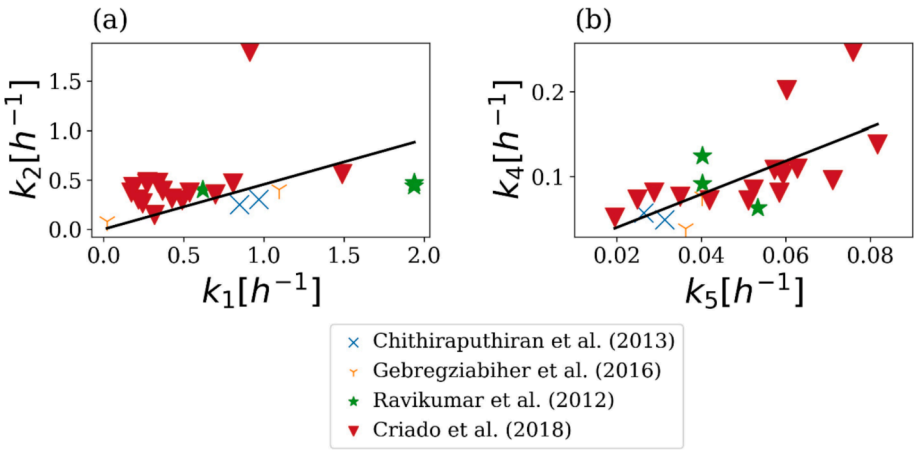

Fig. 9. Comparisons between reaction rates of nucleation and growth (k_1 and k_4) and reaction rates of contraction volume (k_2 and k_5) processes (a) for the first peak; (b) for the second peak. Solid lines stand for Eq. (21) on (a) and Eq. (22) on (b).

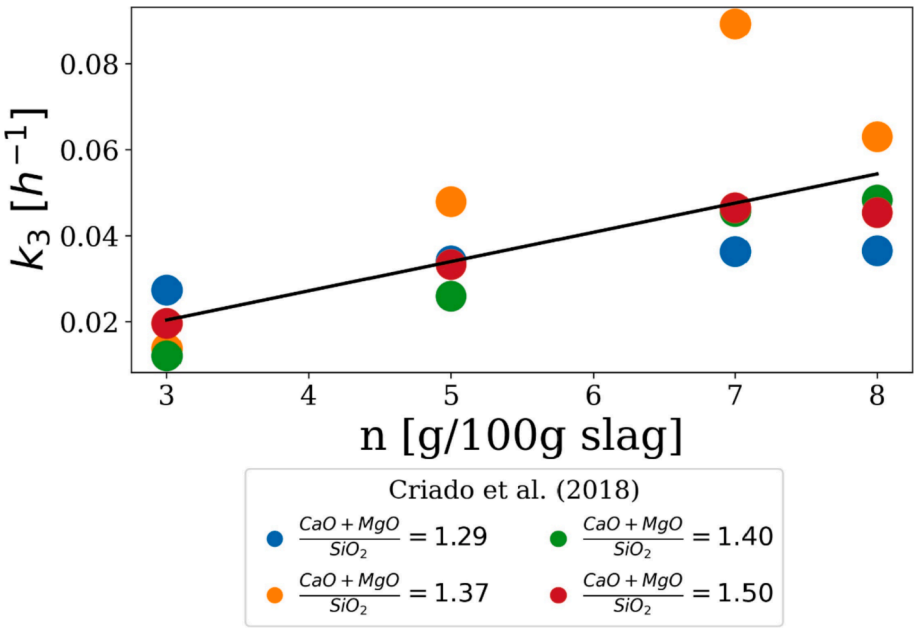

Fig. 10. Correlation between k_3 and n from calibrated data of [24] (colored points). The solid line stands for Eq. (23).

$$\alpha_{tr,1} = 0.27\left(1-\exp\left(-\frac{PWR}{5.41}\right)\right)+0.27 \tag{18}$$

$$1-\alpha_{tr,3} = 0.28\left(1-\exp\left(-\frac{PWR}{7.89}\right)\right)+0.65 \tag{19}$$

Note that $\alpha_{tr,4}-\alpha_{tr,3}$ is the width of the nucleation of the second peak, $\alpha_{tr,5}-\alpha_{tr,3}$ is the width of the nucleation and contraction volume processes of the second peak, $\alpha_{tr,1}$ is the width of the nucleation of the first peak and $1-\alpha_{tr,3}$ is the width of the second peak.

Thus, given *PWR*, all transition degrees can be quantified. From the analysis of results of Criado et al. [16], a correlation can be established between *PWR* and the chemical mix composition parameters viz. $\frac{CaO+MgO}{SiO_2}$ and n as shown in Fig. 8:

$$PWR = \frac{a_\Delta}{\frac{CaO+MgO}{SiO_2}-b_\Delta}\cdot n^2 \tag{20}$$

with $a_\Delta = 8.5\cdot10^{-2}$, $b_\Delta = 1.07$. For this correlation, it can be deduced that if n increases or $\frac{CaO+MgO}{SiO_2}$ decreases, most of the reaction occurs during the second acceleration period.

PWR depends also on M_S as the experimental results of the current study show it. For the mix lS, *PWR* is equal to 24.4, while for the mix hS, *PWR* is equal to 2.8. Thus *PWR* seems to be decreasing with M_S.

For the reaction rates, direct correlations exist between the first nucleation and the first contraction volume mechanisms k_1 and k_2, and also between the second nucleation and the second contraction volume mechanisms k_4 and k_5 as shown in Fig. 9. This suggests a faster contraction volume process in case of a higher nucleation for both peaks, which is logical since more nucleation sites will accelerate the dissolution of slag. Linear relationships are derived between these both sets of parameters:

$$k_2 = 0.5\cdot k_1 \tag{21}$$

$$k_4 = 2.0\cdot k_5 \tag{22}$$

No obvious correlations were found between both reaction rates k_1 or k_2 and the mix characteristics. The average values of around $1.0h^{-1}$ for k_1 and $0.5h^{-1}$ for k_2 seem to be reasonable. Note that the difficulty to find correlations for the first peak could be also due to the fact that it is often superposed with the initial dissolution and wetting of slag that are

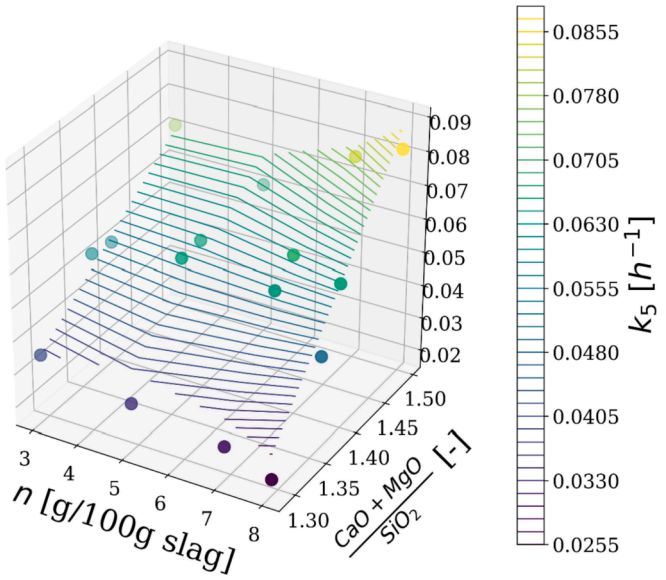

Fig. 11. Correlations between k_5 against $\frac{CaO+MgO}{SiO_2}$ and n from calibrated data of [24] (points). The colored lines correspond to Eq. (24).

not considered in the model.

With results obtained from [24], the reaction rate k_3 and n are linked with the following equation:

$$k_3 = a_3 \cdot n \tag{23}$$

with $a_3 = 6.8.10^{-3}$ [h^{-1}] (see Fig. 10).

This relation suggests that a greater alkalinity, and consequently a greater pH of the system, induces a greater reaction during the induction period and a faster transition from the first peak to the second. This conclusion has also been drawn previously by Zuo & Ye [23] for alkali-activated slag systems.

As shown in Fig. 9, both reaction rates k_4 (second nucleation process) and k_5 (second contraction volume process) are correlated. From the analysis of results in [24], a correlation between k_5 and mix chemical composition ($\frac{CaO+MgO}{SiO_2}$ and n) is derived as shown in Fig. 11:

$$k_5 = \left(a_{5,1}.\frac{CaO+MgO}{SiO_2} + b_{5,1}\right)n^2 + \left(a_{5,2}.\frac{CaO+MgO}{SiO_2} + b_{5,2}\right)n + \left(a_{5,3}.\frac{CaO+MgO}{SiO_2} + b_{5,3}\right) \tag{24}$$

with $a_{5,1} = 1.2.10^{-2}, b_{5,1} = -1.6.10^{-2}, a_{5,2} = -1.0.10^{-1}, b_{5,2} = 1.5.10^{-1}, a_{5,3} = 3.8.10^{-1}, b_{5,3} = -4.7.10^{-1}$ (all the coefficients being expressed in [h^{-1}]). Dependency of k_5 with respect to w/b was also

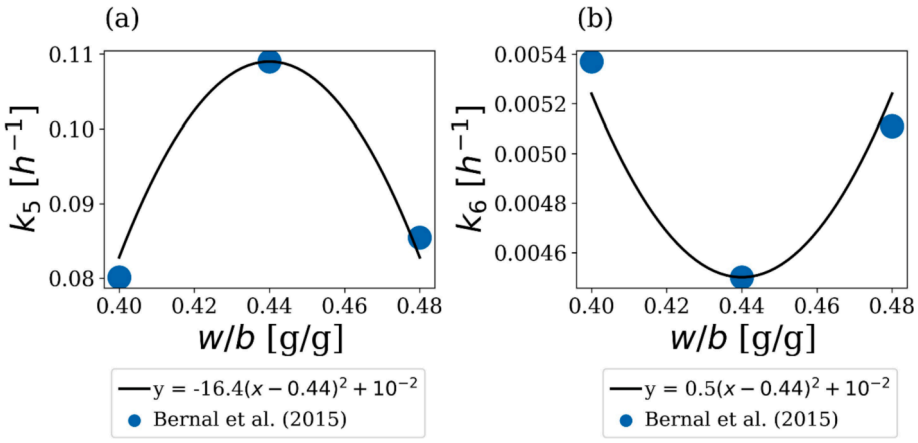

Fig. 12. Correlation of (a) k_5 and (b) k_6 with w/b from calibrated data of [25]

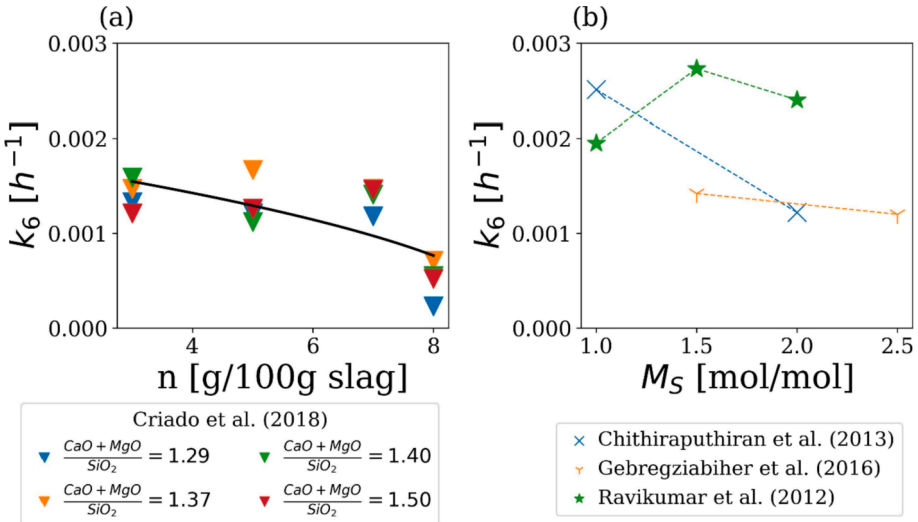

Fig. 13. (a) Correlations of k_6 with $\frac{CaO+MgO}{SiO_2}$ and n from calibrated data of [24] (points). The black line corresponds to Eq. 25. (b) Correlations of k_6 with M_S from calibrated data of [11,15,19].

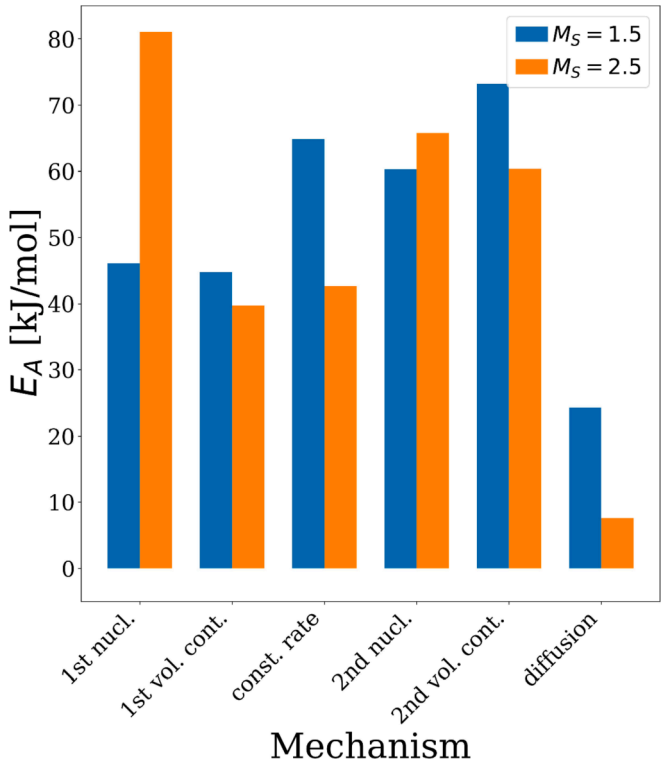

Fig. 14. Calculation of the activation energy for an evolving system with experiments led at 25 °C and 50 °C. Raw data from Gebregziabiher et al. [11].

observed. Following the calibration of the results from [25], a bell-shaped curve, as shown in Fig. 12 (a), would be expected for the relation between w/b and k_5. As proposed by Bernal et al., the optimum value is an indication of competition between the dissolution of calcium improved at lower alkalinities (higher w/b) and higher concentration of silicate improved at lower w/b.

Dependencies of k_6 in terms of $\frac{CaO+MgO}{SiO_2}$ and n are expressed below and shown in Fig. 13 (a):

$$k_6 = a_6 \cdot \sqrt{1 - b_6 \cdot n} \tag{25}$$

with $a_6 = 1.86.10^{-3}[h^{-1}]$, $b_6 = 1.04.10^{-1}$[-]. It seems that k_6 is relatively independent on the slag composition. However, for high n, the reaction rate decreases. The dependency of k_6 with w/b can be seen in Fig. 12 (b). In contrary to k_5, there is a minimum value of k_6 at intermediate w/b. Finally, the correlation between k_6 and M_S is plotted on Fig. 13 (b).

Regarding the influence of the temperature on the degree of reaction, the only results from Gebregziabiher et al. [11] were analyzed. These experiments consist of two mixes with M_S equal to 1.5 and 2.5, cured at the temperatures 25 °C and 50 °C. Using the Arrhenius law, the activation energies $E_{A,i}$ are computed for each reaction mechanism as follows:

$$E_{A,i} = Rln\frac{k_i(T_1)}{k_i(T_2)}/(\frac{1}{T_2} - \frac{1}{T_1}) \tag{26}$$

where $k_i(T_1)$ and $k_i(T_2)$ are the reaction rates for the ith reaction step at $T_1 = 25$ °C and $T_2 = 50$ °C. These activation energies for both mixes are shown in Fig. 14. The activation energies obtained for the first five reaction steps are comparable to results in the literature. For example, Fernandez et al. [35] obtained overall activation energy of the slag activation as 57.6 kJ/mol. In contrary, for the diffusion process, the activation energy is found very low in comparison to what could be expected. Such results have been previously reported in [36] for slag activated with NaOH.

Table 6
Summary of the found correlations between the model parameters and the mix characteristics.

Mix characteristic / Model parameter	$\frac{CaO+MgO}{SiO_2}$	n	w/b	M_S
PWR	Negative correlation	Positive correlation	?	Positive correlation
k_3		Positive correlation		?
k_4 & k_5	Positive correlation	Maximum at moderate w/b and n		
k_6		Positive correlation	Minimum at moderate w/b	Negative correlation

In conclusion, correlations found between the model parameters and the mix characteristics are provided in Table 6. No correlation for k_1 or k_2 was found and this should be analyzed in future studies. Also, all above-mentioned correlations must be confirmed and completed by more experimental studies, especially regarding the effects of w/b, M_S and slag fineness.

5. General discussion

The previous section confirms that the reaction of slag activated with waterglass can be sub-divided into six main parts. 1. a first nucleation and growth process followed by 2. a first contraction volume process; 3. an induction period during which a reaction of zero-order occurs; 4. a second nucleation and growth process followed by 5. a new contraction volume process and 6. a diffusion process. Processes 1 and 2 model the first peak, the processes 4, 5 and 6 the second peak. In this section, these mechanisms are interpreted in terms of microstructure evolution using the experimental evidence available in the literature. The overall interpretation of the microstructure in the context of the reaction mechanism is schematically depicted in Fig. 15.

After the initial dissolution and wetting of the slag surface, following Shi and Day [12], the first peak is associated with the nucleation and growth from a first C-A-S-H product, a C-S-H type product with aluminum enabling cross-linking in the structure [5]. This product forms around crystals of the sodium silicate solution, which act like seeds facilitating nucleation. [23,37]. This phenomenon is very comparable to the use of C-S-H seeds to accelerate the nucleation process for cement-based systems [38]. Thus, the nuclei grow in the space between the grains until a limiting degree of reaction. This limiting degree could be related either to the lack of further place for the growth of the gel, or to the limiting amount of nucleation sites from the activator solution. Gebregziabiher et al. [11] and Brough & Atkinson [39] observe the formation of a homogenous gel and no shell around the slag particles during the first day. The interpretation of this result is that the first nucleation does not occur on the surface of slag particles but around crystals of SiO_2 of the sodium silicate solution, in the inter-particle volume. This was also proposed by Zuo & Ye for alkali-activated slag with waterglass [23]. A similar observation was done for alkali-activated fly-ash systems by Lloyd et al. [40].

After the nucleation and growth step, the kinetic is governed by a contraction volume mechanism occurring at the interface between the slag particle and the pore solution. From Table 5, it seems that the more SiO_2 is present in the activator solution, the higher is this interface reaction process. This could be explained by the fact that during the nucleation and growth step, dissolution of SiO_2 from slag is limited since SiO_2 is already much present in the solution. Thus, at the end of the nucleation and growth step, the surface of the slag particle is relatively bigger and hence the reaction is higher.

The second peak follows the succession of nucleation and growth, contraction volume and diffusion processes, which is the usual

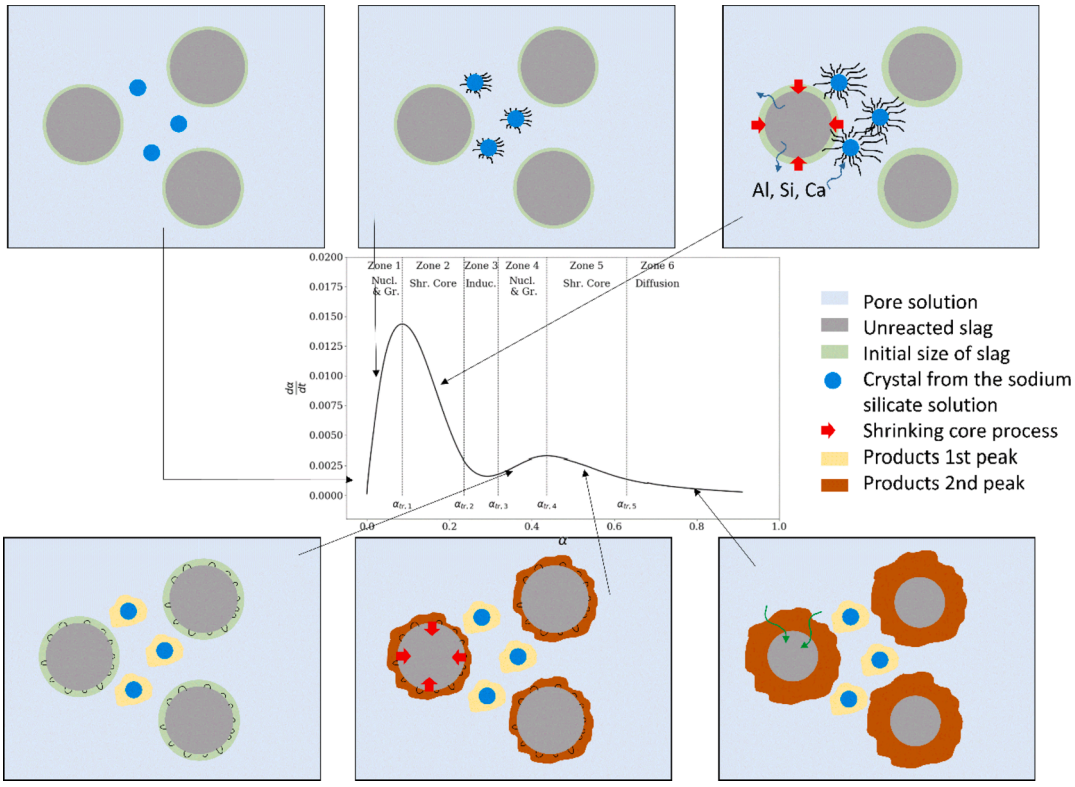

Fig. 15. Proposed kinetic model: initially, the slag is dissolved and wetted during the first 30 min. Then, the first peak of the reaction is attributed to nucleation and growth around SiO_2 crystals from the sodium silicate solution. The kinetic is then controlled by the interaction between the pore solution and the slag particle. It is followed by an induction period comparable to the one present for cement systems. The second peak is the succession of nucleation and growth around slag particles, contraction volume process kinetically controlled by the interaction between the pore solution and the slag particles and finally a diffusion-controlled process due to the formation of a shell around the slag particles.

succession of kinetic-controlling mechanisms describing the hydration of ordinary Portland cement [29]. For Shi & Day [12], this second peak is associated with the precipitation of the primary C-A-S-H gel. Brough & Atkinson [39] show that the C-A-S-H phases formed on the slag surface have a higher Ca/Si ratio. Thus, the second peak might be associated with the formation of high Ca/Si C-A-S-H, in comparison to the low Ca/Si C-A-S-H during the first accelerated peak.

The formation of Mg-rich phases like Hydrotalcite occurs at high degree of reaction [27]. For Brough & Atkinson [39], Mg stays around the slag particles. This would suggest that the formation of the rich-Mg products happens during the second peak. The formation of both (relatively) high Ca/Si C-S-H phases and Hydrotalcite phases would explain why the two reaction rates k_4 and k_5 are positively correlated to the slag quality coefficients $\frac{CaO+MgO}{SiO_2}$. Finally, the diffusion process comes from the formation of a shell [11,39] around the slag particles. The reaction is progressively hindered by the formation of a denser layer around the particles [11,39], which limits the contact between the unreacted slag with water and activators. Since lower M_S and bigger n reduces the reaction rate k_6, associated with the kinetic-controlled diffusion mechanism, one could suggest that such systems with lower M_S and bigger n generate denser products around the particles through which the diffusion is hindered.

The start of nucleation processes for both peaks seems to be very dependent on the global alkalinity of the system, i.e., n and w/b. In [22,28], it is shown that reducing the parameter n retards the second reaction peak. Moreover, there is an intermediate value of w/b for which the reaction is the fastest [25]. Furthermore, as shown in [31], solutions with higher M_S exhibit lower pH. Thus, increasing the pH of the solution (by increasing n or reducing w/b or M_S), decreases the dissolution of CaO [27,32] but increases the dissolution of SiO_2 and Al_2O_3 [32]. Reversely, decreasing the pH increases the dissolution of CaO but decreases the dissolution of SiO_2 and Al_2O_3. Another parameter to consider for the speed of the reaction is the number of nucleation sites directly available in the alkali solution on which the dissolved ions can form a reaction product and grow to form the primary gel [33]. Thus, there is a competition between three phenomena: high pH leads to faster dissolution of SiO_2 and Al_2O_3, low pH leads to faster dissolution of CaO and increasing the number of nucleation sites accelerates the nucleation and growth process. Results from Duran Atis et al. [41] and Taghvayi et al. [42] done for $n \leq 8$ [g Na_2O /100 g slag] and $M_S \leq 1.5$ [mol/mol], show that setting time increases with lower n and lower M_S on this range. Bernal et al. [7] showed that for $M_S \geq 1.6$, setting time increases with higher M_S. These observations can be linked with the competition expressed above between the phenomena. In particular, the impact of M_S should be carefully considered. On one hand, increasing it provides more nucleation sites. This would explain the decreasing setting time for relatively low M_S. On the other hand, increasing it further would retard the dissolution of slag. This would explain the increasing setting time at high M_S.

Finally, looking at the interpretation of results from Bernal et al. [25], the fastest reaction, with the intermediate w/b showed the highest value of reaction rates for the first five reaction steps and the smallest reaction rates for the diffusion process. This seems to be coherent with the formation of a denser structure for this mix due to a bigger reactivity at the beginning, leading to a hindered diffusion process [11,39].

Curing temperature of alkali-activated slag enables to have a faster reaction, in the sense that both peaks occur earlier during the activation. Looking at the activation energy for each mechanism, it is coherent with the idea that temperature influences the microstructure of the system and that generated products can be different. For Portland cement pastes, Lothenbach et al. [43] show that at 40 °C and 50 °C, a denser C-S-H phase is formed in comparison to 20 °C cured pastes. Thus, if the

activation of slag occurs at high temperature, the reaction is more hindered during the diffusion mechanism and can lead to very low apparent activation energies. This is especially true for the mix with a high M_S, when the alkali solution contains more silicon crystals. Li et al. [36] obtained such results and even negative apparent activation energies during the diffusion process for alkali-activated slag and this phenomenon was associated with the shell forming around the slag particle.

6. Conclusions

This study provides a model based on solid-state single-particle models for activation kinetics of slag with waterglass and a framework to interpret model parameters using the calorimetry data of activation of slag by waterglass solutions. Alkali activated slag with waterglass has typically two exothermic peaks, without taking into account the initial dissolution and wetting of slag particles. In the proposed model, these two peaks are represented by the succession of six reactions steps. The first peak is the succession of nucleation and growth and contraction volume processes, while the second peak is the succession of nucleation and growth, contraction volume and diffusion processes. The induction period between the two peaks is modeled by a zero-order reaction. It was demonstrated that the choice of these successive steps is consistent with the microstructure evolution. The developed model provides good fits with a coefficient of determination R^2 above 95 % for a wide range of parameters. Fitting the model for different experiments reported in literature allowed to develop correlations between input parameters and mix parameters and confirmed several hypotheses laid in the literature. Solution composition influences the kinetic rate parameters for all mechanisms and the relative intensity between both peaks. The first acceleration peak occurs depending on n and w/b which influence the pH and so, the dissolution of slag and on M_S, which influences the availability of crystals from the activator solution acting like seeds for the nucleation process. The reaction rate related to the dissolution of slag during the induction period increases with n. The relative intensity of the second peak in comparison to the first peak increases with n due to a better dissolution but decreases with M_S, since at higher M_S more nucleation sites are present for the first nucleation. The slag quality coefficient $\frac{CaO+MgO}{SiO_2}$ explains well the influence of the precursor composition. Its influence is particularly noticeable for the reaction rate parameters of the second peak. The bigger it is, the faster is the second nucleation process and the second contraction volume process. The reaction rate of the diffusion process is strongly correlated to the activator solution (n, M_S, w/b) and the density of the generated products. This would explain the low apparent activation energies obtained for the diffusion mechanism. In the future, the analysis could be completed by further specific experiments on w/b, M_S and the particle size distribution to provide a global model predicting the heat release and the evolution of the microstructure of such systems at early age.

CRediT authorship contribution statement

Richard Caron: Conceptualization, Methodology, Software, Validation, Investigation, Writing – original draft. **Ravi A. Patel:** Conceptualization, Methodology, Validation, Investigation, Writing – review & editing. **Frank Dehn:** Resources, Supervision, Funding acquisition, Writing – review & editing.

Declaration of Competing Interest

The authors declare that they have no known competing financial interests or personal relationships that could have appeared to influence the work reported in this paper.

Acknowledgments

Research presented in this paper was performed within the DuRSAAM project, which has received funding from the European Union's Horizon 2020 research and innovation programme under the grant agreement No 813596. Authors are very grateful to Dr. Maria Criado (Spanish National Research Council – CSIC – Eduardo Torroja Institute for Construction Sciences), Prof. Susan A. Bernal (School of Civil Engineering – University of Leeds, UK) and Prof. John Provis (Department of Materials Science and Engineering, The University of Sheffield, UK) for sharing their experimental data and discussions during the course of this study.

Appendix A. Supplementary data

Supplementary data to this article can be found online at https://doi.org/10.1016/j.conbuildmat.2022.126577.

References

[1] A. Wüstemann, A. König, F. Dehn, Proposal for the classification of alkali-activated binders and geopolymer binders, Cement International. 13 (2015) 63–69.
[2] S.-D. Wang, X.-C. Pu, K.L. Scrivener, P.L. Pratt, Alkali-activated slag cement and concrete: a review of properties and problems, Adv. Cem. Res. 7 (1995) 93–102.
[3] J.S.J. van Deventer, J.L. Provis, P. Duxson, Technical and commercial progress in the adoption of geopolymer cement, Miner. Eng. 29 (2012) 89–104.
[4] J.L. Provis, Geopolymers and other alkali activated materials: why, how, and what? Mater. Struct. 47 (2014) 11–25.
[5] R.J. Myers, S.A. Bernal, J.D. Gehman, J.S.J. van Deventer, J.L. Provis, The Role of Al in Cross-Linking of Alkali-Activated Slag Cements, J. Am. Ceram. Soc. 98 (2015) 996–1004.
[6] S.A. Bernal, MgO content of the slag controls phase evolution and structural changes induced by accelerated carbonation in alkali-activated binders, Cem. Concr. Res. 57 (2014) 33–43.
[7] S.A. Bernal, J.L. Provis, V. Rose, M. de Gutierrez, Ruby., Evolution of binder structure in sodium silicate-activated slag-metakaolin blends, Cem. Concr. Compos. 33 (2011) 46–54.
[8] A. Fernandez-Jimenez, J.G. Palomo, F. Puertas, Alkali-activated slag mortars Mechanical strength behavior, Cem. Concr. Res. 29 (1999) 1313–1321.
[9] A. Fernandez-Jimenez, F. Puertas, Structure of Calcium Silicate Hydrates Formed in Alkaline-Activated Slag: Influence of the Type of Alkaline Activator, J. Am. Ceram. Soc. 86 (2003) 1389–1394.
[10] Bernal, S.A., Provis, J.L., Fernández-Jiménez, A., Krivenko, P.V., Kavalerova, E., Palacios, M. and Shi, C. Binder chemistry–high-calcium alkali-activated materials. In Alkali activated materials. 2014. Springer Netherlands.
[11] Berhan Seium Gebregziabiher, Robert J. Thomas, Sulapha Peethamparan, Temperature and activator effect on early-age reaction kinetics of alkali-activated slag binders, Constr. Build. Mater. 113 (2016) 783–793.
[12] Caijun Shi, Robert L. Day, A calorimetric study of early hydration of alkali-slag cements, Cem. Concr. Res. 25 (1995) 1333–1346.
[13] A. Fernandez-Jimenez, F. Puertas, A. Arteaga, Determination of Kinetic Equations of Alkaline Activation of Blast Furnace Slag by Means of Calorimetric Data, J. Therm. Anal. 52 (1998) 945–955.
[14] L.J. Parrot, D.C. Killoh, Prediction of Cement Hydration, British Ceramic Proceedings. (1984) 41–53.
[15] Zuo, Yibing; Nedeljkovic, Marija; Ye, Guang. 2016. Reaction Kinetics and Thermodynamic Modeling of Sodium Hydroxide Activated Slag Paste. In C. Miao, W. Sun, J. Liu, H. Chen, G. Ye, & K. van Breugel (Eds.), 3rd. 117. 1–8.
[16] Solmoi Park, Selamu Abate, Yihune, Hyeong-Ki Kim, Hydration kinetics modeling of sodium silicate-activated slag: A comparative study, Constr. Build. Mater. 242 (2020), 118144.
[17] Sundararaman Chithiraputhiran, Narayanan Neithalath, Isothermal reaction kinetics and temperature dependence of alkali activation of slag, fly ash and their blends, Constr. Build. Mater. 45 (2013) 233–242.
[18] Zhenming Li, Marija Nedeljković, Boyu Chen, Guang Ye, Mitigating the autogenous shrinkage of alkali-activated slag by metakaolin, Cem. Concr. Res. 122 (2019) 30–41.
[19] Kyle A. Riding; Jonathan L. Poole; Kevin J. Folliard; Maria C. G. Juenger; and Anton K. Schindler. 2012. Modeling Hydration of Cementitious Systems. ACI Materials Journal. 109. 225–234.
[20] A. Bezjak, Nuclei growth model in kinetic analysis of cement hydration, Cem. Concr. Res. 16 (1986) 605–609.
[21] Deepak Ravikumar, Narayanan Neithalath, Reaction kinetics in sodium silicate powder and liquid activated slag binders evaluated using isothermal calorimetry, Thermochim Acta 546 (2012) 32–43.
[22] Deir, Elisabeth; Gebregziabiher, Berhan S.; Peethamparan, Sulapha. 2014. Influence of starting material on the early age hydration kinetics, microstructure and composition of binding gel in alkali activated binder systems. Cement and Concrete Composites. 48. 108–117.

[23] Zuo, Yibing; Ye, Guang. 2020. Preliminary Interpretation of the Induction Period in Hydration of Sodium Hydroxide/Silicate Activated Slag. Materials (Basel, Switzerland). 13.
[24] Maria Criado, Brant Walkley, Xinyuan Ke, John Provis, Susan Bernal, Slag and Activator Chemistry Control the Reaction Kinetics of Sodium Metasilicate-Activated Slag Cements, Sustainability. 10 (2018) 4709.
[25] S.A. Bernal, R. San Nicolas, J.S.V. van Deventer, J.L. Provis, Water content modifies the structural development of sodium metasilicate-activated slag binders, Revista ALCONPAT. 5 (2015) 28–39.
[26] Ammar Khawam, Douglas R. Flanagan, Solid-state kinetic models: basics and mathematical fundamentals, J. Phys. Chem. B 110 (2006) 17315–17328.
[27] Sujin Song, Hamlin M. Jennings, Pore solution chemistry of alkali-activated ground granulated blast-furnace slag, Cem. Concr. Res. 29 (1999) 159–170.
[28] Sh.uhua. Liu, Qiaoling Li, Weiwei Han, Effect of various alkalis on hydration properties of alkali-activated slag cements, J. Therm. Anal. Calorim. 131 (2018) 3093–3104.
[29] Li, Yao; Deng, Yonggang; Liu, Runqing. 2019. Hydration Kinetics of Portland Cement-Silica Fume Binary System at Low Temperature. Materials (Basel, Switzerland). 12.
[30] John Lloyd Provis, On the use of the Jander equation in cement hydration modelling, RILEM Technical Letters. 1 (2016) 62.
[31] J.J. Chang, A study on the setting characteristics of sodium silicate-activated slag pastes, Cem. Concr. Res. 33 (2003) 1005–1011.
[32] Yibing Zuo, Marija Nedeljković, Guang Ye, Pore solution composition of alkali-activated slag/fly ash pastes, Cem. Concr. Res. 115 (2019) 230–250.
[33] F. Puertas, C. Varga, M.M. Alonso, Rheology of alkali-activated slag pastes. Effect of the nature and concentration of the activating solution, Cem. Concr. Compos. 53 (2014) 279–288.
[34] Winnefeld, Frank; Ben Haha, Mohsen; Le Saout, Gwenn; Costoya, Mercedes; Ko, Suz-Chung; Lothenbach, Barbara. 2015. Influence of slag composition on the hydration of alkali-activated slags. Journal of Sustainable Cement-Based Materials. 4. 85–100.
[35] A. Fernandez-Jimenez, Alkali-activated slag cements: kinetic studies, Cem. Concr. Res. 27 (1997).
[36] Ping Li, Jianhui Tang, Xudong Chen, Yin Bai, Qiyao Li, Effect of Temperature and pH on Early Hydration Rate and Apparent Activation Energy of Alkali-Activated Slag, Adv. Mater. Sci. Eng. 2019 (2019) 1–13.
[37] F. Puertas, M.M. Alonso, S. Gismera, M. Lanzón, M.T. Blanco-Varela, Rheology of Cementitious Materials: Alkali-Activated Materials or Geopolymers, MATEC Web of Conferences. 149 (2018) 1002.
[38] Jeffrey J. Thomas, Hamlin M. Jennings, Jeffrey J. Chen, Influence of Nucleation Seeding on the Hydration Mechanisms of Tricalcium Silicate and Cement, The Journal of Physical Chemistry C. 113 (2009) 4327–4334.
[39] A.R. Brough, A. Atkinson, Sodium silicate-based, alkali-activated slag mortars. Part I. Strength, hydration and microstructure, Cem. Concr. Res. 32 (2002) 865–879.
[40] Redmond R. Lloyd, John L. Provis, Jannie S.J. van Deventer, Microscopy and microanalysis of inorganic polymer cements. 2: the gel binder, J. Mater. Sci. 44 (2009) 620–631.
[41] Cengiz Duran Atiş, Cahit Bilim, Özlem Çelik, Okan Karahan, Influence of activator on the strength and drying shrinkage of alkali-activated slag mortar, Constr. Build. Mater. 23 (2009) 548–555.
[42] Hamed Taghvayi, Kiachehr Behfarnia, Mohammadbagher Khalili, The Effect of Alkali Concentration and Sodium Silicate Modulus on the Properties of Alkali-Activated Slag Concrete, J. Adv. Concr. Technol. 16 (2018) 293–305.
[43] Barbara Lothenbach, Thomas Matschei, Göril Möschner, Fred P. Glasser, Thermodynamic modelling of the effect of temperature on the hydration and porosity of Portland cement, Cem. Concr. Res. 38 (2008) 1–18.

Supplementary material of the article “Activation kinetic model and mechanisms for alkali-activated slag cements”

Richard Caron, Ravi A. Patel and Frank Dehn (2022)

Ref.	Slag	w:b	n	Ms	T	$\alpha_{tr,1}$	$\alpha_{tr,2}$	$\alpha_{tr,3}$	$\alpha_{tr,4}$	$\alpha_{tr,5}$	k_1	k_2	k_3	k_4	k_5	k_6	R2
	Unit	[kg:kg]	[g:100g]	[mol:mol]	[°C]	-	-	-	-	-	[h-1]	[h-1]	[h-1]	[h-1]	[h-1]	[h-1]	-
Chithiraputhiran et al. (2013)	-	0.5	5	1	25	0.016	0.059	0.108	0.31	0.72	0.846	0.251	0.048	0.057	0.026	0.0025	0.99
	-	0.5	5	2	25	0.045	0.156	0.252	0.436	0.67	0.969	0.305	0.067	0.049	0.031	0.0012	0.976
Gebregziabiher et al. (2016)	-	0.4	2.5	1.5	25	0.022	0.07	0.16	0.305	0.66	1.095	0.406	0.022	0.076	0.04	0.0014	0.974
	-	0.4	2.5	2.5	25	0.122	0.154	0.193	0.408	0.63	0.021	0.081	0.071	0.039	0.036	0.0012	0.966
	-	0.4	2.5	1.5	50	0.015	0.052	0.118	0.274	0.45	4.623	1.644	0.17	0.502	0.396	0.003	0.962
	-	0.4	2.5	2.5	50	0.044	0.088	0.12	0.245	0.34	0.263	0.279	0.27	0.302	0.239	0.0015	0.974
Li et al. (2019)	-	0.344	4.7	1.5	20	0.031	0.076	0.184	0.271	0.6	9.55	5.433	0.344	0.197	0.047	0.0007	0.974
Ravikumar et al. (2012)	-	0.5	5	1	25	0.019	0.104	0.17	0.294	0.71	1.939	0.473	0.09	0.125	0.04	0.002	0.986
	-	0.5	5	1.5	25	0.012	0.072	0.124	0.319	0.72	1.937	0.442	0.056	0.092	0.04	0.0027	0.99
	-	0.5	5	2	25	0.05	0.12	0.251	0.404	0.6	0.618	0.401	0.033	0.063	0.053	0.0024	0.965
Deir et al. (2014)	-	0.45	5	1.5	50	0.026	0.054	0.088	0.138	0.21	2.958	2.304	0.918	0.786	0.477	0.0006	0.956
	-	0.45	7	1.5	50	0.043	0.128	0.194	0.229	0.32	3.939	1.475	1.417	1.01	0.313	0.0008	0.973
Zuo et al. (2020)	-	0.4	4	1.4	20	0.011	0.04	0.104	0.217	0.37	4.547	1.558	0.075	0.084	0.048	0.0009	0.971
	-	0.4	6	0.9	20	0.012	0.056	0.118	0.172	0.45	5.607	1.321	0.228	0.16	0.037	0.0008	0.963
	-	0.4	8	0.7	20	0.017	0.05	0.101	0.166	0.4	4.831	2.532	0.422	0.195	0.047	0.0006	0.979
Criado et al. (2018)	M14	0.4	3	1	25	0.022	0.049	0.086	0.266	0.42	0.316	0.146	0.027	0.076	0.035	0.0013	0.989
		0.4	5	1	25	0.043	0.074	0.113	0.252	0.41	0.425	0.315	0.034	0.081	0.029	0.0012	0.983
		0.4	7	1	25	0.043	0.077	0.117	0.247	0.47	0.536	0.377	0.036	0.073	0.025	0.0012	0.983
		0.4	8	1	25	0.014	0.041	0.073	0.177	0.39	0.696	0.357	0.036	0.051	0.02	0.0002	0.962
	M06	0.4	3	1	25	0.093	0.119	0.201	0.384	0.63	0.911	1.796	0.014	0.096	0.071	0.0015	0.942
		0.4	5	1	25	0.082	0.114	0.162	0.278	0.39	0.242	0.264	0.048	0.202	0.06	0.0017	0.969
		0.4	7	1	25	0.109	0.136	0.178	0.275	0.4	0.272	0.479	0.089	0.248	0.076	0.0015	0.953
		0.4	8	1	25	0.022	0.058	0.098	0.225	0.39	0.489	0.299	0.063	0.138	0.082	0.0007	0.963
	M07	0.4	3	1	25	0.116	0.132	0.203	0.406	0.67	0.171	0.376	0.012	0.072	0.051	0.0016	0.982
		0.4	5	1	25	0.116	0.147	0.202	0.349	0.59	0.215	0.303	0.026	0.102	0.059	0.0011	0.961
		0.4	7	1	25	0.08	0.119	0.167	0.318	0.54	0.366	0.392	0.046	0.11	0.063	0.0014	0.974
		0.4	8	1	25	0.009	0.032	0.074	0.23	0.41	1.488	0.561	0.048	0.081	0.058	0.0006	0.968
	M08	0.4	3	1	25	0.123	0.142	0.2	0.372	0.62	0.184	0.433	0.02	0.085	0.052	0.0012	0.97
		0.4	5	1	25	0.103	0.129	0.178	0.329	0.58	0.27	0.464	0.033	0.107	0.059	0.0013	0.97
		0.4	7	1	25	0.087	0.115	0.163	0.307	0.52	0.339	0.473	0.047	0.108	0.057	0.0015	0.976
		0.4	8	1	25	0.024	0.06	0.102	0.24	0.42	0.807	0.468	0.045	0.072	0.042	0.0005	0.967
Bernal et al. (2015)	-	0.4	4	1	25	0.004	0.053	0.134	0.315	0.6	21.846	0.978	0.075	0.14	0.08	0.0054	0.981
	-	0.44	4	1	25	0.007	0.065	0.139	0.29	0.56	16.186	1.698	0.135	0.219	0.109	0.0045	0.979
	-	0.48	4	1	25	0.005	0.056	0.134	0.3	0.55	16.193	1.206	0.096	0.169	0.085	0.0051	0.979

Paper 4

Microstructure development of slag activated with sodium silicate solution: Experimental characterization and thermodynamic modeling

Publisher's version

Published in *Journal of Building Engineering*

Volume 71 (7), 2023, p. 106398

DOI: 10.1016/j.jobe.2023.106398

Authors: **Richard Caron**, Ravi A. Patel, George Dan Miron,

Cassandre Le Galliard, Barbara Lothenbach, Frank Dehn

Journal of Building Engineering 71 (2023) 106398

Contents lists available at ScienceDirect

Journal of Building Engineering

journal homepage: www.elsevier.com/locate/jobe

Full length article

Microstructure development of slag activated with sodium silicate solution: Experimental characterization and thermodynamic modeling

Richard Caron [a,b], Ravi A. Patel [a,b,*], George D. Miron [c], Cassandre Le Galliard [d], Barbara Lothenbach [e], Frank Dehn [a,b]

[a] Karlsruhe Institute of Technology (KIT), Institute of Building Materials and Concrete Structures (IMB), DE-76131 Karlsruhe, Germany
[b] Materials Testing and Research Institute Karlsruhe (MPA), Karlsruhe Institute of Technology (KIT), DE-76131 Karlsruhe, Germany
[c] Laboratory for Waste Management (LES), Paul Scherrer Institute (PSI), Forschungsstr. 111, Villigen PSI, 5232, Switzerland
[d] Department of Materials Science and Engineering, The University of Sheffield, Sir Robert Hadfield Building, Sheffield, S1 3JD, United Kingdom
[e] Empa, Concrete & Asphalt Laboratory, Überlandstrasse 129, Dübendorf, 8600, Switzerland

ARTICLE INFO

Keywords:
Alkali-activated slag
Microstructure characterization
Thermodynamic modeling

ABSTRACT

Slag is a by-product of the steel industry that can be used as a binder with alkali solutions. In this study, the microstructural development is discussed for two alkali-activated slag mixes with promising properties for structural applications. The reaction products for both mixes were characterized by X-ray diffraction, thermogravimetry, Fourier-transform infrared spectroscopy and nuclear magnetic resonance. The Ca/Si ratio of C-A-S-H gel and the secondary products such as hydrotalcite, M-S-H and zeolites depend on the activator solution. The dissolution kinetics is followed by isothermal calorimetry and scanning electron microscopy. Calorimetry data can be adjusted with the maximum heat release obtained from thermodynamic modeling to predict the degree of dissolution. Thermodynamic modeling using the Pitzer ion activity model was applied for alkali-activated slag. This model is relevant for the first two days of reaction. For later age, the extended Debye–Hückel ion activity model and the Pitzer ion activity model give identical results. Phase assemblage predicted using thermodynamic modeling with the correct CASH model and consistent M-S-H and zeolite datasets agreed well with experiments.

1. Introduction

Slag is a by-product of the steel industry that can be used as binder in concrete systems [1]. Mixed with an alkali activator, it can provide concrete with good mechanical and improved durability properties. Alkali-activated slag (AAS) leads to reduced decalcification in acid environment [2] and offers better resistance to sulfate attack [3]. One-part system refers to the case where the activator is added in solid form. If the activator is first dissolved in water, it is a two-part system. One-part systems have a longer setting time since alkali must first dissolve in water to increase the pH and start the reaction, but the difference in properties in the hardened state are minimal [4]. Nevertheless, most of the studies in the literature have been made for two-part alkali-activated slag. The most used alkali solutions are sodium hydroxide, sodium silicate (waterglass) and sodium carbonate. Among them, sodium silicate results in better mechanical properties, especially better compressive and flexural strengths [5], which are the most important parameters when considering alkali-activated slag in replacement of Portland cement for structural applications [6].

* Corresponding author at: Karlsruhe Institute of Technology (KIT), Institute of Building Materials and Concrete Structures (IMB), DE-76131 Karlsruhe, Germany.
E-mail addresses: richard.caron@kit.edu (R. Caron), ravi.patel@kit.edu (R.A. Patel), frank.dehn@kit.edu (F. Dehn).

https://doi.org/10.1016/j.jobe.2023.106398
Received 24 January 2023; Received in revised form 16 March 2023; Accepted 26 March 2023
Available online 29 March 2023

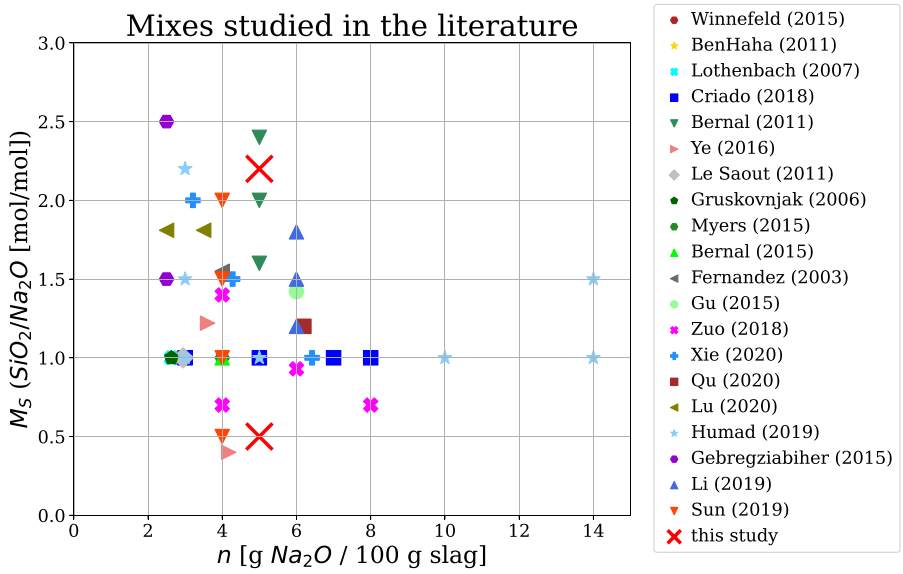

Fig. 1. Used parameters of alkali solutions for AAS mixes studied in the literature, in terms of n [g Na_2O/100 g slag] and M_S (SiO_2/Na_2O [mol/mol]) [5,8,10,14–31]. The longer setting times were reported for mixes with low M_S (0.45) [7] and high M_S (2.4) [10].

The properties of sodium silicate-activated slag vary considerably based on the mix proportions. Compressive strength increases with the increase in the concentration of sodium and silicate ions in the alkali solution [7] and decreases with increasing water/binder ratio [8]. Taghvayi et al. [7] showed that setting time decreases by increasing the silicate ratio M_S = SiO_2/Na_2O from 0.45 to 1.05. Duran-Atis et al. showed that this setting time seems to be smallest for M_S = 1.0 [9], while Bernal et al. found that setting time increases with increasing M_S from 1.6 to 2.4 [10]. Other properties like shrinkage [7,9,11] and carbonation [10,12] depend also on the composition and proportion of binders that are mixed. Our previous study [11] showed that two mixes with $M_S = 0.5$ and $M_S = 2.2$ present interesting properties in terms of workability and mechanical properties. The pastes were workable for at least one hour and the setting time measured with DIN EN 196-3 [13] was superior to four hours for both mixes. The compressive strength of both mixes for concrete was reported in a previous study [11]. It was equal to 56 MPa for the mix lS and 76 MPa for the mix hS. Yet, in the literature, most of the microstructure characterization studies were done for waterglass-activated slags that have a silicate ratio between 1.0 and 2.0, as can be seen in Fig. 1.

Different silicate solutions with alkali dosages n [g Na_2O / 100 g slag] from 2.5 to 14.0 have been used in literature to characterize the reaction products [5,8,10,14–23]. The silicate ratio M_S, defined as SiO_2/Na_2O [mol/mol], is often kept in these studies between 1.0 and 2.0. In this range of slag composition and of alkali dosages and silicate ratio, the experimental characterization of the reaction products showed that the main reaction product was C-A-S-H gel [17,18,32,33]. It has a lower molar Ca/Si ratio than the calcium silicate hydrate C-S-H present in hardened ordinary Portland cement [33] with a greater uptake of aluminum by replacing silicon in the tetrahedral chain [34,35]. The main secondary product is hydrotalcite, if the MgO content in the slag is higher than 3 % in mass [10,12]. At high aluminum contents, other secondary products have been also reported, like strätlingite, katoite and monocarbonate [36]. Finally, zeolites have also been observed in alkali-activated slag systems [10,37]. Thus, the reaction products of AAS differ from the ones of OPC and must be characterized for new mix designs.

Thermodynamic calculations have been used widely for modeling cement systems [38]. They have been recently applied to alkali-activated slags [33,39,40]. The appropriate choice of input thermodynamic models and data to represent the reaction products that define the chemical system is essential and can have a large influence on the results. Firstly, the choice of the ion activity model influences the equilibrium in the pore solution. Most of the studies made for cementitious materials used the extended Debye–Hückel ion activity model [41]. Nevertheless, its range of applicability is limited for systems with relatively low ionic strength (< 1 M) [42,43]. The model developed by Pitzer [44–47] overcomes this issue by taking into account ion interactions. For cementitious materials, and specifically AAS systems, databases have been developed in the past decade to apply this model [42,48–50]. Nevertheless, they have not been applied for AAS despite the higher concentrations of ions and ionic strength in the solution due to the use of alkali solutions in place of water. In addition to the choice of the model in the pore solution, thermodynamic modeling requires also the choice of a database. For cementitious materials, some of them have been developed for example CEMDATA07 [51–53] and CEMDATA14 [54]. These databases have been further extended for applications to blended cements, as well as for alkali-activated materials with the release of CEMDATA18 [55]. The modelization of C-S-H has been studied extensively leading to new models such as solid solution models [56,57]. A solid solution model developed by Myers et al. [24] gives phase prediction of C-(N-)A-S-H gel, using eight sublattice sites. Still in [24], Myers et al. developed a solid solution model for hydrotalcite-like phases. The combination of these two models was complemented by a set of five zeolites (Na-analcime, natrolite, Ca-heulandite, (Ca, Na)-heulandite and sodalite) and can be used to model alkali-activated materials [24]. This combination of models and thermodynamic data has been applied for alkali-activated slag systems in some studies [25,26,58]. Ma & Lothenbach released the

Table 1
Chemical composition of the anhydrous slag.

Oxide	CaO	SiO_2	Al_2O_3	MgO	Fe_2O_3	Na_2O	K_2O	H_2S	Oth.
Mass (%)	38.8	36.3	12.8	8.0	0.6	0.3	0.6	1.0	1.6

zeolite20 database specifically for zeolites [59,60]. The advantage of this database for zeolites, in comparison with the one from Myers et al. [24], is that it is consistent with thermodynamic data for cementitious materials and relies on measured solubilities [59]. However, it has not been used so far for predicting the formation of zeolites of AAS. Finally, a new sublattice multisite solid-solution C-A-S-H model, CASH+, has been provided by Kulik et al. [61] and completed to describe the uptake of alkalis by Miron et al. [62] and the uptake of aluminum (personal communication). This model has not been used to predict the phase assemblage of AAS and thus, no comparative study of the existing thermodynamic data has been so far proposed in the literature.

The first objective of the present study is the micro-structure characterization of the above-mentioned AAS mixes with sodium silicate ratios M_S of 0.5 and 2.2 using different complementary experimental techniques. These mixes have not been studied in past in the literature and this brings novelty to the present work. The phase characterization was conducted at several ages for both mixes with X-ray Diffraction (XRD), Differential Thermogravimetry (DTG), Differential Thermal Analysis (DTA), Fourier-Transform Infrared Spectroscopy (FTIR) and Al Magic Angle Spinning (MAS) Nuclear Magnetic Resonance (NMR). The pore structure was analyzed with Mercury Intrusion Porosimetry (MIP) and cyclic saturation/desaturation of paste. The dissolution kinetics of slag was followed with Scanning Electron Microscopy (SEM) and isothermal calorimetry. The second objective of this study is to compare the phase assemblage predicted by thermodynamic modeling with experimental characterization. For the first time, the Pitzer model was used to account for the ion activity in the pore solution of AAS. Three thermodynamic datasets were used to model the phase assemblage of AAS paste along with time. Among them, CEMDATA18, zeolite20 and CASH+ models have not been used in previous studies to predict the reaction products of AAS. The different computed phase assemblages were compared with the products chemically characterized. Discussion on the application of the thermodynamic model is provided, as well as a critical comparison between the three used datasets to find the dataset that agrees the most with the experimental characterization.

2. Materials and methods

2.1. Materials

In this study, two mixes were prepared and studied. They were generated from the same slag provided by the company EcoCem. Its oxide composition was measured with M4 Tornado (Bruker GmbH Karlsruhe, Germany) using energy dispersive X-ray fluorescence (XRF) spectrometer and is given in Table 1. Silicate-alkali activators are combinations of three components: commercial waterglass, NaOH solution and water. Waterglass was provided by Woellner GmbH. It has a solute concentration of 34.5 % (mass) and a molar ratio SiO_2/Na_2O of 3.4 [mol/mol]. It was mixed with a NaOH solution (mass concentration of 50 %) and water to get two solutions with the following parameters: water/slag ratio $w/s = 0.4$, alkali dosage $n = 5$ [g Na_2O/100 g slag] and silicate ratio M_S = SiO_2/Na_2O [mol/mol] equals either to 0.5 (mix lS) or to 2.2 (mix hS). The choice of these mixes is justified by the setting time. As shown in [7,9,10], the setting time is at the lowest for intermediate M_S, that is for M_S between 1.0 and 2.0. The mix lS is also very similar to the paste used in the RILEM TC 247-DTA round-robin test [63]. Both mix lS and mix hS showed superior compressive strength on a concrete level (greater than 50 MPa at 28 days).

2.2. Methods

Paste samples were analyzed with different methods to obtain the phase assemblage and the degree of dissolution. For XRD, DTG, DTA and FTIR, samples were stored in plastic bags until the desired testing age and were then crushed and powdered. XRD tests were carried out directly after powdering for both mixes after 1, 2, 3, 7, 28 and 56 days with a Brucker D8 Advance instrument with Cu-Kα radiation and a nickel filter after grinding and milling the samples. The step size was 0.02°, for a 2θ from 5° to 70°, with 0.2 s/step. The samples used for DTG and DTA were first dried overnight at 50 °C to remove free water. Around 100 mg were then used with a Netzsch Simultaneous Thermal Analysis STA 409 with a speed of 10 °C/min between 100 °C and 1000 °C in a N_2 atmosphere. FTIR characterization was performed just after powdering with a Bruker Tensor 27 IR with a resolution of 1 cm^{-1} in the range 600–4000 cm^{-1}.

MAS NMR spectroscopy gives information on the local structure of the phases especially the poorly crystalline and amorphous phases of the alkali-activated slag paste and therefore completes the information obtained by the XRD. Solid state Al-MAS NMR was used to determine the tetrahedral and octahedral coordinated Al sites present in the C-A-S-H phases and other secondary products. The studied samples were crushed into 63 μm powder. Solid state MAS NMR was performed on a Bruker Avance III HD 500 (11.7 T) spectrometer, with a 4.0 mm dual resonance CP/MAS probe, operating at a Larmor frequency of 130.32 MHz. For Al-MAS NMR, the spinning speed is 12.5 kHz with a relaxation delay of 5 s, a pulse duration of 1.70 μs and 512 repetitions. Al shift is referenced to an external 1.0 M aqueous solution of $Al(NO_3)_3$. This technique is used for both mixes after 5, 30 and 60 h of reaction.

Porosity and pore size distribution was measured with MIP for 1, 2, 3, 7, 28 and 56-day samples using a Micromeritics AutoPore V. The mercury intrusion pressure was increased up to 400 MPa. The samples were crushed into pieces of 1 cm and dried at 60 °C

overnight. The overall porosity was also followed by saturating parallel specimens at 99 % RH and then drying them in an oven at 105 °C, where the normalized difference in weight corresponds to the total porosity.

The degree of dissolution of the slag of both mixes was investigated at early age (< 7 days) with isothermal calorimetry at 20 °C with the same protocol as described in [64]. This result was completed with SEM. For SEM samples, the activation of paste specimens was stopped via the solvent exchange method described in [65]. Samples were crushed into pieces of 5 mm and plunged into isopropanol. The solvent was renewed after 15 min and every day for one week. After one week, the samples were conditioned in desiccators until test day. The solvent exchange was proved to be the best method to stop the reaction of cementitious systems [66] and was used already for AAS in [26]. The grinding and polishing processes were performed with an AutoMet 250 equipment (Buehler). 2-propanol was used as a lubricant to avoid hydrating the sample during the sample preparation. The samples were rinsed in a 2-propanol ultrasonic bath between the grinding and polishing stages, as well as in between each polishing stage to remove any residue from the previous stage. Three polishing grades with MetaDi Supreme Diamond suspensions spray oil base (Buehler) of 3 μm, 1 μm and 0.25 μm were carried out for 10, 20 and 10 min, respectively. The force applied for each polishing was 10 N. At the end of the polishing, samples were cleaned by N_2 air steam and stored in a desiccator until the day of testing. These specimens were analyzed using a Hitachi benchtop ESEM TM3030 SEM to analyze the matrix. One millimetre of working distance and 15 kV of acceleration voltage was applied. Each sample was previously polished and carbon coated. The magnification factor was 800 for all the images taken. SEM images were then post-processed to highlight the unhydrated parts of the slag using the grey-level histogram. The unhydrated particles are denser and thus brighter. Images were done for pastes of age of 5 h, 30 h, 60 h, 7 days, 28 days and 56 days and 10 images were taken per date. In presence of sodium silicate, the solvent exchange technique can lead to the formation of crystals. This was also observed during sample preparation for this study. However, for the results reported here, these regions were carefully avoided so that they do not interfere with the interpretation of dissolution degree using SEM.

2.3. Thermodynamic modeling

Thermodynamic modeling was done using the Gibbs free Energy Minimization (GEMS) software [67]. The implementation of activity models in this software was described in [68]. In literature, most of the thermodynamic calculations for alkali-activated slag systems [25,26,39,58] were done using the extended Debye–Hückel activity model [41]. With this model, the activity coefficients of aqueous species are expressed as:

$$log\gamma_i = \frac{-A_\gamma z_i^2 \sqrt{I}}{1 + B_\gamma a_i \sqrt{I}} + b_\gamma I \quad (1)$$

where, for each species i, z_i is the charge, a_i is the ion-size parameter, I the effective modal ionic strength, b_γ is a semi-empirical parameter, A_γ and B_γ represent the water solvent parameters. For a NaOH electrolyte, b_γ and a_i are 0.098 and 3.31, respectively. Nevertheless, this model is thought to be valid for ionic strengths up to 1 mol/L [69], or even to 1–2 mol/L for cement/slag systems [42,49]. For alkali-activated slag systems, the ionic strength may be higher than 2 mol/L; particularly at early age. The use of Pitzer activity ion model [44–47] is therefore generally preferable at such high ionic strengths. Pitzer ion activity model contains interaction parameters of different orders between aqueous species that account for short-range interactions in the solution and thus allows modeling of concentrated multi-component aqueous solutions. A detailed description of the Pitzer model can be found in Appendix A. The model formulation implemented in GEMS is the one developed by Harvie, Moller and Weare [70,71]. The interaction parameters needed for the Pitzer model are obtained from Prentice [49]. In addition to considering interactions for polymeric species containing aluminum and silicon, data from Xiong et al. [48] was used. The considered interaction parameters and their values are given in Supplementary Material.

Thermodynamic data for the aqueous species and for cement hydrates is taken from the PSI-Nagra thermodynamic database [72] and CEMDATA18 [55], respectively. For C-A-S-H, Mg phases (hydrotalcite and magnesium silicate hydrates M-S-H) and zeolite phases, a combination of three thermodynamic datasets are compared. The first data set contains the C-A-S-H and hydrotalcite models developed by Myers et al. [24], which will be referred to as Myers15. Five zeolite phases are also considered (Na-analcime, natrolite, Ca-heulandite, (Ca, Na)-heulandite and sodalite) with thermodynamic data given in [24]. The second dataset is a combination of phases from Cemdata18 database using the aam library [55] and the zeolite20 database developed by Ma et al. [59,60]. It will be referred to as C18-Z20. The aam library contains the C-A-S-H and hydrotalcite models from Myers et al. [24]. Additionally, this dataset contains thermodynamic data for M-S-H. These are modeled as 2 end-members of solid solution. Finally, twenty zeolites from Ma et al. [59] replace the zeolites proposed by Myers et al. [24]. The third dataset uses the CASH+ thermodynamic model for the C-(N-)A-S-H gel, coming from [61] and extended in [62] and will be referred to as CASH+Z20. Data for hydrotalcite, M-S-H and zeolites are the same as for the C18-Z20 dataset. The summary of the variations in these three datasets is presented in Table 2.

The slag dissolution kinetics was taken from SEM results presented in Section 3.3. The dissolution of slag can be incongruent (i.e. different oxides dissolve at different rates) during the first hours after mixing the slag in a solution. This is due to the fact that only the less stable silicate species dissolve in the liquid up to the supersaturation in C-S-H, as shown in [73,74]. After this period, the slag dissolution becomes congruent (i.e. dissolution rate of different oxides is the same). More recently, Snellings et al. [75,76] showed that the dissolution of calcium-aluminosilicate glasses and slag depends on the pH of the solution. At pH lower than 10–11, the slag dissolution is incongruent, while above 10–11, the dissolution is congruent. For the pore solution of AAS, the pH is above 12 [26] and thus a congruent dissolution is hypothesized in this study. For the thermodynamic calculations, it means that the steps were made on increments of slag compositions (see Table 1) corresponding to the degree of dissolution. The alkali solution was modeled as an equivalent of SiO_2, Na_2O and H_2O compositions.

Table 2
Description and different of the tested datasets.

Phases	Reference	Myers15	C18-Z20	CASH+Z20
CNASH	[24]	✓	✓	–
CASH+	[61]	–	–	✓
MgAl-OH-LDH	[55]	✓	✓	✓
M-S-H	[55]	–	✓	✓
Zeolites	[24]	✓	–	–
Zeolites	[59,60]	–	✓	✓

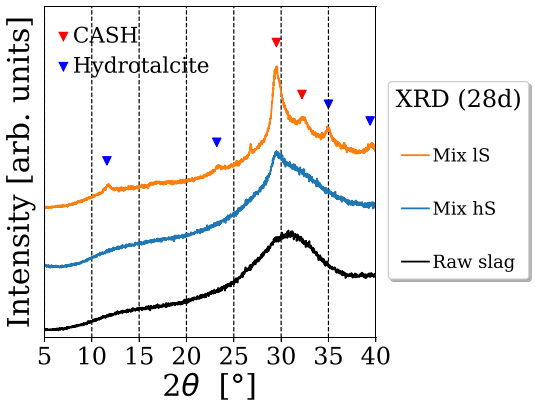

Fig. 2. XRD results with Cu-Kα radiation for both mixes lS and hS after 28 days.

3. Experimental results

The formation of reaction products was followed at several ages with different characterization techniques. The reaction products obtained with chemical characterization techniques are provided first, followed by the porosity results and finally by the results of dissolution kinetics.

3.1. Reaction products

Results from XRD for both mixes at 28 days are given in Fig. 2, as well as for different ages of reaction in Fig. 3. For the mix lS, a very clear development of C-A-S-H phase (peaks at 29.5°, 32° and 50°) can be seen at each measured time. The second main product that was identified is hydrotalcite (peaks at 11.5°, 23°, 35°, 39.5° [18,36,77,78]). It was characterized from two days of reaction. XRD analysis was made on four replicates done for four different castings for each age and each mix. For the mix lS, strätlingite was observed only for one casting after 2 days (peaks at 7°, 18°, 34°, 36° and 47° [36,79]) and at later ages only traces were visible. This could result from the heterogeneities present due to the casting process of the paste samples. The presence of C-A-S-H and hydrotalcite in the mix lS are also confirmed by DTG results (see Fig. 4) with peaks at around 150 °C for C-A-S-H, 220 and 400 °C for hydrotalcite. For the mix hS, no crystalline phases could be observed during the first month (see Fig. 3). Only a small peak could be observed with XRD characterizing the ordered C-A-S-H phase (at 29.5°). Though, DTG shows the presence of C-A-S-H, which must be mainly in a nano-crystalline form (Fig. 4). DTA results after 28 days are given in Fig. 4. For both mixes, the endothermic peak between 100 °C and 200 °C corresponds to water loss contained in pores and in gel [80]. For the mix hS, an exothermic peak is observed at 800–850 °C. It is characteristic either of C-A-S-H with a high Ca/Si ratio [81] or to the crystallization of the M-S-H gel into $MgSiO_3$ [80,82]. Results of DTG and DTA at several ages are given in Supplementary Material.

The results of the FTIR analysis at 28 days are displayed in Fig. 5. The complete spectra between 600 cm^{-1} and 4000 cm^{-1} at several days are provided in Supplementary Material. The band at 650 cm^{-1} is assigned to Si-O-Si bending in C-S-H [83,84] and is present for both mixes. The band at 800–850 cm^{-1} is associated with Si–O stretching of Q^1 tetrahedron [83]. The greater intensity for the mix lS could be characteristic of a bigger Ca/Si ratio in the C-A-S-H structure, as it is the case for C-S-H phases [85]. For both mixes, the main peak of the spectra at 930–940 cm^{-1} is attributed to Si–O stretching modes in C-S-H [84]. The slight shift to a lower wavelength value for the mix lS (934 cm^{-1} for the mix lS, 941 cm^{-1} for the mix hS) is also characteristic of a higher Ca/Si ratio in C-S-H [85]. This peak is also superimposed with the band between 930 cm^{-1} and 960 cm^{-1}. This band is assigned to Q_b^2 from Si–O stretching modes in the bridging tetrahedron [84,85]. The larger band for the mix hS would indicate a more polymerized C-A-S-H gel in comparison to the mix lS. The shoulder at 1000–1050 cm^{-1} for both mixes is associated with Si–O stretching of Q^2 sites in C-A-S-H [84,85]. The band 600–780 cm^{-1}, visible mainly for the mix hS, may be assigned to 4-membered ring vibrations in zeolites of the S4R group (for example analcime or gismondite) or 4= I group (for example natrolite) [86]. The peak at 715 cm^{-1}

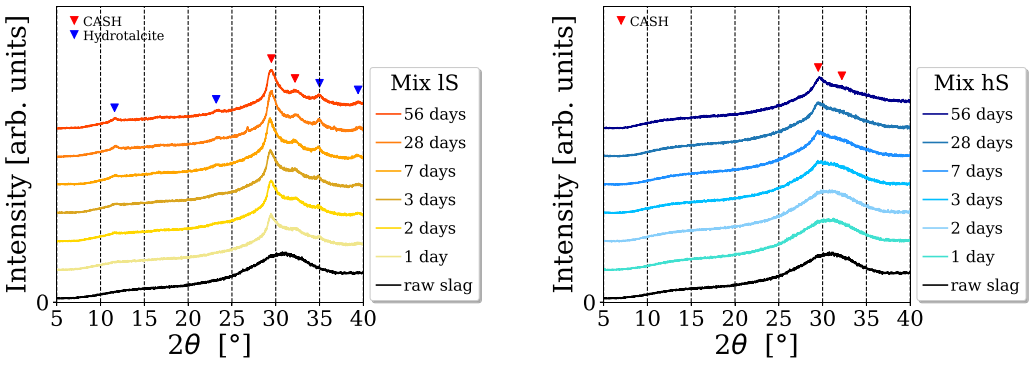

Fig. 3. XRD results with Cu-Kα radiation for both mix lS (left) and mix hS (right) from 1 to 56 days.

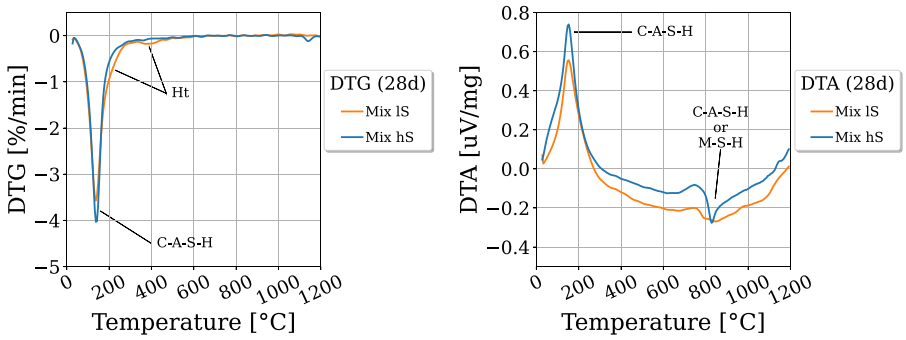

Fig. 4. DTG (left) and DTA (right) results for both mixes lS and hS after 28 days.

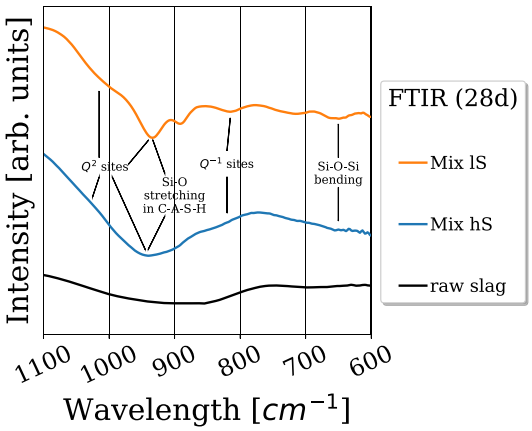

Fig. 5. FTIR results for both mixes lS and hS after 28 days.

visible for both mixes could be attributed to symmetric stretching vibrations of bridge bonds Si–O–Si of zeolite phases [86] or to the bending of Al–O–Si bonds in ring structures [87,88] as such as present in zeolites.

Al-NMR results after 5, 30 and 60 h of reaction are shown in Fig. 6. The peak at 9 ppm for both mixes shows the presence of the octahedral Al sites belonging to the layered double hydroxide (LDH) reaction products. For the mix lS, this peak is much more intense at 30 h in comparison to 5 h, which shows that LDH phases develop during the first hours of hydration. For the mix hS, this peak appears only after 30 h and its intensity is lower than for the mix lS, indicating that the amount of these phases is smaller for the mix hS than for the mix lS. A broad peak from 85 ppm to 50 ppm is observed for the mix lS. It can be attributed to the resonance of the tetrahedral Al sites present in the unreacted slag as well as in C-S-H [89]. The center of gravity shifts from 68 ppm at 5 h to 75 ppm at 30 and 60 h. This shift can be attributed to the formation of C-S-H containing Al. At Ca/Si > 1.0, the main Al(IV) signal of Al present in the bridging site in C-S-H has been observed at 76 ppm, while the signal shifts to 68 at Ca/Si = 0.8 and to 63 at Ca/Si = 0.6 [89]. For the mix hS, the Al-NMR peak centered on 63 ppm could indicate the presence of C-S-H with a very low Ca/Si, and potentially the presence of some additional zeolite phases [90].

The formation of C-A-S-H and hydrotalcite is consistent with observations from the literature. Ben Haha et al. [36] found both C-A-S-H and hydrotalcite with the combination of w/b = 0.4, n = 2.9 Na_2O g/100 g slag and M_S = 1. Ye & Radlińska [26] found

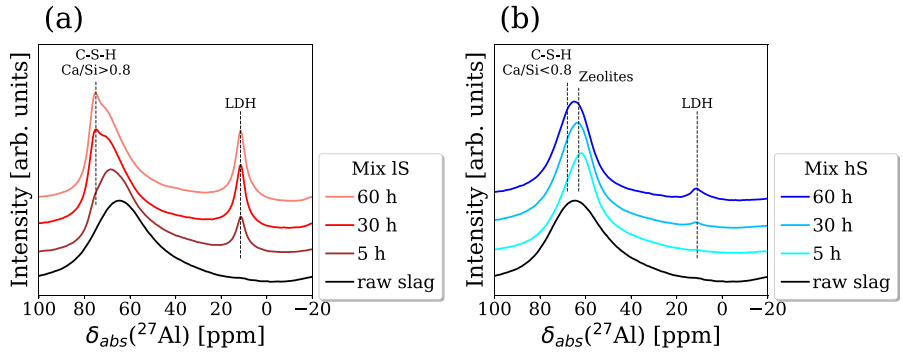

Fig. 6. NMR results for both mixes lS (left) and hS (right) after 5, 30 and 60 h of reaction.

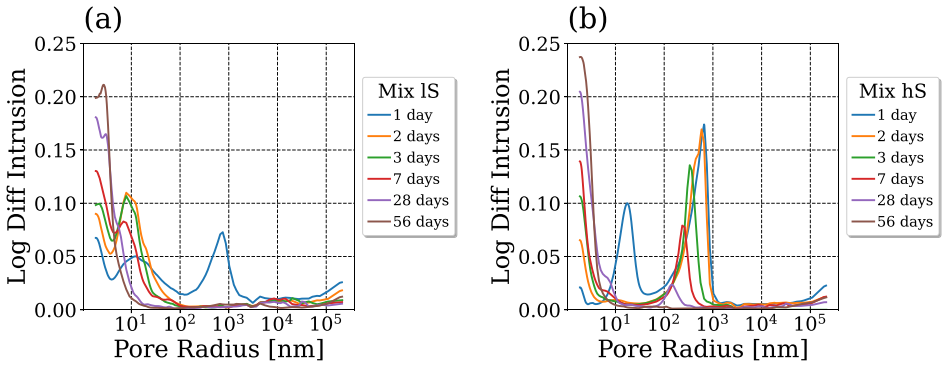

Fig. 7. MIP results along time for both mixes lS (a) and hS (b).

also the presence of C-A-S-H and hydrotalcite for two sodium silicate-activated slags. The presence of hydrotalcite is also dependent on the amount of MgO in the slag, e.g., Bernal et al. [10] found that for a slag with less than 3 % MgO oxide mass content, no hydrotalcite is formed. In [36], strätlingite was also predicted from thermodynamic calculations for an amount of Al_2O_3 higher than 7 % oxide mass in the slag composition. Criado et al. [14] identified strätlingite for two mixes with $w/b = 0.4$, $M_S = 1$ and $n = 3$ or 8 g/100 g slag. Bernal et al. [10] found the presence of gismondine as zeolites in alkali-activated slag for high M_S (1.6, 2.0 and 2.4). For the two mixes of this study, zeolites could not be identified by XRD but only by FTIR and NMR. For this reason, they should be crystalline precursor zeolites. Finally, results from FTIR and NMR tests for the mix hS seem to indicate that the generated C-A-S-H phase for this mix has a low Ca/Si ratio. This would mean that the peak at 800 °C present in the DTA test should be characteristic of M-S-H products. These products were chemically characterized for blended silica fume and MgO systems in [80,82]. They have not been previously reported for alkali-activated slag. However, studies focusing on cement-clay interface, leaching of cement pastes or chloride ingress due to seawater and NaCl have often reported the formation of M-S-H [55,91].

3.2. Pore structure

The evolution of the pore size distribution of both mixes after 1, 2, 3, 7, 28 and 56 days is plotted in Fig. 7. The results of MIP show that the mix lS has mainly small pores (< 50 nm) and almost no capillary pores (> 50 nm) from two days. For the mix hS, the pore structure contains capillary pores for up to 56 days, but its proportion drops progressively. Both mixes present pore distributions with small sizes, which are comparable with what was reported in e.g. [92]. As seen with SEM images (see Fig. 9), some microcracks with a width of a few hundred nanometers are observed. Moreover, the MIP technique has the tendency to shift the results to smaller pores due to the ink-bottle effect. For this reason, some fractions of pores from 100 nm observed with MIP could be a result of micro-cracks. However, the proportion of cracks in SEM images is lower than 1 %. A classification of pores in the AAS matrix is tentatively proposed in Table 3. For both mixes, the reduction of the volume of pores in the range [100 nm–2000 nm] could be due to self-desiccation that closes them progressively and thus explains the higher shrinkage observed for the mix hS as found in [11]. The total porosity measured with MIP between 1 and 56 days decreases from 25 % vol. to 17 % vol. and 27 % vol. to 14 % for the mix lS and mix hS, respectively. The overall porosity measured with a saturation-drying cycle provides higher values but a similar drop is observed. For mix lS and mix hS the porosity drops from 45 % vol. to 39 % vol. and from 43 % vol. to 37 % vol., respectively. As explained in [93] for cement pastes, MIP measures mainly capillary porosity and only a part of the gel porosity of pastes. Thus, the difference between both experimental methods (MIP and saturation-drying cycle) could come from a large number of gel pores not accessible by MIP, as observed for cement pastes [94].

Table 3
Classification of pores and cracks.

Method		MIP	MIP	MIP	dry. 105 °C	SEM
Volumes %	Age [d]	gel pores (< 50 nm)	cap. pores (> 50 nm)	total porosity	total porosity	cracks volume
mix lS	1	11.0	13.9	24.9	44.4	0.02
	2	17.5	4.4	21.9	43.2	0.02
	3	17.2	3.8	21.0	42.9	0.01
	7	15.7	3.5	19.2	41.6	0.02
	28	15.3	2.5	17.8	39.5	0.02
	56	14.6	2.5	17.1	39.0	0.02
mix hS	1	8.5	18.4	26.9	42.8	0.18
	2	3.6	17.2	20.7	41.5	0.05
	3	5.2	11.3	16.5	41.0	0.03
	7	6.7	7.4	14.1	39.2	0.03
	28	11.4	3.1	14.5	38.2	0.03
	56	11.9	1.8	13.7	37.5	0.02

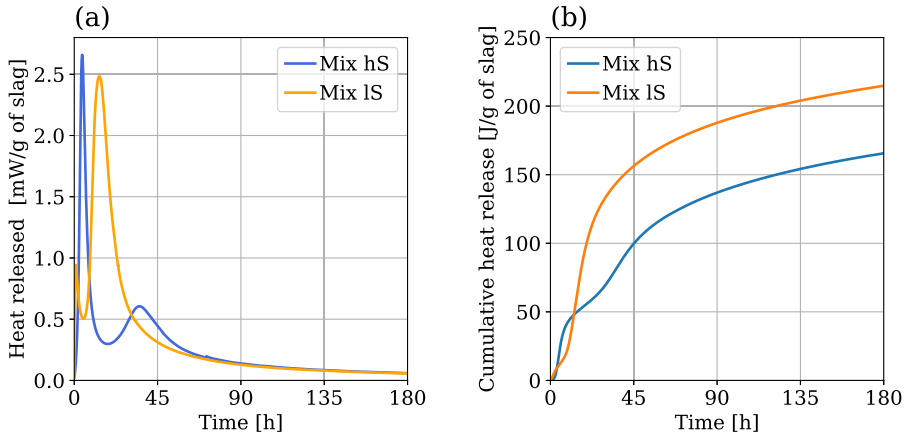

Fig. 8. Isothermal calorimetry results for both mixes hS and lS: (a): heat flow, (b): cumulative heat release.

3.3. Kinetics of the dissolution of slag

The dissolution kinetics of AAS with isothermal calorimetry and SEM at different ages is presented. The results of isothermal calorimetry were already presented and interpreted in [64]. They are shown in Fig. 8. They indicate that both mixes present the characteristic two-peak heat release for sodium silicate-activated slag [95]. Nevertheless, the peak occurrence and intensity differ with the used solution. After 7 days, the heat release of the mix lS is higher than the one of the mix hS.

The post-processing of SEM images was shown to follow the consumption of slag as a function of time [96,97]. An example of a thresholded SEM image is shown in Fig. 9, which clearly shows the unreacted slag particles and thus allows the calculation of the reaction degree. The evolution of the degree of dissolution of slag up to 56 days is given in Fig. 10(a). The error bars correspond to the standard deviation of the image analysis done on ten SEM images for each data point. SEM results show that the slag dissolves faster in the case of the mix lS compared to the mix hS with a degree of dissolution equal to 55 % and 48 %, respectively, after 56 days. Alkali solutions with higher M_S have a lower pH, as shown in [98]. This could explain the lower degree of reaction for the mix hS. Another explanation can be that the alkali solution of the mix hS has more silicon dissolved in it and hence less silicon needs to be dissolved from the slag to reach equilibrium. The degree of dissolution of slag observed in this study is comparable with that in the literature. Ben Haha et al. [17] found a degree of slag reactivity equal to 48 % after 180 days, Le Saoût et al. [28] found it equal to 52 % after 28 days and 54 % after 100 days and Bernal et al. [12] found 45, 58 and 79 % after 56 days for three different slags. As shown in [64], the evolution of the reaction kinetics of alkali-activated slag can be modeled with a diffusion mechanism corresponding to the diffusion of ions through the shell of reaction products surrounding the unreacted particles. The corresponding equation is the Ginstling–Brounshtein equation, as proposed in [64,99]:

$$f(\alpha) = \frac{1}{k}\frac{d\alpha}{dt} = \frac{3}{2((1-\alpha)^{-1/3}-1)} \tag{2}$$

where α [-] is the degree of reaction and k [h^{-1}] the reaction rate. The degree of reaction for any time is obtained by optimizing the reaction rate k from the data of SEM experiments performed after three days using the same approach as described in [64]. The obtained model is plotted in Fig. 10 (a).

A comparison of the reaction degree obtained from both calorimetry and SEM results is shown in Fig. 10(b). For isothermal calorimetry data, the maximum heat release required to normalize the heat release curve to reaction degree is estimated using the

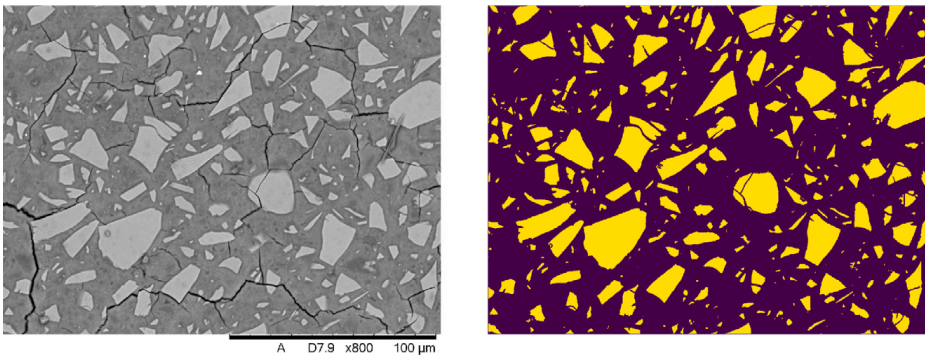

Fig. 9. SEM image with a magnification of 800 (left); Postprocess using grey histogram, yellow pixels correspond to unreacted slag (right). (For interpretation of the references to colour in this figure legend, the reader is referred to the web version of this article.)

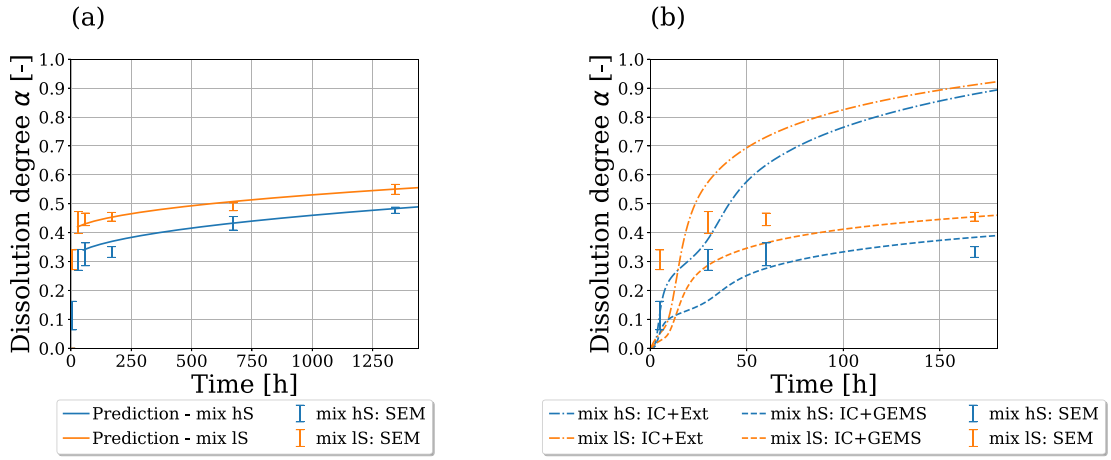

Fig. 10. (a) Prediction of the degree of dissolution with SEM results until 60 days and extrapolation using the Ginstling–Brounshtein equation after three days; (b) Comparison of calorimetry and SEM post-process results for both mixes lS and hS until 7 days: IC+Ext stands for prediction with Isothermal Calorimetry and exponential extrapolation for final heat release; IC+GEMS stands for prediction with Isothermal Calorimetry and GEMS enthalpy calculation for final heat release.

exponential model from [100]. This is a commonly used approach in literature to obtain the reaction degree [30,101,102] The use of isothermal calorimetry data alone greatly overestimate the degree of dissolution of slag at late age (method IC + Ext). This is because the maximum heat release obtained using the extrapolation method is too low. A similar observation has been previously made by Kocaba et al. [103] for slag dissolution in blended cement systems. Kocaba et al. stressed the importance of using SEM data to calibrate isothermal calorimetry. This has direct implications for the kinetic models developed using just calorimetry data. For instance, in the case of a previous study [64], the kinetic parameters obtained for the diffusion mechanism need to be re-calibrated with results using SEM imaging.

An alternative approach is proposed here to obtain realistic estimates of the maximum heat release. It uses the enthalpy of heat release of reactants and products using GEMS. The total enthalpy of the system can be calculated for every thermodynamic calculation and is linked to the heat of reaction with the following equation:

$$\delta Q(t) = H(t) - (H_0 + H_{un.s}) \tag{3}$$

where H_0 corresponds to the enthalpy of the initial alkali solution and $H_{un.s.}$ the enthalpy of the unreacted slag. To obtain the enthalpy of unreacted slag, optimization was carried out on the heat release obtained experimentally after seven days for both mixes [64]. The estimated enthalpy of unreacted slag is around −14.8 kJ/g. This value is comparable to that reported for slags with similar compositions e.g., −13.9 kJ/g in [104] and −14.4 kJ/g in [105]. Using this value of slag enthalpy, the theoretical maximum heat released when all slag is reacted can be computed:

$$\delta Q_{max} = H_{100} - (H_0 + H_{un.s}) \tag{4}$$

where H_{100} corresponds to the theoretical limit where 100 % of the slag has reacted. Such an approach has been used in the past for OPC systems [106]. The obtained values of maximum heat releases are 466.6 J/g for the mix lS and 424.6 J/g for the mix hS. The ratio between the heat release at 7 days and the maximum heat release corresponds to the degree of dissolution at 7 days. It is equal to 45.5 % for the mix lS and 38.3 % for the mix hS using this approach. These values agree with the results using SEM (see Fig. 10(b)). Thus, using the maximum heat release through such calculations to normalize the calorimetry data is a better approach than extrapolating calorimetry data using exponential models.

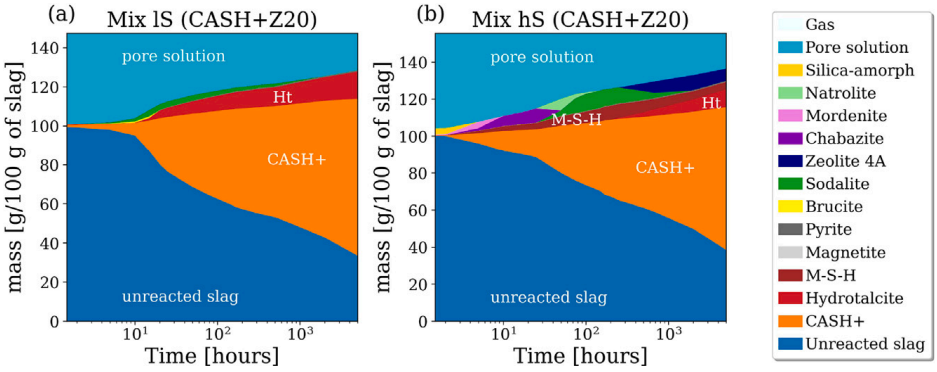

Fig. 11. Thermodynamic calculations with the CASH+Z20 dataset for both mixes lS (a) and hS (b).

4. Thermodynamic modeling

4.1. Phase assemblage obtained with the CASH+ model

The phase assemblages of reaction products expected to form during hydration have been calculated using thermodynamic modeling with the CASH+Z20 dataset using the amount of dissolved slag as input. The amount of dissolved slag is obtained using the kinetic model described in Section 3.3. Fig. 11(a) and (b) provide results of the thermodynamic calculations for both mixes lS and hS, respectively. For the mix lS, the thermodynamic model predicts the formation of C-A-S-H, hydrotalcite and zeolites. This is in accordance with experimental results presented in Section 3.1. Note that for the CASH+ model, the aluminum uptake is relatively high (see Fig. 12) and does not favor the presence of strätlingite. However, it should be noted that a destabilization of the CASH+ by 1 log unit, or a stabilization of strätlingite by 1 log unit, would have led to the prediction of strätlingite. Considering the small differences in the stability of C-A-S-H and strätlingite in these alkali-activated slags and that the error on the thermodynamic data of these phases is in the range of half a log unit, the formation of strätlingite seems to be possible. In addition, an increase of Al uptake in C-S-H with time has been observed experimentally [107], which will further lower the amount of strätlingite. Note that in the performed experiments, strätlingite was observed for one of the replicates. This would imply that the microstructure heterogeneities might impose kinetic constraints that might lead to the formation of strätlingite. For the mix hS, C-A-S-H, hydrotalcite, M-S-H and zeolite phases are predicted. C-A-S-H was observed with DTG in Section 3.1. Hydrotalcite has not been observed through XRD in our study but Al-NMR shows the formation of Hydrotalcite. The prediction of M-S-H for this mix is in coherence with the combination of DTA and Al-NMR results presented also in Section 3.1. The presence of zeolitic precursors is also in accordance with FTIR and NMR results (see Figs. 5 and 6). For both mixes, small amounts of pyrite and magnetite are predicted due to the presence of reduced amounts of Fe and S in the slag.

The Ca/Si ratio obtained for the C-A-S-H phases is higher for the mix lS compared to mix hS (see Fig. 12). This is in accordance with FTIR and Al-NMR results (see Figs. 5 and 6). In Al-NMR, shown in Fig. 6, one can distinguish that the Ca/Si ratio is higher than 0.8 and lower than 0.8 for the mix lS and mix hS, respectively. This observation validates the computed C-A-S-H phase with the thermodynamic calculations for which the computed Ca/Si ratio is equal to 1.03 for the mix lS and 0.77 for the mix hS after 60 h using the CASH+Z20 dataset. From the thermodynamic modeling, two periods can be distinguished for Ca/Si and Al/Si ratios. They correspond to an early age with lower slag reaction and thus relatively low Ca/Si and a later age with higher slag reaction resulting in a higher Ca/Si and a higher aluminum uptake (see Fig. 12). For the mix lS, the transition between both periods occurs at 10 h, corresponding to the beginning of the second acceleration period of the slag activation [64]. For the mix hS, it occurs at around 50 h, corresponding to the end of the second peak in the isothermal calorimetry curve (Fig. 8). This observation supports the idea that two C-A-S-H gel-type phases would be generated with time, as suggested in [95,108].

The comparison between the total porosity obtained from the thermodynamic modeling and experiments is shown in Fig. 13. For the mix lS, the calculated porosity is very close to what is found experimentally with a cycle of saturation-drying at 105 °C. For the mix hS, the calculated porosity is 4 % lower than that obtained from experiments. One can also note that the total porosity measured with MIP is much lower than the one computed with GEMS, as it was already observed for cements in [109].

4.2. Comparisons between the different thermodynamic datasets

The three tested thermodynamic datasets (Myers15, C18-Z20, CASH+20) are analyzed, compared and discussed. The obtained results for both mixes are plotted in Fig. 14.

For both mixes, the CASH+ model (Fig. 11(a) and (b)) predicts a slightly higher mass of formed C-A-S-H after 28 days for 100 g of initial slag than when using the CNASH_ss solid solution model (Fig. 14(a) to (d)). For the mix lS, 59.6 g and 49.0 g are predicted with the CASH+ model and CNASH_ss model, respectively. Similarly, for the mix hS, 52.0 g and 48.4 g are predicted using CASH+ and CNASH_ss models, respectively. The calculated Ca/Si, Al/Si and Na/Si in the C-A-S-H phase for each thermodynamic dataset are shown in Fig. 12. For both mixes, the aluminum uptake in the C-A-S-H gel is lower when using the CNASH_ss solid solution model

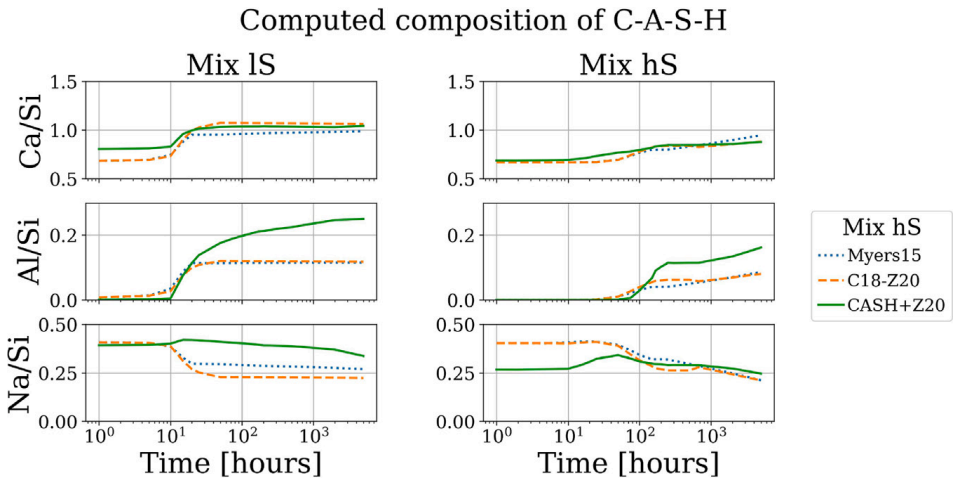

Fig. 12. Calculated Ca/Si, Al/Si and Na/Si ratios along time in the C-A-S-H models for both mixes lS (left) and hS (right).

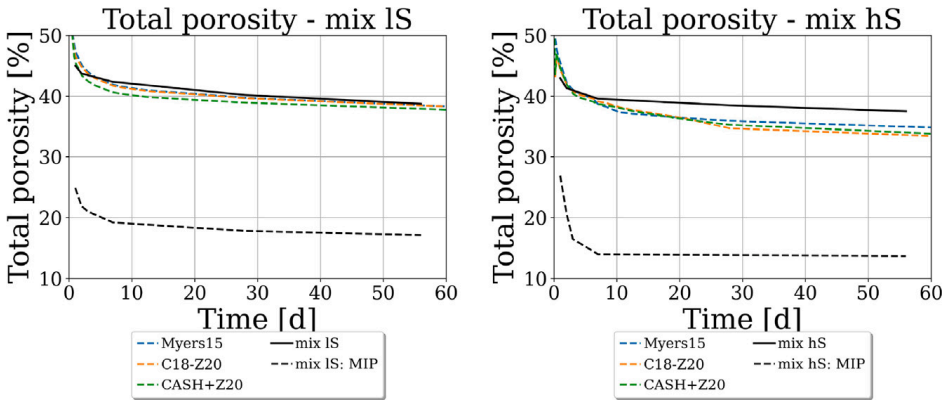

Fig. 13. Calculated total porosity of mixes lS (left) and hS (right) and comparison with experimental results; cycle stands for cycle of saturation-drying at 105 °C; MIP stands for total porosity measured with Mercury Intrusion Porosimetry.

(see Fig. 12). This explains the presence of strätlingite in the computed phase assemblages of the datasets Myers15 and C18-Z20, while it is not present for the dataset CASH+Z20. Here, the CASH+Z20 is more consistent with our experimental observation. Finally, as shown in Fig. 15, the pH of the pore solution for the mix lS stays high for both datasets Myers15 and C18-Z20, while it decreases for the dataset CASH+Z20. For the mix hS, the pH value decreases for the three datasets and the dataset CASH+Z20 has also a lower value.

The ionic strengths are also plotted in Fig. 15. At early-age, the ionic strength for both mixes is high (~ 5) due to the large concentration of Na and Si ions in the initial alkali solutions. After four days, the ionic strength goes below 1. This justifies at early-age the use of the Pitzer model, which is valid for high ionic strengths [43,49]. The extended Debye–Hückel ion activity model (Eq. (1)) is considered to be valid up to 1–2 M [49], which is achieved for the two mixes studied here by the end of two days. The calculations made with both activity models predict the formation of the exact same phases. For the activation of 100 g of slag, the predicted phase assemblages varied between both models by an absolute difference of at most 2.5 g at early age. After two days of reaction, when the ionic strength is lower (~ 1), the absolute difference was less than 0.3 g. The results of the thermodynamic calculations made with the extended Debye–Hückel ion activity model are provided in Supplementary Material. The comparison of both activity models highlights that, even though the ionic strength is much higher at early-ages, the extended Debye–Hückel ion activity model can be used for practical purposes for alkali-activated slag systems.

Brucite ($Mg(OH)_2$) is predicted in very small quantities and at early-age for the mix lS by all three datasets. For the mix hS though, it is either not predicted (C18-Z20 and CASH+ databases) or in relatively higher quantities between 100 to 200 h for the dataset Myers15, where no data for M-S-H are included. However, Myers et al. doubted the presence of brucite in reality [58]. The presence of brucite in the calculations using the dataset of Myers15 should be seen as an artifact resulting from the absence of M-S-H phase in this dataset.

The comparison of computed porosity using the three datasets is shown in Fig. 13. The three datasets provide similar results in terms of total porosity.

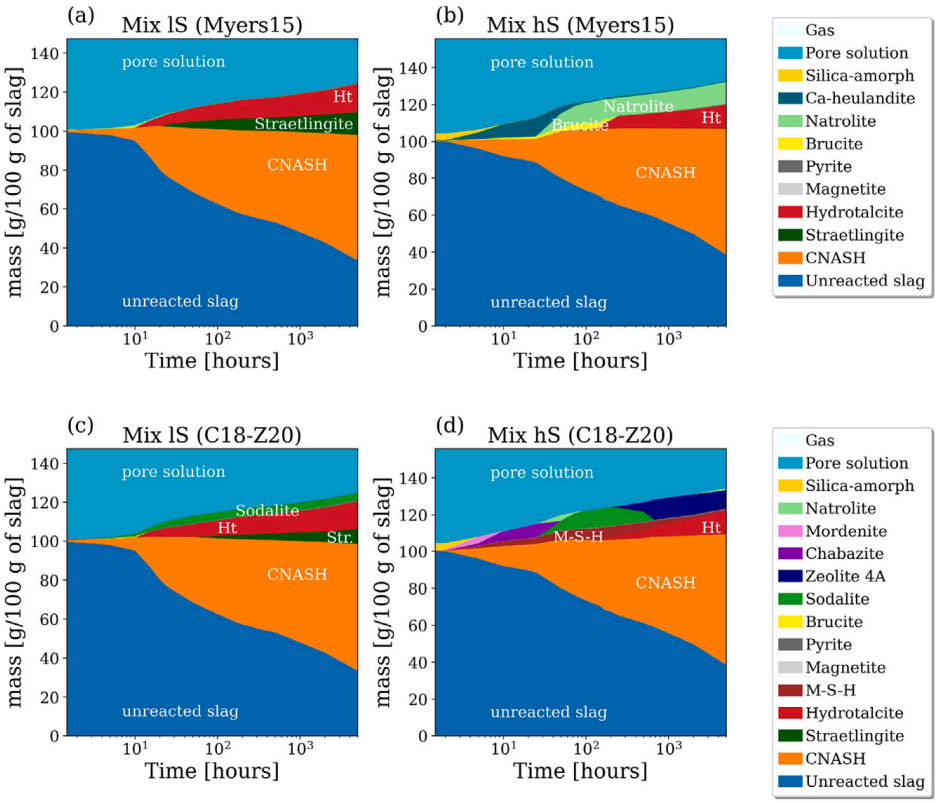

Fig. 14. Thermodynamic calculations with the Myers15 and C18-20 datasets for both mixes lS (left) and hS (right).

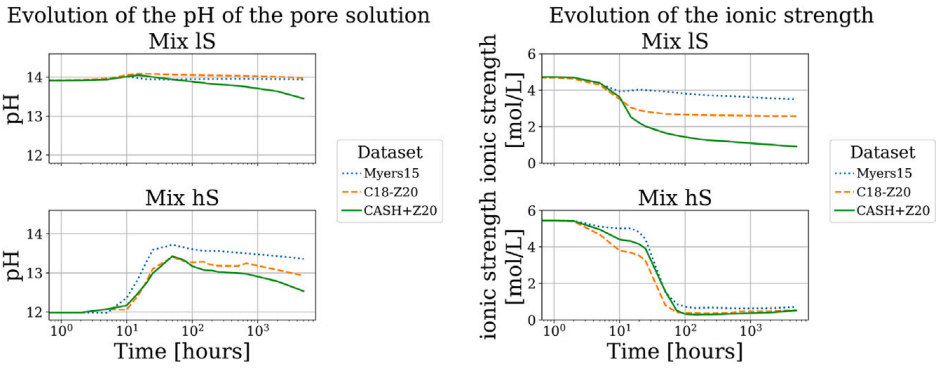

Fig. 15. Calculated pH in the pore solution over time for both mixes lS and hS (left). Calculated ionic strength in the pore solution over time for both mixes lS and hS (right).

4.3. Zeolite precursor modeling for the mix hS

This section focuses on the choice of zeolites in the thermodynamic modeling for the mix hS, for which higher amounts and types of zeolites were predicted. As illustrated in Fig. 11, the calculation for the mix hS predicts the formation of different zeolite precursor phases, viz., chabazite CHA(Na), natrolite NAT, commercial zeolite 4A, sodalite SOD(OH) and traces of mordenite MOR(Na). Not all of these phases are expected to form at ambient conditions, in particular the formation of natrolite and zeolite 4A are not probable. Specific calculations on this mix with the database CASH+Z20 were analyzed, in which one by one, the zeolites were ignored, i.e. deactivated in the GEMS calculations (see Fig. 16).

It can be seen that both CHA(Na) and NAT are in concurrence as reaction products at early age. For the calculation without CHA(Na) (see Fig. 16(a)), the CHA(Na) present from the initial calculation is totally replaced by NAT, and reciprocally for the calculation without NAT (see Fig. 16(b)). Both products disappear for each calculation after three days, corresponding to a degree of dissolution of around 35 %. For the calculations where SOD(OH) is activated, this zeolite disappears after around 1000 h and is replaced by more stable 4A (or NAT when 4A is removed from the calculation). A last calculation was carried out to take

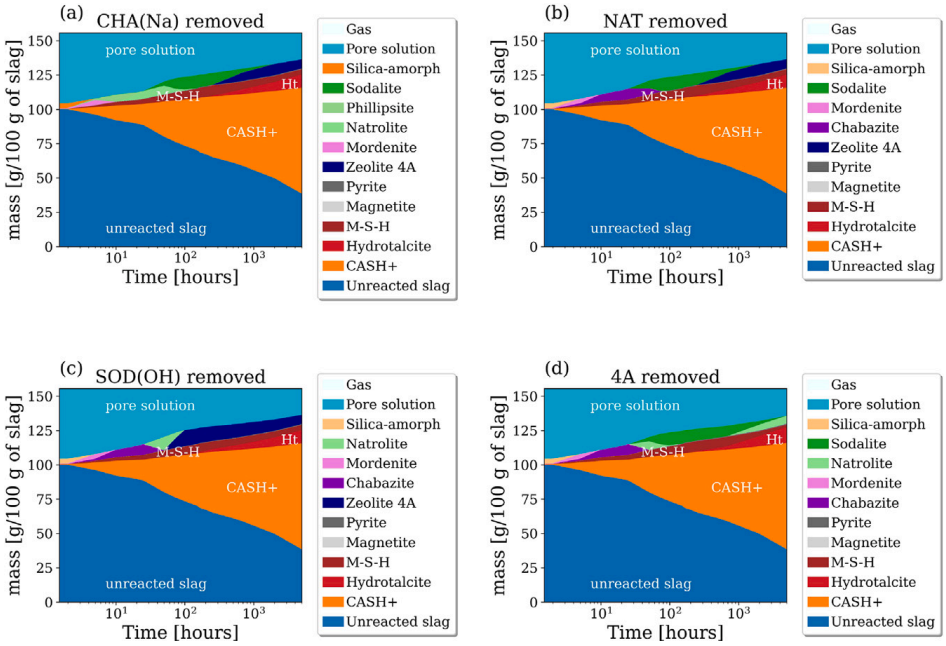

Fig. 16. Specific thermodynamic calculations on the mix hS varying zeolite databases.

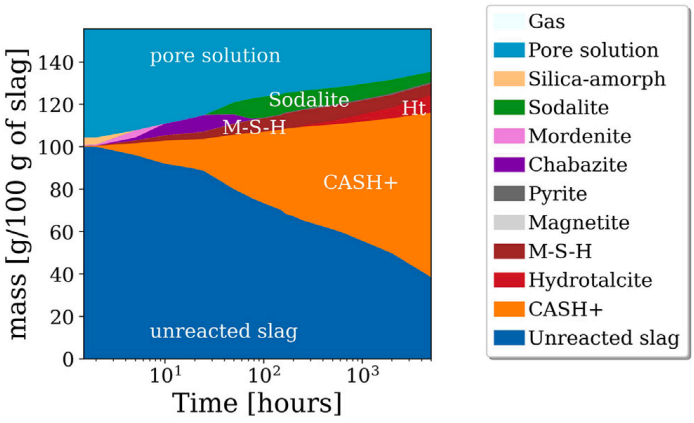

Fig. 17. Thermodynamic calculation for which GIS-LS-P(Ca), NAT, HEU(Ca)-1, HEU(Ca)-2, ANA and 4A were removed from the zeolite dataset.

into account the kinetic hindrance of the formation of some zeolites, as suggested in [59]. Under high alkali concentrations, the formation of gismondine (GIS-LS-P(Ca)) and NAT is hindered. Moreover, seeding is also a prerequisite for the formation of natrolite (NAT), heulandite (HEU(Ca)-1 and HEU(Ca)-2) and analcime (ANA). For these reasons, all of these zeolites were removed from this calculation. Also, the commercial zeolite 4A was removed. The result, plotted in Fig. 17, shows that CHA(Na) is present at early and late age. SOD(OH) appears after 10 h. It is the main zeolite between 20 and 5000 h but is progressively replaced by CHA(Na) from 2000 h. Finally, a small amount of MOR(Na) is predicted to form.

The zeolites are crystalline phases. Although they are predicted by the thermodynamic modeling, they are expected to be present not in well-ordered, crystalline form, but rather as disordered precursors, since they were not observed by XRD but only by FTIR and Al-NMR in this study.

5. Conclusions

In this study, the microstructures of two promising alkali-activated slag mixes were characterized with different experimental techniques. The phase assemblage was determined by XRD, DTG, DTA, Al-NMR and FTIR. C-A-S-H gel was present in both mixes. Al-NMR and FTIR experiments showed that the C-A-S-H gel of the mix hS (with M_S equal to 2.2) had a lower Ca/Si ratio than the mix lS (with M_S equal to 0.5). The results showed also that variations in the activator solution can lead to different secondary products. The main secondary product of the mix lS was hydrotalcite, which was characterized by both Al-NMR and XRD, indicating

a crystalline form. Moreover, the presence of strätlingite in this mix was also found in some replicate specimens and indicates that strätlingite could also form potentially. The mix hS also contained hydrotalcite, as analyzed by the Al-NMR spectrum, but in lower quantity. In addition to hydrotalcite, M-S-H was formed for the mix hS, as identified with DTA results. Zeolites could also be identified for both mixes with Al-NMR. The pore structure of both mixes was analyzed with MIP experiments. They indicated a higher pore refinement for the mix lS than the mix hS.

The dissolution kinetics of slag was followed with SEM and calorimetry. The degree of dissolution of slag after 56 days was equal to 55 % for the mix lS and 48 % for the mix hS. It was suggested to combine isothermal calorimetry results and heat release calculation from thermodynamic modeling using the enthalpy of slag of −14.8 kJ/g for predicting the degree of dissolution.

Thermodynamic calculations were made to predict the phase assemblage as a function of slag dissolution and time with the hypothesis of congruent dissolution. The computed phase assemblage with the Pitzer ion activity model and the CASH+Z20 database matches the experimental characterization of the reaction products of the two investigated mixes. The Pitzer model was used to account for ion interactions in the pore solution. This model is applicable for higher ionic strength, especially at very early-age of slag reaction. The comparison of calculations using the Pitzer ion activity model and the extended Debye–Hückel model showed that the ion activity model does not have a significant effect on the predicted phase assemblage for alkali-activated slag systems. Three thermodynamic datasets were tested for the reaction products. Both Cemdata18 [55] and CASH+ [61,62] models, completed with zeolite20 [59,60], agree in general with the experimental results. M-S-H phases prediction for the mix hS is comparable with experimental results for both C18-Z20 and CASH+Z20 datasets. The prediction of brucite in place of M-S-H for the mix hS with the Myers15 dataset [58] is due to the lack of M-S-H in that dataset. When using the CASH+ model no strätlingite is predicted to form, due to an increased aluminum uptake in the C-S-H structure.

In conclusion, the work done in the study paves a way to predict the time-dependent microstructure of the investigated AAS mixes. From the phase assemblage of these mixes, multi-scale modeling can be applied to predict varieties of material properties. This includes mechanical properties such as strength [94,110], Young's modulus [111] and creep modulus [112–114]. The prediction of the phase assemblage and the solution chemistry through thermodynamic modeling provides also indications on the durability behavior such as carbonation [12] and chloride binding [40]. In the future, we plan to use the computed phase assemblage from thermodynamic modeling as an input to predict Young's modulus and the creep compliance of concrete for the mixes of this study.

CRediT authorship contribution statement

Richard Caron: Conceptualization, Methodology, Software, Investigation, Writing – original draft. **Ravi A. Patel:** Conceptualization, Methodology, Investigation, Writing – review & editing, Supervision. **George D. Miron:** Conceptualization, Methodology, Investigation, Writing – review & editing. **Cassandre Le Galliard:** Methodology, Investigation, Writing – review & editing. **Barbara Lothenbach:** Conceptualization, Methodology, Investigation, Supervision, Writing – review & editing. **Frank Dehn:** Resources, Supervision, Writing – review & editing.

Declaration of competing interest

The authors declare that they have no known competing financial interests or personal relationships that could have appeared to influence the work reported in this paper.

Data availability

Data will be made available on request.

Acknowledgments

The authors would like to thank and acknowledge Dr Khalid Doudin Department of Chemistry, University of Sheffield, for assistance in acquiring the NMR data.

Funding

This work was supported by the European Union's Horizon 2020 research and innovation program under the Marie Skłodowska-Curie grant agreement No 813596.

The Scanning Electron Microscopy (SEM) analysis has been performed on a Hitachi TM3030-SEM belonging to the HADES/MIDAS facility at the University of Sheffield established with financial support from EPSRC, United Kingdom and BEIS, United Kingdom, under grant EP/T011424/1.

Appendix A. Description of the Pitzer model

This model considers ion-specific parameters for modeling the interactions in the pore solution. In the following equations, the subscripts M, c and c' refer to cationic species, while the subscripts X, a and a' refer to anionic species. γ_M and γ_X are the activity coefficients for cationic species and anionic species, respectively. c (resp. a) stands for the summation over all the cationic (resp. anionic) species, while c' (resp. a') stands for the sum over all interaction with dissimilar cations (resp. anions). γ_M is expressed as:

$$\begin{aligned} ln(\gamma_M) &= z_M^2 F + \sum_a m_a(2B_{Ma} + ZC_{Ma}) + \sum_c m_c(2\phi_{Mc} + \sum_a m_a\psi_{Mca}) \\ &+ \sum_{a<}\sum_{a'} m_a m_{a'}\psi_{aa'M} + |z_M|\sum_c\sum_a m_c m_a C_{ca} \end{aligned} \tag{5}$$

The same type of equation exist for determining γ_X, the activity coefficient of anionic species. This model formulation includes the use of a virial coefficient expansion in terms of molality. A Debye–Hückel type term is followed by interaction coefficients that consider the interaction between pairs of aqueous species (B, C and ϕ) and a term that includes ternary species interactions (ψ):

$$\begin{aligned} F &= -A^\phi\left[\frac{\sqrt{I}}{1+b\sqrt{I}} + \frac{2}{b}1 + ln(1+b\sqrt{I})\right] + \sum_c\sum_a m_c m_a B'_{ca} \\ &+ \sum_{c<}\sum_{c'} m_c m_{c'}\phi'_{cc'} + \sum_{a<}\sum_{a'} m_a m_{a'}\phi'_{aa'} \end{aligned} \tag{6}$$

where A^ϕ equals 0.392 for water and b is a universal empirical parameter equal to 1.2, both at 25 °C [44].

$$\begin{aligned} B^\phi_{MX} &= B^{(0)}_{MX} + B^{(1)}_{MX}e^{-\alpha_{MX}\sqrt{I}} + B^{(2)}_{MX}e^{-\alpha'_{MX}\sqrt{I}} \\ B_{MX} &= B^{(0)}_{MX} + B^{(1)}_{MX}g(\alpha_{MX}\sqrt{I}) + B^{(2)}_{MX}g(\alpha'_{MX}\sqrt{I}) \\ B'_{MX} &= \frac{\partial B_{MX}}{\partial I} = B^{(1)}_{MX}\frac{g'(\alpha_{MX}\sqrt{I})}{I} + B^{(2)}_{MX}\frac{g'(\alpha'_{MX}\sqrt{I})}{I} \end{aligned} \tag{7}$$

where $g(x)$ and $g'(x)$ are defined as:

$$\begin{aligned} g(x) &= 2(1-(1+x)e^x)/x^2 \\ g'(x) &= -2(1-(1+x+\tfrac{x^2}{2})e^{-x})/x^2 \end{aligned} \tag{8}$$

It was shown in the literature that up to an ionic strength of 4 mol/L, using the sole B_{MX} terms was sufficient [44,45]. However, to increase the range of validity of the model, the third virial coefficient for binary interactions C_{MX}, and the mixed electrolyte ψ and ϕ coefficients can be added [46,47]. C_{MX} is independent of the ionic strength. ϕ accounts for the interactions between like-charged ions ($\phi_{cc} = \theta_{MM} + {}^E\theta_{MM}$) where the θ_{MM} parameters describe the unsymmetric mixing effects 1–2 or 1–3 ions interactions and ${}^E\theta_{MM}$ can be derived to account for the excess energy of mixing. ϕ describes ternary ion interactions, where the coefficient ψ_{ijk} accounts for ternary interactions between two ions with the same signed charge and one ion with a differently signed charge.

Appendix B. Supplementary data

Supplementary material related to this article can be found online at https://doi.org/10.1016/j.jobe.2023.106398.

References

[1] A. Wüstemann, A. König, F. Dehn, Proposal for the classification of alkali-activated binders and geopolymer binders, Cement Int. 13 (2015) 63–69.

[2] M.M. Komljenović, Z. Baščarević, N. Marjanović, V. Nikolić, Decalcification resistance of alkali-activated slag, J. Hard Mater. 233–234 (2012) 112–121, http://dx.doi.org/10.1016/j.jhazmat.2012.06.063.

[3] M. Komljenović, Z. Baščarević, N. Marjanović, V. Nikolić, External sulfate attack on alkali-activated slag, Constr. Build. Mater. 49 (7) (2013) 31–39, http://dx.doi.org/10.1016/j.conbuildmat.2013.08.013.

[4] J. Ren, H. Sun, Q. Li, Z. Li, L. Ling, X. Zhang, Y. Wang, F. Xing, Experimental comparisons between one-part and normal (two-part) alkali-activated slag binders, Constr. Build. Mater. 309 (2021) 125177, http://dx.doi.org/10.1016/j.conbuildmat.2021.125177, URL https://www.sciencedirect.com/science/article/pii/S0950061821029214.

[5] A. Fernández-Jiménez, F. Puertas, Structure of calcium silicate hydrates formed in alkaline-activated slag: Influence of the type of alkaline activator, J. Am. Ceram. Soc. 86 (8) (2003) 1389–1394.

[6] J.L. Provis, Geopolymers and other alkali activated materials: why, how, and what? Mater. Struct. 47 (1–2) (2014) 11–25, http://dx.doi.org/10.1617/s11527-013-0211-5.

[7] H. Taghvayi, K. Behfarnia, M. Khalili, The effect of alkali concentration and sodium silicate modulus on the properties of alkali-activated slag concrete, J. Adv. Concr. Technol. 16 (7) (2018) 293–305, http://dx.doi.org/10.3151/jact.16.293.

[8] S.A. Bernal, R. San Nicolas, J.S.V. van Deventer, J.L. Provis, Water content modifies the structural development of sodium metasilicate-activated slag binders, Revista ALCONPAT 5 (1) (2015) 28–39, http://dx.doi.org/10.21041/ra.v5i1.75.

[9] C. Duran Atiş, C. Bilim, Ö. Çelik, O. Karahan, Influence of activator on the strength and drying shrinkage of alkali-activated slag mortar, Constr. Build. Mater. 23 (1) (2009) 548–555, http://dx.doi.org/10.1016/j.conbuildmat.2007.10.011.

[10] S.A. Bernal, J.L. Provis, V. Rose, R. Mejía de Gutierrez, Evolution of binder structure in sodium silicate-activated slag-metakaolin blends, Cem. Concr. Compos. 33 (1) (2011) 46–54, http://dx.doi.org/10.1016/j.cemconcomp.2010.09.004.

[11] R. Caron, R.A. Patel, F. Dehn, Extension of the fib MC 2010 for basic and drying shrinkage of alkali–activated slag concretes, Struct. Concrete 64 (48) (2022) 106107, http://dx.doi.org/10.1002/suco.202100901.

[12] S.A. Bernal, R. San Nicolas, R.J. Myers, R. Mejía de Gutierrez, F. Puertas, J.S.J. van Deventer, J.L. Provis, MgO content of the slag controls phase evolution and structural changes induced by accelerated carbonation in alkali-activated binders, Cem. Concr. Res. 57 (2014) 33–43.
[13] DIN EN 196-3, Prüfverfahren für Zement - Teil 3: Bestimmung der Erstarrungszeiten und der Raumbeständigkeit - Deutsche Fassung EN 163-3:1994, Beuth Verlag, 2016.
[14] M. Criado, B. Walkley, X. Ke, J. Provis, S. Bernal, Slag and activator chemistry control the reaction kinetics of sodium metasilicate-activated slag cements, Sustainability 10 (12) (2018) 4709, http://dx.doi.org/10.3390/su10124709.
[15] F. Puertas, A. Fernández-Jiménez, M. Blanco-Varela, Pore solution in alkali-activated slag cement pastes. Relation to the composition and structure of calcium silicate hydrate, Cem. Concr. Res. 34 (1) (2004) 139–148, http://dx.doi.org/10.1016/S0008-8846(03)00254-0.
[16] F. Winnefeld, M. Ben Haha, G. Le Saout, M. Costoya, S.-C. Ko, B. Lothenbach, Influence of slag composition on the hydration of alkali-activated slags, J. Sustain. Cement-Based Mater. 4 (2) (2015) 85–100, http://dx.doi.org/10.1080/21650373.2014.955550.
[17] M.B. Haha, B. Lothenbach, G. Le Saout, F. Winnefeld, Influence of slag chemistry on the hydration of alkali-activated blast-furnace slag — Part I: Effect of MgO, Cem. Concr. Res. 41 (9) (2011) 955–963, http://dx.doi.org/10.1016/j.cemconres.2011.05.002.
[18] A. Gruskovnjak, B. Lothenbach, L. Holzer, R. Figi, F. Winnefeld, Hydration of alkali-activated slag: comparison with ordinary Portland cement, Adv. Cement Res. 18 (3) (2006) 119–128, http://dx.doi.org/10.1680/adcr.2006.18.3.119.
[19] Z.Y. Qu, F. Gauvin, F.Z. Wang, G. Liu, H. Brouwers, Effect of hydrophobicity on autogenous shrinkage and carbonation of alkali activated slag, Constr. Build. Mater. 264 (2020) 120665, http://dx.doi.org/10.1016/j.conbuildmat.2020.120665.
[20] Z. Lu, J.-P. Merkl, M. Pulkin, R. Firdous, S. Wache, D. Stephan, A systematic study on polymer-modified alkali-activated slag-part II: From hydration to mechanical properties, Materials (Basel, Switzerland) 13 (15) (2020) http://dx.doi.org/10.3390/ma13153418.
[21] A.M. Humad, Shrinkage and related properties of alkali-activated binders based on high-MgO blast furnace slag, in: Building Materials, Department of Civil, Environment and Natural Resources Engineering, 2019.
[22] B.S. Gebregziabiher, R. Thomas, S. Peethamparan, Very early-age reaction kinetics and microstructural development in alkali-activated slag, Cem. Concr. Compos. 55 (12) (2015) 91–102, http://dx.doi.org/10.1016/j.cemconcomp.2014.09.001.
[23] J. Li, Q. Yu, H. Huang, S. Yin, Difference in the reaction process of slag activated by waterglass solution and NaOH solution, Struct. Concrete 20 (5) (2019) 1528–1540, http://dx.doi.org/10.1002/suco.201900130.
[24] R.J. Myers, B. Lothenbach, S.A. Bernal, J.L. Provis, Thermodynamic modelling of alkali-activated slag cements, Appl. Geochem. 61 (2015) 233–247, http://dx.doi.org/10.1016/j.apgeochem.2015.06.006.
[25] Y. Zuo, M. Nedeljković, G. Ye, Coupled thermodynamic modelling and experimental study of sodium hydroxide activated slag, Constr. Build. Mater. 188 (4) (2018) 262–279, http://dx.doi.org/10.1016/j.conbuildmat.2018.08.087.
[26] H. Ye, A. Radlińska, Quantitative analysis of phase assemblage and chemical shrinkage of alkali-activated slag, J. Adv. Concr. Technol. 14 (5) (2016) 245–260, http://dx.doi.org/10.3151/jact.14.245.
[27] B. Lothenbach, A. Gruskovnjak, Hydration of alkali-activated slag: thermodynamic modelling, Adv. Cement Res. 19 (2) (2007) 81–92, http://dx.doi.org/10.1680/adcr.2007.19.2.81.
[28] G. Le Saoût, M. Ben Haha, F. Winnefeld, B. Lothenbach, Hydration degree of alkali-activated slags: A 29Si NMR study, J. Am. Ceram. Soc. 94 (12) (2011) 4541–4547, http://dx.doi.org/10.1111/j.1551-2916.2011.04828.x.
[29] Y.-m. Gu, Y.-h. Fang, D. You, Y.-f. Gong, C.-h. Zhu, Properties and microstructure of alkali-activated slag cement cured at below- and about-normal temperature, Constr. Build. Mater. 79 (3) (2015) 1–8, http://dx.doi.org/10.1016/j.conbuildmat.2014.12.068.
[30] F. Xie, Z. Liu, D. Zhang, J. Wang, T. Huang, D. Wang, Reaction kinetics and kinetics models of alkali activated phosphorus slag, Constr. Build. Mater. 237 (7) (2020) 117728, http://dx.doi.org/10.1016/j.conbuildmat.2019.117728.
[31] J. Sun, Z. Chen, Effect of silicate modulus of water glass on the hydration of alkali-activated converter steel slag, J. Therm. Anal. Calorimetry 138 (1) (2019) 47–56, http://dx.doi.org/10.1007/s10973-019-08146-3.
[32] F. Puertas, M. Palacios, H. Manzano, J.S. Dolado, A. Rico, J. Rodríguez, A model for the C-A-S-H gel formed in alkali-activated slag cements, J. Eur. Ceramic Soc. 31 (12) (2011) 2043–2056, http://dx.doi.org/10.1016/j.jeurceramsoc.2011.04.036.
[33] R.J. Myers, S.A. Bernal, J.L. Provis, A thermodynamic model for C-(N-)A-S-H gel: CNASH_ss. Derivation and validation, Cem. Concr. Res. 66 (2014) 27–47, http://dx.doi.org/10.1016/j.cemconres.2014.07.005.
[34] E. L'Hôpital, B. Lothenbach, D.A. Kulik, K. Scrivener, Influence of calcium to silica ratio on aluminium uptake in calcium silicate hydrate, Cem. Concr. Res. 85 (2016) 111–121, http://dx.doi.org/10.1016/j.cemconres.2016.01.014.
[35] R.J. Myers, S.A. Bernal, J.D. Gehman, J.S. van Deventer, J.L. Provis, The role of Al in cross-linking of alkali-activated slag cements, J. Am. Ceram. Soc. 98 (3) (2015) 996–1004, http://dx.doi.org/10.1111/jace.13360.
[36] M.B. Haha, B. Lothenbach, G. Le Saout, F. Winnefeld, Influence of slag chemistry on the hydration of alkali-activated blast-furnace slag — Part II: Effect of Al2O3, Cem. Concr. Res. 42 (1) (2012) 74–83, http://dx.doi.org/10.1016/j.cemconres.2011.08.005.
[37] J.L. Provis, G.C. Lukey, J.S.J. van Deventer, Do geopolymers actually contain nanocrystalline zeolites? A reexamination of existing results, Chem. Mater. 17 (12) (2005) 3075–3085, http://dx.doi.org/10.1021/cm050230i.
[38] B. Lothenbach, F. Winnefeld, Thermodynamic modelling of the hydration of portland cement, Cem. Concr. Res. 36 (2) (2006) 209–226, http://dx.doi.org/10.1016/j.cemconres.2005.03.001.
[39] X. Ke, S.A. Bernal, J.L. Provis, B. Lothenbach, Thermodynamic modelling of phase evolution in alkali-activated slag cements exposed to carbon dioxide, Cem. Concr. Res. 136 (2020) 106158, http://dx.doi.org/10.1016/j.cemconres.2020.106158.
[40] S. Mundra, D.P. Prentice, S.A. Bernal, J.L. Provis, Modelling chloride transport in alkali-activated slags, Cem. Concr. Res. 130 (2020) 106011, http://dx.doi.org/10.1016/j.cemconres.2020.106011.
[41] H.C. Helgeson, D.H. Kirkham, G.C. Flowers, Theoretical prediction of the thermodynamics behavior of aqueous electrolytes at high pressures and temperatures: IV. Calculation of activity coefficients, osmotic coefficients, and apparent molal and standard and relative partial molal properties to 600° C and 5 KB, Am. J. Sci. 281 (1981) 1249–1516.
[42] D.P. Prentice, S.A. Bernal, M. Bankhead, M. Hayes, J.L. Provis, Using the Pitzer model to predict aqueous solution compositions of Portland cements blended with supplementary cementitious materials, Construct. Mater. Syst. (2017) 613–622.
[43] D. Langmuir, Aqueous environmental geochemistry, 1997.
[44] K.S. Pitzer, Thermodynamics of electrolytes. I. Theoretical basis and general equations, J. Phys. Chem. 77 (1973) 268–277.
[45] K.S. Pitzer, G.D. Mayorga, Thermodynamics of electrolytes. II. Activity and osmotic coefficients for strong electrolytes with one or both ions univalent, J. Phys. Chem. 77 (1973) 2300–2308.
[46] K.S. Pitzer, G.D. Mayorga, Thermodynamics of electrolytes. III. Activity and osmotic coefficients for 2–2 electrolytes, J. Solution Chem. 3 (1974) 539–546.
[47] K.S. Pitzer, J.J. Kim, Thermodynamics of electrolytes. IV. Activity and osmotic coefficients for mixed electrolytes, J. Am. Chem. Soc.; (United States) 96, http://dx.doi.org/10.1021/ja00825a004, URL https://www.osti.gov/biblio/6166252.
[48] Y. Xiong, A thermodynamic model for silica and aluminum in alkaline solutions with high ionic strength at elevated temperatures up to 100 C: Applications to zeolites, Am. Mineral. 98 (2012) 141–153, http://dx.doi.org/10.2138/am.2013.4089.
[49] D. Prentice, Thermodynamic modelling of ultra-long-term durability of cementitious binders for waste immobilisation, 2018.

[50] P. Blanc, A. Lach, A. Lassin, M. Falah, R. Obenaus-Emler, S. Guignot, Modeling hydration of mine tailings: Production of hydraulic binders from alkali-activated materials, Cem. Concr. Res. 137 (2020) http://dx.doi.org/10.1016/j.cemconres.2020.106216.
[51] B. Lothenbach, T. Matschei, G. Möschner, F.P. Glasser, Thermodynamic modelling of the effect of temperature on the hydration and porosity of portland cement, Cem. Concr. Res. 38 (1) (2008) 1–18, http://dx.doi.org/10.1016/j.cemconres.2007.08.017.
[52] T. Matschei, B. Lothenbach, F.P. Glasser, Thermodynamic properties of Portland cement hydrates in the system CaO–Al2O3–SiO2–CaSO4–CaCO3–H2O, Cem. Concr. Res. 37 (10) (2007) 1379–1410, http://dx.doi.org/10.1016/j.cemconres.2007.06.002.
[53] G. Möschner, B. Lothenbach, J. Rose, A. Ulrich, R. Figi, R. Kretzschmar, Solubility of Fe–ettringite (Ca6[Fe(OH)6]2(SO4)3.26H2O), Geochim. Cosmochim. Acta 72 (1) (2008) 1–18, http://dx.doi.org/10.1016/j.gca.2007.09.035.
[54] B. Lothenbach, L. Pelletier-Chaignat, F. Winnefeld, Stability in the system CaO–Al2O3–H2O, Cem. Concr. Res. 42 (12) (2012) 1621–1634, http://dx.doi.org/10.1016/j.cemconres.2012.09.002.
[55] B. Lothenbach, D.A. Kulik, T. Matschei, M. Balonis, L. Baquerizo, B. Dilnesa, G.D. Miron, R.J. Myers, Cemdata18: A chemical thermodynamic database for hydrated portland cements and alkali-activated materials, Cem. Concr. Res. 115 (Suppl. 2) (2019) 472–506, http://dx.doi.org/10.1016/j.cemconres.2018.04.018.
[56] D.A. Kulik, Improving the structural consistency of C-S-H solid solution thermodynamic models, Cem. Concr. Res. 41 (5) (2011) 477–495, http://dx.doi.org/10.1016/j.cemconres.2011.01.012.
[57] C.S. Walker, S. Sutou, C. Oda, M. Mihara, A. Honda, Calcium silicate hydrate (C-S-H) gel solubility data and a discrete solid phase model at 25° C based on two binary non-ideal solid solutions, Cem. Concr. Res. 79 (45) (2016) 1–30, http://dx.doi.org/10.1016/j.cemconres.2015.07.006.
[58] R.J. Myers, S.A. Bernal, J.L. Provis, Phase diagrams for alkali-activated slag binders, Cem. Concr. Res. 95 (2017) 30–38, http://dx.doi.org/10.1016/j.cemconres.2017.02.006.
[59] B. Ma, B. Lothenbach, Synthesis, characterization, and thermodynamic study of selected Na-based zeolites, Cem. Concr. Res. 135 (2020) 106111, http://dx.doi.org/10.1016/j.cemconres.2020.106111.
[60] B. Ma, B. Lothenbach, Thermodynamic study of cement/rock interactions using experimentally generated solubility data of zeolites, Cem. Concr. Res. 135 (2020) 106149, http://dx.doi.org/10.1016/j.cemconres.2020.106149.
[61] D.A. Kulik, G.D. Miron, B. Lothenbach, A structurally-consistent CASH+ sublattice solid solution model for fully hydrated C-S-H phases: Thermodynamic basis, methods, and Ca-Si-H2O core sub-model, Cem. Concr. Res. 151 (2022) 106585, http://dx.doi.org/10.1016/j.cemconres.2021.106585.
[62] G.D. Miron, D.A. Kulik, Y. Yan, J. Tits, B. Lothenbach, Extensions of CASH+ thermodynamic solid solution model for the uptake of alkali metals and alkaline earth metals in C-S-H, Cem. Concr. Res. 152 (2022) 106667, http://dx.doi.org/10.1016/j.cemconres.2021.106667.
[63] J.L. Provis, K. Arbi, S.A. Bernal, D. Bondar, A. Buchwald, A. Castel, S. Chithiraputhiran, M. Cyr, A. Dehghan, K. Dombrowski-Daube, A. Dubey, V. Ducman, G.J.G. Gluth, S. Nanukuttan, K. Peterson, F. Puertas, A. van Riessen, M. Torres-Carrasco, G. Ye, Y. Zuo, RILEM TC 247-DTA round robin test: mix design and reproducibility of compressive strength of alkali-activated concretes, Mater. Struct. 52 (5) (2019) 3683, http://dx.doi.org/10.1617/s11527-019-1396-z.
[64] R. Caron, R.A. Patel, F. Dehn, Activation kinetic model and mechanisms for alkali-activated slag cements, Constr. Build. Mater. 323 (2022) 126577, http://dx.doi.org/10.1016/j.conbuildmat.2022.126577.
[65] R. Snellings, J. Chwast, Ö. Cizer, N. de Belie, Y. Dhandapani, P. Durdzinski, J. Elsen, J. Haufe, D. Hooton, C. Patapy, M. Santhanam, K. Scrivener, D. Snoeck, L. Steger, S. Tongbo, A. Vollpracht, F. Winnefeld, B. Lothenbach, RILEM TC-238 SCM recommendation on hydration stoppage by solvent exchange for the study of hydrate assemblages, Mater. Struct. 51 (6) (2018) 111, http://dx.doi.org/10.1617/s11527-018-1298-5.
[66] J. Zhang, G.W. Scherer, Comparison of methods for arresting hydration of cement, Cem. Concr. Res. 41 (10) (2011) 1024–1036, http://dx.doi.org/10.1016/j.cemconres.2011.06.003.
[67] D.A. Kulik, T. Wagner, S.V. Dmytrieva, G. Kosakowski, F.F. Hingerl, K.V. Chudnenko, U.R. Berner, GEM-Selektor geochemical modeling package: revised algorithm and GEMS3K numerical kernel for coupled simulation codes, Comput. Geosci. 26 (012025) (2012) 189, http://dx.doi.org/10.1007/s10596-012-9310-6.
[68] T. Wagner, D.A. Kulik, F.F. Hingerl, S.V. Dmytrieva, Gem-selektor geochemical modeling package: Tsolmod library and data interface for multicomponent phase models, Canadian Mineral. 50 (5) (2012) 1173–1195, http://dx.doi.org/10.3749/canmin.50.5.1173.
[69] B. Merkel, B. Planer-Friedrich, D. Nordstrom, in: D. Nordstrom (Ed.), Groundwater Geochemistry: A Practical Guide to Modeling of Natural and Contaminated Aquatic Systems, in: Groundwater Geochemistry, Springer, Berlin, 2008, http://dx.doi.org/10.1007/b138774, ISBN: 978-3-540-74667-6.
[70] C.E. Harvie, J.H. Weare, The prediction of mineral solubilities in natural waters: the NaKMgCaClSO4H2O system from zero to high concentration at 25° C, Geochim. Cosmochim. Acta 44 (1980) 981–997.
[71] C. Harvie, N. Møller, J. Weare, The prediction of mineral solubilities in natural waters: The Na-K-Mg-Ca-H-Cl-SO4-OH-HCO3-CO3-CO2-H2O system to high ionic strengths at 25° C, Geochim. Cosmochim. Acta 48 (1984) 723–751, http://dx.doi.org/10.1016/0016-7037(84)90098-X.
[72] W. Hummel, U. Berner, E. Curti, F.J. Pearson, T. Thoenen, Nagra/PSI chemical thermodynamic data base, Radiochim. Acta 90 (2002) 805–183.
[73] R. Dron, F. Brivot, Approche du problème de la réactivité du laitier granule, in: 7th International Congress on the Chemistry of Cement, 2, Communications. Editions Septima, Paris, 1980, pp. III–134–9.
[74] M. Regourd, J.H. Thomassin, P. Baillif, J.C. Touray, Blast-furnace slag hydration. Surface analysis, Cem. Concr. Res. 13 (1983) 549–556.
[75] R. Snellings, Solution-controlled dissolution of supplementary cementitious material glasses at pH 13: The effect of solution composition on glass dissolution rates, J. Am. Ceram. Soc. 96 (8) (2013) 2467–2475, http://dx.doi.org/10.1111/jace.12480.
[76] R. Snellings, T. Paulhiac, K. Scrivener, The effect of Mg on slag reactivity in blended cements, Waste Biomass Valoriz. 5 (3) (2014) 369–383, http://dx.doi.org/10.1007/s12649-013-9273-4.
[77] S. Song, H.M. Jennings, Pore solution chemistry of alkali-activated ground granulated blast-furnace slag, Cem. Concr. Res. 29 (1999) 159–170.
[78] F. Jin, K. Gu, A. Al-Tabbaa, Strength and drying shrinkage of reactive MgO modified alkali-activated slag paste, Constr. Build. Mater. 51 (2014) 395–404, http://dx.doi.org/10.1016/j.conbuildmat.2013.10.081.
[79] X. Ke, S.A. Bernal, J.L. Provis, Uptake of chloride and carbonate by Mg-Al and Ca-Al layered double hydroxides in simulated pore solutions of alkali-activated slag cement, Cem. Concr. Res. 100 (2017) 1–13, http://dx.doi.org/10.1016/j.cemconres.2017.05.015.
[80] T. Zhang, L.J. Vandeperre, C.R. Cheeseman, Formation of magnesium silicate hydrate (M-S-H) cement pastes using sodium hexametaphosphate, Cem. Concr. Res. 65 (2014) 8–14, http://dx.doi.org/10.1016/j.cemconres.2014.07.001.
[81] E. Tajuelo Rodriguez, K. Garbev, D. Merz, L. Black, I.G. Richardson, Thermal stability of C-S-H phases and applicability of Richardson and Groves' and Richardson C-(A)-S-H(I) models to synthetic C-S-H, Cem. Concr. Res. 93 (3) (2017) 45–56, http://dx.doi.org/10.1016/j.cemconres.2016.12.005.
[82] Z. Li, T. Zhang, J. Hu, Y. Tang, Y. Niu, J. Wei, Q. Yu, Characterization of reaction products and reaction process of MgO–SiO2–H2O system at room temperature, Constr. Build. Mater. 61 (4) (2014) 252–259, http://dx.doi.org/10.1016/j.conbuildmat.2014.03.004.
[83] P. Yu, R.J. Kirkpatrick, B. Poe, P.F. McMillan, W. Cong, Structure of calcium silicate hydrate (C-S-H): Near-, mid-, and far-infrared spectroscopy, J. Am. Ceram. Soc. 82 (1999) 742–748.
[84] A. Vidmer, G. Sclauzero, A. Pasquarello, Infrared spectra of jennite and tobermorite from first-principles, Cem. Concr. Res. 60 (2014) 11–23, http://dx.doi.org/10.1016/j.cemconres.2014.03.004.
[85] Y. Yan, S.-Y. Yang, G.D. Miron, I.E. Collings, E. L'Hôpital, J.r. Skibsted, F. Winnefeld, K. Scrivener, B. Lothenbach, Effect of alkali hydroxide on calcium silicate hydrate (C-S-H), Cem. Concr. Res. 151 (3) (2022) 106636, http://dx.doi.org/10.1016/j.cemconres.2021.106636.
[86] W. Mozgawa, M. Król, K. Barczyk, FT-ir studies of zeolites from different structural groups, Chemik 65 (2011) 667–674.

[87] N.J. Clayden, S. Esposito, A. Aronne, P. Pernice, Solid state Al NMR and FTIR study of lanthanum aluminosilicate glasses, J. Non-Cryst. Solids 258 (1999) 11–19.
[88] M. Sitarz, M. Handke, W. Mozgawa, Identification of silicooxygen rings in SiO2 based on IR spectra, Spectrochim. Acta 56 (2000) 1819–1823.
[89] S.-Y. Yang, Y. Yan, B. Lothenbach, J. Skibsted, Incorporation of sodium and aluminum in cementitious calcium-alumino-silicate-hydrate C-(A)-S-H Phases Studied by 23 Na, 27 Al, and 29 Si MAS NMR spectroscopy, J. Phys. Chem. C 125 (51) (2021) 27975–27995, http://dx.doi.org/10.1021/acs.jpcc.1c08419.
[90] A.G. Stepanov, Basics of solid-state NMR for application in zeolite science, in: Zeolites and Zeolite-Like Materials, Vol. 103, Elsevier, 2016, pp. 137–188, http://dx.doi.org/10.1016/B978-0-444-63506-8.00004-5.
[91] K.D. Weerdt, B. Lothenbach, M. Geiker, Comparing chloride ingress from seawater and NaCl solution in portland cement mortar, Cem. Concr. Res. 115 (2019) 80–89, http://dx.doi.org/10.1016/j.cemconres.2018.09.014.
[92] Z. Li, T. Lu, X. Liang, H. Dong, G. Ye, Mechanisms of autogenous shrinkage of alkali-activated slag and fly ash pastes, Cem. Concr. Res. 135 (2020) 106107, http://dx.doi.org/10.1016/j.cemconres.2020.106107.
[93] A. Muller, K.L. Scrivener, A reassessment of mercury intrusion porosimetry by comparison with 1H NMR relaxometry, Cem. Concr. Res. 100 (2017) 350–360, http://dx.doi.org/10.1016/j.cemconres.2017.05.024.
[94] M. Zajac, P. Durdzinski, Z. Giergiczny, M. Ben Haha, New insights into the role of space on the microstructure and the development of strength of multicomponent cements, Cem. Concr. Compos. 121 (2021) 104070, http://dx.doi.org/10.1016/j.cemconcomp.2021.104070.
[95] C. Shi, R.L. Day, A calorimetric study of early hydration of alkali-slag cements, Cem. Concr. Res. 25 (6) (1995) 1333–1346.
[96] M.B. Haha, K. de Weerdt, B. Lothenbach, Quantification of the degree of reaction of fly ash, Cem. Concr. Res. 40 (11) (2010) 1620–1629, http://dx.doi.org/10.1016/j.cemconres.2010.07.004.
[97] K.L. Scrivener, Backscattered electron imaging of cementitious microstructures: understanding and quantification, Cem. Concr. Compos. 26 (8) (2004) 935–945, http://dx.doi.org/10.1016/j.cemconcomp.2004.02.029.
[98] J. Chang, A study on the setting characteristics of sodium silicate-activated slag pastes, Cem. Concr. Res. 33 (2003) 1005–1011, http://dx.doi.org/10.1016/S0008-8846(02)01096-7.
[99] J. Provis, On the use of the Jander equation in cement hydration modelling, RILEM Tech. Lett. 1 (2016) 62, http://dx.doi.org/10.21809/rilemtechlett.2016.13.
[100] K. Riding, J. Poole, K. Folliard, M.C.G. Juenger, A.K. Schindler, Modeling hydration of cementitious systems, ACI Mater. J. 109 (2) (2012) 225–234.
[101] Y. Zuo, M. Nedeljković, G. Ye, Reaction kinetics and thermodynamic modeling of sodium hydroxide activated slag paste, 2016.
[102] L.E. Al-Hasani, J. Park, G. Perez, H.N. Herndon, J.B. Brown, Y.K. Cho, T.R. Gentry, K.E. Kurtis, Quantifying concrete adiabatic temperature rise based on temperature-dependent isothermal calorimetry; modeling and validation, Mater. Struct. 55 (7) (2022) 401, http://dx.doi.org/10.1617/s11527-022-02023-6.
[103] V. Kocaba, E. Gallucci, K.L. Scrivener, Methods for determination of degree of reaction of slag in blended cement pastes, Cem. Concr. Res. 42 (3) (2012) 511–525, http://dx.doi.org/10.1016/j.cemconres.2011.11.010.
[104] M. Zajac, J. Skocek, B. Lothenbach, B.H. Mohsen, Late hydration kinetics: Indications from thermodynamic analysis of pore solution data, Cem. Concr. Res. 129 (357) (2020) 105975, http://dx.doi.org/10.1016/j.cemconres.2020.105975.
[105] J. Matousek, The thermodynamic properties of slags, Jom 60 (2008) 62–64, http://dx.doi.org/10.1007/s11837-008-0021-3.
[106] D. Jansen, F. Goetz-Neunhoeffer, B. Lothenbach, J. Neubauer, The early hydration of ordinary portland cement (OPC): An approach comparing measured heat flow with calculated heat flow from QXRD, Cem. Concr. Res. 42 (1) (2012) 134–138, http://dx.doi.org/10.1016/j.cemconres.2011.09.001.
[107] S. Barzgar, M. Tarik, C. Ludwig, B. Lothenbach, The effect of equilibration time on Al uptake in C-S-H, Cem. Concr. Res. 144 (2021) 106438, http://dx.doi.org/10.1016/j.cemconres.2021.106438.
[108] A.R. Brough, A. Atkinson, Sodium silicate-based, alkali-activated slag mortars. Part I. Strength, hydration and microstructure, Cem. Concr. Res. 32 (2002) 865–879.
[109] M. Zajac, J. Skocek, S. Adu-Amankwah, L. Black, M. Ben Haha, Impact of microstructure on the performance of composite cements: Why higher total porosity can result in higher strength, Cem. Concr. Compos. 90 (6) (2018) 178–192, http://dx.doi.org/10.1016/j.cemconcomp.2018.03.023.
[110] M. Königsberger, B. Pichler, C. Hellmich, Multiscale poro-elasticity of densifying calcium-silicate hydrates in cement paste: An experimentally validated continuum micromechanics approach, Internat. J. Engrg. Sci. 147 (4) (2020) 103196, http://dx.doi.org/10.1016/j.ijengsci.2019.103196.
[111] O. Bernard, F.-J. Ulm, E. Lemarchand, A multiscale micromechanics-hydration model for the early-age elastic properties of cement-based materials, Cem. Concr. Res. 33 (9) (2003) 1293–1309, http://dx.doi.org/10.1016/S0008-8846(03)00039-5.
[112] M. Shahidi, B. Pichler, C. Hellmich, Viscous interfaces as source for material creep: A continuum micromechanics approach, Eur. J. Mech. A Solids 45 (5) (2014) 41–58, http://dx.doi.org/10.1016/j.euromechsol.2013.11.001.
[113] M. Königsberger, M. Irfan-ul Hassan, B. Pichler, C. Hellmich, Downscaling based identification of nonaging power-law creep of cement hydrates, J. Eng. Mech. 142 (12) (2016) 15, http://dx.doi.org/10.1061/(ASCE)EM.1943-7889.0001169.
[114] J. Baronet, L. Sorelli, J.-P. Charron, M. Vandamme, J. Sanahuja, A two-scale method to rapidly characterize the logarithmic basic creep of concrete by coupling microindentation and uniaxial compression creep test, Cem. Concr. Compos. 125 (8) (2022) 104274, http://dx.doi.org/10.1016/j.cemconcomp.2021.104274.

Microstructure development of slag activated with sodium silicate solution: experimental characterization and thermodynamic modeling – Supplementary Material

Values of the parameters of the Pitzer model

This part provides the ion interaction parameters used for the Pitzer model.

Table 1: Values of binary species Pitzer parameters taken from [1]

Cation	Anion	$B^{(0)}$	$B^{(1)}$	$B^{(2)}$	$C^{(0)}$
Al^{3+}	HSO_4^-	1.025	5.426		-0.0486
Al^{3+}	SO_4^{2-}	0.822	21.22	-4813	-0.0799
Ca^{2+}	CO_3^{2-}	0.16	2.1	-46	
Ca^{2+}	HCO_3^-	0.39975	2.977		
Ca^{2+}	HS^-	0.069	2.264		
Ca^{2+}	HSO_4^-	0.2145	2.5275		
Ca^{2+}	OH^-	-0.1421	-0.3727	-11.052	-0.0092
Ca^{2+}	SO_4^{2-}	0.2	3.546	-54.24	0.114
Fe^{2+}	HSO_4^-	0.4273	3.48		
Fe^{2+}	SO_4^{2-}	0.2568	3.063	-42	0.0209
H^+	HSO_4^-	0.2709	0.0299		
H^+	SO_4^{2-}	-0.0216	0.1194		0.0317
K^+	AlO_2^-	0.094	0.32		-0.0012
K^+	CO_3^{2-}	0.1305	1.43		0.00024
K^+	HCO_3^-	-0.01558	0.25		0.00469
K^+	HS^-	-0.337	0.884		
K^+	$HSiO_3^-$	0.208	0.34		

Table 1 Continued

K^+	HSO_4^-	-0.0003	0.1735		
K^+	OH^-	0.1298	0.32		0.0041
K^+	SO_3^{2-}	0.065	1		
K^+	SO_4^{2-}	0.0317	0.756		0.00818
Mg^{2+}	CO_3^{2-}	0.18	1.804	-46	
Mg^{2+}	HCO_3^-	0.033	0.84975		
Mg^{2+}	HS^-	0.466	2.264		
Mg^{2+}	HSO_4^-	0.4746	1.729		
Mg^{2+}	SO_4^{2-}	0.2135	3.367	-40.15	0.02875
Na^+	AlO_2^-	-0.0083	0.071		0.00977
Na^+	CO_3^{2-}	0.04625	1.389		0.0044
Na^+	HCO_3^-	-0.05876	0.5535	8.22	
Na^+	HS^-	-0.103	0.884		
Na^+	$HSiO_3^-$	0.162	0.334		
Na^+	HSO_4^-	0.0454	0.398		
Na^+	OH^-	0.0864	0.253		0.0044
Na^+	SO_3^{2-}	0.08015			
Na^+	SO_4^{2-}	0.01959	1.049	0.005416	0.005416

Table 2: Values of mixed electrolyte Pitzer parameters taken from [1]

Aq. species	Aq. species	Parameter type	Parameter value
CO_2	Ca^{2+}	λ_{nc}	0.183
CO_2	K^+	λ_{nc}	0.051
CO_2	Mg^{2+}	λ_{nc}	0.183
CO_2	Na^+	λ_{nc}	0.085
SiO_2	Ca^{2+}	λ_{nc}	0.2925
SiO_2	K^+	λ_{nc}	0.03224
SiO_2	Mg^{2+}	λ_{nc}	0.2925
SiO_2	Na^+	λ_{nc}	0.0925
CO_2	HSO_4^-	λ_{na}	-0.003
CO_2	SO_4^{2-}	λ_{na}	0.075
SiO_2	SO_4^{2-}	λ_{na}	-0.13963

Table 2 Continued

Ca^{2+}	H^+	θ_{cc}	0.092
Ca^{2+}	K^+	θ_{cc}	0.032
Ca^{2+}	Na^+	θ_{cc}	0.07
K^+	H^+	θ_{cc}	0.005
K^+	Na^+	θ_{cc}	-0.012
Mg^{2+}	Ca^{2+}	θ_{cc}	0.007
Mg^{2+}	H^+	θ_{cc}	0.1
Mg^{2+}	Na^+	θ_{cc}	0.07
Na^+	H^+	θ_{cc}	0.0368
AlO_2^-	OH^-	θ_{aa}	-0.2255
CO_3^{2-}	OH^-	θ_{aa}	0.1
CO_3^{2-}	SO_4^{2-}	θ_{aa}	0.02
HCO_3^-	CO_3^{2-}	θ_{aa}	-0.04
HCO_3^-	SO_4^{2-}	θ_{aa}	0.01
OH^-	SO_4^{2-}	θ_{aa}	-0.013

Table 3: Values of mixed electrolyte Pitzer parameters taken from [1]

Aq. species	Aq. species	Aq. species	Parameter type	Parameter value
Ca^{2+}	K^+	SO_4^{2-}	ψ_{cca}	-0.0365
CO_3^{2-}	Na^+	K^+	ψ_{cca}	0.003
H^+	K^+	SO_4^{2-}	ψ_{cca}	0.197
HCO_3^-	Na^+	K^+	ψ_{cca}	-0.003
HSO_4^-	H^+	K^+	ψ_{cca}	-0.0265
HSO_4^-	H^+	Mg^{2+}	ψ_{cca}	-0.0178
HSO_4^-	H^+	Na^+	ψ_{cca}	-0.0129
SO_4^{2-}	Ca^{2+}	Mg^{2+}	ψ_{cca}	0.024
SO_4^{2-}	K^+	Mg^{2+}	ψ_{cca}	-0.048
SO_4^{2-}	Na^+	Ca^{2+}	ψ_{cca}	-0.055
SO_4^{2-}	Na^+	K^+	ψ_{cca}	-0.01
SO_4^{2-}	Na^+	Mg^{2+}	ψ_{cca}	-0.015
K^+	CO_3^{2-}	HCO_3^-	ψ_{aac}	0.012
K^+	OH^-	AlO_2^-	ψ_{aac}	-0.0388

Table 3 Continued

K^+	OH^-	CO_3^{2-}	ψ_{aac}	-0.01
K^+	SO_4^{2-}	CO_3^{2-}	ψ_{aac}	-0.009
K^+	SO_4^{2-}	HSO_4^-	ψ_{aac}	-0.0677
K^+	SO_4^{2-}	OH^-	ψ_{aac}	-0.05
Mg^{2+}	SO_4^{2-}	HCO_3^-	ψ_{aac}	-0.161
Mg^{2+}	SO_4^{2-}	HSO_4^-	ψ_{aac}	-0.0425
Na^+	CO_3^{2-}	HCO_3^-	ψ_{aac}	0.002
Na^+	OH^-	AlO_2^-	ψ_{aac}	-0.0048
Na^+	OH^-	CO_3^{2-}	ψ_{aac}	-0.017
Na^+	SO_4^{2-}	CO_3^{2-}	ψ_{aac}	-0.005
Na^+	SO_4^{2-}	HCO_3^-	ψ_{aac}	-0.005
Na^+	SO_4^{2-}	HSO_4^-	ψ_{aac}	-0.0094
Na^+	SO_4^{2-}	OH^-	ψ_{aac}	-0.009

Table 4: Values of binary species Pitzer parameters taken from [2]

Cation	Anion	$B^{(0)}$	$B^{(1)}$	$B^{(2)}$	$C^{(0)}$
Na^+	$H_3SiO_4^-$	0.043	0.24		
Na^+	$H_2SiO_4^{2-}$	0.32	0.13		
Na^+	$H_5Si_2O_7^-$	-0.0571	0.34		
Na^+	$H_4Si_2O_7^{2-}$	-0.0227	1.56		
Na^+	$H_5Si_3O_{10}^{3-}$	0.078	4.29		
Na^+	$Al(OH)_3HSiO_4^{3-}$	0.078	4.29		
Na^+	$Al(OH)_4^-$	0.051	0.25		-0.0009

Table 5: Values of mixed electrolyte Pitzer parameters taken from [2]

Aq. species	Aq. species	Aq. species	Parameter type	Parameter value
Na^+	H_4SiO_4		λ_{nc}	0.0925
OH^-	$H_2SiO_4^{2-}$		θ_{aa}	-9.35
OH^-	$H_2SiO_4^{2-}$	Na^+	ψ_{aac}	-0.017

References

[1] D. Prentice, Thermodynamic modelling of ultra-long-term durability of cementitious binders for waste immobilisation, 2018.

[2] Y. Xiong, A thermodynamic model for silica and aluminum in alkaline solutions with high ionic strength at elevated temperatures up to 100 c: Applications to zeolites, American Mineralogist 98 (2012) 141–153. doi:10.2138/am.2013.4089.

Supplementary material: experimental results for different ages

This part provides further experimental data of X-Ray Diffraction (XRD), Differential Thermogravimetry (DTG), Differential Thermal Analysis (DTA), Fourier-Transform Infrared Spectroscopy (FTIR) performed at different ages for both mixes lS and hS.

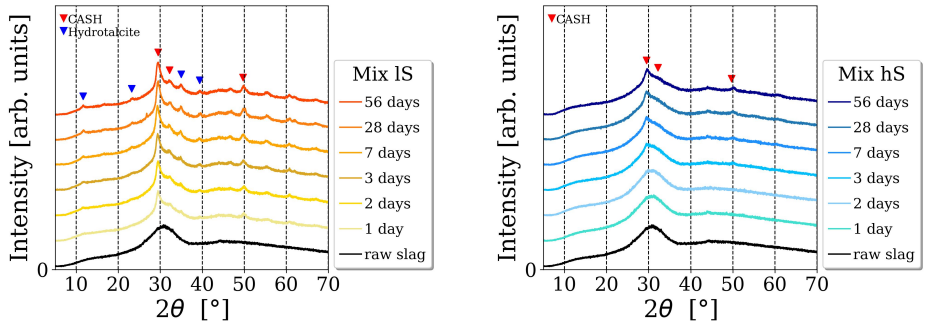

Figure 1: XRD results for both mixes lS (left) and hS (right)

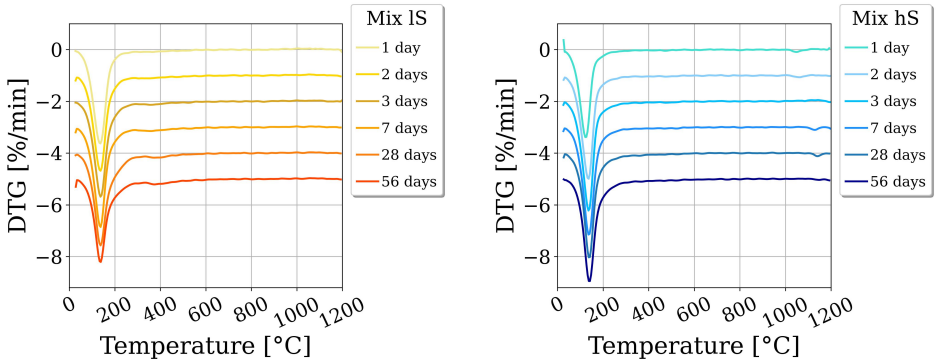

Figure 2: DTG results for both mixes lS (left) and hS (right)

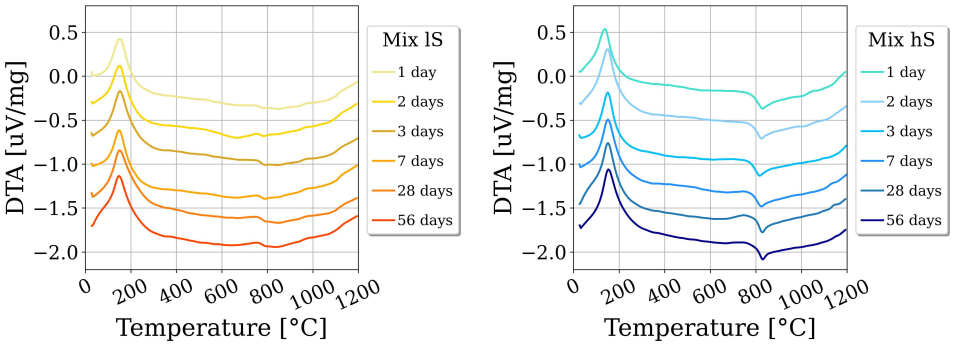

Figure 3: DTA results for both mixes lS (left) and hS (right)

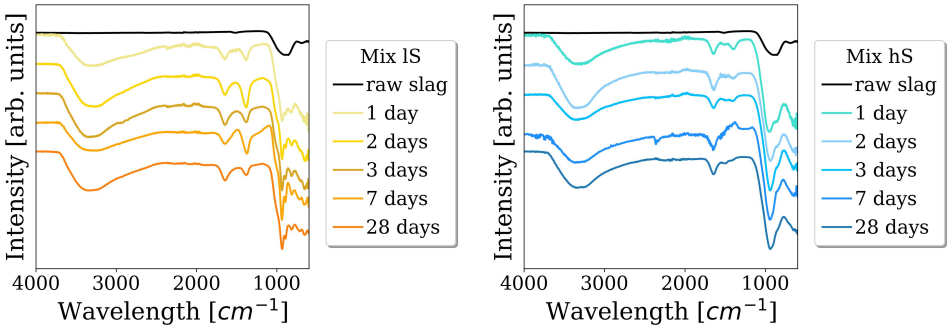

Figure 4: FTIR results for both mixes lS (left) and hS (right)

Supplementary material: Thermodynamic results with use of the extended Debye-Hückel ion activity model

In this part the results of thermodynamic calculations using the extended Debye-Hückel ion activity model instead of the Pitzer model are presented.

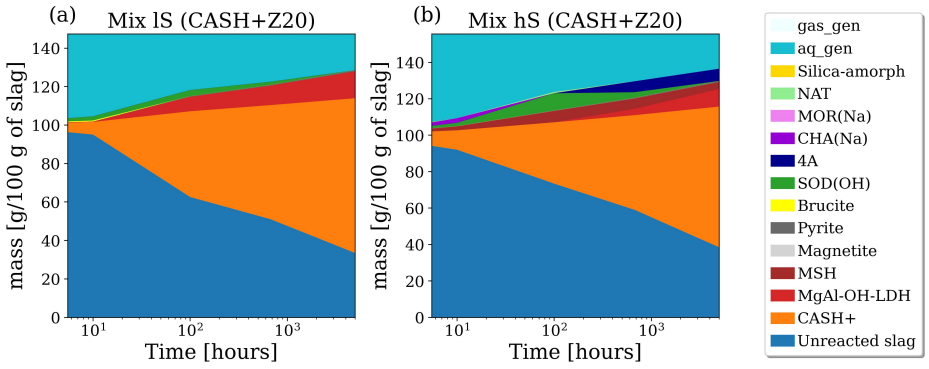

Figure 5: Thermodynamic calculations with the extended Debye-Hückel model and the CASH+Z20 dataset for both mixes lS (a) and hS (b)

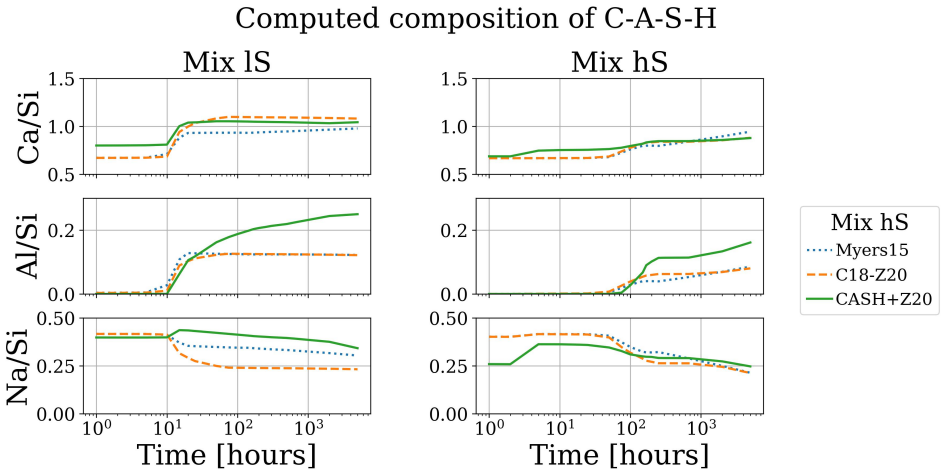

Figure 6: Calculated Ca/Si, Al/Si and Na/Si ratios along time in the C-A-S-H models for both mixes lS (left) and hS (right) using the extended Debye-Hückel model

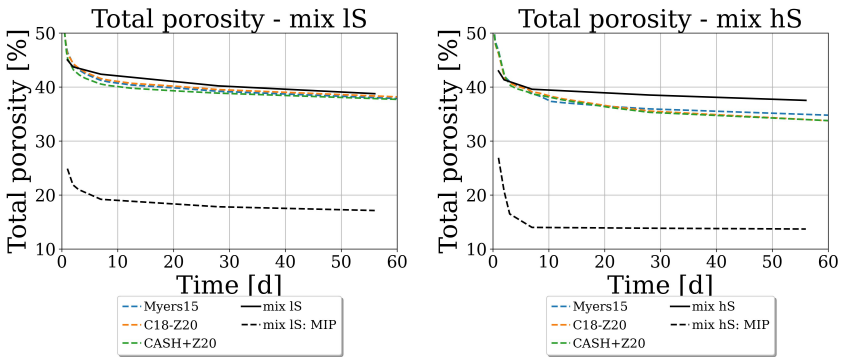

Figure 7: Calculated total porosity of mixes lS (left) and hS (right) with the extended Debye-Hückel model and comparison with experimental results

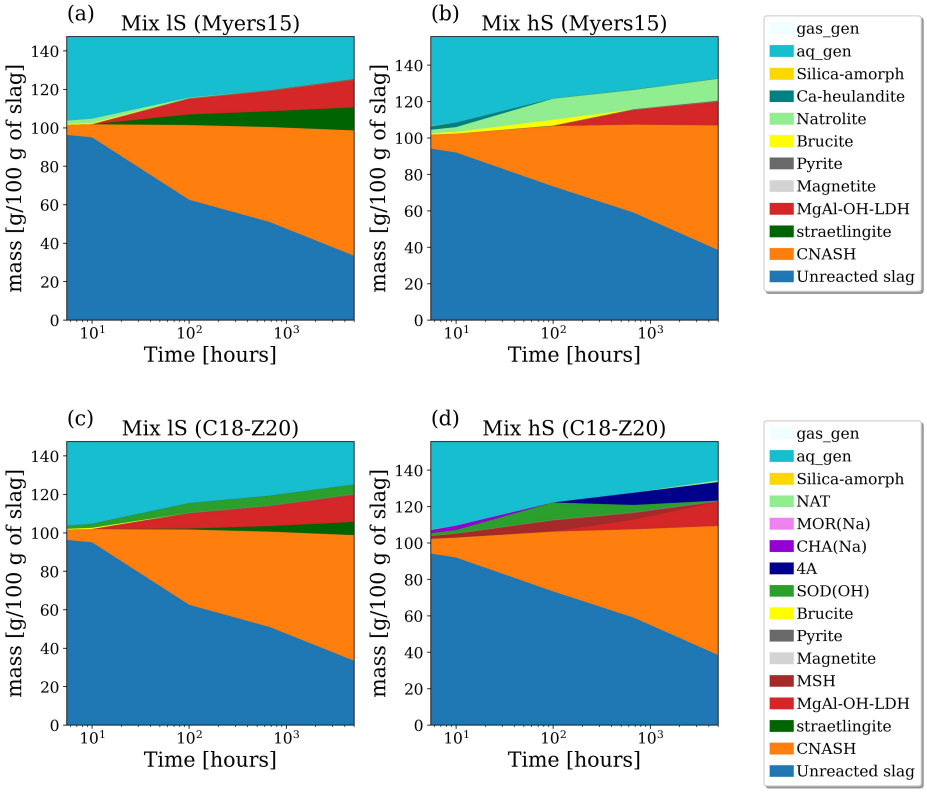

Figure 8: Thermodynamic calculations using the extended Debye-Hückel model with the Myers15 and C18-20 datasets for both mixes lS (left) and hS (right)

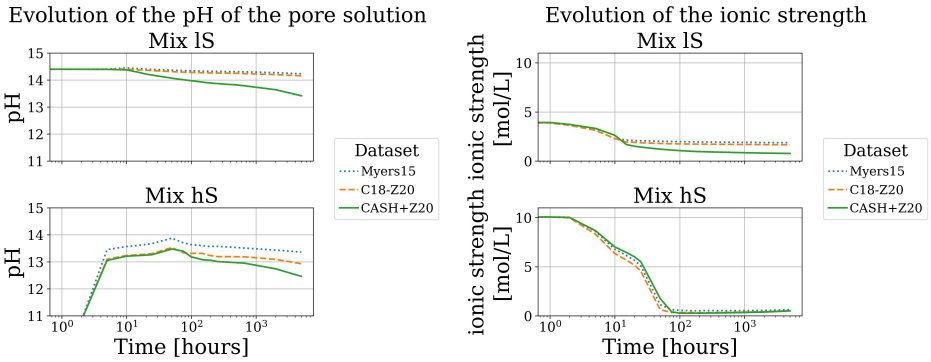

Figure 9: Calculated pH (left) and ionic strength (right) using the extended Debye-Hückel equation in the pore solution along time for both mixes lS and hS.

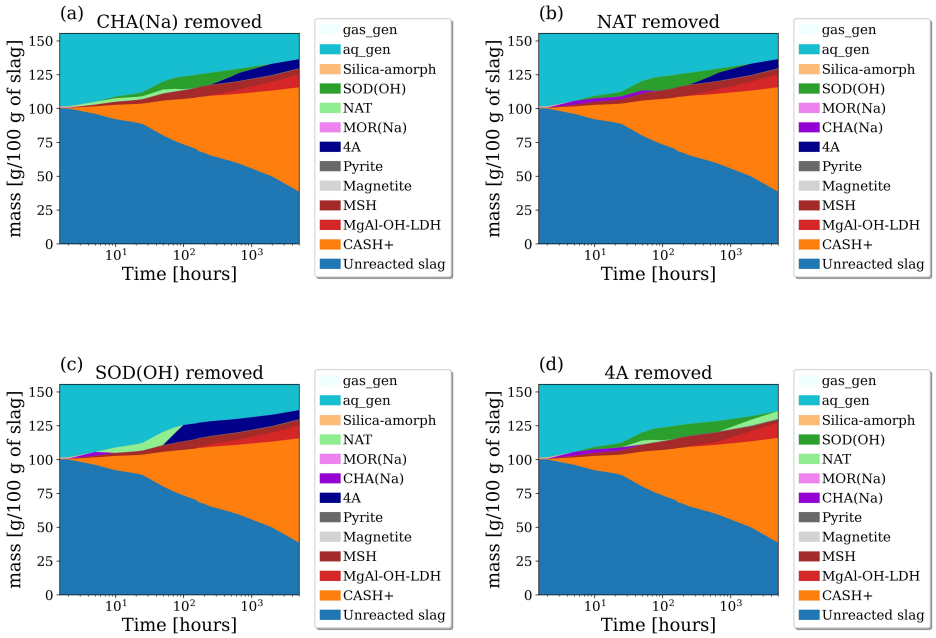

Figure 10: Specific thermodynamic calculations varying zeolite databases for the mix hS

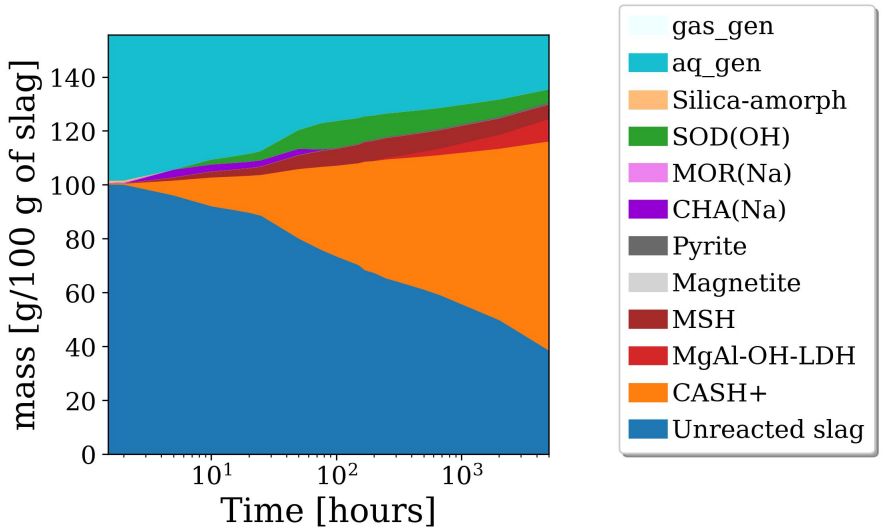

Figure 11: Thermodynamic calculation using the extended Debye-Hückel model for which GIS-LS-P(Ca), NAT, HEU(Ca)-1, HEU(Ca)-2, ANA and 4A were removed from the zeolite dataset

Paper 5

Multi-scale experimental investigation and analytical micro-mechanical modeling to determine Young's modulus of alkali-activated slag concrete

Publisher's version

Published in *Construction and Building Materials*

Volume 383 (12), 2023, 131272

DOI: 10.1016/j.conbuildmat.2022.126577

Authors: **Richard Caron**, Ravi A. Patel, Andreas Bogner,

Frank Dehn

Construction and Building Materials 383 (2023) 131272

Contents lists available at ScienceDirect

Construction and Building Materials

journal homepage: www.elsevier.com/locate/conbuildmat

Multi-scale experimental investigation and analytical micro-mechanical modeling to determine Young's modulus of alkali-activated slag concrete

Richard Caron *, Ravi A. Patel, Andreas Bogner, Frank Dehn

Institute of Building Materials and Concrete Structures (IMB), Karlsruhe Institute of Technology (KIT), Gotthard-Franz-Str. 3, Karlsruhe, DE-76131, Germany
Materials Testing and Research Institute Karlsruhe (MPA), Karlsruhe Institute of Technology (KIT), Gotthard-Franz-Str. 3, Karlsruhe, DE-76131, Germany

ARTICLE INFO

Keywords:
Alkali-activated-slag
Multi-scale modeling
Nano-indentation
Analytical micro-mechanics
Young's modulus

ABSTRACT

In this study, multi-scale experiments and analytical micro-mechanics based modeling are conducted to evaluate Young's modulus of alkali-activated slag (AAS) concrete. The evolution of volume fractions of phases is obtained using a thermodynamic model coupled with a kinetic model. Nano-indentation measurements indicate the existence of a soft and a hard matrix made of reaction products, independently of the mix tested. The homogenization model for Young's modulus is validated against results on paste and concrete with more than 95 % accuracy. Sensitivity analysis reveals Young's modulus of aggregates and of the soft matrix as the main influencing parameters.

1. Introduction

Cement is the most used binder in the concrete industry. However, more and more research has been done on other binders to improve the durability and specific mechanical properties of concrete. These new binders can either be used as Supplementary Cementitious Materials (SCM) [1] to substitute partially cement. Or they completely replace cement by activation through alkali solutions to generate Alkali-Activated Materials (AAM) concrete [2]. Slag is a by-product of the steel industry and can be used both ways, for example in CEM II, CEM III or CEM V as SCM, or as a precursor with alkali solutions such as sodium hydroxide, sodium silicate or sodium carbonate [3]. In this latter case, the generated concrete is named Alkali-Activated Slag (AAS) concrete. Among the possible alkali solutions, Fernandez et al. [3] showed that sodium silicate presented the best strength and that it was even comparable to the one from Ordinary Portland Cement (OPC) systems.

The reaction products of AAS concrete are different from OPC concrete. Hydrotalcite and zeolite-type phases [4,5] have been characterized in AAS concrete, whereas portlandite or ettringite, common for OPC systems, are not present. Nevertheless, both AAS and OPC have similar main products. In OPC, it is a Calcium–Silicate–Hydrate (C–S–H) gel with Ca/Si ratios varying between 0.7 and 2.0 [6–8]. In AAS, the main product is a Calcium–Aluminum–Silicate–Hydrate (C–A–S–H) gel containing higher alumina uptake in the C–S–H phase [9–11]. In addition, alkali metals (Na, K) can be incorporated to form structures as N–C–A–S–H or C–N–A–S–H [5,12]. As C–S–H has a predominant role in the mechanical properties of OPC concrete [13], methods to predict Young's modulus, as analytical micro-mechanics, can be applied to AAS concrete.

Analytical micro-mechanics has been successfully applied in the past decades to predict Young's modulus of OPC concrete. Different approaches were used to describe the concrete microstructure within the framework of analytical micro-mechanics. Bernard et al. [14] represented OPC concrete as a hierarchical microstructure with three levels. The first level corresponds to the C–S–H gel. Two types of C–S–H, viz. low-density (LD) and high-density (HD) C–S–H, are considered as inclusions in the matrix of equivalent homogeneous media. Finally, applying the self-consistent (SC) scheme, elastic properties of C–S–H are obtained. In the second level, at the paste scale, unreacted clinker particles, portlandite crystals, aluminates and macro-porosity are regarded as inclusions in the C–S–H matrix and elastic properties of paste are homogenized with the Mori–Tanaka (MT) scheme. Finally, level three corresponds to the concrete scale and the microstructure is represented as inclusions of aggregates in the matrix of cement paste, which is homogenized using the MT scheme. The effect of ITZ was neglected for concrete. Similarly, Pichler et al. [15] considered the concrete microstructure representation in three levels. However, their description of cement paste microstructure differed from Bernard et al.. Pichler et al. considered that at level one hydrate foam is composed of hydration products and pores as inclusion in the matrix of equivalent homogenized media. They did not distinguish different types of hydration products but rather took the properties of hydration products as

* Corresponding author at: Institute of Building Materials and Concrete Structures (IMB), Karlsruhe Institute of Technology (KIT), Gotthard-Franz-Str. 3, Karlsruhe, DE-76131, Germany.
E-mail address: richard.caron@kit.edu (R. Caron).

https://doi.org/10.1016/j.conbuildmat.2023.131272
Received 1 December 2022; Received in revised form 3 March 2023; Accepted 31 March 2023

averages of different hydration products. The elastic properties of the hydrate foam scale are obtained using SC scheme. At level two, the unreacted clinker particles are considered as inclusions in the matrix of hydrate foam and MT scheme is used to obtain the elastic properties of the paste. Krishnya et al. [16] combined the ideas of Pichler et al. and Bernard et al. for the representation of the cement paste microstructure. In their model, the cement paste microstructure is discomposed into three levels, namely the C–S–H gel, composed of LD and HD C–S–H similar to Bernard et al., the hydrate foam level, and the cement paste level similar to Pichler et al. with the difference that different hydration products are regarded as individual phases. To account for the influence of ITZ at the concrete level, coated sphere model has been developed by Garboczi et al. [17]. ITZ is a zone surrounding fine or coarse aggregates with lower mechanical properties than the paste itself. The analytical model was compared against meso-scale model based on finite-element method. The accuracy of the model was found to be around 90 %. However, the role of ITZ on mechanical behavior has been debated in the literature. From nano-indentation tests, Luo et al. [18] showed that ITZ is not much weaker than the paste itself. However, the model of Bernard et al. [14], neglecting ITZ, resulted in a slight overestimation of concrete Young's modulus. For AAM concrete, few studies applied analytical micro-mechanics. Smilauer et al. used a two-level homogenization scheme to predict Young's modulus of fly ash/metakaolin paste [19] and validated it with experimental results. They obtained the volume fractions of the different phases required as input for homogenization schemes by performing additional characterization of the pore structure. Fang et al. used a two-level homogenization for predicting the properties of AAM paste to check the influence of properties of reaction products on Young's modulus of paste [20]. In general, there is a lack of consistent experimentally validated studies for the prediction of time-dependent mechanical properties of alkali-activated concrete. The lack of analytical models for the determination of the phase assemblage over time limits the applicability of such multi-scale schemes. In addition to phase volume fractions, such models also require elastic properties of individual phases, which can be determined using nano-indentation.

Nano-indentation has been widely used to determine the mechanical properties on the nano-scale for cement-based materials [21–24] as well as for AAMs [19,20,25–28] and in particular for AAS [29–33]. Königsberger et al. [29] studied the nano-properties of slag/fly ash blended systems with sodium silicate. They suggested that the measured Young's modulus of indentation is representative of a phase if this indent is far enough from the phase boundary. Gebregziabiher & Peethamparan [30] also considered that the products form only one phase for waterglass-activated slag. Results from Jia et al. [33] tend to show that an inner and an outer product should exist for sodium silicate-activated slag. Long et al. [31] only distinguished a C(-N-A)-S-H gel and a "partly activated particle" phase to describe the matrix. Thomas et al. [32] discussed how many phases should be considered for the AAS matrix. Similar to Jia et al. [33], they found that two phases exist for slag activated with sodium hydroxide, with the presence of inner and outer products. Nevertheless, they argue that the analysis is more complex for slag activated with sodium silicate and they do not find any distinction between inner and outer products with this activator solution. To summarize, no consensus has been reached to describe the mechanical behavior of AAS paste at the nano-scale.

In this contribution, a consistent multi-scale model based on analytical micro-mechanics is presented to predict Young's modulus of sodium silicate-activated slag. It uses as inputs the volume fractions of phases from a thermodynamic model coupled with a kinetics model, which has been experimentally validated by authors in an independent study [34,35]. The developed model has been validated against an experimental study made at paste and concrete scales for two promising concrete mixes at different ages up to 28 days. In addition, nano-indentation has been performed for the same mixes to determine Young's modulus of individual phases, which is an input for the model. The modeled representation of the microstructure at different levels is systematically discussed and justified. In addition, the role of other microstructure features such as ITZ, micro-cracks and air-voids on Young's modulus of AAS concrete is discussed through sensitivity analysis.

Table 1
Chemical composition of the anhydrous slag.

Oxide	CaO	SiO_2	Al_2O_3	MgO	Fe_2O_3	Na_2O	K_2O	SO_3	Oth.
Mass (%)	38.8	36.3	12.8	8.0	0.6	0.3	0.6	1.9	0.7

Table 2
Mix design on both paste and concrete scale.

Paste scale		Mix lS	Mix hS
w/s	[kg/kg]	0.40	0.40
n	[Na_2O g/100 g slag]	5.0	5.0
M_S	[SiO_2/Na_2O mol/mol]	0.5	2.2
Concrete scale		**Mix lS**	**Mix hS**
w/s	[kg/kg]	0.45	0.45
n	[Na_2O g/100 g slag]	5.0	5.0
M_S	[SiO_2/Na_2O mol/mol]	0.5	2.2
Precursor content	[kg/m^3 of concrete]	450	
Fine Agg. (0–2 mm)	[Vol-%]	40	
Coarse Agg. (2–8 mm)	[Vol-%]	30	
Coarse Agg. (8–16 mm)	[Vol-%]	30	

2. Materials and methods

2.1. Materials

Experiments were conducted on both paste and concrete. The slag used as precursor was provided by the company Ecocem (Netherlands). Energy dispersive X-ray fluorescence (XRF) spectrometry with an M4 Tornado (Bruker GmbH Karlsruhe, Germany) was used to determine the oxide composition. The sulfur content was determined from a CS-2000 from Eltra (Germany). The results of the composition of the slag are given in Table 1. The activator solutions were prepared by mixing a solution of sodium hydroxide (NaOH) of mass concentration of 50%, a commercial waterglass solution and tap water. The used waterglass solution was Betol 39 T from Woellner GmbH (Germany). It is composed of H_2O, Na_2O and SiO_2 with mass percents equal to 64.0%, 8.2%, and 27.8%, respectively. Two activator solutions were prepared. Both have the same alkali dosage $n = 5$ [g Na_2O/100 g slag]. Two silicate ratios (M_S) were investigated, namely 0.5 [mol SiO_2/mol Na_2O] and 2.2 [mol SiO_2/mol Na_2O]. The corresponding mixes are referred to as mix lS and mix hS, respectively. The water/slag ratio used for paste was $w/s = 0.4$ [kg/kg] for both mixes. For concrete, the water/slag ratio was 0.45 [kg/kg] to adapt the workability of the mix. River sand and quartzite aggregates were used. These two mixes were found to be suitable for structural applications. They have a longer setting time than mixes with intermediate silicate ratios (between 1.0 and 2.0), in accordance with literature results [5,36,37]. Furthermore, their compressive strengths are sufficient for applications as structural concrete [38]. The mix design for both mixes is summarized in Table 2 for both paste and concrete.

2.2. Methods

2.2.1. Mixing procedure, casting and storage

The alkali solutions were prepared 24 hours before the first contact with slag to reach the equilibrium temperature with the surrounding environment. For preparing both paste and concrete, the dry ingredients were mixed for 30 s. Then, the alkali solution was added and the fresh paste or concrete was mixed for one minute. It was let rest for thirty seconds and then mixed for another two minutes. The paste was used to fill 4 × 4 × 16 cm^3 prismatic molds for Young's modulus and

$2 \times 2 \times 8$ cm^3 molds for nano-indentation tests. For porosity measurements, thin samples of 5 mm thickness and 2×2 cm^2 surface were cast. For concrete, cylinders of 100 mm diameter and 285 mm height were used for Young's modulus measurements. All the samples were demolded after 24 hours and put in plastic bags to limit drying until the test day.

2.2.2. Young's modulus and compressive strength of paste and concrete samples

For paste samples, two methods were used to measure Young's modulus. The dynamic Young's modulus was measured with the ultrasound technique at a frequency of 20 kHz with a coupled Geotron-Elektronik GDH 200 (Germany) and a Greisinger Ultrashall Generator USG 40 (Germany). Since this method is non-destructive, the dynamic Young's modulus was measured at several ages (1, 2, 3, 7, 14 and 28 days) on six samples each. The standard deviation for this measurement was less than 1.5%.

The static Young's modulus at 28 days was measured with an adapted protocol of DIN EN 12390-13 (method B) for paste. The average compressive strength of three samples was first determined using the standard DIN EN 196-1, for which the samples were just covered, and not stored in water [39]. Then, for three other samples, three loading–unloading cycles at a stress level equal to one-third of the average compressive strength previously measured were carried out. The static Young's modulus was determined with the last loading part of the experiment.

The relation between both static Young's modulus and dynamic Young's modulus is fairly linear [40–42]. For this reason, an equivalent function between the static modulus and the dynamic modulus was then established for each mix:

$$E_{stat}(mix, 28d) = \alpha_E(mix) \cdot E_{dyn}(mix, 28d) \tag{1}$$

For concrete, Young's modulus and the compressive strength were measured with cylinders at test ages of 2, 7, 14, 28 and 56 days. The standard DIN EN 12390-13 (method B) [43] was followed with six samples tested per testing day. The results on concrete were already published in [38].

2.2.3. Nano-indentation tests

Nano-indentation tests were carried out on mature paste samples older than six months for both mixes lS and hS. The sample preparation was performed in four main steps: cutting the sample, embedding the sample in epoxy resin, grinding and polishing of the sample. A prismatic sample of $2 \times 2 \times 8$ cm^3 was cut with an IsoMet 1000 (Buehler). The final sample had the same cross-section 2×2 cm^2 with a depth of around 1 cm. It was then embedded in epoxy resin in cylindrical forms of 3.2 cm diameter and let to rest overnight. The grinding and polishing processes were performed with an AutoMet 250 equipment (Buehler). Grinding was done with an Apex DGD 45 μm (Buehler). Three polishing grades with MetaDi Supreme Diamant suspensions (Buehler) of 9 μm, 3 μm and 1 μm were carried out for 4, 4 and 3 minutes, respectively. A final polishing with a 0.05 μm MasterPrep Al_2O_3 solution was performed for 3 min. The force applied for all steps was 5 N. At the end of the polishing, samples were cleaned by N_2 air steam and stored in a desiccator until the day of testing. The roughness measured after polishing, determined with Atomic Force Microscopy (AFM), was equal to 75 μm, for a grid of 100 μm × 100 μm.

Nano-indentation tests were carried out with a UNHT^3 (Anton Paar Germany GmbH). For each mix, four independent grids of 23×23 points were tested with a spacing of 10 μm, between each point. The applied force was 2 mN, which corresponds to a mean indentation depth of around 400 nm. For Miller et al. [44], the maximum heterogeneous characteristic size d must be well lower than the indentation depth h and the latter must also be lower than the characteristic size of the microstructure D, such as: $d \ll h < D/10$. The measured roughness of the samples with AFM was 75 μm. Thus, the criterion was satisfied. The sample was loaded (and unloaded) with a speed rate of 10 mN/min with a holding time of 180 s.

Following the Oliver–Pharr methodology [45,46], the elastic modulus E and the hardness H under the indent can be evaluated from the loading-penetration (P-h) of nano-indentation tests. The hypothesis of elasticity is made for the unloading phase of the indentation. The contact stiffness S is evaluated at the initial slope of this unloading branch as:

$$S = \frac{dP}{dh} \tag{2}$$

The reduced modulus E_r is defined as:

$$E_r = \frac{S\sqrt{\pi}}{2\beta\sqrt{A_c(h_{max})}} \tag{3}$$

where A_c is the indentation contact area, $\beta(h, \nu)$ is the correction factor for non-symmetrical indenter, being equal to 1.034 for the Berkovich tip [32], and h_{max} is the maximum depth. The elastic modulus E of the tested material is determined by taking into account the non-rigidity of the indenter with:

$$\frac{1}{E_r} = \frac{1-\nu^2}{E} + \frac{1-\nu_i^2}{E_i} \tag{4}$$

where ν is the Poisson's coefficient of the material, taken equal to 0.27, while E_i and ν_i are the elastic modulus and the Poisson's coefficient of the indenter. For diamond, the following values are given: $E_i = 1141$ GPa and $\nu_i = 0.07$.

Each mix (mix lS and mix hS) was post-processed independently. The concatenated data of every nano-indentation test were interpreted with 2D-clustering as it has lately been done in the literature [20,23,24,32,47,48]. The Gaussian mixture is the clustering method that has been the most used in recent years. It is based on the expectation–maximization algorithm using the maximum likelihood function. The clustering was carried out 500 times with random starting points for each calculation to avoid local minima. Different constraints were tested on the covariance viz., spherical, diagonal and full, to check the influence of the choice of the constraint on the shape of clusters. Additionally, two other clustering methods, viz., the k-means and the spectral methods, were also tested to evaluate the influence of the clustering process on the interpretation of nano-indentation results. These methods have been used in past by other researchers [49–51]. So far, there is no consensus on the best clustering method to interpret nano-indentation results in the literature. Each of these methods has advantages and limitations. For instance, k-means and spectral methods are fast to train but very sensitive to outliers. On the other hand, the Gaussian mixture method can effectively deal with outliers but rely on the assumption that data follows normal distribution which may not always be the case. Secondly, the Gaussian mixture method is very sensitive to the choice of the initial parameters and of constraints applied to covariance. Therefore, in this study, the use of different clustering methods is to account for the error due to the clustering process in the sensitivity analysis of the input parameters for the developed multi-scale model. To determine the correct number of clusters, the elbow method was performed. The number of specified clusters varied from 0 to 15. For each order, the sum squared error of the Euclidean distance to centers was calculated. The optimum number of clusters is the inflection point between linear fits of the sum squared error as a function of the number of clusters. This inflection point corresponds to the number of clusters above which the addition of a new cluster does not improve the variance between different points in a given cluster.

2.2.4. Porosity

The total porosity of pastes was measured at ages 1, 2, 3, 7 and 28 days. For each testing day, two samples were put in a chamber at a controlled relative humidity (RH = 99%). When the mass equilibrium $m_{99\%}$ was reached, they were put first in an oven at 50 °C. The dried mass after equilibrium $m_{0\%,50\ °C}$ was reported. The samples were then dried at 105 °C and the mass after equilibrium $m_{0\%,105\ °C}$ was also reported. This method allows to determine two porosities $\phi_{dry,50\ °C}$ and $\phi_{dry,105\ °C}$.

2.2.5. Phase assemblage

The phase assemblage was determined by thermodynamic calculations performed using the Gibbs free Energy Minimization Software GEMS [52]. The extended Debye–Hückel model was used to calculate the activity coefficients of aqueous species [53]:

$$\log \gamma_i = \frac{-A_\gamma z_i^2 \sqrt{I}}{1 + B_\gamma a_i \sqrt{I}} + b_\gamma I \tag{5}$$

where for each species i, z_i is the charge, a_i is the ion-size parameter, I the ionic strength, b_γ is a semi-empirical parameter, A_γ and B_γ represent the water solvent parameters. For a NaOH electrolyte b_γ and a_i are 0.098 and 3.31, respectively. The equilibrated system was composed of pure solids, solid solutions, aqueous electrolytes and gas. For aqueous species, the PSI-Nagra thermodynamic database was used [54]. The C–(N-)A–S–H gel was modeled with the sublattice CASH+ non-ideal solid solution model [55,56]. It considers the gel as a sub-lattice multi-site solid-solution of 16 end-members. The hydrotalcite phases were taken from Myers et al. [11]. Magnesium–Silicate–Hydrates (M–S–H) data from [57] and zeolite phases from [58,59] were also added to the dataset. Other reaction products were modeled with the CEMDATA18 database [57]. The use of these databases was already discussed and compared with experimental phase assemblage in a previous study [34]. This thermodynamic model was further coupled to the dissolution kinetic model [34,35] to follow the evolution of the phase assemblage with time. The volume fractions of the different phases determined with this coupled model were directly used as input in the multi-scale model.

3. Multi-scale structure of concrete for the determination of Young's modulus

The model to obtain Young's modulus of AAS paste and concrete is presented in this section. It is based on multi-scale homogenization performed with analytical micro-mechanics. The basics of the effective media theory are provided in Section 3.1. After, the description of the microstructure and the determination of volume fractions and Young's modulus of each phase are provided. The proposed multi-scale scheme is schematically depicted in Fig. 1. It is composed of five levels. Level 0 represents the homogenization of the reaction product foam, which consists of two types of reaction product matrices identified through nano-indentation tests and gel pores. Level 1 and level 2 correspond to the homogenization of AAS paste. At level 1, capillary pores are considered as an inclusion in the homogenized matrix of reaction product foam. This homogenized phase then acts as a matrix of inclusion of unreacted slag particle to constitute AAS paste. The volume fraction of reaction products, porosity and unreacted slag are determined using coupled thermodynamic-kinetic modeling described previously. Finally, level 3 and level 4 represent mortar and concrete, respectively. In this section, justifications regarding the assumptions of the model as well as further details of the multi-scale modeling scheme are provided.

3.1. Homogenization using analytical micro-mechanics

Homogenization based on analytical micro-mechanics allows the determination of mechanical properties of heterogeneous microstructures composed of several different phases. The homogeneous material is generated from a well-defined representative volume element (RVE), with a characteristic size much larger than the characteristic length of the inhomogeneities and much smaller than the size of the whole body. The properties of this homogeneous material are estimated from the structure of the statistical geometry and morphology of the phases, and from their mechanical properties. The main objective of homogenization problems is to determine the link between the local fields $\sigma(x)$ and $\epsilon(x)$, and the macroscopic fields $\mathbf{\Sigma}$ and $\mathbf{E}$ that are applied on the material. The strain concentration operator $\mathcal{A}$ and the stress concentration operator $\mathcal{B}$ can be defined as:

$$\begin{cases} \epsilon(x) &= \mathcal{A}(\mathbf{E}) \\ \sigma(x) &= \mathcal{B}(\mathbf{\Sigma}) \end{cases} \tag{6}$$

In the case of linear elasticity, the strain and stress concentration operator are fourth-order tensors fields:

$$\begin{cases} \epsilon(x) &= \mathcal{A}(x) &: \mathbf{E} \\ \sigma(x) &= \mathcal{B}(x) &: \mathbf{\Sigma} \end{cases} \tag{7}$$

It can be proved that Σ is the volume average stress $\langle\sigma\rangle$ in the RVE for any equilibrated stress field σ and that E is the volume average strain $\langle\epsilon\rangle$ for any compatible strain field ϵ. For this reason, $\langle\mathcal{A}\rangle = \mathcal{I}$ and $\langle\mathcal{B}\rangle = \mathcal{I}$, where $\langle\cdot\rangle$ represents the tensor volume average. $\mathcal{I}$ is the fourth-order symmetric unity tensor, with $\mathcal{I}_{ijkl} = \frac{1}{2}(\delta_{ik}\delta_{jl} + \delta_{il}\delta_{jk})$

Mechanical properties of each phase r are defined with the constraint tensor C_r and the compliance tensor S_r by:

$$\begin{cases} \sigma &= C_r &: \epsilon \\ \epsilon &= S_r &: \sigma \end{cases} \tag{8}$$

Eshelby [60] solved the problem of a single ellipsoidal inclusion H defined with the constraint tensor C_H embedded in an infinite homogeneous elastic matrix called the reference medium defined with the constraint tensor C_0 subjected to the homogeneous strain $\mathbf{E}$ or stress $\mathbf{\Sigma}$ at infinity. The stress and strain fields in H, σ_H and ϵ_H, respectively are uniform

$$\begin{cases} \epsilon_H &= [\mathcal{I} + \mathcal{P}_{0,H} : (C_H - C_0)]^{-1} : E \\ \sigma_H &= C_H : \epsilon_H \end{cases} \tag{9}$$

where $\mathcal{P}_{0,H}$ is the Hill polarization tensor related to the Eshelby tensor $S_{0,H}^{Esh}$ by

$$S_{0,H}^{Esh} = \mathcal{P}_{0,H} : C_0 \tag{10}$$

This result can be used to estimate the property of a heterogeneous material made of r phases of modulus C_r that can be regarded as ellipsoidal inclusions embedded in an infinite matrix (reference medium) of modulus C_0. Under these assumptions, the estimated modulus of the equivalent matrix C^{est} is equal to:

$$C^{est} = \langle C : [\mathcal{I} + \mathcal{P}_0 : (C - C_0)]^{-1} \rangle : \langle [\mathcal{I} + \mathcal{P}_0 : (C - C_0)]^{-1} \rangle^{-1} \tag{11}$$

When the inclusions are spherical,

$$\begin{cases} S_0^{Esh} &= \alpha_0 \mathcal{J} + \beta_0 \mathcal{K} \\ \alpha_0 &= \frac{3k_0}{3k_0 + 4\mu_0} \\ \beta_0 &= \frac{6(k_0 + 2\mu_0)}{5(3k_0 + 4\mu_0)} \end{cases} \tag{12}$$

k_0 and μ_0 are the bulk modulus and shear modulus, respectively, of the reference medium. $\mathcal{J}$ is the spherical part of $\mathcal{I}$ and $\mathcal{K}$ is its deviatoric part:

$$\begin{cases} \mathcal{J} &= \frac{1}{3}\mathbf{1} \otimes \mathbf{1} \\ \mathcal{K} &= \mathcal{I} - \mathcal{J} \end{cases} \tag{13}$$

where $\mathbf{1}_{ij} = \delta_{ij}$.

The effective bulk modulus k^{est} and shear modulus μ^{est} can be then deduced from the bulk modulus k_r and shear modulus μ_r of each phase r having a volume fraction f_r:

$$\begin{cases} k^{est} = \sum_r f_r k_r (1 + \alpha_0 (\frac{k_r}{k_0} - 1))^{-1} \times [\sum_r f_r (1 + \alpha_0 (\frac{k_r}{k_0} - 1))^{-1}]^{-1} \\ \mu^{est} = \sum_r f_r \mu_r (1 + \beta_0 (\frac{\mu_r}{\mu_0} - 1))^{-1} \times [\sum_r f_r (1 + \beta_0 (\frac{\mu_r}{\mu_0} - 1))^{-1}]^{-1} \end{cases} \tag{14}$$

The last step is to choose the reference medium. In the case where the reference medium is taken equal to the effective considered medium (i.e $k_0 = k^{est}$ and $\mu_0 = \mu^{est}$), all the phases have the same role and can be inverted. The corresponding homogenization scheme is named self-consistent scheme [61–63]. It is implicit and requires a numerical method to find the corresponding solution. When one of the phases

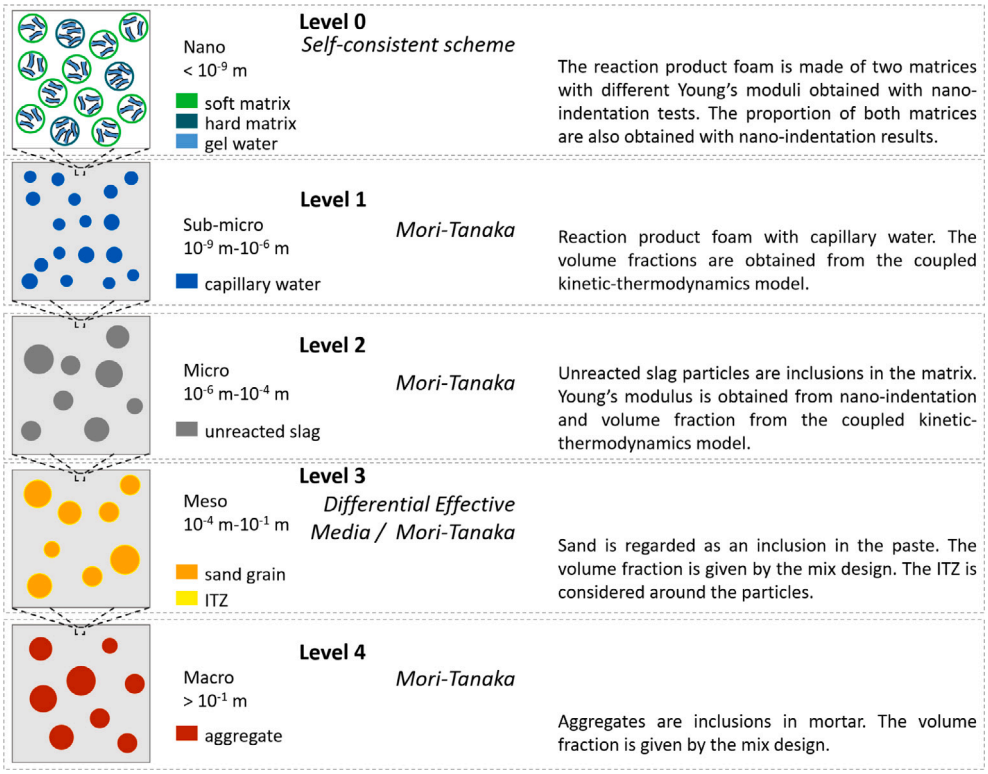

Fig. 1. Homogenization scheme of AAS used in this study. Level 0 corresponds to the reaction product foam; Level 1 corresponds to the inclusion of capillary water in the reaction product foam; Level 2 corresponds to the inclusion of the unreacted slag particles in the homogenized matrix of reaction product foam and capillary water to constitute paste; Level 3 corresponds to the inclusion of sand grains in paste, considering the presence of the ITZ; Level 4 corresponds to concrete.

has the role of a matrix that is regarded as the reference medium in which the other phases are embedded, (i.e $k_0 = k_m$ and $\mu_0 = \mu_m$ where m stands for the matrix) it is referred to as the Mori–Tanaka scheme [64,65].

3.2. Level 0: Reaction product foam

At Level 0, reaction products and gel water are homogenized as a reaction product foam. Reaction products of AAS depend on the chemical composition of both slag and activator solution. The main product that has been often reported is Calcium–Aluminum–Silicate–Hydrates (C–A–S–H) [5,35,66,67]. It has a similar structure as Calcium–Silicate–Hydrates (C–S–H) gel, which is present in cement-based systems, with a higher aluminum and alkali uptake [11]. Hydrotalcite is the second most characterized product [4,35,67], however, it does not form if the amount of MgO is not high enough in the slag [68]. Zeolites have been also characterized [5,35] and predicted by thermodynamic calculations for such systems [35]. Other products like M–S–H [35] or straetlingite [69] have been reported. However, post-processing of nano-indentation does not lead to clustering with as many phases since the indented surfaces are too coarse [70] and the reaction product foam must be regarded as an already homogenized material made of C–A–S–H and other phases such as hydrotalcite, zeolites and other products. Given the results obtained with nano-indentation (see Section 4.2), two types of matrices are considered, viz. a soft matrix and a hard matrix to describe the reaction product foam. This approach is analogous to that proposed for OPC-based systems with a low-density (LD) C–S–H and a high-density (HD) C–S–H [14,21,22,71,72]. The size of the representative volume element (RVE) of the reaction product foam is around 50 nm [73]. The results from nano-indentation experiments are used as inputs and Young's modulus for these two types of matrix phases are denoted as E_{soft} and E_{hard} for the soft matrix and the hard matrix, respectively. These two matrices are homogenized with a self-consistent scheme for which both Poisson's ratio, namely ν_{soft} for the soft matrix and ν_{hard} for the hard matrix, are fixed to 0.24, as for LD C–S–H and HD C–S–H [14]. The proportions of these two soft and hard matrices are determined from nano-indentation results (see Section 4.2). $f_{0,soft}$ stands for the volume fraction of soft matrix in the reaction product foam, while $f_{0,hard}$ stands for the volume fraction of hard matrix in the reaction product foam. Both are linked by the following equation:

$$f_{0,hard} = 1 - f_{0,soft} \tag{15}$$

The presence of gel water is also considered at this scale. According to Jennings et al. [74], the gel water porosity in HD C–S–H is equal to 26% of the volume fraction of C–S–H, while the one in LD C–S–H is equal to 36% of the volume fraction of C–S–H. Calculations from Brouwers [75], using the Powers model, show that the gel porosity

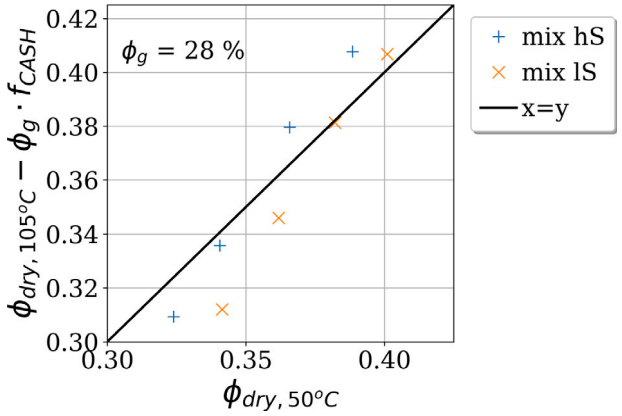

Fig. 2. Determination of gel water. It corresponds to an amount of water equal to ϕ_g = 28% of the C–A–S–H volume amount.

should be between 28 and 32% of the volume fraction of C–S–H. In this study, for AAS slag, the gel water in the reaction product foam $f_{w,gel}$ is fixed and modeled as:

$$f_{w,gel} = \phi_g \cdot f_{CASH} \tag{16}$$

with f_{CASH} the volume fraction of the C–A–S–H gel obtained with the thermodynamic model and $\phi_g = 28\%$. The value of 28% in this study is a fair estimation of gel porosity. It represents the difference between the total porosity obtained by drying at 50 °C $\phi_{dry,50\ °C}$ and at 105 °C $\phi_{dry,105\ °C}$ (see Fig. 2):

$$\phi_{dry,50\ °C} \approx \phi_{dry,105\ °C} - \phi_g \cdot f_{CASH} \tag{17}$$

3.3. Level 1 and Level 2: from the AAS reaction product foam to the AAS paste

The pore structure of AAS paste is very dense. Most of its pores are at the nano-scale and only few pores are above 100 nm, as reported, for example, in [76]. This leads to the size of RVE of reaction product foam being around 300 nm. On the contrary, the typical size of slag particles is 50 μm, and hence, the size of RVE would correspond to 200 μm. Due to this difference in the size of RVE, a two-step homogenization is adapted for AAS paste. First, the capillary water embedded in the reaction product foam (Level 1) is homogenized. The volume fraction of reaction product foam f_0 at Level 1 is given by the thermodynamic model. The volume fraction of capillary water $f_{w,cap}$ is the difference between the water obtained from thermodynamic model f_w and the gel water $f_{w,gel}$

$$f_{w,cap} = f_w - f_{w,gel} = f_w - \phi_g \cdot f_{CASH} \tag{18}$$

As stated in [77], drying at 105 °C induces the dehydration of the C–A–S–H gel, i.e. the evaporation of water (loosely) bounded with C–A–S–H. For this reason, measuring the total porosity with drying at 50 °C is more representative of the capillary porosity. After the inclusion of capillary water in the reaction product foam, the unreacted particles are included in this homogenized material (Level 2). For both scales, homogenization is performed with the Mori–Tanaka scheme in which the inclusions are regarded as spheres. The Young's modulus of the unreacted particles E_{slag} is obtained from nano-indentation results (see Section 4.2). The Poisson's ratio of the slag ν_{slag} is fixed to 0.2 [29] and the volume fraction of the unreacted slag f_{slag} is obtained from the kinetic model. The presence of air voids in AAS paste is neglected.

3.4. Level 3 and Level 4: from AAS paste to mortar and concrete

Once the mechanical properties of the paste are determined, they can be used for obtaining Young's modulus at the mortar scale (Level 3). The size of the RVE at the mortar scale ranges up to a few millimeters. Some authors take into account the presence of the interfacial transition zone (ITZ) between the paste and the sand [18,78–81]. It represents the region in the vicinity of the particles in which the properties of the paste are different from the bulk properties [78,79] due to a higher porosity in this zone [18,80,81]. The three-phase effective medium theory from Christensen [82] can be used to allow the homogenization of the inclusions accounting for the ITZ. This approach has been applied to concrete by Garboczi et al. [17] with the concept of coated spheres [83,84].

The dilute approximation gives the stiffness K and compliance μ of the effective medium for an inclusion of modulus K_1 and μ_1 in a matrix of modulus K_0 and μ_0:

$$K_e - K_0 = \phi(K_0 - K_1)A_1 \tag{19}$$

where ϕ is the volume concentration of the included phase in the composite and A_1 is the strain concentration factor of the inclusion. By doing a differentiation of this equation for spherical inclusions, one gets the following set of equations [17,84]:

$$\begin{cases} \frac{dK_e}{d\phi} = \frac{1}{1-\phi}\frac{(K_e+\frac{4}{3}\mu_e)(K_2-K_e)}{(K_2+\frac{4}{3}\mu_e)} \\ \frac{d\mu_e}{d\phi} = \frac{1}{1-\phi}\frac{(\mu_e+H_e)(\mu_2-\mu_e)}{\mu_2+H_e} \end{cases} \tag{20}$$

where:

$$H_e = \frac{\frac{3}{2}K_e + \frac{4}{3}\mu_e}{K_e + 2\mu_e}\mu_e \tag{21}$$

(20) is a system of two coupled equations that must be solved together via a numerical scheme.

The properties of the medium composed of a spherical particle surrounded by a spherical shell can be homogenized following the work from [82]. Each particle is supposed to be independent of the others with an isolated shell. For a 3D particle mapping, the effective bulk modulus K is given by:

$$K = K_m + \frac{c(K_i - K_m)}{1 + (1-c)\frac{K_i - K_m}{K_m + \frac{4}{3}\mu_m}} \tag{22}$$

The determination of the shear modulus implies the solution of the second-order equation [82]:

$$A(\frac{\mu}{\mu_m})^2 + 2B(\frac{\mu}{\mu_m}) + C = 0 \tag{23}$$

where:

$$\begin{aligned} A = {} & 8(\frac{\mu_i}{\mu_m} - 1)(4 - 5\nu_m)\eta_1 c^{10/3} - 2[63(\frac{\mu_i}{\mu_m} - 1)\eta_2 + 2\eta_1\eta_3]c^{7/3} \\ & + 252(\frac{\mu_i}{\mu_m} - 1)\eta_2 c^{5/3} \\ & - 50(\frac{\mu_i}{\mu_m} - 1)(7 - 12\nu_m + 8\nu_m^2)\eta_2 c + 4(7 - 10\nu_m)\eta_2\eta_3 \end{aligned}$$

$$\begin{aligned} B = {} & -2(\frac{\mu_i}{\mu_m} - 1)(1 - 5\nu_m)\eta_1 c^{10/3} + 2[63(\frac{\mu_i}{\mu_m} - 1)\eta_2 + 2\eta_1\eta_3]c^{7/3} \\ & - 252(\frac{\mu_i}{\mu_m} - 1)\eta_2 c^{5/3} \\ & + 75(\frac{\mu_i}{\mu_m} - 1)(3 - \nu_m)\eta_2\nu_m c + \frac{3}{2}(15\nu_m - 7)\eta_2\eta_3 \end{aligned}$$

$$\begin{aligned} C = {} & 4(\frac{\mu_i}{\mu_m} - 1)(5\nu_m - 7)\eta_1 c^{10/3} - 2[63(\frac{\mu_i}{\mu_m} - 1)\eta_2 + 2\eta_1\eta_3]c^{7/3} \\ & + 252(\frac{\mu_i}{\mu_m} - 1)\eta_2 c^{5/3} + 25(\frac{\mu_i}{\mu_m} - 1)(\nu_m^2 - 7)\eta_2 c - (7 + 5\nu_m)\eta_2\eta_3 \end{aligned}$$

$$\eta_1 = (\frac{\mu_i}{\mu_m} - 1)(7 - 10\nu_m)(7 + 5\nu_i) + 105(\nu_i - \nu_m)$$

$$\eta_2 = (\frac{\mu_i}{\mu_m} - 1)(7 + 5\nu_i) + 35(1 - \nu_i)$$

$$\eta_3 = (\frac{\mu_i}{\mu_m} - 1)(8 - 10\nu_m) + 15(1 - \nu_m)$$

The next step is the homogenization of a distribution of particles of different sizes, surrounded by a shell and included in a matrix. For each particle size, the corresponding volume fractions and distributions are then calculated with [17]:

$$\begin{cases} c' = c\sum_{j=1}^{M} f_j\alpha_j \\ f_j' = \frac{f_j\alpha_j}{\sum_{i=1}^{M} f_i\alpha_i} \end{cases} \tag{24}$$

where $\alpha_j = (\frac{a_j}{b_j})^3$ with a_j and b_j the diameters of the outer shell and of the inner shell, respectively.

The average values of the bulk modulus and of the shear modulus can be then calculated. These average values are then used in Eq. (20) as values for K_2. Finally, the effective medium problem is solved with the fourth-order Runge–Kutta method.

Different ITZ thicknesses d_{ITZ} have been reported in the literature. Sun et al. assumed it as 14 μm [85]. Snyder et al. [86] and Scrivener et al. [87] found that the ITZ thickness varies around 15–20 μm. Honorio et al. hypothesized an ITZ of 20 μm [88]. Lutz et al. found 37 μm by inverse analysis [89]. Nilsen & Monteiro reported that it should be different depending on the type of concrete considered, from 8–10 μm for silica fume concrete to 50 μm for ordinary concrete [78]. Yang [90] showed that considering different ITZ thicknesses implies considering different Young's modulus E_{ITZ} in this zone. The hypothesis of an ITZ of 20 μm would imply Young's modulus in the ITZ equal to 20%–40% of Young's modulus of the paste, while this value should increase to 50%–70% of Young's modulus of the paste in the case of an ITZ thickness equal to 40 μm. In this study, both 20 μm and 40 μm thicknesses of ITZ are used with corresponding Young's modulus equal to 30% and 60%, respectively, of the homogenized paste Young's modulus (E_p). The Poisson's ratio of the ITZ is hypothesized to be equal to the one of the paste, as in [90].

From the mechanical properties obtained on the mortar scale, the homogenization is performed using the Mori–Tanaka scheme to predict Young's modulus of concrete (Level 4). For homogenization, mortar is regarded as the matrix in which aggregates are seen as spherical inclusion. The RVE at this scale is a few centimeters.

Mortar consists of gravels of size < 4 mm embedded in paste [13]. The volume fraction of the fine aggregates (f_{agg-f}) and the coarse aggregates (f_{agg-c}) are taken from the mix design (see Table 2). The Young's modulus of sand (E_{agg-f}) and aggregates (E_{agg-c}) are equal to 50 GPa, as can be found in the literature [14,85,91], while their Poisson's ratio (ν_{agg-f} and ν_{agg-c}) are equal to 0.2 [78,85,91].

3.5. Summary

The choices of parameters for the different homogenization levels are summarized in Table 3. Two sensitivity analyses were carried out to evaluate the error propagation from the different hypotheses of the model. They were performed using the sampling method proposed by Saltelli [92]. For the paste, the sensitivity analysis was conducted for five parameters E_{slag}, E_{soft}, E_{hard}, $f_{0,soft}$ and ϕ_g through 1536 samples. For concrete, paste Young's modulus E_p, Young's modulus of the gravels $E_g = E_{agg-f} = E_{agg-c}$, the ITZ thickness d_{ITZ} and Young's modulus of the ITZ E_{ITZ} were varied with 1024 samples. The data from sensitivity analysis was statistically analyzed using Sobol's method [93] to obtain total-order sensitivity indexes on the covariance matrix. The results will be provided in Section 5.1.

4. Results

4.1. Experimental determination of Young's modulus for AAS paste and concrete

The evolution of the dynamic Young's modulus of AAS paste for both mixes is given in Fig. 3(a). At the paste scale, the mix lS has a higher elastic modulus than the mix hS. The measured values for the elastic modulus of AAS pastes are in a similar range as that reported by Abate et al. [94]. The results of the static Young's modulus obtained at 28 days for both pastes are given in Table 4. The transfer coefficient α_E, linking static and dynamic Young's moduli as defined in Eq. (1), is similar for both mixes. It is equal to 0.72 ± 0.01. Young's modulus of both concretes is given in Fig. 3(b). As for paste, the mix lS has a higher Young's modulus than the mix hS.

Table 3
Input parameters for the proposed multi-scale model.

Level	Parameters	Value
0	E_{soft}	From nano-indentation
	E_{hard}	From nano-indentation
	ν_{soft}	0.24[a]
	ν_{hard}	0.24[a]
	ϕ_g	28%
	$f_{0,soft}$	From nano-indentation
1	f_0	From kin. mod. & therm. calculations
	$f_{w,cap}$	From kin. mod. & therm. calculations
	E_w	0 GPa
	ν_w	0.49999 [–]
2	E_{slag}	From nano-indentation
	ν_{slag}	0.2[b]
	f_{slag}	From kinetics model
3	E_{agg-f}	50 GPa[c]
	ν_{agg-f}	0.2[d]
	f_{agg-f}	38.6%
	d_{ITZ}	20 μm or 40 μm[e]
	E_{ITZ}/E_p	30% if d_{ITZ} = 20 μm; 60% if d_{ITZ} = 40 μm
4	E_{agg-c}	50 GPa[c]
	ν_{agg-c}	0.2[d]
	f_{agg-c}	36.5%

[a]Values from [14].
[b]Values from [29].
[c]Values from [14,85,91].
[d]Values from [78,85,91].
[e]Values from [90].

Table 4
Comparison of the static and dynamic Young's modulus at 28 days for both mix lS and mix hS.

	$E_{stat}(28d)$ [GPa]	$E_{dyn}(28d)$ [GPa]	α_E
mix lS	15.7 ± 0.5	22.1	0.71
mix hS	15.2 ± 0.9	20.8	0.73

4.2. Analysis of nano-indentation data

The results of the elbow method for each studied method are given in Fig. 4. The inflection point of the curve is located at k = 4, with k being the order of clusters. Thus, the nano-indentation results for both mix lS and mix hS were classified into four clusters, as plotted in Fig. 5, with clustering performed using a Gaussian mixture. Among these clusters, the one with the lowest E and H corresponds to pores and defects in the paste. The highest E and H correspond to unreacted slag. The obtained modulus for unreacted slag is in the range of 65–70 GPa. This range is comparable to what can be found in the literature [20,29–32,95].

The indented region during a nano-indentation corresponds to hundreds of nano-meters in width. As most of the reaction products such as C–A–S–H gel, hydrotalcite and zeolitic precursors are amorphous for AAS concrete [96], such large area would not correspond to a single phase but to a mixture of these phases [23,70]. For C–S–H gel often two types viz., LD C–S–H and HD C–S–H, are identified in nano-indentation tests [22,97]. These LD and HD C–S–H corresponds to the reaction products formed at early-age and later age due to the densification [98]. As C–A–S–H gel, the main reaction product of AAS, has a similar structure to C–S–H gel, similar phenomena occurring in C–A–S–H gels are expected. In this study, the clusters corresponding to low-density and high-density C–S–H are not referred to as LD and HD C–A–S–H but rather soft and hard matrices. This is to emphasize the fact that other minor amorphous products should act as inclusion in matrices of C–A–S–H and are not distinguishable by nano-indentation tests.

The elbow method can sometimes underestimate the number of clusters [99]. For this reason, the Bayesian Information Criterion (BIC) was used to check the choice of the number of the clusters, as in [32].

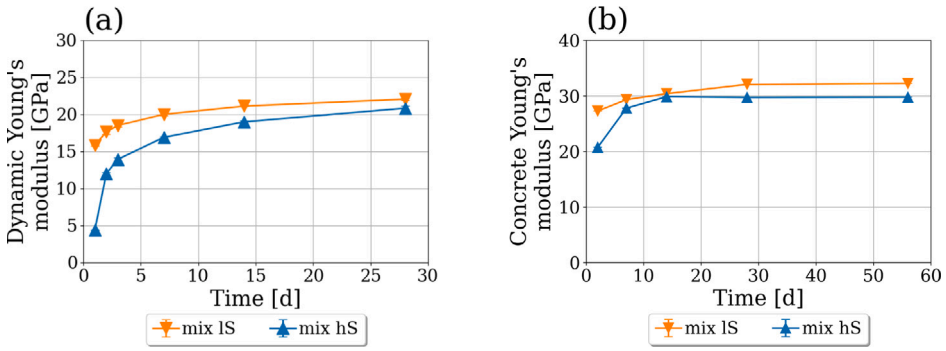

Fig. 3. Strength development of the mixes for both paste and concrete. (a) Dynamic Young's modulus on the paste scale for both mix lS and mix hS. (b) Young's modulus of concrete for both mix lS and mix hS.

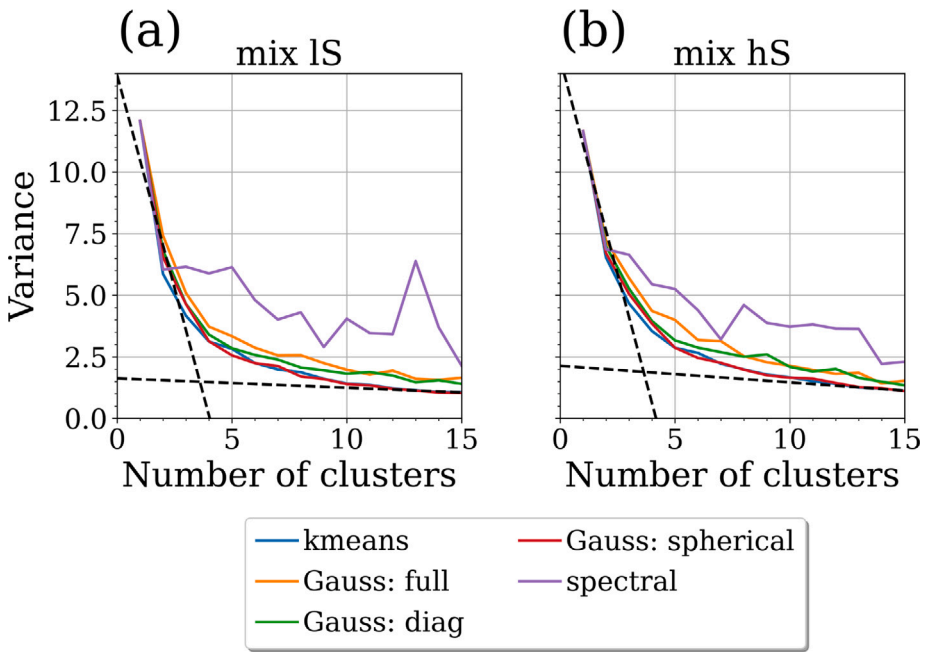

Fig. 4. Elbow method done for each clustering method on both mix lS (a) and mix hS (b). It allows the determination of the relevant number of clusters to consider during the post-process.

The results with BIC showed that either 4 or 5 clusters could be chosen (see supplementary material). For OPC systems, five clusters have been reported by some researchers where the fifth cluster corresponds to crystalline reaction products [22,97]. However, as AAS reaction products are amorphous, this cluster might correspond to the interface between reaction products and slag. In the absence of high-resolution SEM imaging of the indented region, it is not possible to confirm this at this moment. Hence, only four clusters are linked to the corresponding phases in this study.

The modulus of elasticity of the soft matrix (E_{soft}) and hard matrix (E_{hard}) are given in Table 5 for both mixes using different clustering methods. Nano-indentation also allows the determination of the relative proportion of the soft matrix and hard matrix at Level 0 in the reaction product foam (see Table 5). The relative proportion of soft matrix in the reaction product foam is found to be 70%–80%. With the exception of the spectral method for the mix lS, the obtained centers of clusters are quite independent of the clustering method. It can also be noted that the highest moduli are obtained with the highest proportions of soft matrix (e.g. with the k-means method). In addition, Table 5 shows that the nano-indentation results were fairly close for both mixes. For this reason, average values for the proportions as well as Young's modulus, given in Table 6, are used as inputs for multi-scale modeling hereafter.

Often in literature, only one type of matrix is identified for AAS systems [20,29,30]. However, the current study demonstrates the existence of two types of matrices, which is in agreement with Thomas et al. [32]. The values of Young's modulus of soft and hard matrix are also comparable to that for OPC systems [23]. Finally, the volume fraction of soft matrix is comparable to that of LD C–S–H reported as 67% for OPC paste [21].

4.3. Multi-scale modeling

The results of the multi-scale modeling for paste are shown in Fig. 6. They are in good agreement with the experiments. For the modeling, E_{soft}, E_{hard} and $f_{0,soft}$ must be given as input. Their values depend on the method used for the clustering analysis of nano-indentation results, as shown in Section 4.2. However, further calculations indicated that the standard deviation of Young's modulus of the reaction product foam E_{rpf} (Level 0) was lower than 1 GPa (5%) using the results from each clustering method (see Table 5). Besides, the modeling of water plays an important role. The hypothesis of splitting the total

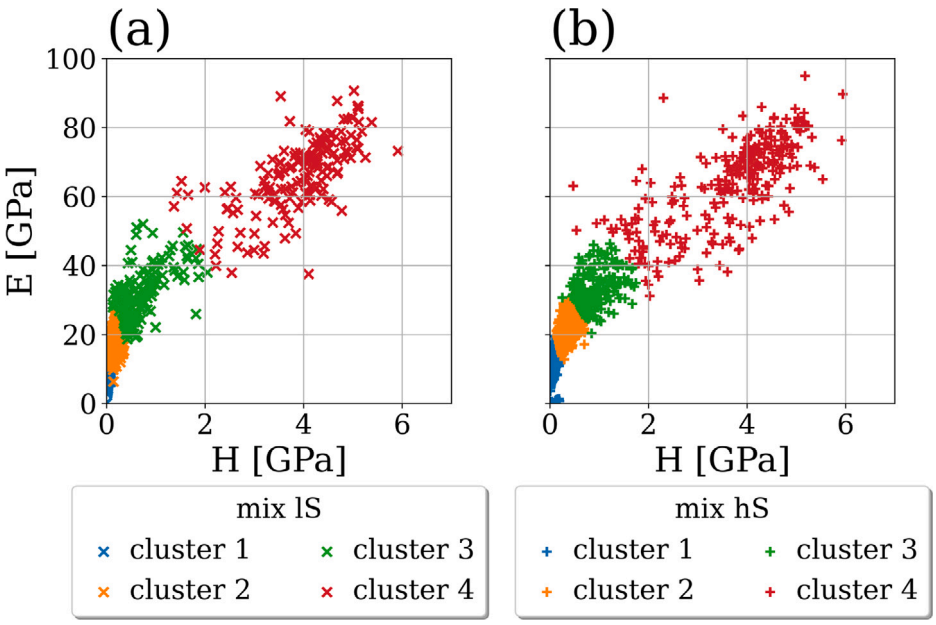

Fig. 5. Post-processing of nano-indentation experiments for both mix lS (a) and mix hS (b). Example of clustering with the Gaussian mixture.

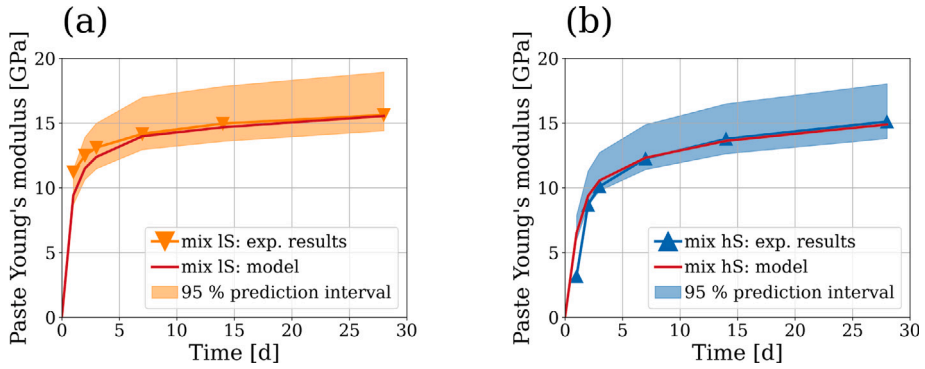

Fig. 6. Validation of the homogenization scheme on paste (Level 2) for both mix lS (a) and mix hS (b). The red curves correspond to calculations made with the coefficients from Tables 3 and 6. The bands correspond to the confidence interval at 95% for the sensitivity analysis done in Section 5.1.

Table 5
Young's modulus obtained from post-processing after nano-indentation results by different clustering methods. E_{rpf} is Young's modulus of the reaction product foam (Level 0).

Mix	Clustering method	E_{soft} [GPa]	E_{hard} [GPa]	$f_{0,soft}$ [%]	E_{rpf} [GPa]
mix lS	kmeans	19.0	37.7	82	21.5
	Gauss (full)	17.2	31.2	78	19.5
	Gauss (diagonal)	17.2	30.8	77	19.6
	Gauss (spherical)	17.0	30.0	71	20.0
	Spectral	14.8	65.6	78	20.0
mix hS	kmeans	23.0	41.6	84	25.1
	Gauss (full)	21.6	40.0	84	23.7
	Gauss (diagonal)	21.2	31.9	80	23.0
	Gauss (spherical)	20.8	28.8	69	23.0
	Spectral	19.3	38.6	80	22.1

Table 6
Clustering analysis of nano-indentation experiments for both mixes. E_{soft}, E_{hard} and E_{slag} are defined as the average Young's modulus of soft reaction products, hard reaction products and unreacted slag particles, respectively. $f_{0,soft}$ is the proportion of soft reaction products at Level 0.

Parameter Unit	E_{soft} [GPa]	E_{hard} [GPa]	E_{slag} [GPa]	$f_{0,soft}$ [%]
mix lS	17.1 ± 1.4	39.1 ± 13.5	70.6 ± 7.2	77 ± 4
mix hS	21.1 ± 1.2	36.1 ± 5.0	65.9 ± 4.1	79 ± 6
Average	19.1	37.6	68.3	78

porosity into gel water for Level 0 and capillary porosity for Level 1 is important to achieve this result. In fact, on the one hand, when mercury intrusion porosity (MIP) is used as water porosity instead of the term $\phi_{tot} - \phi_g \cdot f_{CASH}$, the results of Young's modulus are overestimated. As demonstrated by Müller et al. [100], the MIP porosity is representative of the capillary pores and a part of the gel pores. On the other hand, when the total water porosity is regarded only as an inclusion at Level 1 ($\phi_g = 0\%$, i.e. no gel water), the results of Young's modulus are largely underestimated. Thus, it is necessary to distinguish both gel water and capillary water and to take into account gel water in the properties of soft and hard matrix through nano-indentation. This is also justified as the sub-lattice solid solution representation of C–A–S–H only accounts for the inter-layer water [55,101]. Also, as shown in [34], the porosity computed from thermodynamic modeling is fairly close to total porosity which is obtained with a cycle of saturation-drying at 105 °C.

The results of the model for concrete are presented in Fig. 7 for both mix lS and mix hS. The computed Young's moduli of the paste are taken as input to predict Young's modulus of AAS concrete. As discussed in Section 3.4, both ITZ thicknesses of $d_{ITZ} = 20$ µm with $E_{ITZ}/E_p = 30\%$, and $d_{ITZ} = 40$ µm with $E_{ITZ}/E_p = 60\%$ are investigated.

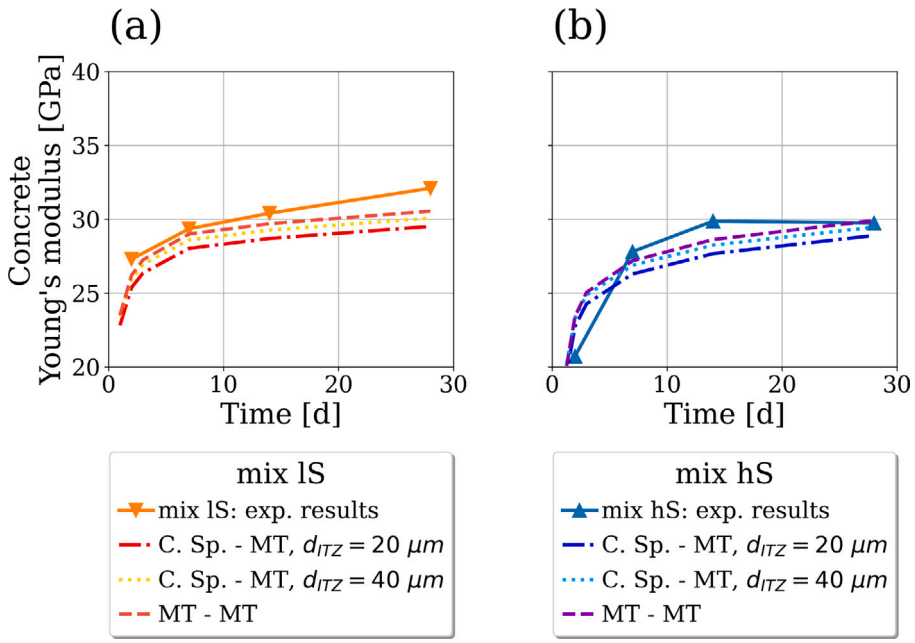

Fig. 7. Validation of the homogenization scheme on concrete (Level 4) for both mix lS (a) and mix hS (b). The calculations "Coated Spheres-Mori–Tanaka" curves correspond to the calculations done in Section 4.3 for both considered ITZ thickness (20 μm and 40 μm). The "Mori–Tanaka-Mori–Tanaka" curves are the calculations done with the hypothesis of perfect bound between sand grains and paste (see Section 5.3) with the succession of 2 Mori–Tanaka homogenization steps.

For both mixes, results obtained with the two hypotheses are close to each other, in accordance with the conclusions from Yang [90]. The difference between the model prediction and the experimental data is less than 3% for both mixes and this validates the multi-scale model.

4.4. Prediction of Young's modulus on the paste scale for different slag and activator compositions

After being validated in Section 4.3, the multi-scale model scheme has been used to predict paste Young's modulus for various slag and activator compositions. The calculations for different slag compositions were carried out by varying mass fractions of key oxides viz., CaO, SiO_2, Al_2O_3 and MgO. Minor oxides viz., Fe_2O_3, Na_2O, K_2O and SO_3 were kept constant and amounts were set equal to those of the slag used for the experiments in this study. As in the study from Myers et al. [102], the slag SiO_2 content is set to either 30% or 40% for visualization purposes. Two alkali solutions were studied. The first solution composition is that used for the mix lS ($n = 5$ [g Na_2O/100 g slag], $M_S = 0.5$ [mol/mol]). This alkali solution is very similar to the solution used for round-robin tests from RILEM [103] and provides promising properties for structural applications [38]. The second alkali solution has a higher M_S value ($n = 5$ [g Na_2O/100 g slag], $M_S = 1.0$ [mol/mol]). This solution is similar to that often used in the literature [67,68,104]. For both slag mixes w/s was set to 0.4 [kg/kg]. The amount of reacted slag was fixed to 60 % following Myers et al. [102]. It should be noted that for some combinations of mixes, 60% reactivity of slag may not be reached due to kinetics constraints. This is due to the fact that the dissolution of the same slag in different alkali solutions is observed to occur at different rates [34]. Similarly, two slags with different compositions mixed with the same alkali solution do not lead to a similar dissolution rate [68]. The thermodynamic calculations are done at 20 °C. The results are presented in ternary diagrams in Fig. 8, where the three oxides CaO, Al_2O_3 and MgO proportions are normalized such that CaO + Al_2O_3 + MgO = 100 %. The results show that Young's modulus is higher when the SiO_2 content of the slag is lower. For the same slag composition and the same degree of reaction, increasing M_S tends to increase Young's modulus. The computed phase assemblages indicate that this is mainly due to the increased generation of C–A–S–H and to the reduced chemical shrinkage in the case of M_S = 1.

The influence of the alkali solution is studied by varying w/s, n and M_S. The ratio between the mass of the activator solution and the mass of slag, a/s is kept constant, where a the activator solution mass is made of H_2O, Na_2O and SiO_2. Two cases with a/s equal to 0.47 and 0.57 are studied. In the ternary diagrams presented in Fig. 9, the results are given in function of the proportions of H_2O, Na_2O and SiO_2 in the activator solution, for a fixed a/s ratio. These calculations cover ranges of w/s (0.34–0.53 kg/kg), n (1.88–13.68 g/100 g slag) and M_S (0.1–5.6 mol/mol). In the ternary diagrams (see Fig. 9), the silicate content is expressed in % $SiO_2 = \frac{M_{SiO_2}}{M_{Na_2O}} \cdot M_S \cdot n$. The slag that is used to generate the mixes is the one studied experimentally (see Table 1). Here again, the calculations are done for a dissolution extent of 60% and at a temperature of 20 °C. The results indicate that for both considered a/s, the maximum Young's modulus is obtained for one of the highest SiO_2 content in the alkali solution. It corresponds to the mixes with the lowest porosities and highest amount of C–A–S–H products.

The comparison between the impacts of the slag and activator compositions shows that the activator composition seems to have a more dominant influence on Young's modulus than the slag composition. When the activator compositions are varied for the same slag, Young's modulus varies from 12.4 to 22.9 GPa (Fig. 9), whereas it varies from 15.6 to 19.8 GPa and from 16.1 to 20.5 GPa when the slag composition is varied with M_S equal to 0.5 mol/mol and 1.0 mol/mol, respectively (see Fig. 8). This can be directly linked to the microstructure predicted by thermodynamic modeling. From the calculations discussed above, Young's modulus can be plotted as a function of the water volume fraction f_w (where the gel and capillary water are taken together). Fig. 10 shows that Young's modulus decreases almost linearly with increasing of total porosity.

5. Discussions

In this section, different hypotheses made in the multi-scale modeling approach described in Section 3 are revisited and critically evaluated. This includes the sensitivity analyses of input parameters used for obtaining Young's modulus of paste and concrete, the influence of the

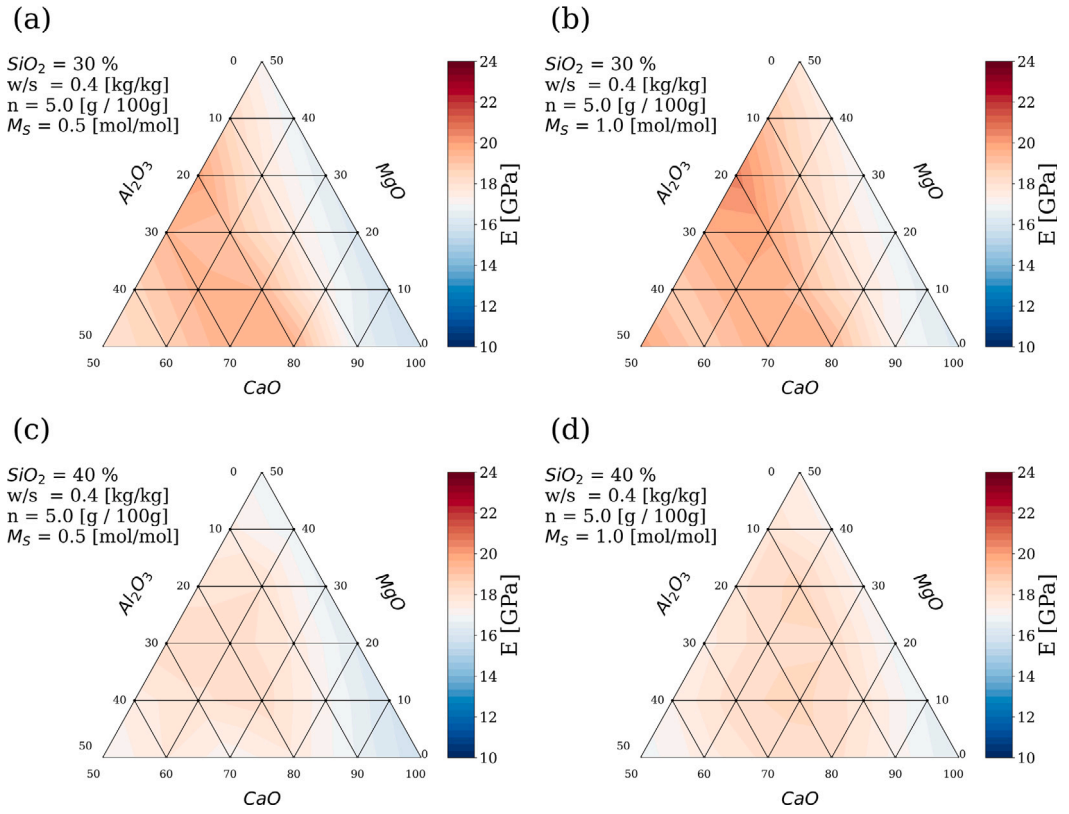

Fig. 8. Prediction of Young's modulus for different slag compositions, with a degree of reaction of 60%. w/s = 0.4 [kg/kg] and n = 5.0 [g Na_2O/100 g slag] for all the calculations. (a) M_S = 0.5 [mol/mol] and SiO_2 = 30%. (b) M_S = 1.0 [mol/mol] and SiO_2 = 30%. (c) M_S = 0.5 [mol/mol] and SiO_2 = 40%. (d) M_S = 1.0 [mol/mol] and SiO_2 = 40%. The same color scale is used for the four figures. (For interpretation of the references to color in this figure legend, the reader is referred to the web version of this article.)

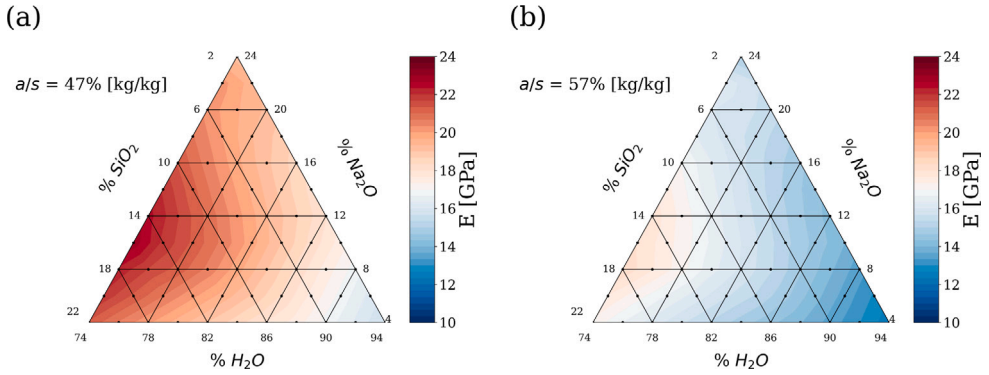

Fig. 9. Prediction of Young's modulus for different activator compositions with a degree of reaction of 60%. The composition of the slag is the one used in this contribution. Two activator/slag ratios a/s are studied: (a) 0.47 [kg/kg] and (b) 0.57 [kg/kg].

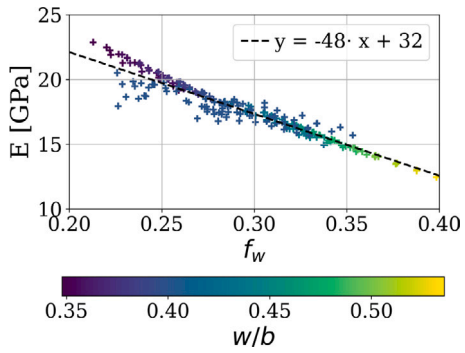

Fig. 10. Correlations between the volume fraction of water f_w and paste Young's modulus for different slag and activator compositions.

presence of air voids due to the chemical shrinkage and the presence of cracks due to autogenous shrinkage. For concrete, the relevance of considering the ITZ while predicting Young's modulus is also discussed.

5.1. Sensitivity analysis on both paste and concrete

The results of nano-indentation given in Table 6 were used to compute Young's modulus of paste. To account for the variations and errors of nano-indentation results (see Section 4.2) and evaluate the hypotheses on the fraction of gel porosity, a sensitivity analysis is done on five parameters, viz., E_{slag}, E_{soft}, E_{hard}, $f_{0,soft}$ and ϕ_g. The corresponding ranges are summarized in Table 7. The uncertainty in the prediction of the model resulting from the sensitivity analysis is shown in Fig. 6. The confidence range at 95% is plotted and corresponds to a value of ± 3 GPa after 28 days. The statistical analysis carried out

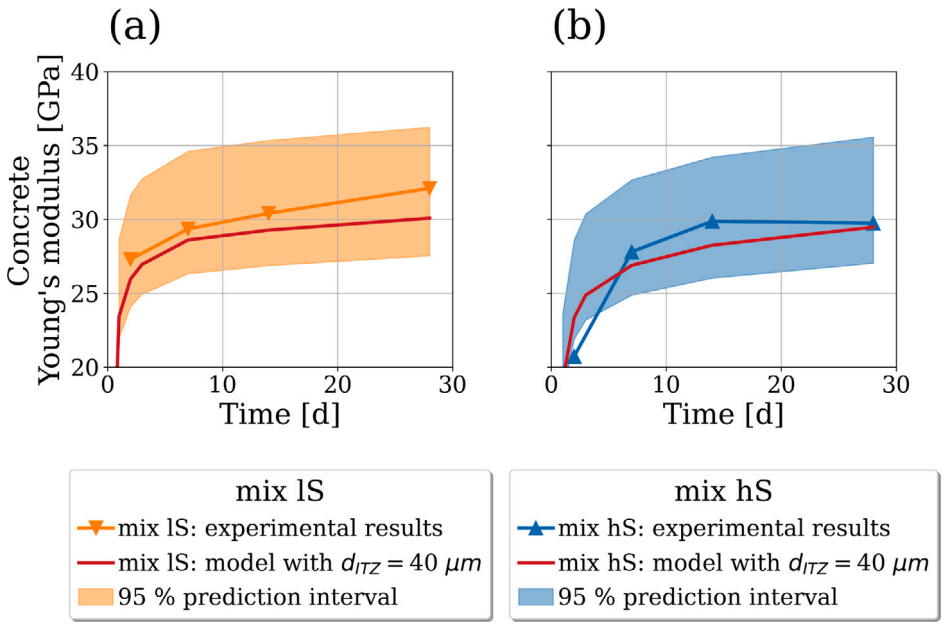

Fig. 11. Validation of the homogenization scheme on the concrete scale (Level 4) for both mix lS (a) and mix hS (b). The red curves correspond to calculations made in Section 4.3 for the investigated ITZ thicknesses. The bands correspond to the confidence interval at 95% for the sensitivity analysis done in Section 5.1.

Table 7
Ranges of parameters for both sensitivity analysis carried out on paste and on concrete.

Paste scale			
Parameter	Unit	Minimum	Maximum
E_{slag}	GPa	60	80
E_{soft}	GPa	17	23
E_{hard}	GPa	28	38
$f_{0,soft}$	%	60	80
ϕ_g	%	25	35
Concrete scale			
Parameter	Unit	Minimum	Maximum
E_p	GPa	$0.93 \times E_p^m$	$1.21 \times E_p^m$
E_g	GPa	40	60
d_{ITZ}	µm	20	40
E_{ITZ}/E_p	%	$1.5 \cdot d_{ITZ}$ - 10	$1.5 \cdot d_{ITZ}$ + 10

E_p^m corresponds to the paste Young's modulus obtained with the analytical model.

Table 8
Total-order sensitivity indexes obtained from the sensitivity analysis carried out on paste and on concrete.

Paste scale		
Parameter	Mix lS	Mix hS
E_{slag}	0.023	0.025
E_{soft}	0.589	0.602
E_{hard}	0.150	0.154
$f_{0,soft}$	0.155	0.160
ϕ_g	0.119	0.093
Concrete scale		
Parameter	Mix lS	Mix hS
E_p	0.197	0.203
E_g	0.799	0.792
d_{ITZ}	0.005	0.006
E_{ITZ}/E_p	0.011	0.011

for both mixes with Sobol's method [93] provided the same total-order sensitivity indexes with variation of ± 0.02 as given in Table 8. The sensitivity analysis indicates that E_{soft} is the predominant parameter that influences Young's modulus of the paste. E_{hard}, $f_{0,soft}$ and ϕ_g have lower influence and E_{slag} has a negligible total-order sensitivity index.

For the sensitivity analysis on the concrete scale, E_p, E_g, d_{ITZ} and E_{ITZ} are varied in ranges given in Table 7 based on the results for paste and on the literature review made in Section 3.4. The variations for E_p correspond to the propagation of the error obtained by the sensitivity analysis for paste between 93% and 121% of Young's modulus computed with the multi-scale model E_p^m. The ITZ thickness is varied between 20 µm and 40 µm. As explained in Section 3.4, the ratio E_{ITZ}/E_p increases from 30% to 60% for ITZ increasing from 20 µm to 40 µm. Thus, E_{ITZ}/E_p [%] and d_{ITZ} [µm] can be correlated by a linear equation ($E_{ITZ}/E_p = \delta \cdot d_{ITZ}$, with $\delta = 1.5\ \mu m^{-1}$). The sensitivity analysis on this ratio is a band of ±10% around this relation.

The results for both mixes provided the same magnitude results in terms of total-order sensitivity indexes with variations of less than 2%. The results are given in Table 8 and Fig. 11. For these calculations, the sensitivity analysis indicates that E_g has the biggest total-order sensitivity index, followed by E_p. Thus, the influence of the paste Young's modulus in the considered range of the sensitivity analysis is relatively low in comparison to Young's modulus of aggregates. The results on E_{ITZ}/E_p and d_{ITZ} indicate that the parameters of the ITZ have very little influence on Young's modulus of concrete. The role of ITZ is discussed in more detail in Section 5.3.

5.2. Influence of air voids and cracks

The proposed scheme in Section 3 neglects the presence of air voids and micro-cracks resulting from autogenous shrinkage as a consequence of chemical shrinkage. Chemical shrinkage is defined as the relative volume reduction of the global volume of unreacted particles, solution and products with time [13]. It takes place due to the smaller volume occupied by the products than by the unreacted particles and solution. The thermodynamic calculations for both mixes are shown in Fig. 12. They indicate that during the first few days, the total volume of the system remains constant or slightly increases for the mix lS and mix hS, respectively. The fact that no chemical shrinkage is predicted at early-age is contradictory with the experimental results that can be found in the literature, but after a few days, the results are comparable to what can be found experimentally [9,76,105–107]. The error in prediction

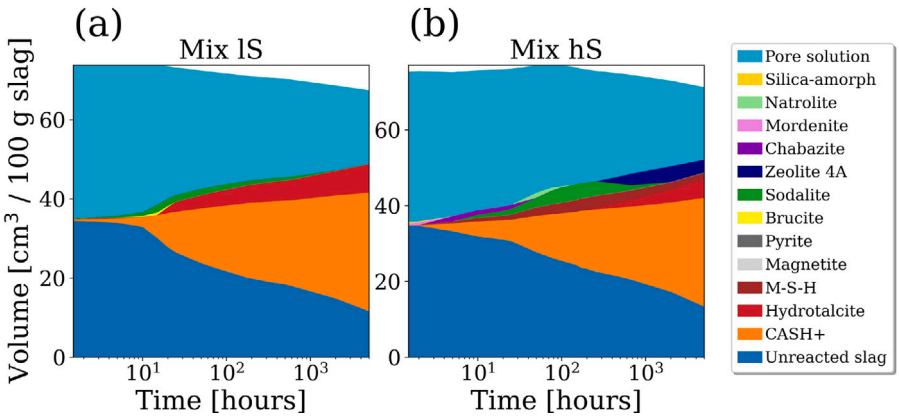

Fig. 12. Phase assemblage for mix lS (a) and mix hS (b) predicted by the thermodynamic model presented in [34]. The chemical shrinkage corresponds to the decrease in volume of the liquid and solid part of the system.

at early-age could be due to artefacts from incorrect molar volumes of zeolites or M–S–H products in the thermodynamic databases. A part of the chemical shrinkage can lead to the formation of air voids. These have not been taken into account in the model. Measurements with a saturation-drying cycle indicated that the volume fraction of air voids is less than 5%. This leads to a reduction of the predicted Young's modulus of the paste by less than 1 GPa.

AAS undergoes high shrinkage [37,38,76] at early-age resulting in lots of microcracks. The amount of microcracks can be characterized with the crack density parameter η [–]. It has been proven in the literature that accounting for the presence of cracks leads to a reduction of the elastic properties [108] (see Appendix A). As illustrated in Fig. 13(a) and (b), if η increases, both bulk modulus and shear modulus decrease significantly. For example, the bulk modulus is divided by two for $\eta = 0.21$. Also, as proven in [109] and shown in Fig. 13, the geometry of the crack does not have a big influence on Young's modulus of the material. In fact, circular and ribbon shapes are two extreme cases of 3-D elliptic cracks and show similar results (see Fig. 13(a) and (b)).

The characterization of microcracks can be conducted with Scanning Electron Microscopy (SEM) [30,108]. SEM images obtained from our previous study [34] were used to determine η. Each SEM image was post-processed following the methodology explained in [108] and recalled in Appendix A. The post-processing of SEM results for different ages indicates that η is equal to 0.005 for the mix lS and 0.02 for the mix hS and that these values are constant with time (see Fig. 13(c)). The results of computed paste Young's modulus taking into account the cracks are shown in Fig. 14. In comparison to the model without cracks, Young's modulus of paste are reduced by 1.0% and 3.5% for the mix lS and mix hS, respectively. It is interesting to note that the mix hS has more cracks and also a stiffer reaction product foam (see Table 6). Given this interplay between micro-cracks and Young's modulus of hard and soft matrix, an additional set of calculations were conducted for both mixes using the nano-indentation results for each mix as reported in Table 6 and considering cracks. From the results shown in Fig. 14, it can be seen that Young's modulus of the mix lS is underestimated by 1 GPa. The computed Young's modulus of the mix hS agrees very well with the experimental data. Thus, taking the same phase Young's modulus for different mix designs and neglecting the presence of cracks provides the same range of results as this more complex analysis, which requires the determination of the crack density parameter.

5.3. Discussion on the consideration of an ITZ

As discussed in Section 3.4, the ITZ is a zone around sand particles with lower mechanical properties. Its Young's modulus is lower than Young's modulus of the paste or the one of the aggregates [90]. To evaluate the influence of this ITZ on Young's modulus of concrete, another scheme has been implemented, for which Level 3 was simply an inclusion–matrix problem with perfectly bounded aggregates. This means that the Mori–Tanaka scheme was used on the mortar level. Sand grains are regarded as inclusions embedded in the paste. The mechanical properties and the volume fractions used for the computation are the same as the ones of the initial proposed multi-scale model (see Table 3). The comparison between the models with ITZ and without ITZ are shown in Fig. 7. At 28 days, Young's modulus obtained from the simplified model is 1 GPa higher than that considering ITZ, indicating that ITZ has a limited influence. Similar conclusions have been drawn by other researchers on the influence of ITZ [110,111].

6. Conclusion

In this study, a multi-scale model for Young's modulus of AAS concrete has been presented and compared with experimental results obtained on paste and concrete at several ages for two AAS concrete mixes. The multi-scale model is based on hierarchical upscaling with analytical micro-mechanics and covers the different scales of heterogeneities of the material. The volume fractions of the phases were obtained with a coupled kinetic-thermodynamic model, which has been validated previously. The stiffnesses of the phases, required as input for multi-scale modeling, were determined with nano-indentation experiments.

For both AAS mixes, the experimental results from nano-indentation can be separated into four clusters, namely pores and defects, unreacted slag and two types of matrices of reaction products, one softer and one harder. Since the main reaction product of AAS is C–A–S–H gel, the distinction between a softer matrix and a harder matrix could indicate that its structure could be similar to LD C–S–H and HD C–S–H for OPC. The results are in the same range for the two studied mixes. The choice of the clustering method involves variations in the moduli of both matrices of less than 10 GPa and in the proportion of soft matrix of less than 6%. Yet, these differences did not have a significant impact on the calculated Young's modulus of paste and concrete. The experimental study on Young's modulus of paste and concrete reveals that the mix with a lower silicate ratio had higher values. For pastes, a unique ratio of static Young's modulus to dynamic Young's modulus after 28 days equal to 0.72 ± 0.01 was obtained for both mixes.

The analytical micro-mechanics-based multi-scale model predicted Young's modulus with an accuracy of 95% at 28 days. The model accounts for the distinction between the softer matrix and the harder matrix as is the case for OPC. The distinction between gel water

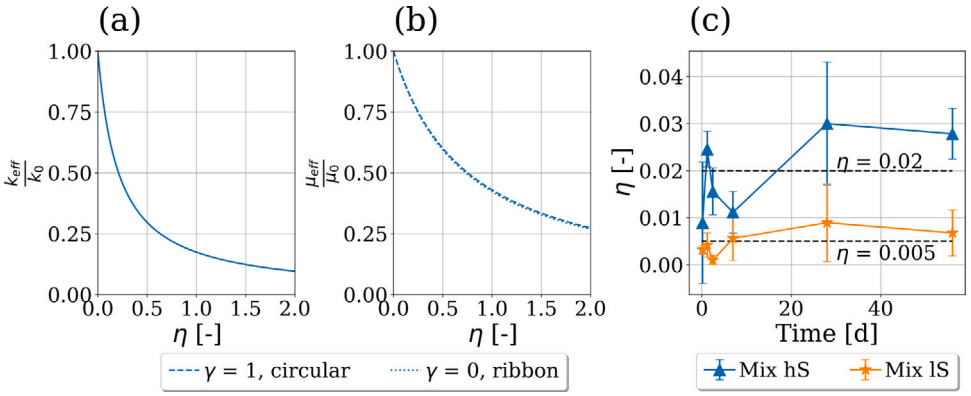

Fig. 13. (a) Evolution of the crack density parameter η with time for both mix lS and mix hS. Reduction of (b) k_{eff} and (c) μ_{eff} of a cracked body. k_{eff} and μ_{eff} stand for the effective bulk and shear modulus of the material, while k_0 and μ_0 are the modulus of the material without cracks.

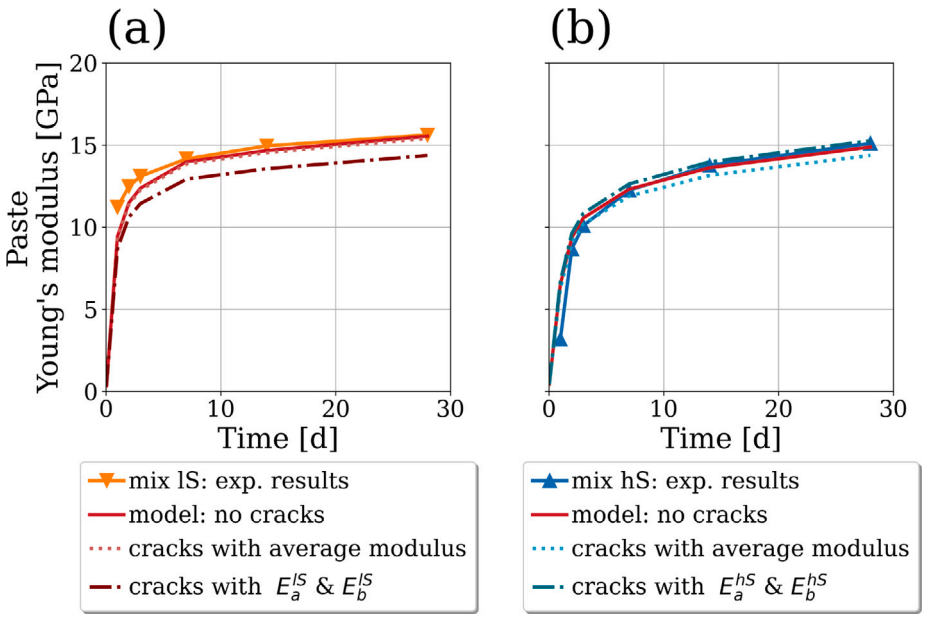

Fig. 14. Homogenization calculations made for paste taking into account the presence of cracks, with average or differentiated Young's modulus for both mix lS (a) and mix hS (b). For the mix lS, E^{lS}_{soft} = 17.1 GPa and E^{lS}_{hard} = 39.2 GPa; for the mix hS, E^{hS}_{soft} = 21.1 GPa and E^{hS}_{hard} = 36.0 GPa. The averages are respectively: E_{soft} = 19.1 GPa and E_{hard} = 37.6 GPa.

and capillary water from total porosity obtained from thermodynamic modeling is essential to correctly predict Young's modulus of concrete. Using the developed model, predictions of Young's modulus for several sodium silicate-activated slags were carried out, for which slag and activator solution compositions were varied. The modeled results indicate that the activator solution has a much higher impact on Young's modulus than the slag composition.

The influences of the model parameters were also tested through sensitivity analyses at paste and concrete scales. For paste, the most influencing factors for Young's modulus are parameters associated with the soft matrix. On the concrete scale, the sensitivity analysis shows that Young's modulus of the aggregates and Young's modulus of paste had the most substantial impact on Young's modulus of concrete. The effect of cracks due to autogenous shrinkage and air voids was investigated. It was found that these defects have a limited influence on Young's modulus predictions. Finally, the influence of ITZ at the concrete scale was found to have a minor impact on the final Young's modulus of concrete.

This study demonstrates that thermodynamic modeling and micromechanics together with nano-indentation can be used for successfully predicting Young's modulus of AAM concretes by using the mix design as input parameters. Young's modulus is practically relevant for predicting other time-dependent behaviors such as creep and internal forces generated by capillary pressure during shrinkage. In the future, we aim at extending the modeling work in these directions.

CRediT authorship contribution statement

Richard Caron: Conceptualization, Methodology, Software, Validation, Investigation, Writing – original draft. **Ravi A. Patel:** Conceptualization, Methodology, Validation, Investigation, Writing – review & editing. **Andreas Bogner:** Conceptualization, Methodology, Validation, Investigation, Writing – review & editing. **Frank Dehn:** Resources, Writing – review & editing, Supervision, Funding acquisition.

Declaration of competing interest

The authors declare that they have no known competing financial interests or personal relationships that could have appeared to influence the work reported in this paper.

Data availability

Data will be made available on request.

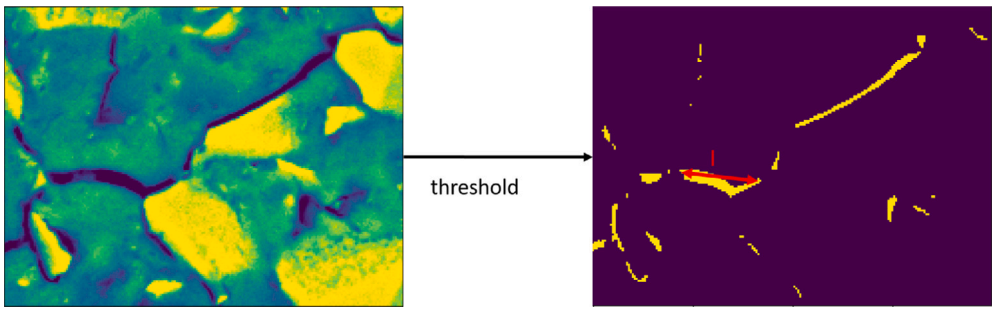

Fig. A.15. Determination of the crack density parameter η on thresholded figures on which the length, areas and numbers of cracks are obtained.

Acknowledgments

Funding

This work was supported by the European Union's Horizon 2020 research and innovation program under the Marie Skłodowska-Curie grant agreement No. 813596.

Appendix A. Determination of the crack density parameter and influence on the bulk modulus and on the shear modulus

To determine the crack density parameter η, SEM images are used. After a threshold on the pixel value, regions corresponding to pores and cracks are characterized. If the length of the region was more than 3 times larger than its width, the region is regarded as a crack (See Fig. A.15.).

η can be determined following the methodology of [108]:

$$\eta = \frac{2N}{\pi}\left\langle \frac{A^2}{P} \right\rangle \tag{A.1}$$

N is the total number of cracks per unit volume, A is the area of the crack, and P is the perimeter of the crack and $\langle\cdot\rangle$ designates the volume average of a quantity.

Then,

$$\eta = \frac{8}{\pi^3} \cdot M \cdot \langle l \rangle^2 \tag{A.2}$$

where $\langle l \rangle$ is the average length of the cracks and M is the total crack number per unit in an SEM image. The length l of the crack is considered as the length of the major axis of the equivalent ellipse circumscribed to the crack.

From a mechanical point of view, these cracks can be regarded as ellipsoidal inclusions that reduce the mechanical properties of the material [108,109]. The effective bulk modulus k_{eff} and the effective shear modulus μ_{eff} in presence of ribbon-shaped cracks are given by [109]:

$$\begin{cases} k_{eff} = \dfrac{k_0}{1-\frac{16}{9}\frac{(1-\nu_0^2)}{1-2\nu_0}\eta} \\ \mu_{eff} = \dfrac{\mu_0}{1+\frac{8}{45}(10-7\nu_0)\eta} \end{cases} \tag{A.3}$$

with k_0 and ν_0 the bulk modulus and the Poisson's coefficient of the material without crack.

Appendix B. Supplementary data

Supplementary material related to this article can be found online at https://doi.org/10.1016/j.conbuildmat.2023.131272.

References

[1] B. Lothenbach, K. Scrivener, R.D. Hooton, Supplementary cementitious materials, Cem. Concr. Res. 41 (12) (2011) 1244–1256, http://dx.doi.org/10.1016/j.cemconres.2010.12.001.
[2] J.L. Provis, Geopolymers and other alkali activated materials: Why, how, and what? Mater. Struct. 47 (1–2) (2014) 11–25, http://dx.doi.org/10.1617/s11527-013-0211-5.
[3] A. Fernández-Jiménez, F. Puertas, Structure of calcium silicate hydrates formed in alkaline-activated slag: Influence of the type of alkaline activator, J. Am. Ceram. Soc. 86 (8) (2003) 1389–1394.
[4] M.B. Haha, B. Lothenbach, G. Le Saout, F. Winnefeld, Influence of slag chemistry on the hydration of alkali-activated blast-furnace slag — Part I: Effect of MgO, Cem. Concr. Res. 41 (9) (2011) 955–963, http://dx.doi.org/10.1016/j.cemconres.2011.05.002.
[5] S.A. Bernal, J.L. Provis, V. Rose, R. Mejía de Gutierrez, Evolution of binder structure in sodium silicate-activated slag-metakaolin blends, Cem. Concr. Compos. 33 (1) (2011) 46–54, http://dx.doi.org/10.1016/j.cemconcomp.2010.09.004.
[6] H.F.W. Taylor, Proposed structure for calcium silicate hydrate gel, J. Am. Ceram. Soc. 69 (6) (1986) 464–467, http://dx.doi.org/10.1111/j.1151-2916.1986.tb07446.x.
[7] I.G. Richardson, The nature of C–S–H in hardened cements, Cem. Concr. Res. 29 (8) (1999) 1131–1147, http://dx.doi.org/10.1016/S0008-8846(99)00168-4.
[8] A. Gmira, R.J.-M. Pellenq, I. Rannou, L. Duclaux, C. Clinard, T. Cacciaguerra, N. Lequeux, H. van Damme, A structural study of dehydration/rehydration of tobermorite, a model cement compound, in: Characterization of Porous Solids VI, Proceedings of the 6th International Symposium on the Characterization of Porous Solids (COPS-VI), in: Studies in Surface Science and Catalysis, vol. 144, Elsevier, 2002, pp. 601–608, http://dx.doi.org/10.1016/S0167-2991(02)80186-0.
[9] J.J. Thomas, A.J. Allen, H.M. Jennings, Density and water content of nanoscale solid C–S–H formed in alkali-activated slag (AAS) paste and implications for chemical shrinkage, Cem. Concr. Res. 42 (2) (2012) 377–383, http://dx.doi.org/10.1016/j.cemconres.2011.11.003.
[10] R.J. Myers, S.A. Bernal, J.L. Provis, A thermodynamic model for C–(N–)A–S–H gel: CNASH_ss. Derivation and validation, Cem. Concr. Res. 66 (2014) 27–47, http://dx.doi.org/10.1016/j.cemconres.2014.07.005.
[11] R.J. Myers, S.A. Bernal, J.D. Gehman, J.S.J. van Deventer, J.L. Provis, The role of Al in cross-linking of alkali-activated slag cements, J. Am. Ceram. Soc. 98 (3) (2015) 996–1004, http://dx.doi.org/10.1111/jace.13360.
[12] P. Krivenko, Why alkaline activation — 60 years of the theory and practice of alkali-activated materials, J. Ceram. Sci. Technol. 8 (2017) 323–334, http://dx.doi.org/10.4416/JCST2017-00042.
[13] P.K. Mehta, P.J.M. Monteiro, Concrete: Microstructure, Properties, and Materials, third ed., McGraw-Hill, New York, 2006.
[14] O. Bernard, F.-J. Ulm, E. Lemarchand, A multiscale micromechanics-hydration model for the early-age elastic properties of cement-based materials, Cem. Concr. Res. 33 (9) (2003) 1293–1309, http://dx.doi.org/10.1016/S0008-8846(03)00039-5.
[15] B. Pichler, C. Hellmich, Upscaling quasi-brittle strength of cement paste and mortar: A multi-scale engineering mechanics model, Cem. Concr. Res. 41 (5) (2011) 467–476, http://dx.doi.org/10.1016/j.cemconres.2011.01.010.
[16] S. Krishnya, Y. Yoda, E. Yogarajah, A two-stage model for the prediction of mechanical properties of cement paste, Cem. Concr. Compos. 115 (2021) 103853, http://dx.doi.org/10.1016/j.cemconcomp.2020.103853.
[17] E.J. Garboczi, J.G. Berryman, Elastic moduli of a material containing composite inclusions: Effective medium theory and finite element computations, Mech. Mater. 33 (2001) 455–470.
[18] Z. Luo, W. Li, K. Wang, A. Castel, S.P. Shah, Comparison on the properties of ITZs in fly ash-based geopolymer and portland cement concretes with equivalent flowability, Cem. Concr. Res. 143 (2021) 106392, http://dx.doi.org/10.1016/j.cemconres.2021.106392.

[19] V. Šmilauer, P. Hlaváček, F. Škvára, R. Šulc, L. Kopecký, J. Němeček, Micromechanical multiscale model for alkali activation of fly ash and metakaolin, J. Mater. Sci. 46 (20) (2011) 6545–6555, http://dx.doi.org/10.1007/s10853-011-5601-x.

[20] G. Fang, M. Zhang, Multiscale micromechanical analysis of alkali-activated fly ash-slag paste, Cem. Concr. Res. 135 (2020) 106141, http://dx.doi.org/10.1016/j.cemconres.2020.106141.

[21] G. Constantinides, F.-J. Ulm, The effect of two types of C–S–H on the elasticity of cement-based materials: Results from nanoindentation and micromechanical modeling, Cem. Concr. Res. 34 (1) (2004) 67–80, http://dx.doi.org/10.1016/S0008-8846(03)00230-8.

[22] M. Vandamme, F.-J. Ulm, Nanoindentation investigation of creep properties of calcium silicate hydrates, Cem. Concr. Res. 52 (2013) 38–52, http://dx.doi.org/10.1016/j.cemconres.2013.05.006.

[23] W. Wilson, L. Sorelli, A. Tagnit-Hamou, Automated coupling of NanoIndentation and quantitative energy-dispersive spectroscopy (NI-QEDS): A comprehensive method to disclose the micro-chemo-mechanical properties of cement pastes, Cem. Concr. Res. 103 (2018) 49–65, http://dx.doi.org/10.1016/j.cemconres.2017.08.016.

[24] M. Haist, T. Divoux, K.J. Krakowiak, J. Skibsted, R.J.-M. Pellenq, H.S. Müller, F.-J. Ulm, Creep in reactive colloidal gels: A nanomechanical study of cement hydrates, Phys. Rev. Res. 3 (4) (2021) 68, http://dx.doi.org/10.1103/PhysRevResearch.3.043127.

[25] J. Němeček, V. Šmilauer, L. Kopecký, Nanoindentation characteristics of alkali-activated aluminosilicate materials, Cem. Concr. Compos. 33 (2) (2011) 163–170, http://dx.doi.org/10.1016/j.cemconcomp.2010.10.005.

[26] H. Lee, V. Vimonsatit, P. Chindaprasirt, Mechanical and micromechanical properties of alkali activated fly-ash cement based on nano-indentation, Constr. Build. Mater. 107 (7) (2016) 95–102, http://dx.doi.org/10.1016/j.conbuildmat.2015.12.013.

[27] H. Lee, V. Vimonsatit, P. Chindaprasirt, T. Ngo, P. Mendis, Creep properties of cement and alkali activated fly ash materials using nanoindentation technique, Constr. Build. Mater. 168 (26) (2018) 547–555, http://dx.doi.org/10.1016/j.conbuildmat.2018.02.166.

[28] S. Chen, C. Wu, D. Yan, Binder-scale creep behavior of metakaolin-based geopolymer, Cem. Concr. Res. 124 (2019) 105810, http://dx.doi.org/10.1016/j.cemconres.2019.105810.

[29] M. Königsberger, L. Zelaya-Lainez, O. Lahayne, B.L.A. Pichler, C. Hellmich, Nanoindentation-probed oliver-pharr half-spaces in alkali-activated slag-fly ash pastes: Multimethod identification of microelasticity and hardness, Mech. Adv. Mater. Struct. 3 (2021) 1–12, http://dx.doi.org/10.1080/15376494.2021.1941450.

[30] B.S. Gebregziabiher, S. Peethamparan, Characterization of alkali activated slag gel using nano-indentation, 2013.

[31] W.-J. Long, B.-X. Xiao, Y.-C. Gu, F. Xing, Micro- and macro-scale characterization of nano-SiO_2 reinforced alkali activated slag composites, Mater. Charact. 136 (2018) 111–121, http://dx.doi.org/10.1016/j.matchar.2017.12.013.

[32] R.J. Thomas, B.S. Gebregziabiher, A. Giffin, S. Peethamparan, Micromechanical properties of alkali-activated slag cement binders, Cem. Concr. Compos. 90 (1) (2018) 241–256, http://dx.doi.org/10.1016/j.cemconcomp.2018.04.003.

[33] Z. Jia, C. Chen, H. Zhou, Y. Zhang, The characteristics and formation mechanism of the dark rim in alkali-activated slag, Cem. Concr. Compos. 112 (2020) 103682, http://dx.doi.org/10.1016/j.cemconcomp.2020.103682.

[34] R. Caron, R.A. Patel, G.D. Miron, C. Le Galliard, B. Lothenbach, F. Dehn, Microstructure development of slag activated with sodium silicate solution: experimental characterization and thermodynamic modeling, Journal of Building Engineering (2023) 106398, http://dx.doi.org/10.1016/j.jobe.2023.106398, https://www.sciencedirect.com/science/article/pii/S2352710223005776.

[35] R. Caron, R.A. Patel, F. Dehn, Activation kinetic model and mechanisms for alkali-activated slag cements, Constr. Build. Mater. 323 (2022) 126577, http://dx.doi.org/10.1016/j.conbuildmat.2022.126577.

[36] H. Taghvayi, K. Behfarnia, M. Khalili, The effect of alkali concentration and sodium silicate modulus on the properties of alkali-activated slag concrete, J. Adv. Concr. Technol. 16 (7) (2018) 293–305, http://dx.doi.org/10.3151/jact.16.293.

[37] C. Duran Atiş, C. Bilim, Ö. Çelik, O. Karahan, Influence of activator on the strength and drying shrinkage of alkali-activated slag mortar, Constr. Build. Mater. 23 (1) (2009) 548–555, http://dx.doi.org/10.1016/j.conbuildmat.2007.10.011.

[38] R. Caron, R.A. Patel, F. Dehn, Extension of the fib MC 2010 for basic and drying shrinkage of alkali-activated slag concretes, Struct. Concr. n/a (n/a) http://dx.doi.org/10.1002/suco.202100901.

[39] DIN EN 196-1, Prüfverfahren für Zement - Teil 1: Bestimmung der Festigkeit; Deutsche Fassung EN 196-1:2016, Beuth Verlag, 2016.

[40] D.F. Orchard, J.A. Walker, D.T. Stewart, A study of the relationship between the static and dynamic modulus of elasticity and other properties of certain materials, in: A. R. R. B. Proceedings, vol. 3, (Part 2) 1966, pp. 1068–1091.

[41] S. Kolias, R.I.T. Williams, Relationships between the static and the dynamic moduli of elasticity in cement stabilised materials, Mater. Struct. 13 (2) (1980) 99–107, http://dx.doi.org/10.1007/BF02473806.

[42] K. Jurowski, S. Grzeszczyk, Influence of selected factors on the relationship between the dynamic elastic modulus and compressive strength of concrete, Materials 11 (4) (2018) http://dx.doi.org/10.3390/ma11040477.

[43] DIN EN 12390-13, Prüfung von Festbeton – Teil 13: Bestimmung des Elastizitätsmoduls unter Druckbelastung (Sekantenmodul); Deutsche und Englische Fassung prEN 12390-13:2019, Beuth Verlag, 2019.

[44] M. Miller, C. Bobko, M. Vandamme, F.-J. Ulm, Surface roughness criteria for cement paste nanoindentation, Cem. Concr. Res. 38 (4) (2008) 467–476, http://dx.doi.org/10.1016/j.cemconres.2007.11.014.

[45] W.C. Oliver, G.M. Pharr, An improved technique for determining hardness and elastic modulus using load and displacement sensing indentation experiments, J. Mater. Res. 7 (6) (1992) 1564–1583, http://dx.doi.org/10.1557/JMR.1992.1564.

[46] Q. Kan, W. Yan, G. Kang, Q. Sun, Oliver–pharr indentation method in determining elastic moduli of shape memory alloys—A phase transformable material, J. Mech. Phys. Solids 61 (10) (2013) 2015–2033, http://dx.doi.org/10.1016/j.jmps.2013.05.007.

[47] C. Hu, Nanoindentation as a tool to measure and map mechanical properties of hardened cement pastes, MRS Commun. 5 (1) (2015) 83–87, http://dx.doi.org/10.1557/mrc.2015.3.

[48] P. Stemmermann, K. Garbev, B. Gasharova, G. Beuchle, M. Haist, T. Divoux, Chemo-mechanical characterization of hydrated calcium-hydrosilicates with coupled Raman- and nanoindentation measurements, Appl. Geochem. 118 (3) (2020) 104582, http://dx.doi.org/10.1016/j.apgeochem.2020.104582.

[49] E.P. Koumoulos, K. Paraskevoudis, C.A. Charitidis, Constituents phase reconstruction through applied machine learning in nanoindentation mapping data of mortar surface, J. Compos. Sci. 3 (3) (2019) 63, http://dx.doi.org/10.3390/jcs3030063.

[50] B.C. Sousa, C. Viera, R. Neamtu, D.L. Cote, Clustering algorithms for nanomechanical property mapping and resultant microstructural constituent and phase quantification, in: TMS 2022 151st Annual Meeting & Exhibition Supplemental Proceedings, in: The Minerals, Metals & Materials Series, vol. 7, Springer International Publishing, Cham, 2022, pp. 713–724, http://dx.doi.org/10.1007/978-3-030-92381-5_68.

[51] X. Chen, D. Hou, Y. Han, X. Ding, P. Hua, Clustering analysis of grid nanoindentation data for cementitious materials, J. Mater. Sci. 56 (21) (2021) 12238–12255, http://dx.doi.org/10.1007/s10853-021-05848-8.

[52] D.A. Kulik, T. Wagner, S.V. Dmytrieva, G. Kosakowski, F.F. Hingerl, K.V. Chudnenko, U.R. Berner, GEM-selektor geochemical modeling package: Revised algorithm and GEMS3K numerical kernel for coupled simulation codes, Comput. Geosci. 26 (012025) (2012) 189, http://dx.doi.org/10.1007/s10596-012-9310-6.

[53] H.C. Helgeson, D.H. Kirkham, G.C. Flowers, Theoretical prediction of the thermodynamics behavior of aqueous electrolytes at high pressures and temperatures: IV. Calculation of activity coefficients, osmotic coefficients, and apparent molal and standard and relative partial molal properties to 600°C and 5 KB, Am. J. Sci. 281 (1981) 1249–1516.

[54] W. Hummel, U. Berner, E. Curti, F.J. Pearson, T. Thoenen, Nagra/PSI chemical thermodynamic data base, Radiochim. Acta 90 (2002) 805–813.

[55] D. Kulik, G. Miron, B. Lothenbach, A structurally-consistent CASH+ sublattice solid solution model for fully hydrated C–S–H phases: Thermodynamic basis, methods, and Ca–Si–H_2O core sub-model, Cement and Concrete Research 151 (2021) http://dx.doi.org/10.1016/j.cemconres.2021.106585.

[56] G.D. Miron, D.A. Kulik, Y. Yan, J. Tits, B. Lothenbach, Extensions of CASH+ thermodynamic solid solution model for the uptake of alkali metals and alkaline earth metals in C–S–H, Cement and Concrete Research 152 (2022) 106667, http://dx.doi.org/10.1016/j.cemconres.2021.106667, https://www.sciencedirect.com/science/article/pii/S0008884621003161.

[57] B. Lothenbach, D.A. Kulik, T. Matschei, M. Balonis, L. Baquerizo, B. Dilnesa, G.D. Miron, R.J. Myers, Cemdata18: A chemical thermodynamic database for hydrated portland cements and alkali-activated materials, Cem. Concr. Res. 115 (Suppl. 2) (2019) 472–506, http://dx.doi.org/10.1016/j.cemconres.2018.04.018.

[58] B. Ma, B. Lothenbach, Synthesis, characterization, and thermodynamic study of selected Na-based zeolites, Cem. Concr. Res. 135 (2020) 106111, http://dx.doi.org/10.1016/j.cemconres.2020.106111.

[59] B. Ma, B. Lothenbach, Thermodynamic study of cement/rock interactions using experimentally generated solubility data of zeolites, Cem. Concr. Res. 135 (2020) 106149, http://dx.doi.org/10.1016/j.cemconres.2020.106149.

[60] J.D. Eshelby, The determination of the elastic field of an ellipsoidal inclusion, and related problems, Proc. R. Soc. A 241 (1957) 376–396.

[61] B. Budiansky, On the elastic moduli of some heterogeneous materials, J. Mech. Phys. Solids 13 (4) (1965) 223–227, http://dx.doi.org/10.1016/0022-5096(65)90011-6.

[62] R. Hill, A self-consistent mechanics of composite materials, J. Mech. Phys. Solids 13 (4) (1965) 213–222, http://dx.doi.org/10.1016/0022-5096(65)90010-4.

[63] J.G. Berryman, Long-wavelength propagation in composite elastic media II. Ellipsoidal inclusions, J. Acoust. Soc. Am. 68 (1980) 1820–1831.

[64] Z. Hashin, Assessment of the self consistent scheme approximation: Conductivity of particulate composites, J. Compos. Mater. 2 (1968) 284–300.

[65] T.A. Mori, K. Tanaka, Average stress in matrix and average elastic energy of materials with misfitting inclusions, Acta Metall. 21 (1973) 571–574.

[66] K. Gong, C.E. White, Impact of chemical variability of ground granulated blast-furnace slag on the phase formation in alkali-activated slag pastes, Cem. Concr. Res. 89 (1) (2016) 310–319, http://dx.doi.org/10.1016/j.cemconres.2016.09.003.

[67] M. Criado, B. Walkley, X. Ke, J. Provis, S. Bernal, Slag and activator chemistry control the reaction kinetics of sodium metasilicate-activated slag cements, Sustainability 10 (12) (2018) 4709, http://dx.doi.org/10.3390/su10124709.

[68] S.A. Bernal, R. San Nicolas, R.J. Myers, R. Mejía de Gutierrez, F. Puertas, J.S.J. van Deventer, J.L. Provis, MgO content of the slag controls phase evolution and structural changes induced by accelerated carbonation in alkali-activated binders, Cem. Concr. Res. 57 (2014) 33–43.

[69] M.B. Haha, B. Lothenbach, G. Le Saout, F. Winnefeld, Influence of slag chemistry on the hydration of alkali-activated blast-furnace slag — Part II: Effect of Al_2O_3, Cem. Concr. Res. 42 (1) (2012) 74–83, http://dx.doi.org/10.1016/j.cemconres.2011.08.005.

[70] D. Davydov, M. Jirásek, L. Kopecký, Critical aspects of nano-indentation technique in application to hardened cement paste, Cem. Concr. Res. 41 (1) (2011) 20–29, http://dx.doi.org/10.1016/j.cemconres.2010.09.001.

[71] C. Pichler, R. Lackner, A multiscale creep model as basis for simulation of early-age concrete behavior, Comput. Concr. 5 (2008) http://dx.doi.org/10.12989/cac.2008.5.4.295.

[72] J. Němeček, V. Králík, J. Vondřejc, Micromechanical analysis of heterogeneous structural materials, Cem. Concr. Compos. 36 (9) (2013) 85–92, http://dx.doi.org/10.1016/j.cemconcomp.2012.06.015.

[73] H. Jennings, Refinements to colloid model of C–S–H in cement: CM-II, Cem. Concr. Res. 38 (2008) 275–289, http://dx.doi.org/10.1016/j.cemconres.2007.10.006.

[74] H.M. Jennings, J.J. Thomas, J.S. Gevrenov, G. Constantinides, F.-J. Ulm, A multi-technique investigation of the nanoporosity of cement paste, Cem. Concr. Res. 37 (3) (2007) 329–336, http://dx.doi.org/10.1016/j.cemconres.2006.03.021.

[75] H.J.H. Brouwers, The work of powers and brownyard revisited: Part 1, Cem. Concr. Res. 34 (9) (2004) 1697–1716, http://dx.doi.org/10.1016/j.cemconres.2004.05.031.

[76] Z. Li, T. Lu, X. Liang, H. Dong, G. Ye, Mechanisms of autogenous shrinkage of alkali-activated slag and fly ash pastes, Cem. Concr. Res. 135 (2020) 106107, http://dx.doi.org/10.1016/j.cemconres.2020.106107.

[77] Z. Zhang, Y. Zhu, H. Zhu, Y. Zhang, J.L. Provis, H. Wang, Effect of drying procedures on pore structure and phase evolution of alkali-activated cements, Cem. Concr. Compos. 96 (1) (2019) 194–203, http://dx.doi.org/10.1016/j.cemconcomp.2018.12.003.

[78] A.U. Nilsen, P.J.M. Monteiro, Concrete: A three phase material, Cem. Concr. Res. 23 (1993) 147–151.

[79] G. Li, Y. Zhao, S.S. Pang, Four-phase sphere modeling of effective bulk modulus of concrete, Cem. Concr. Res. 29 (1999) 839–845.

[80] K. Scrivener, K. Nemati, The percolation of pore space in the cement paste/aggregate interfacial zone of concrete, Cem. Concr. Res. 26 (1996) 35–40, http://dx.doi.org/10.1016/0008-8846(95)00185-9.

[81] E.J. Garboczi, D.P. Bentz, Analytical formulas for interfacial transition zone properties, Adv. Cem. Based Mater. 6 (1997) 99–108.

[82] R.M. Christensen, A critical evaluation for a class of micro-mechanics models, J. Mech. Phys. Solids 38 (1990) 379–404.

[83] É. Herve, A. Zaoui, n-layered inclusion-based micromechanical modelling, Internat. J. Engrg. Sci. 31 (1993) 1–10.

[84] S. Torquato, Random heterogeneous materials: Microstructure and macroscopic properties, Appl. Mech. Rev. 55 (4) (2002) B62–B63, http://dx.doi.org/10.1115/1.1483342.

[85] Z. Sun, E.J. Garboczi, S.P. Shah, Modeling the elastic properties of concrete composites: Experiment, differential effective medium theory, and numerical simulation, Cem. Concr. Compos. 29 (1) (2007) 22–38, http://dx.doi.org/10.1016/j.cemconcomp.2006.07.020.

[86] K.A. Snyder, D.N. Winslow, D.P. Bentz, E.J. Garboczi, Effects of interfacial zone percolation on cement-based composite transport properties, MRS Proc. 245 (1991).

[87] K. Scrivener, A.K. Crumbie, P. Laugesen, The interfacial transition zone (ITZ) between cement paste and aggregate in concrete, Interface Sci. 12 (2004) 411–421.

[88] T. Honorio, B. Bary, F. Benboudjema, Multiscale estimation of ageing viscoelastic properties of cement-based materials: A combined analytical and numerical approach to estimate the behaviour at early age, Cem. Concr. Res. 85 (2016) 137–155, http://dx.doi.org/10.1016/j.cemconres.2016.03.010.

[89] M.P. Lutz, P.J.M. Monteiro, R.W. Zimmerman, Inhomogeneous interfacial transition zone model for the bulk modulus of mortar, Cem. Concr. Res. 27 (1997) 1113–1122.

[90] C.C. Yang, Effect of the transition zone on the elastic moduli of mortar, Cem. Concr. Res. 28 (1998) 727–736.

[91] S. Krishnya, Y. Elakneswaran, Y. Yoda, Proposing a three-phase model for predicting the mechanical properties of mortar and concrete, Mater. Today Commun. 29 (2021) 102858, http://dx.doi.org/10.1016/j.mtcomm.2021.102858.

[92] A. Saltelli, Sensitivity analysis for importance assessment, Risk Anal. 22 (2002) 579–590, http://dx.doi.org/10.1111/0272-4332.00040.

[93] I.M. Sobol, Global sensitivity indices for nonlinear mathematical models and their Monte Carlo estimates, Math. Comput. Simulation 55 (2001) 271–280, http://dx.doi.org/10.1016/S0378-4754(00)00270-6.

[94] S.Y. Abate, S. Park, H.-K. Kim, Parametric modeling of autogenous shrinkage of sodium silicate-activated slag, Constr. Build. Mater. 262 (2020) 120747, http://dx.doi.org/10.1016/j.conbuildmat.2020.120747.

[95] Y. Wei, X. Gao, S. Liang, A combined SPM/NI/EDS method to quantify properties of inner and outer C–S–H in OPC and slag-blended cement pastes, Cem. Concr. Compos. 85 (4) (2018) 56–66, http://dx.doi.org/10.1016/j.cemconcomp.2017.09.017.

[96] Jae Eun Oh, Paulo J. M. Monteiro, Ssang Sun Jun, Sejin Choi, Simon M. Clark, The evolution of strength and crystalline phases for alkali-activated ground blast furnace slag and fly ash-based geopolymers, Cem. Concr. Res. 40 (2) (2010) 189–196, http://dx.doi.org/10.1016/j.cemconres.2009.10.010, URL https://www.sciencedirect.com/science/article/pii/S0008884609002932.

[97] G. Konstantopoulos, E.P. Koumoulos, C.A. Charitidis, Testing novel portland cement formulations with carbon nanotubes and intrinsic properties revelation: Nanoindentation analysis with machine learning on microstructure identification, Nanomaterials 10 (4) (2020) http://dx.doi.org/10.3390/nano10040645.

[98] A.C.A. Muller, K.L. Scrivener, A.M. Gajewicz, P.J. McDonald, Densification of C–S–H measured by 1 h NMR relaxometry, J. Phys. Chem. C 117 (1) (2013) 403–412, http://dx.doi.org/10.1021/jp3102964.

[99] E. Schubert, Stop using the elbow criterion for k-means and how to choose the number of clusters instead, 2022, http://dx.doi.org/10.48550/ARXIV.2212.12189, arXiv, URL https://arxiv.org/abs/2212.12189.

[100] A.C.A. Muller, K.L. Scrivener, A reassessment of mercury intrusion porosimetry by comparison with 1H NMR relaxometry, Cem. Concr. Res. 100 (2017) 350–360, http://dx.doi.org/10.1016/j.cemconres.2017.05.024.

[101] D.A. Kulik, Improving the structural consistency of C–S–H solid solution thermodynamic models, Cem. Concr. Res. 41 (5) (2011) 477–495, http://dx.doi.org/10.1016/j.cemconres.2011.01.012.

[102] R.J. Myers, S.A. Bernal, J.L. Provis, Phase diagrams for alkali-activated slag binders, Cem. Concr. Res. 95 (2017) 30–38, http://dx.doi.org/10.1016/j.cemconres.2017.02.006.

[103] J.L. Provis, K. Arbi, S.A. Bernal, D. Bondar, A. Buchwald, A. Castel, S. Chithiraputhiran, M. Cyr, A. Dehghan, K. Dombrowski-Daube, A. Dubey, V. Ducman, G.J.G. Gluth, S. Nanukuttan, K. Peterson, F. Puertas, A. van Riessen, M. Torres-Carrasco, G. Ye, Y. Zuo, RILEM TC 247-DTA round robin test: Mix design and reproducibility of compressive strength of alkali-activated concretes, Mater. Struct. 52 (5) (2019) 3683, http://dx.doi.org/10.1617/s11527-019-1396-z.

[104] J. Sun, Z. Chen, Effect of silicate modulus of water glass on the hydration of alkali-activated converter steel slag, J. Therm. Anal. Calorim. 138 (1) (2019) 47–56, http://dx.doi.org/10.1007/s10973-019-08146-3.

[105] Y.H. Fang, Y.M. Gu, Q.B. Kang, Effect of fly ash, MgO and curing solution on the chemical shrinkage of alkali-activated slag cement, Adv. Mater. Res. 168–170 (2010) 2008–2012, http://dx.doi.org/10.4028/www.scientific.net/AMR.168-170.2008.

[106] A.R. Sakulich, D.P. Bentz, Mitigation of autogenous shrinkage in alkali activated slag mortars by internal curing, Mater. Struct. 46 (8) (2013) 1355–1367, http://dx.doi.org/10.1617/s11527-012-9978-z.

[107] C. Cartwright, F. Rajabipour, A. Radlińska, Shrinkage characteristics of alkali-activated slag cements, J. Mater. Civ. Eng. 27 (7) (2015) 509, http://dx.doi.org/10.1061/(ASCE)MT.1943-5533.0001058.

[108] H.H. Pan, Y.W. Chen, D.-H. Lin, Determination of representative crack density of cementitious materials, 2007.

[109] H.-H. Pan, Elastic moduli of heterogeneous solids with ellipsoidal inclusions and elliptic cracks, Acta Mech. 110 (1995) 73–94, http://dx.doi.org/10.1007/BF01215417.

[110] G. Fang, Q. Wang, M. Zhang, Micromechanical analysis of interfacial transition zone in alkali-activated fly ash-slag concrete, Cem. Concr. Compos. 119 (10) (2021) 103990, http://dx.doi.org/10.1016/j.cemconcomp.2021.103990.

[111] P. Mondal, S. Shah, L. Marks, Nanomechanical properties of interfacial transition zone in concrete, Nanotechnol. Constr. 3 (2009) 315–320, http://dx.doi.org/10.1007/978-3-642-00980-8_42.

Supplementary material
Multi-scale experimental investigation and analytical micro-mechanical modeling to determine Young's modulus of alkali-activated slag concrete

1. Evaluation of the number of clusters from nano-indentation data with the Bayesian Information Criterion

In this section, further analysis of the determination of the number of clusters for nano-indentation tests are presented. The Bayesian Information Criterion (BIC) is used to determine the number of clusters on the concatenated dataset made of both mix lS and mix hS for a Gaussian mixture clustering technique for illustration. The BIC provides a measure of the goodness of the clustering method accounting for overfitting penalties. Following this criterion, four or five clusters can be considered as the optimum number of clusters, as shown in Figure 1. Figure 2 shows the difference in clustering depending on whether four or five clusters are used. The corresponding clustering centers are given in Table 1. The results show that in the case of five clusters, the cluster with higher E and H is split into two clusters. In fact, the centers of both denominated soft matrix and hard matrix are identical. It can also be seen that the points of the fifth cluster are not centered around a clear point. Thus, it seems more likely that the points centered on H = 2.75 GPa and E = 51.3 GPa correspond to indents located at the border of unreacted particles. In that case, they are not a physical cluster corresponding to a specific phase with defined elastic properties. As a consequence, only four clusters can be considered for describing the microstructure of waterglass-activated slag.

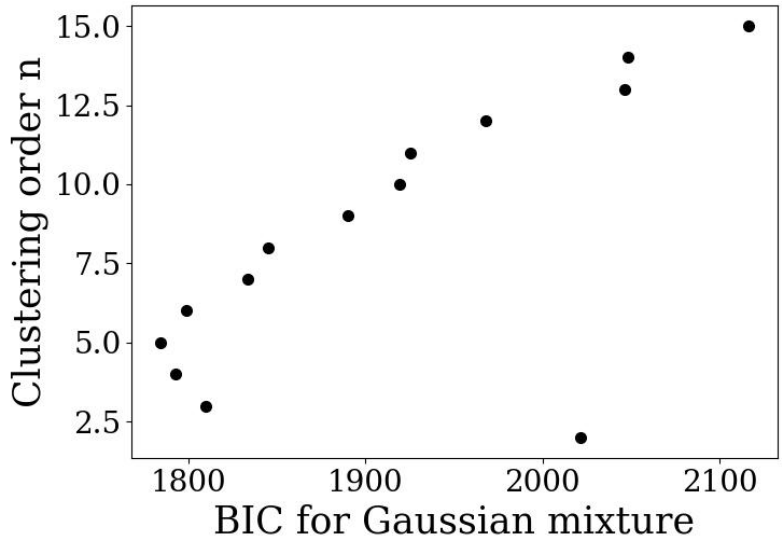

Figure 1 BIC values for Gaussian mixture model with different orders.

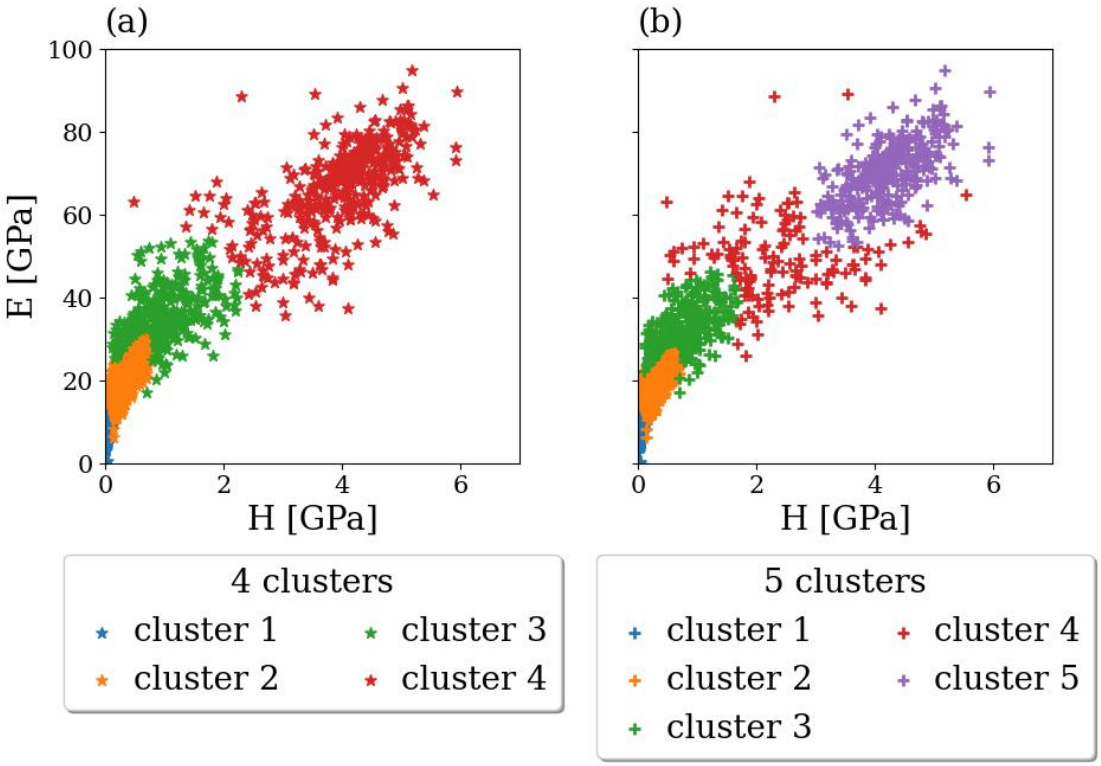

Figure 2 Clustering of nano-indentation data with four clusters (a) or five clusters (b) with Gaussian mixture.

Table 1 Cluster centers of the Gaussian mixture model considering both cases with four or five clusters.

Cluster nb	With four clusters		With five clusters	
	H	E	H	E
1	0.07	10.8	0.07	10.8
2	0.36	20.6	0.34	20.1
3	0.98	35.1	0.77	31.6
4	3.95	66.0	2.75	51.3
5			4.20	70.3

2. Model calculations considering an interfacial transition zone around the coarse aggregates

The original model takes into account the interfacial transition zone (ITZ) around sand particles but not around coarse aggregates. This is motivated by the fact that the interfacial transition zone is modeled with a constant thickness equal to either 20 µm or 40 µm. These ITZ have a very low volume fraction for coarse aggregates greater than 4 mm.

The modeling of the ITZ around the coarse aggregates follows the same methodology as for sand. The use of concept of coated spheres is applied, as introduced by Garboczi et al. [1] and described in Section 3. The results are shown in Figure 3 and Figure 4 for both considered ITZ thicknesses of 20 µm and 40 µm. It can be seen that accounting for the ITZ around coarse aggregates reduces Young's modulus by less than 1 GPa in comparison to the calculation with ITZ around fine aggregates but not neglecting them around coarse aggregates. This value is negligible and falls within the uncertainty of the model predictions discussed in Section 5.

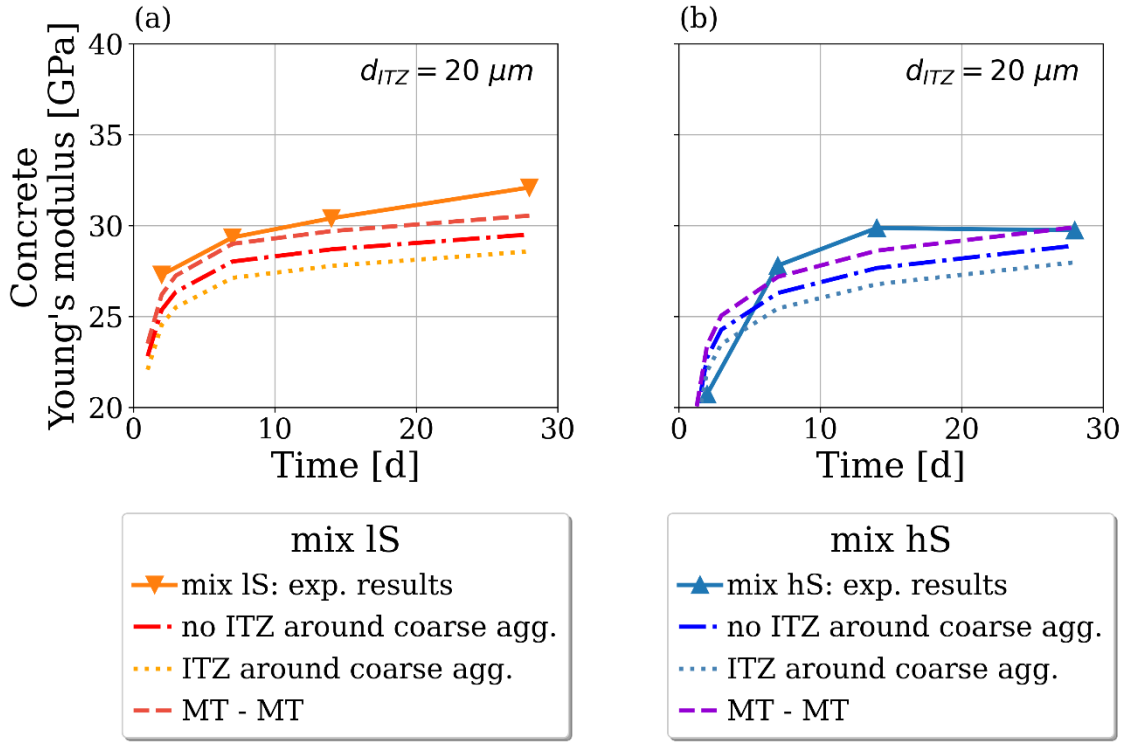

Figure 3 Concrete Young's modulus modeled with different hypotheses on the presence of ITZ: either no ITZ (MT-MT), or ITZ only around fine aggregates (no ITZ around coarse agg.) or around fine and coarse aggregates (ITZ around coarse agg.). In this figure, the calculations are made for an ITZ thickness of 20 µm

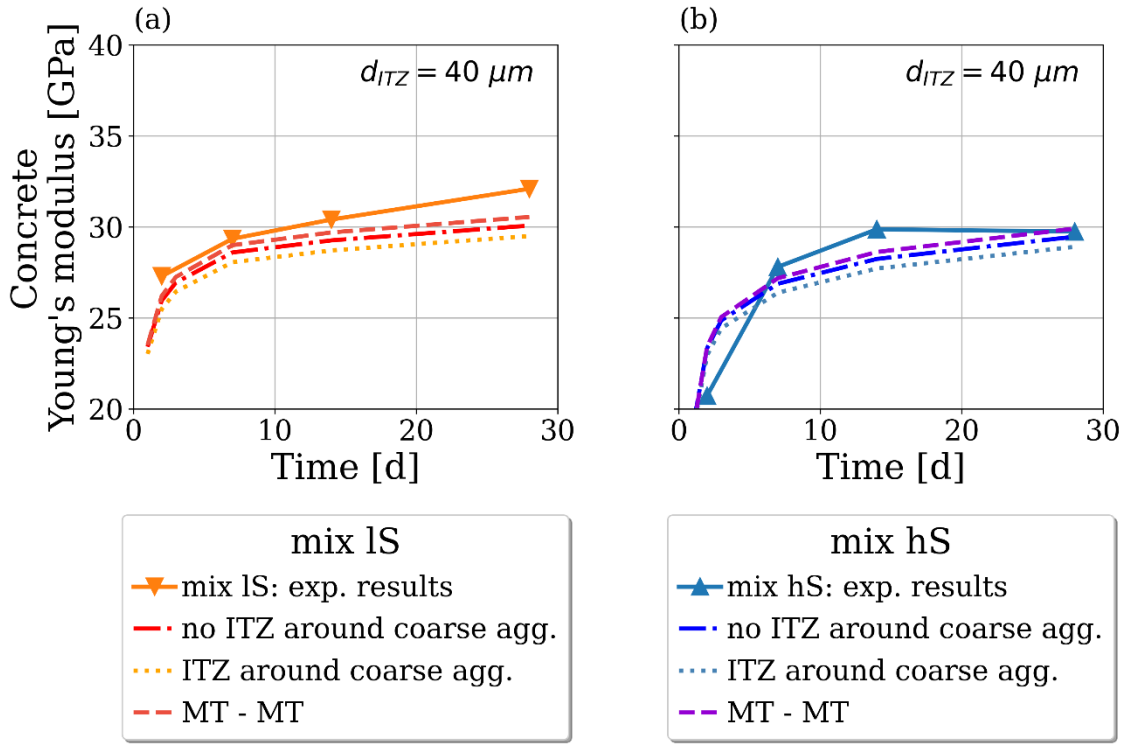

Figure 4 Concrete Young's modulus modeled with different hypotheses on the presence of ITZ: either no ITZ (MT-MT), or ITZ only around fine aggregates (no ITZ around coarse agg.) or around fine and coarse aggregates (ITZ around coarse agg.). In this figure, the calculations are made for an ITZ thickness of 40 µm

Paper 6

Insights into creep mechanisms of AAS concrete: multi-scale characterization and micromechanical modeling

Preprint version

Authors: **Richard Caron**, Ravi A. Patel, Andreas Bogner,

Frank Dehn

Insights into creep mechanisms of alkali-activated slag concrete: multi-scale characterization and micromechanical modeling

Richard Caron[1,2], Ravi A. Patel[1,2], Andreas Bogner[1,2], Frank Dehn[1,2]

[1]Institute of Building Materials and Concrete Structures (IMB), Karlsruhe Institute of Technology (KIT)
[2]Materials Testing and Research Institute Karlsruhe (MPA), Karlsruhe Institute of Technology (KIT)

Abstract

The creep of alkali-activated slag (AAS) concrete is higher than that of ordinary Portland cement. This can reduce the serviceability of AAS structures. In this contribution, an analytical multi-scale micromechanics-based model is applied to downscale the creep properties of the matrix of reaction products. Only a deviatoric creep of the matrix of reaction products is considered. This creep is split into an early-stage creep modeled with a Kelvin-Voigt unit and a long-term creep modeled with a logarithmic function. In addition, the basic creep of two AAS creep mixes loaded at 7 and 28 days are experimentally studied. Nanoindentation tests are performed on the same mixes to investigate creep properties at the nanoscale. The creep contact modulus obtained by nanoindentation is in the same range as the downscaled long-term creep modulus of the model. The cause of the creep of AAS concrete is the deviatoric creep of the matrix of reaction products. Finally, AAS creeps more because of the higher amount of gel water and fewer crystalline secondary products.

Keywords: Alkali-Activated Slag; Homogenization Scheme; Creep

1 Introduction

Time-dependent strains of concrete can reduce the safety and service life of structures. For example, the KB Bridge in Palau, made of prestressed box girder segments, collapsed after only 20 years of service life due to excessive creep deformations that strongly reduced the prestressing [1]. Creep is defined as the delayed deformations of the material

under sustained loading. If the sample is protected from drying, the corresponding creep is named basic creep. Basic creep is often considered as a material-related property [2–4] and is modeled as linear-viscoelastic for compressive loads below 40-50 % of the compressive strength of concrete [1, 4, 5]. Under these loads, the creep behavior of OPC concrete can be predicted with the B4 model [1], based on the solidification theory [6], or with the *fib* MC 2010 [5]. However, these models are empirical or semi-empirical and require the use of scaling coefficients for new mix designs [1, 7]. Moreover, these models predict creep from mix design parameters and not from microstructure features.

Mechanisms of basic creep of ordinary Portland cement (OPC) concrete are studied from the microstructure features of the material, especially from the creep behavior of calcium-silicate-hydrate (C-S-H), the main reaction product of OPC. Ye [8] reviewed the main mechanisms of creep of C-S-H. In the seepage theory [9], creep is due to the movement of gel water from load-bearing areas to non-bearing ones. This theory has been extended by the microprestress-solidification theory [10, 11] to account for the generation of disjoining pressure in micropores. In the thermal activation energy theory, creep would be because of the weakening of interparticle bonds by adsorbed water [12]. Creep could be also due to the rearrangement of C-S-H [13]. The dissolution-diffusion-reprecipitation theory hypothesizes that C-S-H can dissolve at high-stress fields and reform where the stress is lower contributing to creep [14]. The crystallization of silicate layers in the C-S-H interlayer was also proposed as a mechanism of creep [15]. Other authors consider that shear forces cause a slipping between C-S-H layers and thus creep [16]. Molecular dynamic simulations [17] showed that the long-term logarithmic behavior of creep could be explained by the sliding of C-S-H layers over each other. Experimental results performed with Raman spectroscopy indicated that the dominant mechanism for creep should be due to intragrain deformations [18]. Further studies with the same technique showed that these intragrain deformations would be due to the preferential alignment of C-S-H nanocrystallites to the compressive stress. This reorientation of C-S-H would be accompanied by a higher packing density of C-S-H [19, 20]. Also, the evolution of the creep strain of C-S-H was found to be dependent on the calcium/silicium (Ca/Si) ratio by nanoindentation tests [21–23].

The creep behavior of concrete can be modeled using multi-scale homogenization schemes [2–4, 21, 24]. To apply these models, a description of the microstructure and of the creep properties of the different phases is required. Smilauer & Bazant [2] used the hydration model CEMHYD3D [25] for the microstructure of cement and the creep behavior of the B3 model [26–28] to calculate the creep behavior of C-S-H. They found that the compliance function of the B3 model could be applied to the creep behavior of C-S-H with scaling coefficients. Pichler & Lackner [29] developed a multi-scale model to predict creep behavior. They determined the creep properties of C-S-H by downscaling experimental results. They found that the long-term creep compliance of C-S-H depends

on the relative humidity and the water/cement ratio of the mix design. They also proposed a simplified multi-scale engineering model in three scales using the creep behavior of C-S-H as the main parameter to predict the creep of concrete. Königsberger et al. [30] used three micromechanics models with different hypotheses on the considered representative volume element (RVE) and the geometry of the inclusions to identify the intrinsic creep properties of C-S-H. They found that the three proposed models are in the good range of experimental results made on six mixes loaded at different ages and that accounting for non-spherical shapes of C-S-H improves the predictions. Honorio et al. [31] studied the creep behavior for OPC concrete at an early age using an analytical and numerical multi-scale approach. They considered the presence of both low-density (LD) C-S-H as outer product and high-density (HD) C-S-H as inner product. Capillary pores and other reaction products were included in these matrices. They used the space-filling hypothesis to model the solidification of concrete. Their results were in agreement with experiments. They also showed that considering the interfacial transition zone around sand particles does not affect the overall creep behavior. Lavergne et al. [4] used a multi-scale model to predict the creep results of the NU database [32, 33]. They used a coupled hydration-thermodynamics model to predict the volume fractions of the phases. The creep of the phases was given by nanoindentation results. Their results indicate that it is possible to accurately predict concrete basic creep when the composition of the mix design is given. The predictions are even better when samples are loaded after three days or more. The long-term creep of concrete has also been predicted successfully by homogenization schemes using contact creep modulus obtained by nanoindentation results. For example, using the hypothesis of the slippery interface between paste and aggregates, Vandamme & Ulm [21] and Baronet et al. [34] were able to predict the creep modulus of concrete from the contact creep modulus of paste. Suwanmaneechot et al. [35] used the same approach for multi-scale analysis to downscale the creep properties of cement paste to that of C-S-H from microindentation technique measurements. They found that the long-term creep modulus of C-S-H increases for lower relative humidity.

For the past decades, other binders have been investigated as alternatives to OPC, for example alkali-activated slag (AAS). The main product of AAS is calcium-aluminum-silicate-hydrates (C-A-S-H) [36]. It has a similar structure as C-S-H and many studies on the fundamental behavior of creep of concrete include the behavior of C-S-H and C-A-S-H [19]. As reported in a few studies, AAS creep is higher than that of OPC [37–39]. For Humad et al. [39], this could be due to the presence of more cracks in the AAS matrix. However, the creep mechanisms of AAS have hardly been investigated and no analytical multi-scale micromechanics-based model has been used for predicting the creep behavior of AAS.

This study develops an analytical multi-scale micromechanics-based model for the creep of alkali-activated slag. It uses a coupled kinetic-thermodynamics model to describe

the microstructure. The latter has been validated in a previous study to predict Young's modulus of AAS concrete [40]. It is here applied to downscale the basic creep behavior of two AAS concretes and to determine the intrinsic creep properties of the AAS matrix of reaction products. The creep of the matrix of reaction products is here modeled with a Kelvin-Voigt unit for the early stage and a logarithmic function for the late stage. The numerical implementation of the model is based on the work of Sanahuja [41]. Finally, an evaluation of the creep mechanisms of C-A-S-H and AAS is conducted.

2 Materials and Methods

2.1 Materials

The precursor used in this study was a slag provided by the company Ecocem (Netherlands). Its oxide composition was determined with energy dispersive X-ray fluorescence spectrometry (XRF) with an M4 Tornado (Brucker GmbH Karlsruhe, Germany) (see Table 1). The activator used was a blend of commercially available waterglass solution, NaOH solution and tap water. The waterglass was Betol 39 T provided by Wöllner GmbH (Germany). It consists of 64 wt % of water, 8.2 wt % of Na_2O and 27.8 wt % of SiO_2. The NaOH solution had a 50 % mass concentration of solid NaOH. Two mixes, namely mix lS and mix hS, were cast and analyzed for both paste and concrete. The alkali dosage n was equal to 5.0 [g Na_2O / 100 g slag] for both mixes. The silicate ratio was equal to $M_S = 0.5$ [mol SiO_2 / mol Na_2O] for the mix lS and $M_S = 2.2$ [mol SiO_2 / mol Na_2O] for the mix hS. The water/slag ratio w/s was equal to 0.40 [kg/kg] for paste and 0.45 [kg/kg] for concrete. This slight increase was necessary to assure reasonable workability for concrete. The different mix designs are given in Table 2.

Table 1: Chemical composition of the anhydrous slag

Oxide	CaO	SiO_2	Al_2O_3	MgO	Fe_2O_3	Na_2O	K_2O	SO_3	Oth.
Mass(%)	38.8	36.3	12.8	8.0	0.6	0.3	0.6	1.9	0.7

2.2 Methods

2.2.1 Mixing procedure, casting and storage

For each casting, the alkali solution was prepared 24 hours in advance so that the solution reaches the temperature of the surrounding environment. The dry ingredients were mixed for 30 seconds. They were then mixed with the alkali solution for one minute. After 30 seconds of rest, the ingredients were mixed for two more minutes. Paste samples were used for nanoindentation tests. They were cast in $2 \times 2 \times 8$ cm^3 prisms. For measuring

Table 2: Mix design for both paste and concrete

Paste scale		Mix lS	Mix hS
w/s	[kg/kg]	0.40	0.40
n	[Na_2O g/ 100 g slag]	5.0	5.0
M_S	[SiO_2/Na_2O mol/mol]	0.5	2.2
Concrete scale		Mix lS	Mix hS
w/s	[kg/kg]	0.45	0.45
n	[Na_2O g/ 100 g slag]	5.0	5.0
M_S	[SiO_2/Na_2O mol/mol]	0.5	2.2
Precursor content	[kg/m^3 of concrete]	450	
Fine Agg. (0-2 mm)	[Vol-%]	40	
Coarse Agg. (2-8 mm)	[Vol-%]	30	
Coarse Agg. (8-16 mm)	[Vol-%]	30	

creep, concrete samples were cast in cylindrical specimens with a diameter of 100 mm and a height of 300 mm. All the samples were demolded after 24 hours and covered with aluminum-butyl foil to prevent water loss. The samples were stored in a climate room at 20 °C.

2.2.2 Creep tests on concrete samples

The deformations of concrete were measured with linear variable differential transformers (LVDTs) provided by the company Hottinger Brüel & Kjaer GmbH (Germany). Three LVDTs were spaced at an angle of 120° on the sample. The creep setup is described in Figure 1. It consists of a hollow steel spring filled with hydraulic oil, a loading frame and a pressure pipe with the loading device. The hollow steel was connected to a pressure tank through a pipe filled with oil and nitrogen. After that, the specimens equipped with the LVDTs were mounted on the loading frame and the above transverse was put on the spherical cap and fixed with a screw-nut system. Oil was then released from the pressure tank to reach the wanted value of pressure. Throughout the test, the pressure changes were recorded by an absolute pressure transducer P8AP (Hottlinger Baldwin Messtechnik GmbH).

Basic creep was studied for both mixes with two replicates per mix. The creep stress-strength ratio was equal to 33 %. The loading age t' was equal to either 7 or 28 days. The experimental creep test program is summarized in Table 3. Parallel specimens were also used to determine the basic shrinkage of both mixes with the same measuring tool as for creep. Two replicates were used for each mix. The shrinkage contribution was subtracted from the creep measurements on loaded specimens to obtain creep strains. In addition, further parallel specimens were cast to determine Young's modulus and the compressive strength at creep loading age (7 or 28 days) for each mix. The norm EN 12390-13 [42] (method B) was applied with six samples per test. The surface of the samples used for

Young's modulus and creep tests were ground at an age of at least 6 days.

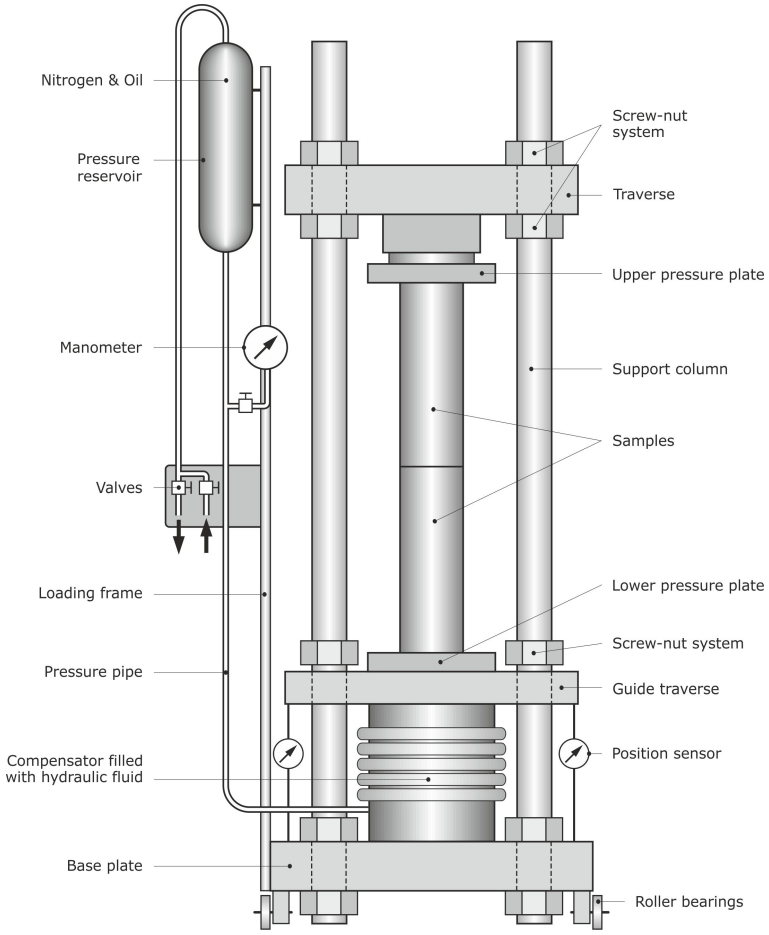

Figure 1: Experimental creep setup used in this study

Table 3: Experimental program for creep tests

Specimen	Mix design	loading age [d]
lS-7d	mix lS	7
lS-28d	mix lS	28
hS-7d	mix hS	7
hS-28d	mix hS	28

2.2.3 Creep from nanoindentation tests

Nanoindentation tests were performed on paste. The grinding and polishing process was the same as the one described in [40]. A sample of a 2×2 cm^2 surface was cut with an Isomet 1000 saw (Buehler) and coated in epoxy resin. The sample was then ground with Automet 250 equipment (Buehler) and polished in four steps, with 9 µm, 3 µm and 1 µm MetaDi Supreme Diamant suspensions (Buehler), and 0.05 µm MasterPrep Al_2O_3 solution (Buehler). The polishing times for each polishing step were 4, 4, 3 and 3 minutes, respectively, and the applied force during the polishing was 5 N. After the polishing, the

samples were cleaned with N_2 air steam and stored in a desiccator until the day of testing. The roughness of the final sample was measured with Atomic Force Microscopy and was equal to 75 µm on a grid of 100 µm × 100 µm.

The nanoindentation tests were done with a UNHT^3 (Anton Paar, Austria). Four grids of 23 × 23 points with a spacing of 10 µm between each point were used for the measurement. A sustained force of 2 mN was applied for 180 s. The loading rate and the unloading rate were 10 mN/min.

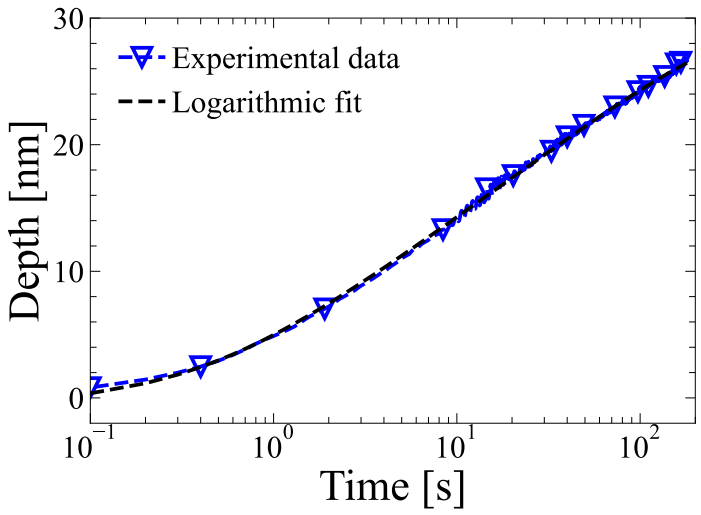

Figure 2: Typical change of penetration depth with time from nanoindentation test for a sustained load of 180 s and corresponding logarithmic fit.

The Oliver-Pharr methodology [43] was used for determining both the hardness and elastic modulus of the matrix. Experimental points were then classified into clusters following the Gaussian mixture approach, as already applied for these mixes in a previous study [40]. This clustering approach has been used by several researchers in the literature since it allows the correct identification of phases from their nanomechanical properties [44–49]. The contact creep modulus for each indented point was obtained by applying the approach from Vandamme et al. [21]. The change in depth with time, written $\Delta h(t)$, can be modeled by the following function:

$$\Delta h(t) = x_1 ln(t/x_2 + 1) + x_3 t + x_4 \tag{1}$$

An example of fitting of indentation data is provided in Figure 2. The contact creep compliance rate $\dot{L}(t)$ is defined as:

$$\dot{L}(t) = \frac{2a_u \dot{h}(t)}{P_{max}} \tag{2}$$

P_{max} is the maximum load (equal to 2 mN here), a_u is the radius of the projected area of

contact between the indenter and the indented surface A_c ($a_u = \sqrt{A_c/\pi}$). The long-term contact creep compliance rate $\dot{L}(t)$ is given by:

$$\begin{cases} \dot{L}(t) &= \frac{1}{Ct} \\ C &= \frac{P_{max}}{2a_u x_1} \end{cases} \tag{3}$$

where C is the contact creep modulus.

3 Analytical micro-mechanics-based model for a non-aging linear-viscoelasticity material

This section describes the micro-mechanics-based model applied in this study to link the creep of the matrix of reaction products and the creep of concrete. Firstly, the equations of linear-viscoelasticity are recalled in Sections 3.1 and 3.2. Then, the numerical implementation based on time discretization is presented in Section 3.3. The description of AAS microstructure is described in Section 3.4. Finally, the downscaling of the creep behavior of concrete is explained in Section 3.5.

3.1 Basics of linear-viscoelasticity

In linear-viscoelasticity, the microscopic stress tensor σ and the microscopic strain tensor ϵ are linked by the following equation:

$$\sigma(t) = \int_{-\infty}^{t} \mathcal{C}(t,t') : d\epsilon(t') \tag{4}$$

where $\mathcal{C}$ is the fourth-order tensor relaxation tensor.

The corresponding compliance tensor $\mathcal{S}$ is defined as:

$$\epsilon(t) = \int_{-\infty}^{t} \mathcal{S}(t,t') : d\sigma(t') \tag{5}$$

$\mathcal{S}$ is the inverse of $\mathcal{C}$. For isotropic material, the decompositions of $\mathcal{C}$ and $\mathcal{S}$ into spherical and deviatoric parts read:

$$\begin{cases} \mathcal{C}(t,t') &= 3k(t,t')\mathcal{J} &+ 2g(t,t')\mathcal{K} \\ \mathcal{S}(t,t') &= \frac{1}{3}J^k(t,t')\mathcal{J} &+ \frac{1}{2}J^g(t,t')\mathcal{K} \end{cases} \tag{6}$$

where k is the bulk relaxation, g the shear relaxation, J^k the bulk compliance and J^g the shear compliance. $\mathcal{J}$ and $\mathcal{K}$ are the spherical and deviatoric parts, respectively, of the fourth-order symmetric unity tensor $\mathcal{I}$ ($\mathcal{I}_{ijkl} = \frac{1}{2}(\delta_{ik}\delta_{jl} + \delta_{il}\delta_{jk})$). In the following, both

equations (4) and (5) are written in a more compact form with the notation $\overset{\circ}{\vdots}$, as in [41]:

$$\left\{ \begin{array}{rcl} \sigma(t) & = & \mathcal{C}(t,.) \overset{\circ}{\vdots} \epsilon(.) \\ \epsilon(t) & = & \mathcal{S}(t,.) \overset{\circ}{\vdots} \sigma(.) \end{array} \right. \tag{7}$$

or also:

$$\left\{ \begin{array}{rcl} \sigma & = & \mathcal{C} \overset{\circ}{\vdots} \epsilon \\ \epsilon & = & \mathcal{S} \overset{\circ}{\vdots} \sigma \end{array} \right. \tag{8}$$

where the time dependencies have been omitted.

The strain concentration operator $\mathcal{A}$ links ϵ and the macroscopic strain tensor $\mathbf{E}$ for each point x by:

$$\epsilon(x,t) = \mathcal{A}(x,t,.) \overset{\circ}{\vdots} \mathbf{E}(.) \tag{9}$$

Since $\mathbf{E}$ is the macroscopic strain over the whole RVE, i.e. $< \epsilon(x,t) >= E(t)$, the average of the strain concentration operator is equal to:

$$< \mathcal{A}(x,t,.) >= H(t-t')\mathcal{I} \tag{10}$$

where $H(t-t')\mathcal{I}$ is the identity element of the Volterra integral operator.

The effective behavior is equal to [41]:

$$\mathcal{C}^{eff}(t,t') =< \mathcal{C}(x,t,.) \overset{\circ}{\vdots} \mathcal{A}(x,.,t') > \tag{11}$$

3.2 Dilute scheme for a non-aging linear-viscoelastic material

For a two-phase composite material, the local relaxation tensor of each phase i = 1,2 is equal to:

$$\mathcal{C}_i(t,t') = 3k_i(t,t')\mathcal{J} + 2g_i(t,t')\mathcal{K} \tag{12}$$

where k_i and g_i are the bulk and shear relaxations of phase i.

The effective relaxation tensor of the homogenized material can be expressed as [41]:

$$\mathcal{C}^{eff}(t,t') = \mathcal{C}_2(t,t') + f_1\Big(\mathcal{C}_1(t,.) - \mathcal{C}_2(t,t')\Big) \overset{\circ}{\vdots} < \mathcal{A}(x,.,t') >_1 \tag{13}$$

with f_1 the volume fraction of phase 1.

As shown in [41], $< \mathcal{A}(x,t,t') >_1$ can be expressed as:

$$< \mathcal{A}(x,t,t') >_1 = \mathcal{A}_1^2(t,t') = {}^jA_1^2(t,t')\mathcal{J} + {}^kA_1^2(t,t')\mathcal{K} \tag{14}$$

where ${}^jA_1^2(t,t')$ and ${}^kA_1^2(t,t')$ are the spherical and deviatoric parts of $< \mathcal{A}(x,t,t') >_1$.

The Volterra integral operator "o" between two-variable scalar functions f and g is

defined as:

$$y(t,\tau) = (f \circ g)(t,\tau) = \int_{-\infty}^{t} f(t,t')d_{t'}g(t',\tau) \tag{15}$$

Using this operator, ${}^{j}A_1^2(t,t')$ and ${}^{k}A_1^2(t,t')$ can be expressed as [41]:

$$\left\{\begin{array}{rcl} {}^{j}A_1^2(t,t') & = & (3k_1+4g_2)^{-1}(t,.) \circ (3k_2(.,t')+4g_2(.,t')) \\ {}^{k}A_1^2(t,t') & = & H + 2(2H+3D_2) \circ (2g_1 \circ (2H+3D_2)+ \\ & & \qquad g_2 \circ (6H-D_2))^{-1} \circ (g_2-g_1) \end{array}\right. \tag{16}$$

where

$$D_2 = (k_2+g_2)^{-1} \circ \frac{2}{3}g_2 \tag{17}$$

The effective bulk and shear relaxations are then obtained by projection of Eq. (13) onto $\mathcal{J}$ and $\mathcal{K}$:

$$\left\{\begin{array}{rcl} k^{dil} & = & k_2 + f_1(k_1-k_2) \circ {}^{j}A_1^2 \\ g^{dil} & = & g_2 + f_1(g_1-g_2) \circ {}^{k}A_1^2 \end{array}\right. \tag{18}$$

The previous equation can be generalized for an arbitrary number of phases. In this case, the equation is:

$$\mathcal{C}^{eff} = \sum_i f_i\mathcal{C}_i \ \vdots^{\circ} \ \mathcal{A}_i \tag{19}$$

The Mori-Tanaka scheme identifies the effective medium with one of the phases regarded as an infinite matrix noted here with the index 0. In this case,

$$\mathcal{C}^{MT} = \left(\sum_{i=0}^{N} f_i\mathcal{C}_i \ \vdots^{\circ} \ \mathcal{A}_i^0\right) \ \vdots^{\circ} \ \left(\sum_{i=0}^{N} f_i\mathcal{A}_i^0\right) \tag{20}$$

and

$$\left\{\begin{array}{rcl} k^{MT} & = & \left(\sum_{i=0}^{N} f_i k_i \ \vdots^{\circ} \ {}^{j}A_i^0\right) \circ \left(\sum_{i=0}^{N} f_i \ {}^{j}A_i^0\right)^{-1} \\ g^{MT} & = & \left(\sum_{i=0}^{N} f_i g_i \ \vdots^{\circ} \ {}^{k}A_i^0\right) \circ \left(\sum_{i=0}^{N} f_i \ {}^{k}A_i^0\right)^{-1} \end{array}\right. \tag{21}$$

with ${}^{j}A_0^0 = {}^{k}A_0^0 = H$ for the matrix.

The self-consistent scheme identifies the reference medium with the effective medium. This leads to the following equation:

$$\left\{\begin{array}{rcl} k^{SC} & = & \left(\sum_{i=1}^{N} f_i k_i \vdots^{\circ} {}^{j}A_i^0\right) \circ \left(\sum_{i=1}^{N} f_i {}^{j}A_i^0\right)^{-1} \\ g^{SC} & = & \left(\sum_{i=1}^{N} f_i g_i \vdots^{\circ} {}^{k}A_i^0\right) \circ \left(\sum_{i=1}^{N} f_i {}^{k}A_i^0\right)^{-1} \end{array}\right. \tag{22}$$

Here, the index 0 corresponds to the reference medium. The tensors ${}^{j}A_i^0$ and ${}^{k}A_i^0$ depend on k^{SC} and g^{SC} and the equation is implicit.

3.3 Numerical implementation of the Volterra integral operator and its inverse

The homogenization scheme for linear-viscoelasticity presented in section 3.2 requires the evaluation of the Volterra integral operator o as defined between two-variable scalar functions f and g in Eq. (15). This operator is found in Eqs. (16), (17), (18), (21) and (22). For example, in Eq. (17), $f(t,t')$ corresponds to $(k_2(t,t') + g_2(t,t'))^{-1}$ and $g(t,t')$ corresponds to $\frac{2}{3}g_2(t,t')$. Note that $\overset{\circ}{:}$ is the extension of the Volterra integral operator for tensors (see Eqs. (8) and (19)).

The evaluation of this operator can be solved numerically using the Laplace-Carson transformation [29]. However, in this study, this evaluation is done numerically with the time discretization for two-variable scalar functions, as implemented by Sanahuja [41]. The discretization is performed by introducing the different times t_i, $i = 0, 1, ..., n$ with $0 < t_0 < t_1, ... < t_n$. $f(t,t')$ is discretized in matrix $[\![f]\!]$ of size (n+1) $\cdot$ (n+1):

$$2f_{i,j} = \begin{cases} f(t_0,0) + f(t_0,t_0) & i = j = 0 \\ f(t_i,0) - f(t_i,t_1) & i \geq 1,\ j = 0 \\ f(t_i,t_{j-1}) - f(t_i,t_{j+1}) & i \geq 2,\ 1 \leq j \leq i-1 \\ f(t_i,t_{i-1}) + f(t_i,t_i) & i \geq 1,\ j = 1 \\ 0 & 1 \leq i+1 \leq j \leq n \end{cases} \tag{23}$$

A similar matrix $[\![g]\!]$ can be obtained for $g(t,t')$. The trapezoidal approximation of Eq. (15) is the matrix product between $[\![f]\!]$ and $[\![g]\!]$:

$$[\![y]\!] = [\![f]\!] \cdot [\![g]\!] \tag{24}$$

In this study, the time is discretized with 31 points logarithmically spaced.

3.4 Description of the microstructure

The multi-scale description of the structure of concrete is made of five levels as already studied in [40] (see Figure 3). Level 0 represents the homogenization of the matrix of reaction products, which consists of two types of reaction product matrix identified by nanoindentation tests and gel pores. Level 1 and level 2 correspond to the homogenization of AAS paste. At level 1, capillary pores are regarded as inclusions in the matrix of reaction products. At level 2, the unreacted slag particles are embedded in the previous matrix and the homogenized material constitutes AAS paste. Finally, level 3 and level 4 represent mortar and concrete, respectively.

As modeled in [40], the matrix of reaction products is modeled as a mixture of two types of matrix, a soft matrix and a hard matrix. This approach is similar to LD C-S-H

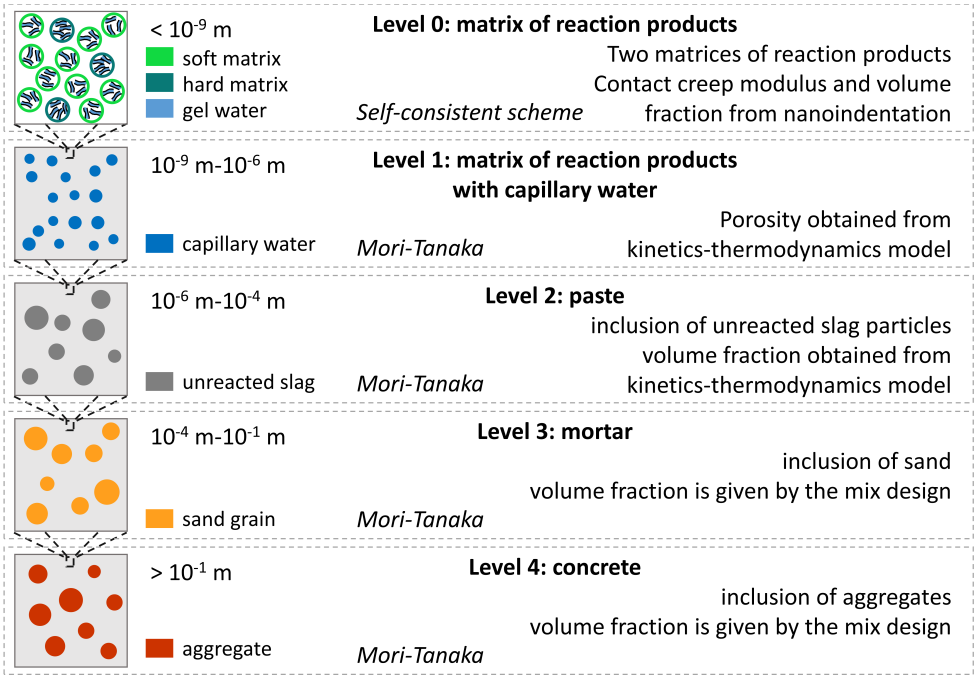

Figure 3: Description of the microstructure and multi-scale homogenization scheme for AAS developed in [40]. Level 0 corresponds to the matrix of reaction products. Level 1 corresponds to the inclusion of capillary water in the matrix of reaction products. Level 2 corresponds to the inclusion of the unreacted slag particles to constitute paste. Level 3 corresponds to the inclusion of sand grains in paste. Level 4 corresponds to concrete.

and HD C-S-H for OPC.

The porosity and the volume fractions of reaction products and unreacted slag particles are determined using coupled thermodynamic-kinetic modeling described in [50]. For kinetics, both isothermal calorimetry and Scanning Electron Microscopy were used to determine the evolution of the degree of dissolution of slag. The phase assemblage is obtained from thermodynamic calculations using the software GEMS as described in [50]. This model was validated by experimental tests to characterize the reaction products. The main reaction product of AAS was C-A-S-H gel. The secondary reaction products are hydrotalcite, magnesium-silicate-hydrates and zeolites, the quantities of which depend on the mix design parameters. In [40], it was also shown that the volume fraction of gel porosity $f_{w,gel}$ was proportional to the volume fraction of C-A-S-H gel f_{CASH}:

$$f_{w,gel} = \phi_g \cdot f_{CASH} \tag{25}$$

with $\phi_g = 28$ % the gel porosity in C-A-S-H. The volume fraction of capillary porosity $f_{w,cap}$ is then obtained by:

$$f_{w,cap} = f_w - f_{w,gel} = f_w - \phi_g \cdot f_{CASH} \tag{26}$$

where f_w is the volume fraction of water obtained by the thermodynamic model. The

volume fractions of paste, sand and aggregates needed for the multi-scale model are obtained from the mix design.

3.5 Downscaling of concrete creep to obtain creep characteristics of AAS at nanoscale

The analytical micromechanics-based model presented in sections 3.1 and 3.2 is applied to link the creep compliance of AAS concrete and the creep compliance of the matrix of reaction products. The elastic compliance has already been modeled in [40]. Here, the focus is placed on viscous creep compliance defined as the change in compliance from the loading age and starts at 0 at the loading age. The homogenization of the material is made at Levels 1, 2, 3 and 4, which were described in section 3.4. At each level, the creep behavior for the matrix-inclusion-type problem requires the evaluation of the tensor Volterra integral operator $\overset{\circ}{:}$ and of its inverse. This is solved numerically using the scheme of section 3.3. The creep behaviors of each phase can be described by the relaxation tensor $\mathcal{C}$ or by its inverse the compliance tensor $\mathcal{S}$. The hypotheses of the model are as follows.

At Level 1, the matrix of reaction products creeps deviatorically and the governing function is a two-term sum. The first one corresponds to a Kelvin-Voigt model and describes the early-stage creep (Figure 4). It can be characterized by two constants: Young's modulus E and the characteristic time τ.

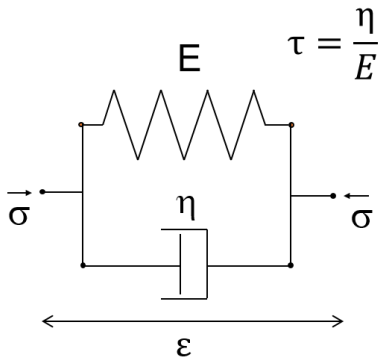

Figure 4: Kelvin-Voigt model.

The second one is a logarithmic behavior as justified in [17] for OPC. It is often used in the literature to describe long-term creep [4, 21, 29]. These hypotheses read:

$$\left\{ \begin{array}{lcl} J_0^k(t,t') & = & 0 \\ J_0^g(t,t') & = & \frac{1}{E_h}(1 - exp(-\frac{t-t'}{\tau})) + \frac{1}{C_h} ln(t - t' + 1) \end{array} \right. \tag{27}$$

where J_0^k and J_0^g are the spherical and deviatoric parts of the creep of the matrix of

reaction products, respectively. E_h [GPa] and τ [d] are the parameters of the Kelvin-Voigt unit and C_h [GPa] is the creep modulus governing the long-term creep behavior.

It is hypothesized that capillary water does not take part in the creep process. It means that the equilibrium pressure in the bigger pores is assumed to be reached instantaneously. Thus, the capillary water is modeled with:

$$\left\{ \begin{array}{rcl} k_{cap}(t) & = & 0 \\ \mu_{cap}(t) & = & 0 \end{array} \right. \tag{28}$$

where k_{cap} and μ_{cap} are the bulk and shear moduli of capillary water kept constant to 0 GPa.

The homogenization of Level 1 provides the spherical part $J_1^k(t)$ and deviatoric part $J_1^g(t)$ of the creep of the matrix made of the matrix of reaction products and capillary water. At level 2, unreacted slag particles are considered non-creeping spherical inclusions in this matrix. This hypothesis reads:

$$\left\{ \begin{array}{rcl} J_{us}^k(t) & = & 0 \\ J_{us}^g(t) & = & 0 \end{array} \right. \tag{29}$$

$J_{us}^k(t)$ and $J_{us}^g(t)$ are the spherical and deviatoric parts, respectively, of the creep of unreacted slag particles. At the end of this homogenization step, the spherical part $J_2^k(t)$ and deviatoric part $J_2^g(t)$ of paste creep are obtained.

Similarly, creep at Level 3 and Level 4 is obtained with the hypothesis that sand and aggregates are non-creeping spherical inclusions. $J_3^k(t)$ and $J_3^g(t)$ correspond to the spherical part and deviatoric part, respectively, of the creep of mortar, while $J_4^k(t)$ and $J_4^g(t)$ correspond to the spherical part and deviatoric part, respectively, of the creep of concrete. The creep measured experimentally corresponds to the 1111-component of the tensor compliance creep function $J_{1111}^{mod}(t)$. The values of the parameters of Eq. (27) are determined by minimizing the error between the measured creep function J^{exp} and the model-predicted compliance creep function:

$$e = \sum_i |J^{exp}(t_i) - J_{1111}^{mod}(t_i)|^2 \tag{30}$$

4 Results

In this section, basic shrinkage and basic creep results of concrete are presented as well as nanoindentation results on paste. In addition, creep properties downscaling using the model described in section 3 is presented.

4.1 Experimental results on concrete

Young's modulus and compressive strength results on concrete are provided in Table 4. The shrinkage of both mix lS and mix hS from the age of 1 day is plotted in Figure 5. It can be seen that the shrinkage of mix hS is around three times higher than the one of mix lS. The fact that the mix with the higher M_S has the higher shrinkage is coherent with other results from the literature [51, 52]. It can also be noticed that the shrinkage of the mix hS increases a lot between the first and the third day of the reaction. This is because the kinetics of this mix is delayed in comparison to the mix lS and the last acceleration-deceleration period takes place later for this mix, as explained in [53].

Table 4: Young's modulus and compressive strength of concrete

Mix	Age [d]	Young's modulus [GPa]	Compressive strength [MPa]
Mix lS	7	29.3	42.7
	28	32.1	55.9
Mix hS	7	27.8	56.7
	28	29.7	75.6

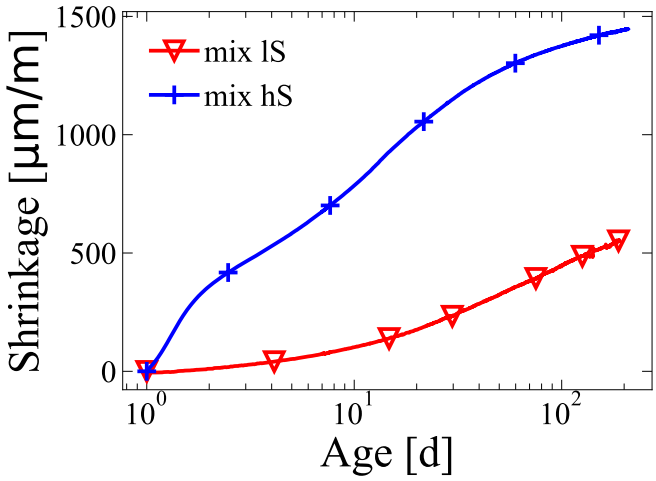

Figure 5: Shrinkage results on concrete for both mix lS and mix hS

The compliances of both mix lS and hS for loading ages of 7 and 28 days are plotted in Figure 6. It can be seen that creep decreases when the loading age is increased. This is because the reaction is more advanced at 28 days and the corresponding total porosity is lower [50]. For both mixes, the compliance just after loading is lower at 28 days than at 7 days. This is due to the increase in Young's modulus between both ages, as reported in [40]. It can be also observed that the creep of the mix hS is higher than that of the mix lS. For the loading after 7 days, the compliance is equal to 52 µm/m/MPa and 70 µm/m/MPa after 150 days of loading for the mix lS and the mix hS, respectively. For the loading at 28 days, the compliance is equal to 38 µm/m/MPa and 44 µm/m/MPa

after 150 days of loading for the mix lS and the mix hS, respectively. Thus, the difference in compliance between both mixes is equal to 18 µm/m/MPa for the loading at 7 days but only 6 µm/m/MPa for the loading at 28 days. This can be because the difference in porosity between both mixes is more pronounced at 7 days than at 28 days, as measured in [50]. Hence, it would mean that higher porosity at loading age would imply higher creep.

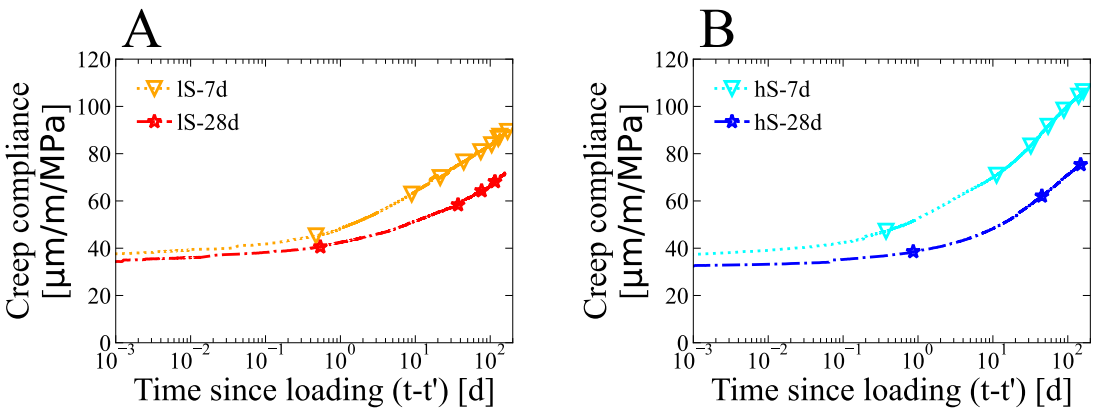

Figure 6: Creep results of concrete for both mix lS (A) and mix hS (B) loaded at 7 or 28 days

4.2 Results of nanoindentation tests

The results of nanoindentation tests on paste are plotted in Figure 7. The clustering analysis discomposes the results into four groups. In [40], two clusters corresponding to the matrix of reaction products could be characterized. The two matrices are referred to as soft matrix and hard matrix. The cluster centers of contact creep modulus of the soft matrix C_{soft}, the hard matrix C_{hard} and the unreacted slag particles C_{slag} for both mixes are given in Table 5. The elastic modulus of the phases, noted E_{soft}, E_{hard} and E_{slag} for the soft matrix, hard matrix and unreacted slag particles, respectively, are also provided. The unreacted slag particles have the highest elastic modulus and contact creep modulus. As observed for OPC systems [21], the reaction products with higher elastic modulus have also higher contact creep modulus. It can also be seen that the mix lS has lower elastic moduli (E_{soft} and E_{hard}) and contact creep moduli (C_{soft} and C_{hard}) than the mix hS. However, the difference is larger for creep moduli. Compared to identified contact creep moduli for OPC systems, the obtained values of C_{soft} and C_{hard} are quite low. In [21], Vandamme & Ulm found that the contact creep modulus of LD C-S-H ranges from 91 to 134 GPa and the one of HD C-S-H ranges from 132 to 225 GPa for different mix designs. In [54], Lee et al. found that the moduli of LD C-S-H and HD C-S-H were 162 GPa and 334 GPa, respectively. Haist et al. [49] found that the contact creep modulus of LD C-S-H ranges from 120 to 310 GPa, and the one of HD C-S-H ranges from

220 to 540 GPa. Thus, at the nano-scale, it seems that the contact creep modulus of the matrix of reaction products of slag is lower than that of OPC.

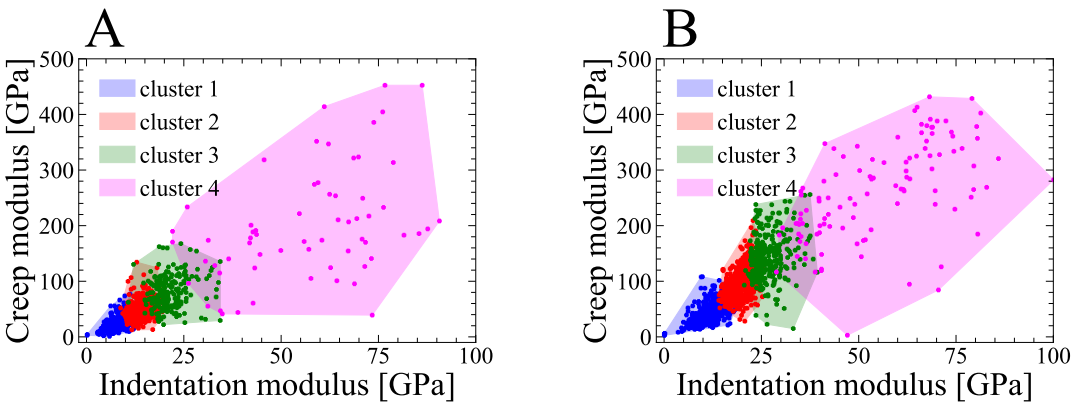

Figure 7: Clustering of indentation modulus and creep modulus obtained from nanoindentation tests for both mix lS (A) and mix hS (B)

Table 5: Results of nanoindentation tests after clustering

Mix	C_{soft} [GPa]	C_{hard} [GPa]	C_{slag} [GPa]	E_{soft} [GPa]	E_{hard} [GPa]	E_{slag} [GPa]
mix lS	48	78	207	17.2	31.2	65.6
mix hS	106	144	275	21.6	40.0	70.8

4.3 Downscaling of creep properties of the matrix of reaction products

Figure 8 shows the results of the multi-scale modeling for which the optimization of Eq. (30) was made on the parameters E_h, τ and C_h of Eq. (27). It can be seen that the model captures correctly the creep evolution for each experiment. The optimized parameters for each mix and loading age are provided in Table 6.

Table 6: Downscaling of creep parameters of the AAS matrix of reaction products (Level 1)

Specimen	C_h [GPa]	E_h [GPa]	τ [10^{-3} d]
lS-7d	105.9	229.5	2.2
lS-28d	124.2	119.9	2.8
hS-7d	89.4	85.9	11.1
hS-28d	110.4	357.4	1.0
average	107.5	198.2	4.3

Vandamme & Ulm showed that the loading age has little influence on the compliance rate for OPC [21]. Their result is in accordance with the downscaled deviatoric creep

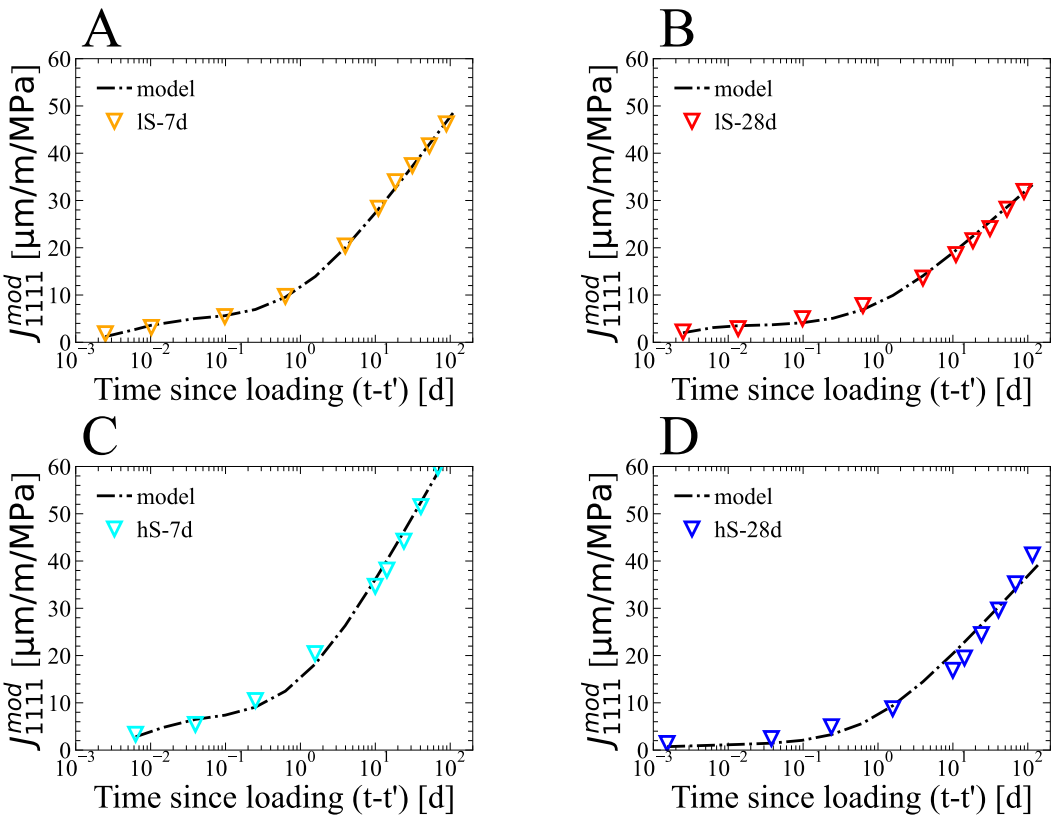

Figure 8: Comparison between concrete creep experiments and the optimized multi-scale model: (A) mix lS loaded at 7 days, (B) mix lS loaded at 28 days, (C) mix hS loaded at 7 days, (D) mix hS loaded at 28 days.

modulus of the matrix of reaction products C_h that can be regarded as a constant equal to 107.5 ± 12.4 GPa. This indicates that the long-term creep rate does not depend on the loading age or the mix design. The fact that C_h does not depend on the mix design can be explained by the fact that both mixes have the same main reaction product, namely C-A-S-H gel, in comparable amounts as characterized in a previous study [50].

The optimized values of E_h and τ are in the same ranges between experiments, as given in Table 6. The order of magnitude of the calibrated values of τ (10^{-3} days) corresponds to a few minutes. The reorganization of the structure at early stage could be due to water movements as explained by the seepage theory [9]. It can be noticed that τ of the mix hS loaded at 7 days is an order of magnitude higher than the other calibrated values and that E_h is lower for this mix. This difference could be explained by the fact that the pore structure of mix hS at 7 days has more capillary pores [50] into which gel water could easily seep. The amount of capillary porosity was determined in another study for both mixes [50]. The results are provided in Table 7. In the case of the mix hS loaded at 7 days, the additional resistance to creep due to gel water would take place later. For the other conditions (mix hS at 28 days or mix lS), the pore structure is more refined and has a very small amount of capillary pores.

Table 7: Capillary porosity of both mix lS and mix hS after 7 and 28 days. Results from [50].

Mix	Age [d]	Capillary porosity [%]
Mix lS	7	3.5
	28	2.5
Mix hS	7	7.4
	28	3.1

5 Discussion

In this section, the downscaled creep modulus of the matrix of reaction products is compared with the one that can be deduced from nanoindentation results. Then, the multi-scale model is applied to test further hypotheses regarding the modeling of the creep of phases. The results tend to show that the deviatoric strains of the matrix of reaction products are the main cause of concrete creep. Finally, the creep mechanisms of AAS concrete are discussed.

5.1 Comparison of nanoindentation results with the calibrated results of the model

The calibrated creep modulus of the matrix of reaction products C_h obtained from downscaling of experiments made on concrete was in the range of 89.4-124.2 GPa. The post-processing of nanoindentation tests showed that C_{soft} is in the range of 48-106 GPa and C_{hard} in the range of 78-144 GPa. After homogenization of the soft matrix and hard matrix with the self-consistent scheme, it is found that the creep modulus of the matrix of reaction products homogenized from nanoindentation results C_n is in the range of 54-112 GPa. The values of C_h and C_n are close. This means that the creep rate of concrete samples at a late stage can be correctly predicted from the results of nanoindentation tests. This possibility has already been investigated by Vandamme & Ulm [21]. Yet, in comparison to the work from Vandamme & Ulm, the model of the present study does not consider the effect of the imperfect bond between the paste and the aggregates. Moreover, the present model does not take into account the interfacial transition zone, which has often been described in the literature as a zone around the aggregates where the paste is weaker because of higher porosity. As for Young's modulus, it seems that this weak zone could be neglected to predict the creep behavior of AAS concrete [40]. It is also the conclusion of Honorio et al. [31].

It is also interesting to note that the contact creep modulus obtained from nanoindentation tests is higher for the mix hS, while the creep rate is also higher for the mix hS. This can be due to the fact that, firstly, the degree of reaction of the mix hS is lower than the mix lS at both 7 and 28 days and the mix hS presents a higher amount of capillary

pores (see Table 7). Thus, the resistance to creep of the paste is lower. Secondly, as shown in [40] for the same mixes, more cracks are formed for the mix hS in comparison to the mix lS. Hence, at the nanoscale, the mix hS has a higher contact creep modulus than the mix lS but this is compensated by other microstructure features.

5.2 Role of the deviatoric creep of the matrix of reaction products

Table 8: Description of further hypotheses tested with the analytical multi-scale model

model	matrix of reaction products		Cap. water
initial model	dev. KV unit	log-type function	-
log	-	log-type function	-
KV sph	sph. KV unit	log-type function	-
dev + sph	sph. KV & dev. KV	log-type function	-
KV cap	-	log-type function	dev. KV unit

KV stands for Kelvin-Voigt unit; dev. stands for deviatoric; sph. stands for spherical

Further calculations with the multi-scale have been performed to test some hypotheses on the creep of the matrix at an early stage. In this section, only the results made for experiment lS-28d are presented but the observations could be extended to the other experiments (see supplementary material). The first implemented model does not consider the Kelvin-Voigt unit of the initial model. It is referred to as "log". Two other scenarios consider that the creep of the matrix of reaction products has a spherical component modeled by a Kelvin-Voigt unit. Either this spherical component replaces the deviatoric Kelvin-Voigt unit (hypothesis "KV sph") or it is added to it (hypothesis "dev+sph"). The last hypothesis is that the Kelvin-Voigt unit is not applied at the matrix of reaction products level but for the capillary pores (hypothesis KV cap). This would mean that the early-stage creep would correspond to water movements in the capillary pores until the equilibrium is reached there. The different investigated hypotheses are summarized in Table 8.

The results of the modeling are plotted in Figure 9. For each hypothesis, the corresponding root mean square error of the best fit (see Eq. (30)) up to 10 days is given in Table 9. It can be seen that the "log" model captures very poorly the creep behavior for $t - t' < 10$ days. This result indicates that the creep of AAS concrete can not be explained with the sole logarithmic behavior. Furthermore, the model "KV sph" does not correctly reproduce the creep behavior either. It means that the deviatoric component for the matrix of reaction products is necessary to explain the creep of concrete. Adding a spherical component to the initial model with the model "dev+sph" does not improve much the model. The calculated error (Table 9) is almost identical to the initial model despite the higher number of parameters for the optimization. This means that consid-

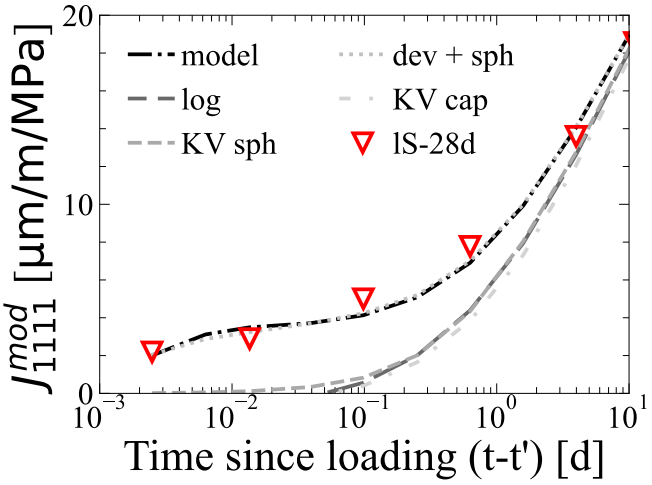

Figure 9: Comparison of different hypotheses about creep behavior of phases with the creep results of the specimen lS-28d.

ering a spherical creep component for the matrix of reaction products does not better predict the observed behavior at the macro-scale. Finally, the model "KV cap" does not correctly reproduce experimental results and the error is higher than for the initial model (see Table 9), meaning that the potential movements of capillary water do not influence the creep of concrete. To summarize, these further calculations tend to show that the observed creep of concrete at an early stage is mainly explained by the deviatoric creep of the matrix of reaction products modeled by a Kelvin-Voigt unit.

Table 9: Root mean square of each tested model against the viscous creep compliance of the specimen lS-28d

model	error
initial model	4.2
log	98.3
KV sph	86.4
dev + sph	3.1
KV cap	112.8

5.3 Creep mechanisms of AAS and comparison to OPC

The early-stage strains can be attributed to water movements in the C(-A)-S-H structure. This was already hypothesized in the seepage theory [9]. For OPC, NMR measurements showed that water is redistributed from gel pores to larger pores [55] and that this redistribution is mainly reversible. This justifies the use of the Kelvin-Voigt unit for early-stage creep.

At a later stage, there is a global consensus in the literature that the creep of concrete

is due to deviatoric stresses [18, 19, 29, 49, 56, 57]. This is confirmed by the results of this study for AAS concrete. The response of both C-A-S-H and C-S-H to deviatoric stresses leads to irreversible strains [19, 58–60]. Two main mechanisms have been described in the literature to explain the long-term creep of concrete. The first type considers a sliding of C(-A)-S-H layers [49, 56, 57]. In [59], Manzano et al. proved with molecular simulations that the structure of glassy C-S-H presents predefined slip planes enabling the sliding of C-S-H nanoparticles. Haist et al. [49] concluded that the slippage between C-S-H nanoparticles was the main contributing factor of creep. The second mechanism is a reorganization of the structure because of deviatoric stresses. Thomas & Jennings suggested that creep is due to the rearrangement of C-S-H globules [13]. It can be noted that for Alizadeh et al. [57], both mechanisms (sliding of C-A-S-H and rearrangement of C-A-S-H) are similar and lead to a higher packing density. From synchrotron-radiation-based XRD experiments, Geng et al. [58] showed that nanocrystals of C-A-S-H align with the compressive load. Further studies with the same technique were carried out by Gartner et al. and Li et al. in [18–20]. The results from Li et al. [19] indicated that the preferred reorientation of C(-A)-S-H is accompanied by a more compacted microstructure i.e. a higher packing density. In [20], Li et al. showed that the preferred orientation of C(-A)-S-H is the creep mechanism for deviatoric stresses under 100 MPa and the sliding of C(-A)-S-H nanoparticles is the creep mechanism for deviatoric stresses above 100 MPa. However, in practice, typical stresses on C(-A)-S-H are in the range of tens of MPa. Independently of the mechanism, sliding of C(-A)-S-H or reorganization of the microstructure, the different theories agree on the fact that creep takes place in the interlayer of C(-A)-S-H. Either sliding occurs there [56, 57, 59] or intergranular space is reduced [20]. In addition, molecular simulations showed that the intralayer structure has a negligible shear deformation [56]. Both theories conclude that interlayer water has a lubricant role for the creep behavior [17, 19, 56, 59]. Kai et al. [56] added that Ca^{2+} and OH^- facilitates also the sliding of C(-A)-S-H nanoparticles.

In comparison to OPC concrete, AAS concrete creeps more. At the early stage, it could be due to the denser pore structure of AAS with more pores under 50 nm, as investigated in a previous study [50]. Water redistribution and corresponding stress redistribution could lead to higher strains. As shown in section 5.1, the contact creep modulus obtained by nanoindentation is lower for AAS compared to OPC. Thus, the matrix of reaction products tends to creep more. Gardner et al. [18] showed that there are differences in the responses to deviatoric stresses for C-A-S-H and C-S-H. For cross-linked C-A-S-H gel, relaxation of Si-O tetrahedra takes place, while for the non-crosslinked C-S-H, the Si-O bond behaves as for an isomorphic contraction and interlayer sliding can occur leading to breaking chains. Another explanation for the higher creep rate for AAS is that aluminum in C-A-S-H increases the amount of bounded water [61] that can act as a lubricant for creep, as discussed before. Lastly, the difference between the creep of AAS

concrete and OPC concrete could be due to the types of secondary reaction products. For OPC, they are mainly crystalline and do not contribute to creep [19]. On the contrary, secondary reaction products of AAS are mainly amorphous [62] and can have a higher tendency to creep.

6 Conclusion

In this contribution, a multi-scale micromechanics-based model is developed to downscale creep properties of the matrix of reaction products of Alkali-Activated Slag (AAS). The downscaling is performed on experimental results on concrete. The results are compared to the contact creep modulus obtained from nanoindentation tests. The following conclusions can be drawn:

- the basic creep of AAS is higher than that of OPC. It increases with the silicate modulus M_S. This could be due to a higher amount of capillary porosity in the case of higher M_S.
- Nanoindentation tests show that the contact creep modulus of AAS is lower than that reported in the literature for OPC.
- nanoindentation tests show that the contact creep modulus of AAS is lower than that reported in the literature for OPC. The contact creep modulus obtained by nanoindentation tests provides a correct estimation of the long-term creep modulus of the matrix of reaction products.
- the higher creep of AAS compared to OPC could be explained by lower contact creep modulus at the nanoscale, more gel water and lower crystallinity of the secondary reaction products in the case of AAS.
- the cause of the creep of AAS concrete is the deviatoric creep of the matrix of reaction products. The latter can be split into an early-stage creep and a long-term creep. The early-stage creep, modeled by a Kelvin-Voigt unit, would correspond to reversible creep due to water movements from gel pores to capillary pores. The long-term creep can be modeled by a logarithmic function for the deviatoric part of the compliance function. This supports both mechanisms of sliding of C-A-S-H and the preferred orientation of C-A-S-H to explain the creep of AAS concrete.

Further investigations should be led to determine the creep behavior when samples are loaded at a very early age. Experimental results made on OPC indicated that it has a large contribution [63, 64]. Additional mechanisms corresponding to the dissolution of unreacted particles could explain the creep behavior as suggested in the solidification theory [6].

References

1. RILEM draft recommendation: TC-242-MDC multi-decade creep and shrinkage of concrete: material model and structural analysis. *Materials and Structures* **48,** 753–770. ISSN: 1359-5997 (2015).
2. Šmilauer, V. & Bažant, Z. P. Identification of viscoelastic C-S-H behavior in mature cement paste by FFT-based homogenization method. *Cement and Concrete Research* **40,** 197–207. ISSN: 00088846 (2010).
3. Göbel, L., Königsberger, M., Osburg, A. & Pichler, B. Viscoelastic Behavior of Polymer-Modified Cement Pastes: Insight from Downscaling Short-Term Macroscopic Creep Tests by Means of Multiscale Modeling. *Applied Sciences* **8,** 487 (2018).
4. Lavergne, F. & Barthélémy, J.-F. Confronting a refined multiscale estimate for the aging basic creep of concrete with a comprehensive experimental database. *Cement and Concrete Research* **136,** 106163. ISSN: 00088846 (2020).
5. FIB. fib Model Code for Concrete Structures 2010. *International Federation for Structural Concrete (fib), Lausanne* (2013).
6. Bažant, Z. P. & Prasannan, S. Solidification theory for aging creep. *Cement and Concrete Research* **18,** 923–932. ISSN: 00088846. `https://www.sciencedirect.com/science/article/pii/0008884688900282` (1988).
7. Tošić, N., de La Fuente, A. & Marinković, S. Creep of recycled aggregate concrete: Experimental database and creep prediction model according to the fib Model Code 2010. *Construction and Building Materials* **195,** 590–599. ISSN: 09500618 (2019).
8. Ye, H. Creep Mechanisms of Calcium–Silicate–Hydrate: An Overview of Recent Advances and Challenges. *International Journal of Concrete Structures and Materials* **9,** 453–462. ISSN: 1976-0485 (2015).
9. Powers, T. C. The thermodynamics of volume change and creep. *Materials and Structures* **1,** 487–507. ISSN: 1359-5997. `https://doi.org/10.1007/BF02473638` (1968).
10. Bazant, Z., Hauggaard-Nielsen, A. & Baweja, S. Microprestress-Solidification Theory for Concrete Creep. I: Aging and Drying Effects. *Journal of Engineering Mechanics - ASCE* **123,** 1188–1194. ISSN: 0733-9399 (1997).
11. Jirásek, M. & Havlásek, P. Microprestress–solidification theory of concrete creep: Reformulation and improvement. *Cement and Concrete Research* **60,** 51–62. ISSN: 00088846 (2014).
12. Wittmann, F. H. Interaction of Hardened Cement Paste and Water. *Journal of the American Ceramic Society* **56,** 409–415. ISSN: 0002-7820 (1973).

13. Thomas, J. J. & Jennings, H. M. A colloidal interpretation of chemical aging of the C-S-H gel and its effects on the properties of cement paste. *Cement and Concrete Research* **36,** 30–38. ISSN: 00088846 (2006).

14. Pachon-Rodriguez, E. A., Guillon, E., Houvenaghel, G. & Colombani, J. Wet creep of hardened hydraulic cements — Example of gypsum plaster and implication for hydrated Portland cement. *Cement and Concrete Research* **63,** 67–74. ISSN: 00088846 (2014).

15. Feldman, R. F. Mechanism of creep of hydrated portland cement paste. *Cement and Concrete Research* **2,** 521–540. ISSN: 00088846. `https://www.sciencedirect.com/science/article/pii/000888467290107X` (1972).

16. Ruetz, W. A hypothesis for the creep of hardened cement paste and the influence of simultaneous shrinkage. *International Conference On the Structure of Concrete, Cement and Concrete Association, London, England* (1968).

17. Morshedifard, A., Masoumi, S. & Abdolhosseini Qomi, M. J. Nanoscale origins of creep in calcium silicate hydrates. *Nature communications* **9,** 1785 (2018).

18. Gardner, D. W. *et al.* Plastic deformation mechanism of calcium-silicate hydrates determined by deviatoric-stress Raman spectroscopy. *Cement and Concrete Research* **146,** 106476. ISSN: 00088846 (2021).

19. Li, J., Zhang, W. & Monteiro, P. J. Preferred orientation of calcium aluminosilicate hydrate compacts: Implications for creep and indentation. *Cement and Concrete Research* **143,** 106371. ISSN: 00088846 (2021).

20. Li, J. & Zhang, W. Preferred orientation of calcium silicate hydrate and its implication to concrete creep. *Composites Part B: Engineering* **247,** 110297. ISSN: 13598368 (2022).

21. Vandamme, M. & Ulm, F.-J. Nanoindentation investigation of creep properties of calcium silicate hydrates. *Cement and Concrete Research* **52,** 38–52. ISSN: 00088846 (2013).

22. Vandamme, M. *The nanogranular origin of concrete creep: a nanoindentation investigation of microstructure and fundamental properties of calcium-silicate-hydrates* `https://navier-lab.fr/wp-content/uploads/2020/02/vandamme-thesis.pdf` (2008).

23. Nguyen, D.-T. *Microindentation Creep of Calcium-Silicate-Hydrate and Secondary Hydrated Cement Systems* PhD thesis (Université d'Ottawa / University of Ottawa, 2014).

24. Aili, A., Vandamme, M., Torrenti, J.-M., Masson, B. & Sanahuja, J. Time evolutions of non-aging viscoelastic Poisson's ratio of concrete and implications for creep of C-S-H. *Cement and Concrete Research* **90,** 144–161. ISSN: 00088846 (2016).

25. Bentz, D. P. *CEMHYD3D* Gaithersburg, MD, 2005.

26. Baweja, S. & Bazant, Z. Creep and shrinkage prediction model for analysis and design of concrete structures - model B3. *Materials and Structures* **28,** 357–365. ISSN: 1359-5997 (1995).

27. Bazant, Z. P. & Baweja, S. Justification and refinements of model B3 for concrete creep and shrinkage 1. statistics and sensitivity. *Materials and Structures* **28,** 415–430. ISSN: 1359-5997 (1995).

28. Bazant, Z. P. & Baweja, S. Justification and refinements of model B3 for concrete creep and shrinkage 2. Updating and theoretical basis. *Materials and Structures* **28,** 488–495. ISSN: 1359-5997 (1995).

29. Pichler, C. & Lackner, R. A multiscale creep model as basis for simulation of early-age concrete behavior. *Computers and Concrete* **5,** 295–328. ISSN: 1598-8198 (2008).

30. Königsberger, M., Honório, T., Sanahuja, J., Delsaute, B. & Pichler, B. L. Homogenization of nonaging basic creep of cementitious materials: A multiscale modeling benchmark. *Construction and Building Materials* **290,** 123144. ISSN: 09500618 (2021).

31. Honorio, T., Bary, B. & Benboudjema, F. Multiscale estimation of ageing viscoelastic properties of cement-based materials: A combined analytical and numerical approach to estimate the behaviour at early age. *Cement and Concrete Research* **85,** 137–155. ISSN: 00088846 (2016).

32. Comprehensive Database on Concrete Creep and Shrinkage. *ACI Materials Journal* **105.** ISSN: 0889-325X (2008).

33. Herrera, R., Kinrade, S. D. & Catalan, L. J. A Comparison of Methods for Determining Carbonation Depth in Fly Ash-Blended Cement Mortars. *ACI Materials Journal* **112.** ISSN: 0889-325X (2015).

34. Baronet, J., Sorelli, L., Charron, J.-P., Vandamme, M. & Sanahuja, J. A two-scale method to rapidly characterize the logarithmic basic creep of concrete by coupling microindentation and uniaxial compression creep test. *Cement and Concrete Composites* **125,** 104274. ISSN: 09589465 (2022).

35. Suwanmaneechot, P., Aili, A. & Maruyama, I. Creep behavior of C-S-H under different drying relative humidities: Interpretation of microindentation tests and sorption measurements by multi-scale analysis. *Cement and Concrete Research* **132,** 106036. ISSN: 00088846 (2020).

36. Myers, R. J., Bernal, S. A. & Provis, J. L. Phase diagrams for alkali-activated slag binders. *Cement and Concrete Research* **95,** 30–38. ISSN: 00088846 (2017).

37. Ma, J. & Dehn, F. Shrinkage and creep behavior of an alkali-activated slag concrete. *Structural Concrete* **18,** 801–810. ISSN: 14644177 (2017).

38. Zhou, X., Wang, Y., Zheng, W., Chen, P. & Zeng, Y. Effect of Stress–Strength Ratio on Creep Property of Sodium Silicate–Based Alkali-Activated Slag Concrete. *Applied Sciences* **9,** 3643 (2019).

39. Humad, A. M., Provis, J. L., Habermehl-Cwirzen, K., Rajczakowska, M. & Cwirzen, A. Creep and Long-Term Properties of Alkali-Activated Swedish-Slag Concrete. *Journal of Materials in Civil Engineering* **33,** 635. ISSN: 0899-1561 (2021).

40. Caron, R., Patel, R. A., Bogner, A. & Dehn, F. Multi-scale experimental investigation and analytical micro-mechanical modeling to determine Young's modulus of alkali-activated slag concrete. *Construction and Building Materials* **383,** 131272. ISSN: 09500618 (2023).

41. Sanahuja, J. Effective behaviour of ageing linear viscoelastic composites: Homogenization approach. *International Journal of Solids and Structures* **50,** 2846–2856. ISSN: 00207683 (2013).

42. DIN EN 12390-13. Prüfung von Festbeton – Teil 13: Bestimmung des Elastizitätsmoduls unter Druckbelastung (Sekantenmodul); Deutsche und Englische Fassung prEN 12390-13:2019. *Beuth Verlag* (2019).

43. Oliver, W. & Pharr, G. An improved technique for determining hardness and elastic modulus using load and displacement sensing indentation experiments. *Journal of Materials Research* **7,** 1564–1583 (1992).

44. Hu, C. Nanoindentation as a tool to measure and map mechanical properties of hardened cement pastes. *MRS Communications* **5,** 83–87. ISSN: 2159-6859 (2015).

45. Wilson, W., Sorelli, L. & Tagnit-Hamou, A. Automated coupling of NanoIndentation and Quantitative Energy-Dispersive Spectroscopy (NI-QEDS): A comprehensive method to disclose the micro-chemo-mechanical properties of cement pastes. *Cement and Concrete Research* **103,** 49–65. ISSN: 00088846 (2018).

46. Thomas, R. J., Gebregziabiher, B. S., Giffin, A. & Peethamparan, S. Micromechanical properties of alkali-activated slag cement binders. *Cement and Concrete Composites* **90,** 241–256. ISSN: 09589465 (2018).

47. Fang, G. & Zhang, M. Multiscale micromechanical analysis of alkali-activated fly ash-slag paste. *Cement and Concrete Research* **135,** 106141. ISSN: 00088846 (2020).

48. Stemmermann, P. *et al.* Chemo-mechanical characterization of hydrated calcium-hydrosilicates with coupled Raman- and nanoindentation measurements. *Applied Geochemistry* **118,** 104582. ISSN: 08832927 (2020).

49. Haist, M. *et al.* Creep in reactive colloidal gels: A nanomechanical study of cement hydrates. *Physical Review Research* **3,** 68 (2021).

50. Caron, R. *et al.* Microstructure development of slag activated with sodium silicate solution: Experimental characterization and thermodynamic modeling. *Journal of Building Engineering* **71,** 106398. ISSN: 23527102 (2023).

51. Taghvayi, H., Behfarnia, K. & Khalili, M. The Effect of Alkali Concentration and Sodium Silicate Modulus on the Properties of Alkali-Activated Slag Concrete. *Journal of Advanced Concrete Technology* **16,** 293–305. ISSN: 1346-8014 (2018).

52. Kumarappa, D. B., Peethamparan, S. & Ngami, M. Autogenous shrinkage of alkali activated slag mortars: Basic mechanisms and mitigation methods. *Cement and Concrete Research* **109,** 1–9. ISSN: 00088846. `https://www.sciencedirect.com/science/article/pii/S0008884617308086` (2018).

53. Caron, R., Patel, R. A. & Dehn, F. Activation kinetic model and mechanisms for alkali-activated slag cements. *Construction and Building Materials* **323,** 126577. ISSN: 09500618 (2022).

54. Lee, H., Vimonsatit, V., Chindaprasirt, P., Ngo, T. & Mendis, P. Creep properties of cement and alkali activated fly ash materials using nanoindentation technique. *Construction and Building Materials* **168,** 547–555. ISSN: 09500618 (2018).

55. Wyrzykowski, M. *et al.* Water Redistribution–Microdiffusion in Cement Paste under Mechanical Loading Evidenced by 1 H NMR. *The Journal of Physical Chemistry C* **123,** 16153–16163. ISSN: 1932-7447 (2019).

56. Kai, M. F., Zhang, L. W. & Liew, K. M. New insights into creep characteristics of calcium silicate hydrates at molecular level. *Cement and Concrete Research* **142,** 106366. ISSN: 00088846 (2021).

57. Alizadeh, R., Beaudoin, J. J. & Raki, L. Viscoelastic nature of calcium silicate hydrate. *Cement and Concrete Composites* **32,** 369–376. ISSN: 09589465 (2010).

58. Geng, G. *et al.* Preferred orientation of calcium aluminosilicate hydrate induced by confined compression. *Cement and Concrete Research* **113,** 186–196. ISSN: 00088846 (2018).

59. Manzano, H., Masoero, E., Lopez-Arbeloa, I. & Jennings, H. M. Shear deformations in calcium silicate hydrates. *Soft Matter* **9,** 7333. ISSN: 1744-683X (2013).

60. Su, L., Wang, Y.-f., Mei, S.-q. & Li, P.-f. Experimental investigation on the fundamental behavior of concrete creep. *Construction and Building Materials* **152,** 250–258. ISSN: 09500618 (2017).

61. Kapeluszna, E., Kotwica, Ł., Różycka, A. & Gołek, Ł. Incorporation of Al in C-A-S-H gels with various Ca/Si and Al/Si ratio: Microstructural and structural characteristics with DTA/TG, XRD, FTIR and TEM analysis. *Construction and Building Materials* **155,** 643–653. ISSN: 09500618 (2017).

62. Jae Eun Oh, Paulo J.M. Monteiro, Ssang Sun Jun, Sejin Choi & Simon M. Clark. The evolution of strength and crystalline phases for alkali-activated ground blast furnace slag and fly ash-based geopolymers. *Cement and Concrete Research* **40,** 189–196. ISSN: 00088846. `https://www.sciencedirect.com/science/article/pii/S0008884609002932` (2010).

63. Delsaute, B., Torrenti, J.-M. & Staquet, S. Modeling basic creep of concrete since setting time. *Cement and Concrete Composites* **83,** 239–250. ISSN: 09589465 (2017).

64. Wyrzykowski, M., Scrivener, K. & Lura, P. Basic creep of cement paste at early age - the role of cement hydration. *Cement and Concrete Research* **116,** 191–201. ISSN: 00088846 (2019).

Insights into creep mechanisms of alkali-activated slag concrete: multi-scale characterization and micromechanical modeling
Supplementary Material

Richard Caron[1,2], Ravi A. Patel[1,2], Andreas Bogner[1,2], Frank Dehn[1,2]

May 9, 2023

This document provides further results of the analysis of creep at an early stage for the specimens lS-7d, hS-7d and hS-28d. The results of the modeling with the different hypotheses presented in Section 5.2 are provided in Table 1 and Figure 1.

Table 1: Root mean square of each tested model against viscous creep compliance of mix lS-7d, hS-7d and hS-28d

model	error for lS-7d	error for hS-7d	error for hS-28d
initial model	2.7	16.4	27.5
log	108.2	239.4	50.0
KV sph	85.1	202.5	46.6
dev + sph	1.0	14.5	25.2
KV cap	130.4	283.9	52.4

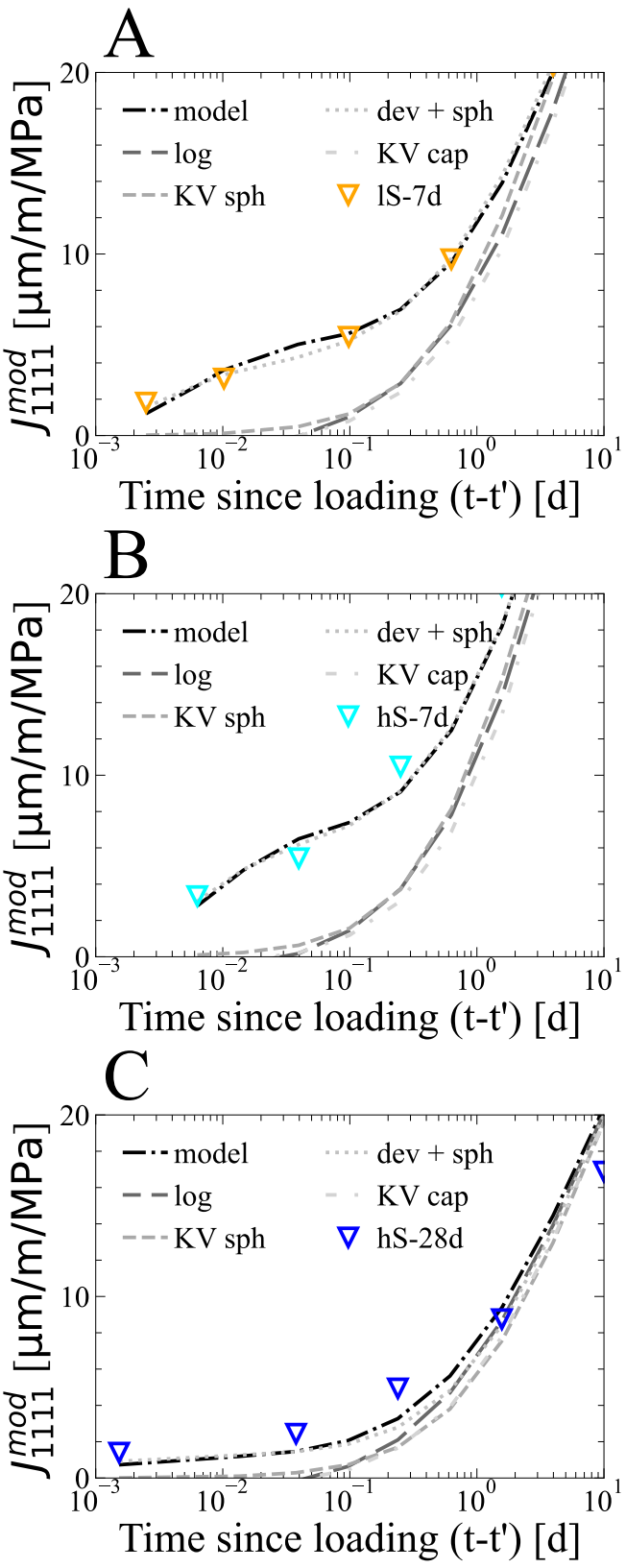

Figure 1: Comparison of different hypotheses about creep behavior of phases with the creep results of the specimen (A) lS-7d, (B) hS-7d and (C) hS-28d.